



SAPIENZA
UNIVERSITÀ DI ROMA

Probing new physics on the horizon of black holes with gravitational waves

Scuola di dottorato Vito Volterra

Dottorato di Ricerca in Fisica – XXXIV Ciclo

Candidate

Elisa Maggio

ID number 1468241

Thesis Advisor

Prof. Paolo Pani

2022

Thesis defended on 22 February 2022
in front of a Board of Examiners composed by:
Prof. Alfredo Urbano (chairman)
Prof. Massimo Bianchi
Prof. Enrico Barausse

Probing new physics on the horizon of black holes with gravitational waves

Ph.D. thesis. Sapienza – University of Rome

© 2022 Elisa Maggio. All rights reserved

This thesis has been typeset by \LaTeX and the Sapthesis class.

Author's email: elisa.maggio@uniroma1.it

Abstract

Black holes are the most compact objects in the Universe. According to general relativity, black holes have a horizon that hides a singularity where Einstein's theory breaks down. Recently, gravitational waves opened the possibility to probe the existence of horizons and investigate the nature of compact objects. This is of particular interest given some quantum-gravity models which predict the presence of horizonless and singularity-free compact objects. Such exotic compact objects can emit a different gravitational-wave signal relative to the black hole case. In this thesis, we analyze the stability of horizonless compact objects, and derive a generic framework to compute their characteristic oscillation frequencies. We provide an analytical, physically-motivated template to search for the gravitational-wave echoes emitted by these objects in the late-time postmerger signal. Finally, we infer how extreme mass-ratio inspirals observable by future gravitational-wave detectors will allow for model-independent tests of the black hole paradigm.

Contents

Preface	ix
Introduction	xiii
1 Tests of the black hole paradigm	1
1.1 Gravitational waves from compact binary coalescences	1
1.1.1 Review of current observations	1
1.1.2 Stages of the waveform	2
1.2 Inspiral-merger-ringdown consistency test	4
1.3 Parametrized tests	5
1.3.1 Constraints on generic deviations in the waveform	5
1.3.2 Measurement of the spin-induced quadrupole moment	7
1.3.3 Tests of the remnant properties	8
1.3.4 Searches for gravitational-wave echoes	10
1.4 Prospects with next-generation detectors	11
2 Exotic compact objects	13
2.1 Motivation	13
2.2 A parametrized classification	15
2.2.1 The Buchdhal theorem	16
2.3 Review of some remarkable models	17
2.3.1 Boson stars	17
2.3.2 Gravastars	19
2.3.3 Wormholes	19
2.3.4 Fuzzballs	20
2.3.5 Anisotropic stars	20
2.3.6 Firewalls, nonlocal stars, and superspinars	20
2.4 Phenomenology of exotic compact objects	21
2.4.1 Tests of the multipolar structure	21
2.4.2 Tests of the tidal heating	22
2.4.3 Measurements of the tidal deformability	22
2.4.4 Ringdown tests	23

3	Spectroscopy of horizonless compact objects	25
3.1	A static model	25
3.2	Ringdown spectrum of ultracompact objects	26
3.2.1	Linear perturbations in the Schwarzschild background	26
3.2.2	Boundary conditions	28
3.2.3	Numerical procedure	29
3.2.4	Black hole vs horizonless compact object spectrum	30
3.3	Membrane paradigm for compact objects	32
3.3.1	Setup	32
3.3.2	Boundary conditions	33
3.3.3	Effective reflectivity of compact objects	34
3.3.4	Quasi-normal mode spectrum	36
3.3.5	Current constraints and prospects of detectability	39
3.4	Appendix: Boundary condition for perfectly reflecting objects	42
3.5	Appendix: Continued fractions method	44
3.6	Appendix: Membrane paradigm	46
3.7	Appendix: Fisher information matrix	54
4	Ergoregion instability	55
4.1	A spinning model	55
4.2	The ergoregion	56
4.3	The Penrose process	57
4.4	Ergoregion instability in horizonless compact objects	58
4.4.1	Linear perturbations in the Kerr background	58
4.4.2	Boundary conditions	60
4.4.3	Numerical procedure	61
4.4.4	Instability in the quasi-normal mode spectrum	62
4.5	How to quench the ergoregion instability	65
4.6	Appendix: The Detweiler transformation	68
4.7	Appendix: Boundary condition for spinning perfectly reflecting objects	69
4.8	Appendix: Analytical quasi-normal modes	71
5	Gravitational-wave echoes	75
5.1	Schematic picture	75
5.2	Analytical template	77
5.2.1	Transfer function	77
5.2.2	Black hole reflection coefficient in the low-frequency approximation	78
5.2.3	Modeling the black hole response at infinity	79
5.2.4	Modeling the black hole response at the horizon	80
5.2.5	Parameters and validity of the template	81
5.3	Properties of gravitational-wave echoes	83
5.3.1	Mixing of polarizations	84

5.3.2	Phase inversion	85
5.3.3	Energy emission and superradiant instability	87
5.3.4	Frequency content	88
5.4	Modifications to the prompt ringdown	89
5.5	Prospects of detection with current and future detectors	91
5.5.1	Conservative case: 5 ringdown+3 ECO parameters	92
5.5.2	Optimistic case: 3 ECO parameters	93
5.5.3	Constraints on the reflectivity	93
5.6	Appendix: Black hole response for particular sources	95
6	Extreme mass-ratio inspirals around a horizonless source	97
6.1	A model for the central compact object	97
6.2	Linear perturbations from a point particle	98
6.2.1	Central black hole	99
6.2.2	Central horizonless compact object	100
6.3	Numerical procedure	101
6.4	Energy fluxes and excitation of resonances	103
6.5	Adiabatic evolution and dephasing	109
6.5.1	Non-spinning central object	109
6.5.2	Spinning central object	110
6.5.3	The role of the compactness	111
6.6	Waveform and overlap	113
6.7	A case study: Boltzmann reflectivity	114
	Conclusions and future prospects	117
	Bibliography	119

Preface

The work presented in this thesis has been carried out mainly at the Physics Department of Sapienza University of Rome in the research group of gravity theory and gravitational wave phenomenology. Part of this work was carried out at the Consortium for Fundamental Physics, School of Mathematics and Statistics, University of Sheffield, United Kingdom, and at the Centro de Astrofísica e Gravitação (CENTRA), Instituto Superior Técnico, Universidade de Lisboa, Portugal. I thank these institutions for their kind hospitality.

List of publications

The work in this thesis was accomplished with different scientific collaborations, whose members I kindly acknowledge.

- Chapter 2 is the outcome of a collaboration with Paolo Pani and Guilherme Raposo based on:

E. Maggio, P. Pani, G. Raposo, “Testing the nature of dark compact objects with gravitational waves,” Invited chapter for C. Bambi, S. Katsanevas, K.D. Kokkotas (editors), *Handbook of Gravitational Wave Astronomy*, Springer, Singapore (2021), [arXiv:2105.06410](https://arxiv.org/abs/2105.06410), https://doi.org/10.1007/978-981-15-4702-7_29-1.

- Chapter 3 is the outcome of a collaboration with Luca Buoninfante, Anupam Mazumdar and Paolo Pani based on:

E. Maggio, L. Buoninfante, A. Mazumdar, P. Pani, “How does a dark compact object ringdown?,” *Phys. Rev. D* **102**, 064053 (2020), [arXiv:2006.14628](https://arxiv.org/abs/2006.14628).

- Chapter 4 is the outcome of a collaboration with Vitor Cardoso, Sam Dolan, Valeria Ferrari and Paolo Pani based on:

E. Maggio, P. Pani, and V. Ferrari, “Exotic compact objects and how to quench their ergoregion instability,” *Phys. Rev. D* **96**, 104047 (2017), [arXiv:1703.03696](https://arxiv.org/abs/1703.03696).

E. Maggio, V. Cardoso, S. Dolan, and P. Pani, “Ergoregion instability of exotic compact objects: electromagnetic and gravitational perturbations and the role of absorption,” *Phys. Rev. D* **99**, 064007 (2019), [arXiv:1807.08840](#);

- Chapter 5 is the outcome of a collaboration with Swetha Bhagwat, Paolo Pani and Adriano Testa based on:

E. Maggio, A. Testa, S. Bhagwat, and P. Pani, “Analytical model for gravitational-wave echoes from spinning remnants,” *Phys. Rev. D* **100**, 064056 (2019), [arXiv:1907.03091](#).

- Chapter 6 is the outcome of a collaboration with Maarten van de Meent and Paolo Pani based on:

E. Maggio, M. van de Meent, P. Pani, “Extreme mass-ratio inspirals around a spinning horizonless compact object,” *Phys. Rev. D* in press (2021), [arXiv:2106.07195](#).

As a part of the activities during my PhD, I served as a member of the LISA Consortium, being involved in the writing of the LISA Fundamental Physics and the LISA Waveform White Papers, the LISA Figure of Merit analysis, and the LISA Early Career Scientists (LECS) group. Part of the outcome of these activities is in preparation or has been submitted for publication and is not included in this thesis.

Conventions

In this work, geometrized units, $G = c = 1$, are adopted where G is the gravitational constant, and c is the speed of light.

The signature of the metric adopts the $(-, +, +, +)$ convention. The Greek letters run over the four-dimensional spacetime indices. The comma stands for an ordinary derivative, and the semi-colon stands for a covariant derivative.

\mathbf{M}^* is the complex conjugate of a matrix, and \mathbf{M}^\top is the transpose of a matrix. $\Re(n)$ and $\Im(n)$ are the real and the imaginary part of a number, respectively.

Abbreviations

BH	Black Hole
ECO	Exotic Compact Object
EMRI	Extreme Mass-Ratio Inspiral
ISCO	Innermost Stable Circular Orbit
LIGO	Large Interferometer Gravitational-wave Observatory
LISA	Laser Interferometer Space Antenna
GR	General Relativity
GW	Gravitational Wave
NS	Neutron Star
PN	Post-Newtonian
QNM	Quasi-Normal Mode
SNR	Signal-to-Noise Ratio
TH	Tidal Heating
ZAMO	Zero Angular Momentum Observer

Introduction

The landmark detection of gravitational waves (GWs) provides the unique opportunity to test gravity in the strong-field regime and infer the nature of astrophysical sources. So far, the ground-based detectors LIGO and Virgo have detected ninety GW events from the coalescence of compact binaries [1, 2, 3, 4]. These detections allowed us to observe for the first time the coalescence of two black holes (BHs) and revealed that their masses can be heavier than the ones observed in the electromagnetic spectrum [5, 2]. Recent important discoveries include the first multi-messenger observation of a binary neutron star (NS) merger [6, 7] and the observation of the formation of an intermediate-mass BH [8].

Furthermore, GWs provide a new channel for probing Einstein's theory of gravity in a regime inaccessible to traditional astronomical observations, namely the strong-field and highly dynamical one. Several consistency tests of the GW data with the predictions of general relativity (GR) have been performed. No evidence for new physics has been reported within current measurement accuracies [5, 9, 10, 11].

The GW signal emitted by compact binary coalescences is characterized by three main stages: the *inspiral* phase, when the two bodies orbit around each other and the emission of GWs makes the orbit shrink, the *merger* phase, when the two bodies coalesce, and the *ringdown* when the final remnant relaxes to an equilibrium solution. The study of the different stages of the GW signal allows us to infer the properties of the compact objects and understand their nature.

Several extensions of GR predict the existence of regular and horizonless compact objects, also known as exotic compact objects (ECOs) [12, 13]. Indeed, the presence of the horizon poses some theoretical problems, the most notable ones being the existence of a singularity in the black-hole interior and the Hawking information loss paradox [14].

ECOs can mimic the features of BHs through electromagnetic observations since they can be as compact as BHs [15]. Indeed, the supermassive object at the center of the M87 galaxy observed by the Event Horizon Telescope poorly constrains few models of ECOs [16]. Furthermore, current GW observations do not exclude ECOs that could potentially explain events in the mass gap between NSs and BHs and due to pair-instability supernova processes [8, 17, 18].

One way to distinguish ECOs from BHs is by analyzing the ringdown stage of a compact binary coalescence. The ringdown is dominated by the complex characteristic frequencies – the so-called quasi-normal modes (QNMs) – of the remnant, that differ dramatically if the latter is a BH or an ECO [19]. By inferring the QNMs of the remnant, we can test whether they are compatible with the predicted spectrum for a BH.

Current observations of the fundamental QNM in the ringdown of binary coalescences are compatible with remnant BHs as predicted by GR [9, 10, 11]; however, the characterization of the remnant is still an open problem. The no-hair theorems establish that BHs in GR are determined uniquely by two parameters, i.e., their mass and angular momentum [20, 21]. Therefore, the measurement of one complex QNM allows us only to estimate the parameters of the BH. A test of the BH paradigm would require the identification of at least two complex QNM frequencies. Louder GW events, to be collected as detector sensitivity improves, and more sophisticated parametrized waveforms will allow us to extract more information about the remnant.

If the remnant of a merger is an ECO that is almost as compact as a BH, the prompt ringdown signal would be nearly indistinguishable from that of a BH [19]. A characteristic fingerprint of ECOs would be the appearance of a modulated train of GW echoes at late times due to the absence of the horizon [19, 22]. Tentative evidence for GW echoes in LIGO/Virgo data has been reported in the last few years [23], but recent independent searches argued that the statistical significance for GW echoes is consistent with noise [24, 10, 11].

Besides ECO fingerprints in the GW emission, in this thesis we analyze the astrophysical viability of ECOs as BH alternatives. Indeed, spinning horizonless compact objects are prone to the so-called ergoregion instability when spinning sufficiently fast [25, 26, 27]. The endpoint of the instability could be a slowly-spinning ECO [28, 29] or dissipation within the object could lead to a stable remnant [30, 31, 32]. If confirmed, the ergoregion instability could provide a strong theoretical argument in favor of the BH paradigm for which rapidly spinning compact objects must have a horizon.

The prospect for detectability of new physics will improve in the future with the next-generation detectors like the ground-based observatories Einstein Telescope [33] and Cosmic Explorer [34], and the space-based Laser Interferometer Space Antenna (LISA) [35]. In particular, LISA is an extremely promising observatory of fundamental physics. Planned for launch in 2034, LISA will detect GWs in a lower frequency band than ground-based detectors. LISA will observe a plethora of astrophysical sources, particularly extreme mass-ratio inspirals (EMRIs) in which a stellar-mass object orbits around the supermassive object at the center of a galaxy [36].

EMRIs are unique probes of the nature of supermassive compact objects. Since LISA will observe inspirals that can last for years, the phase shift of the waveform will be tracked with high precision and deviations from GR will be

measured accurately. During the inspiral around a horizonless supermassive object, extra resonances would be excited leaving a characteristic imprint in the waveform [37, 38]. Any evidence of partial reflectivity at the surface of the object would also indicate a departure from the classical BH picture [39, 38].

Within this broad and flourishing context, this thesis aims to investigate the nature of compact objects and test the existence of horizons with GWs. This work is organized as follows.

Chapter 1 is dedicated to the tests of the BH paradigm that have been currently performed using GWs. A review of the recent GW observations is presented, and the stages of the gravitational waveform are analyzed. In particular, the consistency tests of GR and the parametrized tests of deviations from GR are described. Finally, the prospects of detecting deviations from GR with next-generation detectors are assessed.

Chapter 2 illustrates the theoretical motivations for studying horizonless compact objects. A parametrized classification of horizonless compact objects is presented depending on their deviations from the standard BH picture. Some remarkable models of ECOs are reviewed, and their phenomenology is compared to the BH case.

Chapter 3 derives the GW signatures of static horizonless compact objects, particularly their QNM spectrum in the ringdown. The system is described by perturbation theory. The imposition of the boundary conditions that describe the response of the compact object to perturbations requires careful analysis. A numerical procedure for the derivation of the QNMs is illustrated. The QNMs of horizonless compact objects are derived both for remnants almost as compact as BHs and with smaller compactness. In the former case, the presence of characteristic low frequencies in the QNM spectrum is highlighted. In the latter case, an extended version of the BH membrane paradigm is applied to derive model-independent deviations from the BH QNM spectrum. Finally, current constraints on horizonless compact objects and prospects of detectability are assessed.

Chapter 4 analyzes spinning horizonless compact objects that are prone to the ergoregion instability above a critical threshold of the spin. The QNMs of spinning horizonless compact objects are derived. From the analysis of the imaginary part of the QNMs, the conditions for which horizonless compact objects are unstable are identified. An analytical description of the QNMs in terms of superradiance is detailed, and ways of quenching the ergoregion instability are provided.

Chapter 5 describes the GW echoes that would be emitted after the prompt ringdown in the case of a horizonless merger remnant. An analytical, physically-motivated template for GW echoes is provided that can be implemented to perform a matched-filter-based search for echoes. Finally, the properties of GW echoes are analyzed, and the prospects of detection with current and future detectors are assessed.

Chapter 6 is devoted to the analysis of EMRIs with a central horizonless

compact object. During the inspiral, extra resonances are excited when the orbital frequency matches the characteristic frequencies of the central ECO. The impact of the resonances in the GW dephasing with respect to the BH case is assessed. This analysis shows that LISA will be able to probe the reflectivity of compact objects with unprecedented accuracy.

Chapter 1

Tests of the black hole paradigm

Si, ma dapprincipio non lo si sapeva, - precisò Qfwfq, - ossia, uno poteva anche prevederlo, ma così, un po' a naso, tirando a indovinare. Io, non per vantarmi, fin da principio scommisi che l'universo ci sarebbe stato, e l'azzeccai, e anche sul come sarebbe stato vinsi parecchie scommesse, col Decano (k)yK.

Italo Calvino, *Le Cosmicomiche*

Astrophysical BHs are the end result of gravitational collapse and hierarchical mergers. The no-hair theorems in GR establish that rotating BHs are well described by the Kerr geometry [20, 21]. Kerr BHs are determined uniquely by two parameters, i.e., their mass M and angular momentum J defined through the dimensionless spin parameter $\chi \equiv J/M^2$. As such, every property of BHs is characterized only by two parameters, i.e., the mass and the spin. Observations of deviations from the properties of Kerr BHs would be an indication of departure from GR.

In this chapter, the tests of the BH paradigm that have been performed with current GW observations are reviewed. Moreover, the prospects of detection of deviations from GR with next-generation detectors are assessed.

1.1 Gravitational waves from compact binary coalescences

1.1.1 Review of current observations

On September 14, 2015, the first GW emitted by the coalescence of a compact binary was detected [40]. The signal, GW150914, is compatible with the inspiral of two BHs as predicted by GR [5]. The remnant BH has final mass $M = 62_{-4}^{+4}M_{\odot}$ and spin $\chi = 0.67_{-0.07}^{+0.05}$, where $\sim 3.0M_{\odot}c^2$ were radiated in GWs.

During the first observing run (O1), which ran from September 12, 2015 to January 19, 2016, the two Advanced LIGO detectors [41] observed a total of three GW events from the coalescence of binary BHs [1]. The second observing run (O2), which ran from November 30, 2016 to August 25, 2017, was joined by the Advanced Virgo detector [42] in the last month of data taking, enabling the first three-detector observations of GWs.

On August 17, 2017, the detectors made their first observation of a binary NS inspiral [6]. The signal, GW170817, was detected with a combined signal-to-noise ratio (SNR) of 32.4, which is the highest SNR in both the O1 and O2 datasets. GW170817 is the most precisely localized event and allowed for the first multi-messenger observation in the electromagnetic spectrum [7]. Indeed, a short γ -ray burst was associated with the NS merger, followed by a transient kilonova counterpart across the electromagnetic spectrum in the same sky location. In addition to GW170817, during O2, a total of seven binary BH mergers were detected [1].

During the first half of the third observing run (O3a), which ran from April 1, 2019 to October 1, 2019, forty-four GW events were detected [2, 3]. For the first time, the observations include binary systems with asymmetric mass ratios [18, 43] and an intermediate-mass BH with $142_{-16}^{+28}M_{\odot}$ [8]. The event, GW190521, is consistent with the merger of two BHs whose primary component lies in the mass gap produced by pulsational pair-instability supernova processes. Indeed, it is predicted that stars with a helium core are subject to an instability which leaves the remnants with mass less than $65M_{\odot}$ [44]. BHs with mass larger than this value might form via hierarchical mergers of smaller BHs. Recent studies showed that the event GW190521 is also consistent with the head-on collision of two horizonless vector boson stars forming a remnant BH [17].

During O3a, the event GW190814 [18] was also detected, whose secondary mass lies in the lower mass gap of $2.5 - 5M_{\odot}$ between known NSs and BHs [45]. Some ECOs such as boson stars and gravastars can potentially support masses beyond $2.5M_{\odot}$. The nature of GW190814 is unknown, and the hypothesis of an exotic secondary is not excluded.

In the second half of the third observing run (O3b), which ran from November 1, 2019 to March 27, 2020, thirty-five GW events were detected including the first observations of NS-BH coalescences [46, 4].

1.1.2 Stages of the waveform

The signal emitted by a compact binary coalescence is characterized by three main stages, as shown in Fig. 1.1.

- (i) The *inspiral* is a phase during which the two compact objects spiral in towards each other as they lose energy to gravitational radiation. At this stage, the two compact objects have large separations and small velocities. The gravitational waveform is well approximated by the post-Newtonian

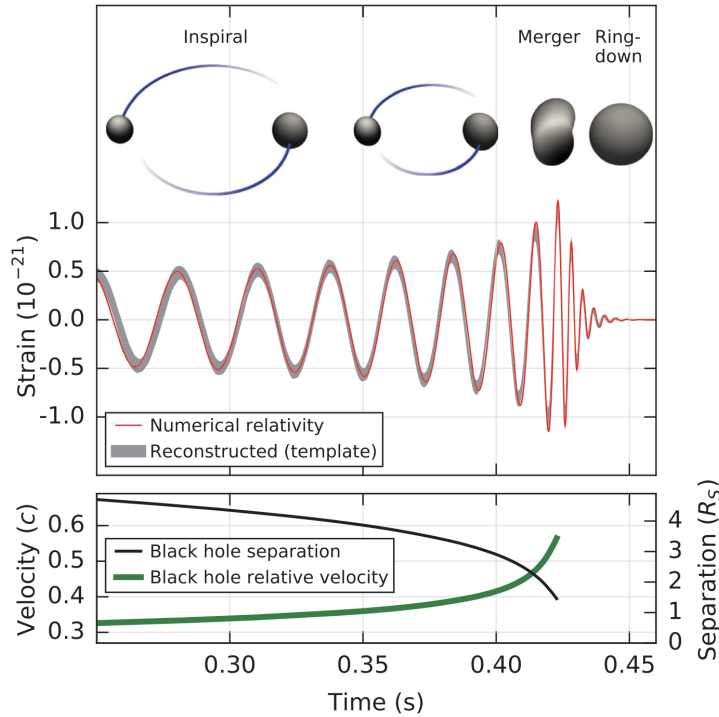


Figure 1.1. Top: The stages of a compact binary coalescence. Estimated GW strain amplitude from the event GW150914 compared to the numerical waveform of a binary BH coalescence. Bottom: The Keplerian effective separation in units of Schwarzschild radii ($R_S = 2M$) and the effective relative velocity of the binary system. [40]

(PN) theory [47, 48, 49, 50, 51]. The latter is a perturbative approach to solve the Einstein field equations in which an expansion in terms of the velocity parameter v/c is performed.

- (ii) The *merger* is a rapid phase in which the two compact objects coalesce to form a final remnant. This stage can be described only by numerical simulations that take into account the nonlinearities of the dynamics.
- (iii) The *ringdown* is a final phase in which the remnant settles down to its stationary state. This stage is described by perturbation theory. The ringdown is dominated by the complex characteristic frequencies of the remnant, the so-called quasi-normal modes (QNMs), which describe the response of the compact object to a perturbation [52, 53, 54, 55, 56, 57, 58]. The BH ringdown signal can be modeled as a superposition of exponentially damped sinusoids

$$h = \sum_{\ell mn} A_{\ell mn}(r) e^{-t/\tau_{\ell mn}} \sin(\omega_{\ell mn} t + \phi_{\ell mn}) {}_{-2}S_{\ell m}(\theta, \varphi), \quad (1.1)$$

where $\omega_{\ell mn}$ are the characteristic frequencies of the remnant, $\tau_{\ell mn}$ are the damping times, $A_{\ell mn}(r) \propto 1/r$ is the amplitude of the signal at a

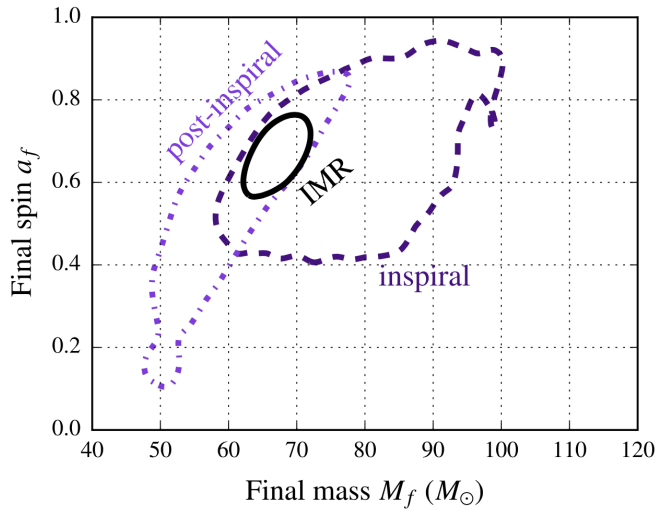


Figure 1.2. 90% credible regions in the joint posterior distributions for the mass M_f and spin a_f of the merger remnant as determined from the inspiral and postinspiral signals, and a full inspiral-merger-ringdown analysis. The posterior distributions have a significant region of overlap. [5]

distance r , $\phi_{\ell mn}$ is the phase, and ${}_sS_{\ell m}(\theta, \varphi) \propto e^{im\varphi}$ are the spin-weighted spheroidal harmonics which depend on the location of the observer to the source. Each mode is described by three integers, namely the angular number ($\ell \geq 0$), the azimuthal number m (such that $|m| \leq \ell$), and the overtone number ($n \geq 0$). From the detection of the ringdown it is possible to infer the QNMs of the remnant and understand the nature of the compact object.

1.2 Inspiral-merger-ringdown consistency test

One way of testing that a gravitational waveform is consistent with the predictions of GR for a binary BH is the inspiral-merger-ringdown test [59]. The test consists in comparing the estimates of the mass and the spin of the remnant obtained from the inspiral (low-frequency) and postinspiral (high-frequency) parts of the waveform. If GR describes well both the adiabatic and the nonlinear regimes, the estimates on the parameters from the two phases are consistent with each other within the statistical uncertainties.

The inspiral-merger-ringdown consistency test was performed in the first GW event, GW150914 [5]. Fig. 1.2 shows the 90% credible contours in the estimates of the remnant mass M_f and spin $a_f \equiv \chi_f M_f$ from the inspiral and the postinspiral stages. The two posterior distributions have a significant region of overlap. Moreover, they agree with the estimate performed using full inspiral-merger-ringdown waveforms.

To constrain possible departures from GR, the following parameters are defined

$$\frac{\Delta M_f}{M_f} = 2 \frac{M_f^{\text{insp}} - M_f^{\text{postinsp}}}{M_f^{\text{insp}} + M_f^{\text{postinsp}}}, \quad (1.2)$$

$$\frac{\Delta \chi_f}{\chi_f} = 2 \frac{\chi_f^{\text{insp}} - \chi_f^{\text{postinsp}}}{\chi_f^{\text{insp}} + \chi_f^{\text{postinsp}}}, \quad (1.3)$$

that quantify the fractional difference between the estimates of the remnant mass and dimensionless spin from the inspiral and postinspiral stages. In GW150914, the joint posterior distribution of the parameters is compatible with the $(0, 0)$ result expected in GR [5].

The inspiral-merger-ringdown test has also been applied to the events in the third LIGO–Virgo GW transient catalog with $\text{SNR} > 6$ both in the inspiral and postinspiral regions. The measurement constraints are

$$\frac{\Delta M_f}{M_f} = 0.03^{+0.14}_{-0.13}, \quad \frac{\Delta \chi_f}{\chi_f} = -0.05^{+0.37}_{-0.38}, \quad (1.4)$$

which are consistent with the expectations of GR [11].

1.3 Parametrized tests

Several parametrized tests have been performed to quantify generic deviations from GR. These tests introduce parametrized modifications to the GR waveform to constrain the degree to which the data agree with GR predictions. The following sections analyze generic deviations from inspiral-merger-ringdown waveforms, the BH spin-induced quadrupole moment, the BH QNMs, and review some searches for GW echoes.

1.3.1 Constraints on generic deviations in the waveform

Deviations from GR can be introduced via parametric deformations of the inspiral-merger-ringdown waveform predicted by GR, without relying on any specific alternative theory of gravity. In this framework [60, 61], the deviations from GR are modeled as fractional changes $\delta \hat{p}_i$ in the parameters p_i that parametrize the GW phase as $p_i \rightarrow (1 + \delta \hat{p}_i) p_i$. The fractional changes are parameters that are introduced to be constrained by the data and check the consistency with the GR values.

The parameters p_i denote collectively all the inspiral $\{\varphi_i\}$ and postinspiral $\{\alpha_i, \beta_i\}$ parameters. In particular, the early-inspiral stage is known analytically up to the order $(v/c)^7$ and is parametrized in terms of the PN coefficients φ_j with $j = 0, \dots, 7$ and the logarithmic terms φ_{jl} with $j = 5, 6$. In addition, the coefficient at $j = -2$ is included corresponding to an effective -1PN term

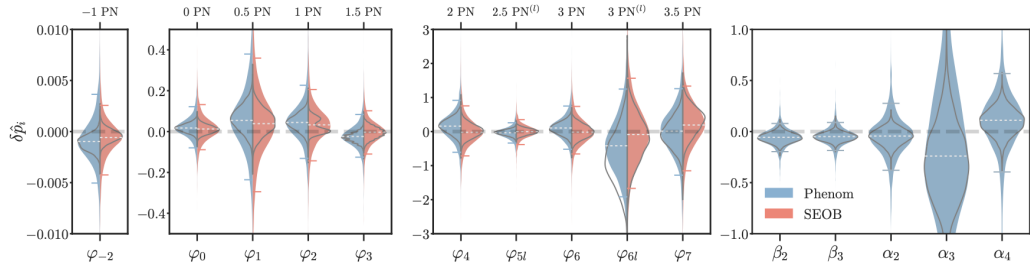


Figure 1.3. Combined results for parametrized deviations from GR obtained from the binary BH events in the second GW transient catalog, for each deviation parameter. Phenom (SEOB) results were obtained with IMRPHENOMPv2 (SEOBNRv4_ROM) and are shown in blue (red). The error bars denote symmetric 90%-credible intervals, and the white dashed line marks the median. The dashed horizontal line at $\delta\hat{p}_i = 0$ highlights the expected GR value. [10]

that, in some circumstances, can be interpreted as arising from the emission of dipolar radiation. The transition between the inspiral and the merger-ringdown phase is parametrized in terms of the phenomenological coefficients β_j with $j = 2, 3$. Finally, the merger-ringdown phase is parametrized in terms of the phenomenological coefficients α_j with $j = 2, 3, 4$. Parameters that are degenerate with either the reference time or the reference phase are not considered.

It is possible to perform two kinds of tests: a *single-parameter* analysis, in which only one of the parameters is allowed to vary freely while the remaining ones are fixed to their GR value, and a *multiple-parameter* analysis, in which all the parameters are allowed to vary simultaneously. The multiple-parameter analysis accounts for correlations between the parameters and provides a more conservative estimate on the agreement between a single GW event and GR.

Fig. 1.3 shows the combination of the parametric deviations of GR from a single-parameter analysis for the binary BH coalescences in the second GW transient catalog [10]. From left to right, the plot shows increasingly high-frequency regimes: the early-inspiral stage is from 0PN to 3.5PN, whereas the parameters β_i and α_i correspond to the intermediate and merger-ringdown stages, respectively. Phenom (SEOB) results were obtained with IMRPHENOMPv2 (SEOBNRv4_ROM) waveform model. The error bars are symmetric 90%-credible intervals, and the white dashed line is the median. The dashed horizontal line at $\delta\hat{p}_i = 0$ highlights the expected GR value.

The parameter that is constrained most tightly by the combined analysis is $\delta\hat{\varphi}_{-2} = -0.05_{-1.25}^{+0.99} \times 10^{-3}$, within 90% credibility [11]. The 0PN term is the second best constrained parameter with $|\delta\hat{\varphi}_0| \lesssim 4.4 \times 10^{-2}$ [10]. However, the latter constraint is weaker than the bound inferred from the double pulsar J0737-3039 by a factor ~ 3 due to the long observation time [62]. All the other PN orders are constrained significantly more tightly with GW observations rather than electromagnetic observations.

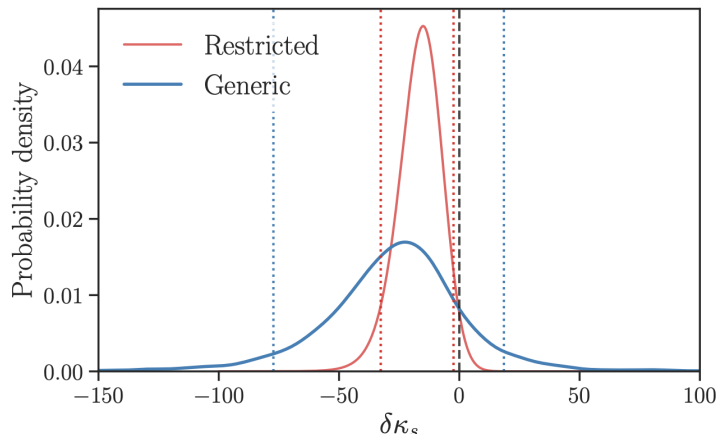


Figure 1.4. Combined measurement of the spin-induced quadrupole moment parameter $\delta\kappa_s$ for all the events in the third GW transient catalog [11]. The blue curve is the posterior obtained without assuming a unique value of $\delta\kappa_s$ in all the events, whereas the red curve is the posterior obtained by restricting $\delta\kappa_s$ to take the same value for all the events. The dotted lines bound symmetric 90%-credible intervals. The Kerr BH value ($\delta\kappa_s = 0$) is marked by a dashed line. [11]

The results of the parametrized analysis can be used to place constraints on specific theories of gravity by building a theory-dependent mapping [63, 64].

1.3.2 Measurement of the spin-induced quadrupole moment

The oblateness of a compact object due to its spin creates a deformation in the surrounding gravitational field, which is measured by the spin-induced quadrupole-moment [65]. The effect of the quadrupole moment on the orbital motion of a binary system is imprinted in the gravitational waveform at specific PN orders with a 2PN leading-order effect.

For a compact object with mass M and spin χ , the spin-induced quadrupole moment can be parametrized as

$$Q = -\kappa\chi^2 M^3, \quad (1.5)$$

where κ is the spin-induced quadrupole moment coefficient that depends on the mass, spin, and internal composition of the compact object. Due to the no-hair theorems, κ is unity for BHs in GR [20, 66]. For spinning NSs, κ can vary between ~ 2 and ~ 14 depending on the equation of state [67, 68], whereas for slowly spinning boson stars, κ can vary between ~ 10 and ~ 150 [69, 70].

The measurement of the spin-induced quadrupole moment coefficients of the binary components, κ_1 and κ_2 , is challenging given the strong correlations between the binary parameters [71]. For this reason, the individual deviations

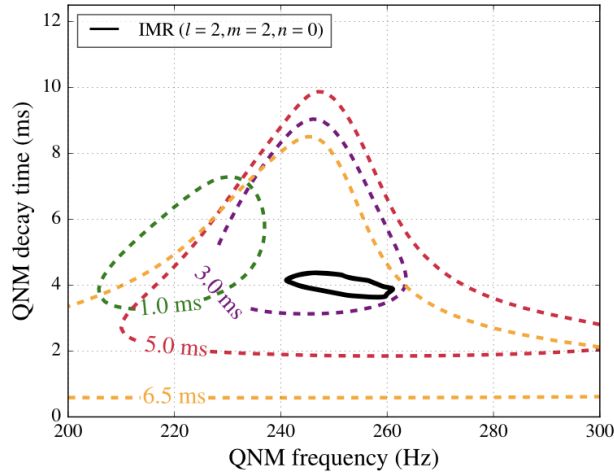


Figure 1.5. 90% credible regions in the joint posterior distributions for the QNM frequency and decay time, for several values of the starting time of the ringdown after the merger. The solid black line shows the 90% credible region for the frequency and decay time of the least-damped ($\ell = m = 2, n = 0$) QNM, as derived from the posterior distributions of the remnant mass and spin from inspiral-merger-ringdown waveforms. [5]

from unity are defined, $\delta\kappa_1$ and $\delta\kappa_2$, and the symmetric and anti-symmetric combinations of the individual deviation parameters are [10]

$$\delta\kappa_s = (\delta\kappa_1 + \delta\kappa_2) / 2, \quad (1.6)$$

$$\delta\kappa_a = (\delta\kappa_1 - \delta\kappa_2) / 2. \quad (1.7)$$

For simplicity, the analysis is restricted to $\delta\kappa_a = 0$, requiring that the binary components are of the same nature. Nevertheless, the measurement of $\delta\kappa_s$ from individual GW events is poorly constrained. Fig. 1.4 shows the distributions on $\delta\kappa_s$ obtained by combining all the events in the third GW transient catalog [11]. The blue curve represents the posterior obtained without assuming a unique value of $\delta\kappa_s$ in all the events, whereas the red curve is the posterior obtained by restricting $\delta\kappa_s$ to take the same value for all the events. Under the latter assumption, the following constraint is estimated $\delta\kappa_s = -16.0^{+13.6}_{-16.7}$ [11].

1.3.3 Tests of the remnant properties

From the analysis of the postmerger signal of a compact binary coalescence, it is possible to infer the nature of the compact remnant. Due to the no-hair theorems [20, 21], the QNM spectrum of a BH in GR depends only on the mass and spin of the remnant. Therefore, the measurement of one complex QNM allows us only to infer the mass and the spin of the remnant. Conversely, the measurement of more than one QNMs would allow us to perform independent tests of the Kerr metric. This set of analyses is referred to as *BH spectroscopy* [72, 73, 74, 75, 76, 77].

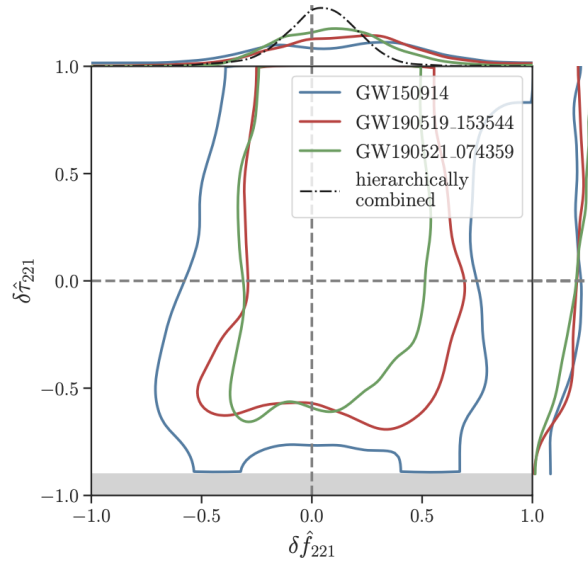


Figure 1.6. The 90% credible region of the joint posterior distribution of the fractional deviations of the frequency and the damping time for the $\ell = m = 2, n = 1$ mode. The measurement of the fractional deviation of the frequency is consistent with GR. The fractional deviation of the damping time is mostly unconstrained. [10]

One test of the remnant properties consists in checking the consistency of the data with the least-damped QNM predicted for a remnant BH. The posterior estimates for the QNM frequency and decay time are a function of the unknown starting time of the ringdown after the merger. Fig. 1.5 shows the 90% credible contours for the QNM frequency and decay time as a function of the ringdown time offset for the event GW150914 [5]. The solid black line shows the 90% credible region of the least-damped QNM as derived from the posterior distributions of the remnant mass and spin from full inspiral-merger-ringdown waveforms. The 90% posteriors overlap with the GR prediction starting from $t_0 = 3$ ms, which is the offset time when the description of the ringdown in terms of QNMs is valid.

To test the BH paradigm, one would need to detect at least two QNMs in the ringdown. One test consists in incorporating the first overtone ($\ell = m = 2, n = 1$) in the ringdown template in time domain [75, 76]. The starting time of the ringdown is chosen based on an estimate of the peak of the strain from the full inspiral-merger-ringdown analyses. The data show evidence for the presence of overtones only for loud signals. Fig. 1.6 shows the joint posterior distributions for the fractional deviations in the frequency and damping time to their GR predictions for the first overtone, where

$$f_{221} = f_{221}^{\text{GR}} (1 + \delta \hat{f}_{221}), \quad (1.8)$$

$$\tau_{221} = \tau_{221}^{\text{GR}} (1 + \delta \hat{\tau}_{221}), \quad (1.9)$$

and the “GR” superscript indicates the Kerr value corresponding to a remnant with a given mass and spin [10]. A hierarchical analysis of the events in the third GW transient catalog constrains the frequency deviations to $\delta\hat{f}_{221} = 0.01_{-0.28}^{+0.27}$, whereas the damping time is essentially unconstrained [11]. Recently, the observation of the $\ell = m = 3, n = 0$ mode has been claimed in the event GW190521 [78].

The fractional deviations in the frequency and the damping time of the least-damped QNM are $\delta\hat{f}_{220} = 0.03_{-0.09}^{+0.10}$ and $\delta\hat{\tau}_{220} = 0.10_{-0.39}^{+0.44}$, which are obtained by combining the information from different events using a hierarchical approach [79]. The event GW150914 gives the single-event most-stringent constraint with $\delta\hat{f}_{220} = 0.05_{-0.07}^{+0.11}$ and $\delta\hat{\tau}_{220} = 0.07_{-0.07}^{+0.11}$ [79], corresponding to a maximum allowed deviation from the least-damped QNM of a Kerr BH of $\sim 16\%$ and $\sim 33\%$ for the real and the imaginary part of the QNM, respectively.

The bounds for the fractional deviations for the modes can be used to put constraints on possible deviations in the ringdown spectrum caused by horizonless remnant objects, as detailed in Secs. 3.3.4 and 3.3.5.

1.3.4 Searches for gravitational-wave echoes

If the remnant of a compact binary coalescence is a horizonless compact object, a train of modulated pulses – known as GW echoes – is emitted in the late postmerger stage in addition to the ringdown expected from BHs [13, 80]. The detection of the GW echoes would be clear evidence of the existence of horizonless objects whose compactness is similar to the BH one (see Sec. 5.1 for details).

Several matched-filtered searches have been performed to search for GW echoes. A waveform template in the time domain is based on the standard inspiral-merger-ringdown template in GR, $\mathcal{M}(t)$, with five additional parameters, i.e., [23]

$$h(t) = A \sum_{i=0}^{\infty} (-1)^{i+1} \gamma^i \mathcal{M}(t + t_{\text{merger}} + t_{\text{echo}} - i\Delta t_{\text{echo}}, t_0), \quad (1.10)$$

where $\mathcal{M}(t, t_0) = \Theta(t, t_0)\mathcal{M}(t)$ and $\Theta(t, t_0)$ is a smooth cut-off function. The five free parameters are: the time-interval in between successive echoes, Δt_{echo} ; the time of arrival of the first echo, t_{echo} , that can be affected by the non-linear dynamics near the merger; the cut-off time, t_0 , which quantifies the part of the GR template that produce the subsequent echoes; the damping factor of successive echoes, γ ; the overall amplitude of the echo template, A . The $(-1)^i$ term represents the phase inversion of the waveform in each pulse. Extensions of the original template have been developed in Refs. [81, 82].

A phenomenological template in the time domain is based on the superposition of sine-Gaussians with several free parameters [83]. Furthermore, some templates in the frequency domain depend explicitly on the physical

parameters of the horizonless compact object, i.e., its compactness and reflectivity [84, 85, 22].

Some unmodeled searches have also been performed. Several analyses are based on the superposition of generalized wavelets adapted from burst searches [86, 87]. Moreover, searches with Fourier windows [88, 89] use the fact that the echoes should pile up at specific frequencies.

Tentative evidence for GW echoes in LIGO/Virgo O1 and O2 events has been reported [23, 88, 90], although independent searches argued that the statistical significance for GW echoes is low and consistent with noise [24, 91]. Recently, some negative searches have been performed [92, 87, 93]. Furthermore, a dedicated search for GW echoes has been performed by the LIGO/Virgo Collaboration in the events of the second and third GW transient catalogs, finding no evidence for GW echoes [10, 11].

1.4 Prospects with next-generation detectors

Next-generation detectors are planned to observe GWs in a different frequency range than current detectors and with improved sensitivity, opening up the possibility of observing new GW sources [94]. The ground-based observatories Einstein Telescope [33] and Cosmic Explorer [34] will observe GWs in the 5 – 4000 Hz band with a sensitivity of a factor of 10 better than current detectors.

The future space-based interferometer LISA [35] will detect GWs in the 10^{-4} –1 Hz frequency band from a variety of astrophysical sources. For instance, massive BHs (with masses ranging from $10^5 M_\odot$ to $10^9 M_\odot$) are hosted in the center of galaxies and are expected to coalesce in bigger systems. The inspiral, merger, and ringdown phases are predicted to be in the LISA frequency band of observation with $\text{SNR} \sim 1000$ [95].

EMRIs are one of the target sources of LISA [36]. EMRIs are binary systems in which a stellar-mass object (with mass ranging 10 – $100 M_\odot$) orbits around a supermassive object at the center of a galaxy. EMRIs occur over long timescales since the stellar-mass compact object spends 10^3 – 10^5 orbits in the close vicinity of the central object. A large number of orbital cycles allows for precise measurements of the parameters of the binary. Moreover, and to put GR to the most stringent tests.

EMRIs are unique probes of the nature of the central supermassive object. The mass quadrupole moment of the central object and possible deviations from the Kerr metric will be probed by LISA with large accuracy [96, 97]. In Sec. 6, the prospects of detection of LISA for the reflectivity of compact objects are assessed.

Chapter 2

Exotic compact objects

Per voi cadere è sbattersi giù magari dal ventesimo piano d'un grattacielo, o da un aeroplano che si guasta in volo: precipitare a testa sotto, annaspate un po' nell'aria, ed ecco che la terra è subito lì, e ci si piglia una gran botta.

Italo Calvino, *Le Cosmicomiche*

2.1 Motivation

BHs are the most compact objects in the Universe. According to GR, stationary BHs have an event horizon surrounding a curvature singularity where Einstein's theory breaks down. On the astrophysical side, the existence of BHs with masses ranging from a few to hundred solar masses has been confirmed by GW observations [1, 2, 4]. Moreover, supermassive BHs at the center of galaxies have been observed with stellar orbits [98] and the electromagnetic emission from accretion disks [99]. All the observations are compatible with BHs as predicted by GR and support the *Kerr hypothesis* for which any compact object heavier than a few solar masses is well described by the Kerr metric. Indeed, the Carter-Robinson uniqueness theorem establishes that the Kerr geometry is the only physically acceptable stationary solution to the Einstein vacuum field equations [20, 21].

Given the observational robustness of BHs, it is natural to question the motivation for further tests of the nature of compact objects. It is worth remarking that the evidence for BHs is the observation of dark, compact, and massive objects. The Kerr geometry has been probed in the exterior spacetime approximately until the location of the light ring [99] which is the innermost stable circular orbit (ISCO) of photons. Investigations of the spacetime in the vicinity of the event horizon have not been performed with current measurement accuracies. For this reason, it is relevant to quantify the evidence for BHs by constraining the compactness and darkness of the objects observed so far via gravitational and electromagnetic channels.

On the theoretical side, Kerr BHs have singularities and are pathological in their interior. In particular, the existence of a curvature singularity with infinite tidal forces shows a breakdown of the Einstein equations. Moreover, the spacetime within the BH horizon can contain closed time-like curves which violate causality. Some attempts to regularize the BH solution predict that quantum fluctuations might prevent the formation of the horizon and the singularity therein [100, 101].

In the semiclassical approximation, when a massless scalar field such as that of the photon is quantized in the Schwarzschild background, one finds that the BH radiates a thermal spectrum at the Hawking temperature $T_H = \hbar/(8\pi k_B M)$ [102]. The inverse dependence of the Hawking temperature on the mass implies that a BH in thermal equilibrium with its Hawking radiation has negative specific heat, hence is thermodynamically unstable [103]. Energy conservation plus the thermal radiation spectrum also imply that the BH has enormous entropy [104] which is far over a typical stellar progenitor.

Finally, one of the main open problems in BH physics is the information-loss paradox [14] which is related to loss of unitarity at the end of the BH evaporation due to Hawking’s radiation. Several attempts to address this issue involve the formulation of a consistent quantum gravity theory that predicts modifications at the horizon relative to the classical picture (e.g., nonlocal theories [105, 106, 107] and string theories [108, 109, 101, 110]) and new ways to compute the entropy [111, 112, 113].

ECOs are horizonless objects that are predicted in quantum gravity extensions of GR [114, 115, 116, 117, 80] and in the context of GR in the presence of exotic matter fields [118, 119, 12]. These ideas have inspired a plethora of models including gravastars [100, 109], boson stars [120, 121, 122, 123], wormholes [124, 125, 126], fuzzballs [101, 110], and others [127, 128, 129, 130, 131]. Some models are solutions to consistent field theories coupled to gravity [118, 109], whereas some phenomenological models do not arise from specific theories and are simple toy models to test deviations from the classical BH picture [126, 132].

ECOs without a classical horizon can nonetheless mimic the features of BHs through electromagnetic observations since they can be as compact as BHs [15]. For this reason, ECOs are also generically called “BH mimickers” [133, 134]. In most models, the dynamical formation of ECOs has not been explored consistently, with some notable exceptions [135, 118].

From a more phenomenological standpoint, BHs and NSs might be just two species of a larger zoo of compact objects. New species can be used to devise precision tests on the nature of compact objects. In particular, GW events that fall in the mass gap forbidden by standard stellar evolution (i.e., GW190814 [18] and GW190521 [8, 136]) could be interpreted as mergers of exotic objects [17].

In summary, ECOs are a tool that allows us to quantify the observational evidence for BHs and search for signatures of alternative proposals in GW and

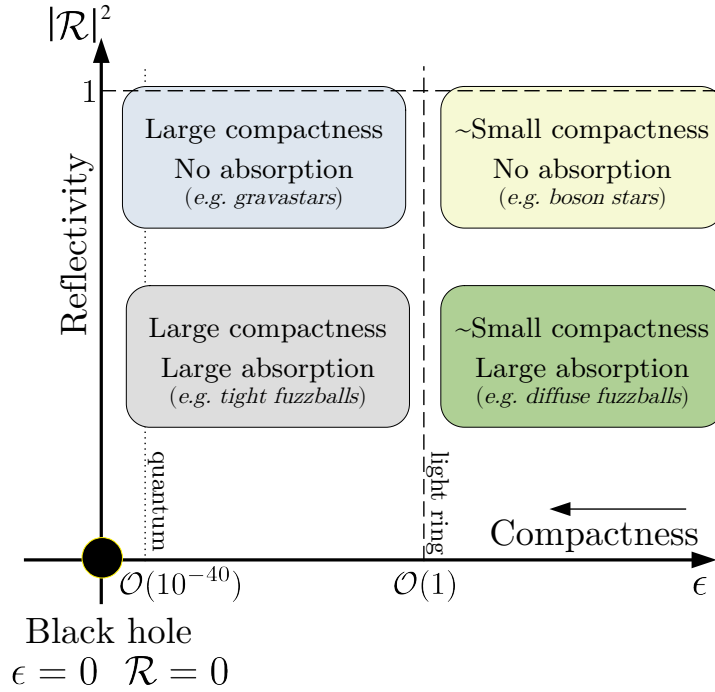


Figure 2.1. Schematic representation of the parameter space of ECOs. The closeness parameter ϵ (horizontal axis) is related to the effective radius of the object by $r_0 = r_+(1 + \epsilon)$, where r_+ is the horizon of a Kerr BH with the same mass and spin. The reflectivity \mathcal{R} (vertical axis) is related to the object’s interior and is generically complex and frequency-dependent. [137]

electromagnetic data.

2.2 A parametrized classification

Horizonless compact objects deviate from BHs for two parameters (see Fig. 2.1):

- their *compactness*, i.e., the inverse of their effective radius in units of the total mass M . It is customary to define a closeness parameter ϵ from the horizon of a BH such that the effective radius of the horizonless compact object is located at

$$r_0 = r_+(1 + \epsilon), \quad (2.1)$$

where $r_+ = M + \sqrt{M^2 - a^2}$, and a is the spin of the compact object. The closeness parameter is related to the compactness of the horizonless object via

$$\mathcal{C} \equiv \frac{M}{r_0} = \frac{M}{r_+(1 + \epsilon)}, \quad (2.2)$$

where $0.5 \leq \mathcal{C} \leq 1$ for a Kerr BH with $0 \leq a \leq M$. In this framework, the BH limit corresponds to $\epsilon \rightarrow 0$;

- their *reflectivity* \mathcal{R} at the effective radius of the compact object. The properties of the interior of a horizonless compact object can be parametrized in terms of its surface reflectivity, which is generically complex and frequency-dependent. In this framework, the $\mathcal{R} = 0$ case describes a totally absorbing object that reduces to the standard BH case when $\epsilon \rightarrow 0$. The $|\mathcal{R}|^2 = 1$ case describes a perfectly reflecting object for perturbations moving towards the compact object. This is the case, for example, of NSs where the most efficient absorption mechanism is due to viscosity. However, the absorption of the incoming radiation is negligible as detailed in Sec. 4.5, therefore the radiation passes unperturbed across the NS from a three-dimensional perspective. Intermediate values of \mathcal{R} describe partially absorbing compact objects through viscosity, dissipation, fluid mode excitations, nonlinear effects, etc.

Depending on their compactness, two categories of ECOs are [138]: horizonless objects with small compactness, whose effective radius is comparable with the light ring of BHs with $\epsilon = \mathcal{O}(0.1 - 1)$; and ultracompact objects, where Planckian corrections at the horizon as $r_0 \approx r_+ + l_{\text{Planck}}$ correspond to $\epsilon = \mathcal{O}(10^{-50} - 10^{-40})$ for supermassive to stellar objects depending on their mass. Several models of ultracompact horizonless objects are conceived by assuming that quantum fluctuations might prevent the formation of the horizon [100]. These models are so compact that the round-trip time of the light between the light ring and the radius of the object is longer than the instability timescale of the photon orbits.

If the remnant of a merger is a compact object with small compactness, the ringdown signal differs from the BH ringdown at early stages, as detailed in Sec. 5.4. Conversely, if the remnant of a merger is an ultracompact horizonless object, the prompt ringdown is nearly indistinguishable from that of a BH since it is excited at the light ring which is at the same location both in the BH and the horizonless case [19]. The details of the object’s interior appear at late times in the form of a modulated train of GW echoes, as detailed in Sec. 5.1.

Another mention-worthy property used to classify ECOs is their *softness*, which is associated with the spacetime curvature at their surface. When the underlying theory of an ECO model has a new length scale $\mathcal{L} \ll M$, the curvature (e.g., the Kretschmann scalar \mathcal{K}) at the surface can be much larger than the curvature at the horizon, i.e., $\mathcal{K} \gg 1/M^4$. On the other hand, models of ECOs that are not motivated by length scales other than M cannot sustain large curvatures at their surfaces. The former case is referred to as “hard” ECOs, whereas the latter case is denoted by “soft” ECOs [139].

2.2.1 The Buchdhal theorem

A useful compass to navigate through the ECO atlas is provided by the Buchdhal theorem [140] which states that, under certain assumptions, the

maximum compactness of a self-gravitating object is $M/r_0 = 4/9$ (i.e., $\epsilon \geq 1/8$). This theorem prevents the existence of ECOs with compactness arbitrarily close to that of a BH. In particular, the assumptions of the Buchdhal theorem are:

- GR is the theory of gravity;
- the solution is spherically symmetric;
- the interior matter is a single perfect fluid;
- the fluid is at most mildly anisotropic, i.e., the radial pressure is larger than the tangential one, $p_r \gtrsim p_t$;
- the radial pressure and the energy density are positive, i.e., $p_r \geq 0$ and $\rho \geq 0$;
- the energy density decreases by moving outwards, i.e., $d\rho/dr < 0$.

Relaxing some of these assumptions provides a way to circumvent the theorem and suggests a route to classify ECOs [141, 13]. For example, the assumption of GR is violated in any modified-gravity theory, i.e., in fuzzballs in string theory [101, 110] and nonlocal stars in infinite derivative gravity [117, 131].

A common property of ECOs is the presence of an anisotropic pressure. Indeed, strong tangential stresses are necessary to support compact self-gravitating configurations. This is the case, for instance, of ultracompact anisotropic stars [142, 143].

Several models of ECOs are spherically symmetric solutions of GR supported by an exotic distribution of matter violating the energy conditions. This is the case of gravastars [100, 109, 144] with a dark energy interior, and wormholes [125, 145, 126] with a thin shell of exotic matter at the throat.

2.3 Review of some remarkable models

2.3.1 Boson stars

Boson stars are self-gravitating compact solutions formed by massive bosonic fields which are coupled minimally to GR [146, 147, 118]. The action of the Einstein-Klein-Gordon theory is [148]

$$\mathcal{S} = \int \left(\frac{R}{16\pi} + \mathcal{L}_{\mathcal{M}} \right) \sqrt{-g} d^4x, \quad (2.3)$$

where R is the Ricci scalar of the spacetime with metric $g_{\mu\nu}$ and determinant $\sqrt{-g}$, and the term $\mathcal{L}_{\mathcal{M}}$ describes the matter of the scalar field Φ ,

$$\mathcal{L}_{\mathcal{M}} = -\frac{1}{2} \left[g^{\mu\nu} \nabla_{\mu} \Phi^* \nabla_{\nu} \Phi + V(|\Phi|^2) \right], \quad (2.4)$$

where Φ^* is the complex conjugate of the scalar field and $V(|\Phi|^2)$ is the bosonic potential. By varying the action in Eq. (2.3) with respect to the metric $g^{\mu\nu}$, the Einstein field equations are obtained; whereas by varying the action with respect to the scalar field Φ , the Klein-Gordon equation is derived.

If the scalar field is complex, the boson star is a static and spherically symmetric geometry with an oscillating field [121, 122]

$$\Phi(r, t) = \Phi_0(r)e^{i\omega t}, \quad (2.5)$$

where $\Phi_0(r)$ is the profile of the star and ω is the angular frequency of the phase of the field. On the other hand, real scalar fields give rise to long-term stable oscillating geometries with a non-trivial time-dependent stress-energy tensor, called oscillatons [123]. Both solutions arise naturally as the end-state of the gravitational collapse in the presence of bosonic fields [135, 149].

Boson stars are the most robust model of ECOs since their formation, stability, and binary coalescence have been analyzed in detail numerically [150, 151, 152]. Boson stars are natural candidates for dark matter. They are not meant to replace all the BHs in the Universe since their compactness is lower than the BH one. Indeed, boson stars have properties similar to NSs, e.g., having a maximum mass above which they are unstable against gravitational collapse.

There are several models of boson stars depending on the bosonic potential and the classes of self-interactions, namely:

- *mini boson stars* which are characterized by a non-interacting scalar field where [153]

$$V(|\Phi|^2) = \mu^2|\Phi|^2, \quad (2.6)$$

where μ is the bare mass of the field theory. The maximum boson star mass is $M_{\max} \sim 0.633M_{\text{Planck}}^2/\mu$. Their mass-radius diagram is qualitatively similar to the one of static NSs;

- *massive boson stars* which are characterized by a scalar field with a quartic self-interaction potential [154]

$$V(|\Phi|^2) = \mu^2|\Phi|^2 + \frac{\lambda}{2}|\Phi|^4, \quad (2.7)$$

where λ is a dimensionless coupling constant. The maximum mass can be of the order of the Chandrasekhar mass or larger, $M_{\max} \sim 0.062 \lambda^{1/2}M_{\text{Planck}}^3/\mu^2$. This effect is caused by the self-interaction of the potential that provides an extra pressure against the gravitational collapse;

- *solitonic boson stars* which are characterized by a potential with an attractive term [155, 156]

$$V(|\Phi|^2) = \mu^2|\Phi|^2 \left(1 - 2\frac{|\Phi|^2}{\sigma_0^2}\right), \quad (2.8)$$

where σ_0 is a constant that is generically assumed to be of the same order as μ . The maximum mass of the boson star is $M_{\max} \sim M_{\text{Planck}}^4 / (\mu\sigma_0)^2$. Stationary, soliton-like configurations have also been found for complex and massive Proca fields [119].

2.3.2 Gravastars

Gravitational-vacuum stars or gravastars are configurations supported by a negative pressure in their interior [109, 157, 158]. The region with negative pressure forces the gravastar to violate some energy conditions and evade the Buchdhal theorem. The model is singularity-free, thermodynamically stable and has no information paradox.

Gravastars can have an arbitrary compactness depending on the model to describe the pressure. The original formulation of the gravastar has a five-layer construction with a de Sitter core, a thin shell connecting to a perfect-fluid region, and another thin shell connecting to the Schwarzschild exterior. A simpler model is the thin-shell gravastar [157] that is constructed with a de Sitter core connected to the Schwarzschild exterior by a thin shell of perfect-fluid matter.

The formation of a gravastar can occur at the endpoint of a gravitational collapse when quantum gravitational vacuum phase transition could intervene before the event horizon can form [100]. However, the dynamical formation of a non-singular gravastar is still an open issue.

2.3.3 Wormholes

Wormholes were introduced originally by Einstein and Rosen [124] in the attempt to build a geometrical model of an elementary particle in GR. Wormholes are constructed by taking two copies of a static and spherically symmetric metric with an asymptotically flat region. The two regions are connected by a wormhole whose throat occurs at the radius r_0 . This procedure is called Schwarzschild surgery [125, 145].

The spacetime is everywhere vacuum except at the throat, where the surgery requires a thin shell of matter. The Einstein field equations yield an exotic distribution of matter that has a negative energy density and violates the weak and the dominant energy conditions.

Wormholes can be constructed with arbitrary mass and compactness, therefore they can mimic the observational features of BHs [126]. Wormholes solutions have also been constructed in more generic gravity theories, some of which do not violate energy conditions [159]. Nevertheless, their formation mechanism is not well understood, and wormholes are unstable under linear perturbations [160, 161].

2.3.4 Fuzzballs

The fuzzball models are conceived in string theory to solve the loss of unitarity in the BH evaporation and the huge Bekenstein-Hawking entropy of BHs [162, 108, 101, 110]. A classical BH is interpreted as an ensemble of regular, horizonless geometries that describes its quantum microstates [115, 163, 164]. These geometries are solutions to string theory and have the same mass and charge of the corresponding BH. In this description, quantum gravity effects are not confined close to the BH horizon, but the BH interior is formed by fluctuating geometries. For this reason, this picture is referred to as the “fuzzball” description of BHs.

The construction of the microstates has been achieved only under specific assumptions, i.e., in higher-dimensional or in non-asymptotically-flat spacetimes. None of the geometries that can be constructed in four-dimensional spacetimes could represent astrophysical BHs since these solutions are typically non-rotating, charged, and extremal. A general class of extremal and charged solutions in four dimensions is described by the metric [115, 165, 166]

$$ds^2 = -e^{2U}(dt + w)^2 + e^{-2U} \sum_{i=1}^3 dx_i^2, \quad (2.9)$$

where U is a function of eight harmonic functions associated with the electric and the magnetic charges [167, 168]. The fuzzballs are constructed by distributing the charges of the eight harmonic functions among N centers. The geometry is regular and characterized by the absence of horizons and closed timelike curves.

2.3.5 Anisotropic stars

Anisotropic stars are compact objects which are supported by large anisotropic stresses [169, 170, 171, 172] that arise at high densities, in superfluidity, solid cores, etc. Anisotropic stars have been studied in GR, mostly in the context of static and spherically symmetric solutions [173, 174, 175, 176, 177]. Depending on the anisotropy scale, the compactness of anisotropic stars can be arbitrarily close to the BH one [143]. Furthermore, anisotropic stars can cover a wide range of masses, hence they can mimic both stellar BHs and the supermassive BHs at the center of galaxies.

2.3.6 Firewalls, nonlocal stars, and superspinars

Firewalls are horizonless compact objects with a BH exterior spacetime and some “hard” structure localized close to the horizon due to quantum origin [178, 179]. Furthermore, a classical BH with modified dispersion relations for the graviton could effectively appear as having a hard surface [180, 181].

Nonlocal stars emerge in theories with infinite derivatives in which the non-locality of the gravitational interaction can smear out the curvature singularity

and avoid the presence of a horizon [182, 117, 183, 131]. A nonlocal star is a self-gravitational bound system of gravitons interacting nonlocally. Outside the nonlocal star, the spacetime is well described by the Schwarzschild metric, whereas inside there is a nonvacuum spacetime that is conformally flat at the origin.

Superspinars are string-inspired Kerr geometries spinning above the Kerr bound [128, 132, 184]. Indeed, in GR the angular momentum J of a Kerr BH is bounded by $J \leq M^2$. When the Kerr bound is violated, the geometry does not possess an event horizon. Furthermore, some unknown quantum effects need to be invoked to create an effective surface to avoid naked singularities and closed timelike curves.

2.4 Phenomenology of exotic compact objects

2.4.1 Tests of the multipolar structure

Uniqueness theorems in GR predict that the outcome of the gravitational collapse is a Kerr BH which is determined uniquely by two parameters, i.e., its mass M and angular momentum J [20, 21]. The multipolar structure of Kerr BHs can be written as [66]

$$\mathcal{M}_\ell^{\text{BH}} + i\mathcal{S}_\ell^{\text{BH}} = M^{\ell+1} (i\chi)^{\ell+1}, \quad (2.10)$$

where \mathcal{M}_ℓ and \mathcal{S}_ℓ are the mass and current multiple moments, respectively, $M = \mathcal{M}_0$ is the mass, $\chi = J/M^2$ is the dimensionless spin, and $J = \mathcal{S}_1$ is the angular momentum. In addition, Kerr BHs have vanishing mass (current) multiple moments when ℓ is odd (even) since the metric is axially and equatorially symmetric. The BH multipole moments do not depend on the azimuthal number m given the axisymmetry of the metric.

For ECOs, the tower of multipole moments is, in general, richer due to the presence of moments that break the equatorial symmetry or the axisymmetry, as in the case of multipolar boson stars [185] and fuzzball microstate geometries [186, 167, 168, 187]. The deformation of the multipoles depends on the specific ECO model and vanishes in the high-compactness limit approaching the Kerr value [188, 139, 189]. The multipole moments of an ECO can be parametrized as

$$\mathcal{M}_{\ell m}^{\text{ECO}} = \mathcal{M}_\ell^{\text{BH}} + \delta\mathcal{M}_{\ell m}, \quad \mathcal{S}_{\ell m}^{\text{ECO}} = \mathcal{S}_\ell^{\text{BH}} + \delta\mathcal{S}_{\ell m}, \quad (2.11)$$

where $\delta\mathcal{M}_{\ell m}$ and $\delta\mathcal{S}_{\ell m}$ are model-dependent corrections to the mass and current multipole moments.

“Soft” ECOs motivated by new physics effects whose length scale is comparable to the mass cannot have arbitrarily large deviations from the BH multipole moments. In the BH limit, the multipole moment deviations must vanish sufficiently fast. For axisymmetric spacetimes, spin-induced moments

must vanish logarithmically (or faster), whereas non-spin induced moments vanish linearly (or faster) [139], i.e.,

$$\frac{\delta\mathcal{M}_\ell}{\mathcal{M}^{\ell+1}} \sim a_\ell \frac{\chi^\ell}{\log \epsilon} + b_\ell \epsilon, \quad (2.12)$$

and equivalently for the current multipole moments, where a_ℓ and b_ℓ are constants.

The multipolar structure of an object leaves a footprint in the GW signal emitted by a compact binary coalescence, modifying the PN structure of the waveform at different orders. The lowest order contribution is the quadrupole moment which enters at 2PN order [190] as detailed in Sec. 1.3.2. Current constraints on the parametrized PN deviations with GW observations [9, 10] can be mapped into constraints on $\delta\mathcal{M}_{20}$. However, such tests are challenging given the correlations between the binary component spins and the quadrupole moment where the former have not been measured accurately.

EMRIs are expected to put stronger bounds on the multipolar structure of the central supermassive object, due to a large number of cycles before the merger. The future space mission LISA is expected to provide accurate measurements of the spin-induced quadrupole and a large set of high-order multipole moments [96, 191, 192].

2.4.2 Tests of the tidal heating

If the components of a binary system are dissipative objects, energy and angular momentum are dissipated in their interior in addition to the GW emission to infinity. This is the case of BHs in which energy and angular momentum are absorbed by the horizon. This effect is known as tidal heating (TH) and can contribute to thousands of radians of accumulated orbital phase for EMRIs in the LISA band [193, 194, 195].

If at least one component of the binary system is an ECO, the dissipation in their interior would be smaller than in the BH case. Indeed, exotic matter is expected to interact weakly with GWs leading to a suppressed contribution to the GW accumulated phase from TH. This effect would allow distinguishing binary BHs from binary systems involving ECOs [196]. For EMRIs in the LISA band, the absence of TH could be used to put a stringent upper bound on the reflectivity of ECOs [39, 38].

2.4.3 Measurements of the tidal deformability

In the coalescence of a compact binary system, the gravitational field of each component acts as a tidal field on its companion, inducing some multipolar deformation in the spacetime. Tidal effects change the orbital phase and in turn the GW emission [197]. This effect can be quantified in terms of the ‘‘tidal-induced multipole moments’’. Indeed, a weak tidal field can be

decomposed into electric (or polar) tidal field moments, $\mathcal{E}_{\ell m}$, and magnetic (or axial) tidal field moments, $\mathcal{B}_{\ell m}$. In the nonrotating case, the ratio between the multipole moments and the tidal field moments that induce them defines the tidal deformability of the body, i.e.,

$$\lambda_E^{(\ell)} = \frac{\mathcal{M}_{\ell m}}{\mathcal{E}_{\ell m}}, \quad \lambda_B^{(\ell)} = \frac{\mathcal{S}_{\ell m}}{\mathcal{B}_{\ell m}}. \quad (2.13)$$

The dimensionless tidal Love numbers can be defined as

$$k_\ell^E = \text{const} \frac{\lambda_E^{(\ell)}}{M^{2\ell+1}}, \quad k_\ell^B = \text{const} \frac{\lambda_B^{(\ell)}}{M^{2\ell+1}}, \quad (2.14)$$

that depend on the internal composition of the central object.

A remarkable result in GR is that the tidal Love numbers of BHs are null. This was demonstrated for nonrotating BHs [198, 199], then extended to slowly rotating BHs [200, 201, 202] and recently to Kerr BHs [203, 204, 205]. Conversely, the tidal Love numbers of ECOs are generically different from zero and can provide a smoking-gun test of the nature of compact objects [206]. The tidal Love numbers were computed for several models of ECOs such as boson stars [206, 207, 208], gravastars [188, 206, 209] and anisotropic stars [143].

In the case of “hard” ECOs, the tidal Love numbers vanish logarithmically in the BH limit [206]

$$k_\ell^{\text{ECO}} \rightarrow \frac{c_\ell}{1 + d_\ell \log \epsilon}, \quad \epsilon \rightarrow 0, \quad (2.15)$$

where axial and polar Love numbers coincide in the BH limit. Conversely, “soft” ECOs – such as anisotropic stars in certain regimes – have a polynomial vanishing behavior in the BH limit [143]

$$k_\ell^{\text{ECO}} \rightarrow f_\ell \left(\frac{\epsilon}{M} \right)^n, \quad (2.16)$$

where n is a parameter that depends on the specific model.

The effect of tidal deformability alters the GW signal emitted by a compact binary coalescence at 5PN order. Current and future GW detectors will be able to measure the tidal Love numbers of compact objects to distinguish ECOs from BHs [206, 196, 207].

2.4.4 Ringdown tests

The postmerger phase of a compact binary coalescence is dominated by the QNMs of the remnant. In the case of a horizonless compact remnant, the QNM spectrum deviates from the one predicted for a BH in GR. The estimation of the fractional deviations from the GR modes in the GW events allows us to constrain possible deviations in the spectrum due to a horizonless remnant, as detailed in Sec. 1.3.3.

The vibration spectra of ECOs have been computed in a wide class of models: boson stars [210, 211], gravastars [212, 213, 214, 215], wormholes [19, 216, 217], and quantum structures [218, 219, 220, 221, 222, 32]. Typically, the QNMs of ECOs differ from the BH QNMs due to the presence of an effective radius instead of the horizon, the excitation of the internal oscillation modes [223, 224, 225], and the excitation of extra degrees of freedom in modified-gravity theories [226, 227, 228].

The isospectrality of axial and polar modes of BHs in GR [55] is broken in ECOs, which are expected to emit a characteristic *mode doublet*. The detection of such doublet would be an irrevocable signature of new physics, whose prospects of detection are detailed in Sec. 3.3.5.

The formation of an ECO can also be constrained by looking for GW echoes in the postmerger signal of a compact binary coalescence. GW echoes are an additional signal that would be emitted after the prompt ringdown if the remnant is an ultracompact ECO. In Sec. 1.3.4 we reviewed the searches for GW echoes that have been currently performed.

Third-generation detectors are expected to detect the ringdown signal of massive binaries with a large SNR, which would allow putting strong constraints on the compactness and the reflectivity of the compact objects [85, 22].

Chapter 3

Spectroscopy of horizonless compact objects

Esatto, quel tempo là ci impiega, mica meno, - disse Qfwfq, - io una volta passando feci un segno in un punto dello spazio, apposta per poterlo ritrovare duecento milioni d'anni dopo, quando saremmo ripassati di là al prossimo giro.

Italo Calvino, *Le Cosmicomiche*

3.1 A static model

Let us analyze a static and spherically symmetric horizonless compact object. We assume that GR is a reliable approximation outside the radius of the compact object and some modifications appear at the horizon scale as in some quantum-gravity models. Owing to the Birkhoff theorem, the exterior spacetime of a static and spherically symmetric compact object is described by the Schwarzschild metric

$$ds^2 = -f(r)dt^2 + \frac{1}{f(r)}dr^2 + r^2(d\theta^2 + \sin^2\theta d\varphi^2), \quad (3.1)$$

where (t, r, θ, φ) are the Boyer-Lindquist coordinates, $f(r) = 1 - 2M/r$ and M is the total mass of the object.

The radius of the horizonless compact object is as in Eq. (2.1), where $r_+ = 2M$ is the would-be horizon of a Schwarzschild BH with the same mass. Ultracompact horizonless objects ($\epsilon \ll 1$) have a compactness that is almost the same as the one of a Schwarzschild BH, i.e., $\mathcal{C} \simeq 0.5$, whereas horizonless objects with a small compactness [$\epsilon = \mathcal{O}(0.1 - 1)$] have $\mathcal{C} \simeq 0.45 - 0.25$. In the

following, we shall not assume a specific model for the interior of the compact object that is parametrized in terms of the reflectivity at the effective radius.

In Sec. 3.2, we shall derive the QNM spectrum of ultracompact objects, whereas in Sec. 3.3, we shall derive a model-independent framework for the QNMs of horizonless compact objects using the membrane paradigm.

3.2 Ringdown spectrum of ultracompact objects

Horizonless compact objects are characterized by a completely different QNM spectrum with respect to the BH case. In this section, we derive the QNM spectrum of a static ultracompact object ($\epsilon \ll 1$) with surface reflectivity $\mathcal{R}(\omega)$.

3.2.1 Linear perturbations in the Schwarzschild background

Let us perturb the background geometry in Eq. (3.1) with a spin- s perturbation, where $s = 0, \pm 1, \pm 2$ for scalar, electromagnetic and gravitational perturbations, respectively. The perturbation can be decomposed as

$$\Psi_s(t, r, \theta, \varphi) = \int d\omega e^{-i\omega t} \sum_{\ell m} e^{im\varphi} {}_s S_{\ell m}(\theta) {}_s \psi_{\ell m}(r), \quad (3.2)$$

where ${}_s S_{\ell m}(\theta) e^{im\varphi}$ are the spin-weighted spherical harmonics, ℓ is the angular number ($\ell \geq 0$) and m is the azimuthal number ($-\ell \leq m \leq \ell$) of the perturbation. In the following, we shall omit the s, ℓ, m subscripts for brevity. The radial component of the perturbation is governed by a Schrödinger-like equation [229, 230]

$$\frac{d^2 \psi(r)}{dr_*^2} + [\omega^2 - V(r)] \psi(r) = 0, \quad (3.3)$$

where the tortoise coordinate is defined such that $dr_*/dr = 1/f(r)$, i.e.,

$$r_* = r + 2M \log \left(\frac{r}{2M} - 1 \right). \quad (3.4)$$

Let us notice that the tortoise coordinate allows us to explore a region in close proximity to the horizon of a BH since the tortoise coordinate is finite at the effective radius, i.e., $r_*(r_0) = \text{const} \equiv r_*^0$, and diverges at the would-be horizon, i.e., $r_*(2M) \rightarrow -\infty$.

The effective potential in Eq. (3.3) is [229, 230]

$$V_{\text{axial}} = f(r) \left[\frac{\ell(\ell+1)}{r^2} + (1-s^2) \frac{2M}{r^3} \right], \quad (3.5)$$

$$V_{\text{polar}} = 2f(r) \left[\frac{q^2(q+1)r^3 + 3q^2Mr^2 + 9M^2(qr+M)}{r^3(qr+3M)^2} \right], \quad (3.6)$$

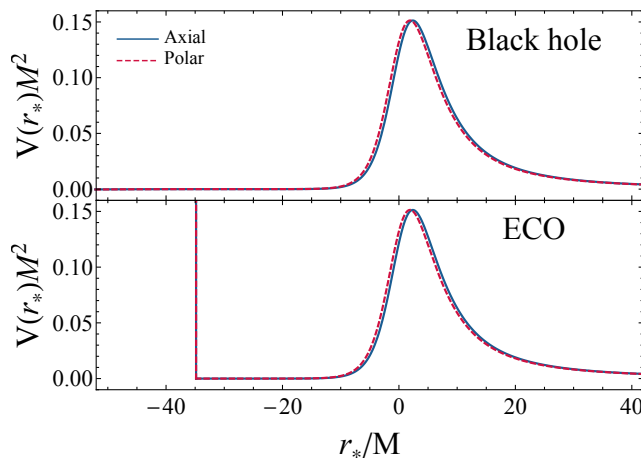


Figure 3.1. Effective potential as a function of the tortoise coordinate of a Schwarzschild BH (top panel) and a static horizonless compact object with radius $r_0 = 2M(1 + \epsilon)$ and $\epsilon = 10^{-8}$ (bottom panel), for axial (continuous line) and polar (dashed line) $\ell = 2$ gravitational perturbations. The effective potentials have a maximum approximately at the photon sphere, $r \approx 3M$. In the horizonless case, the effective potential features a characteristic cavity between the radius of the object and the photon sphere [19, 220, 13, 137].

where $q = (\ell - 1)(\ell + 2)/2$. The potential in Eq. (3.5) describes scalar, electromagnetic and axial gravitational perturbations, whereas the potential in Eq. (3.6) describes polar gravitational perturbations. The tensor spherical harmonics can be classified according to their behavior under parity change,

$$\mathcal{P} \left({}_s S_{\ell m}(\theta) e^{im\varphi} \right) \rightarrow {}_s S_{\ell m}(\pi - \theta) e^{im(\pi + \varphi)}. \quad (3.7)$$

In particular, we refer to axial perturbations as those with parity $(-1)^{\ell+1}$, whereas we refer to polar perturbations as those with parity $(-1)^\ell$. The former are described by the Regge-Wheeler wave function [229], while the latter by the Zerilli wave function [230]. Fig. 3.1 shows the effective potential as a function of the tortoise coordinate for axial and polar gravitational perturbations for a Schwarzschild BH (top panel) and for a static horizonless compact object (bottom panel) with $\epsilon = 10^{-8}$.

Let us notice that the effective potential of a Schwarzschild BH tends to zero asymptotically both at infinity ($r_* \rightarrow +\infty$) and the horizon ($r_* \rightarrow -\infty$). As a consequence, the solution of the perturbation equation in Eq. (3.3) is a wave of frequency ω at the asymptotics both at infinity and the horizon. Furthermore, the effective potential displays a maximum located approximately at the photon sphere, $r \approx 3M$, that is the unstable circular orbit of photons around a Schwarzschild BH.

In the case of a horizonless ultracompact object ($\epsilon \ll 1$), the effective potential coincides with the one of a BH except for the presence of a radius at

a constant r_*^0 . The effective potential features a characteristic cavity between the radius of the object and the photon sphere. The cavity can support quasi-trapped modes that are responsible for a completely different QNM spectrum with respect to the BH case.

Let us emphasize that this description is valid when $\epsilon \ll 1$ and the effective potential is vanishing at the radius of the object, thus the solution of Eq. (3.3) is a superposition of ingoing and outgoing waves at the radius of the object. Conversely, when $\epsilon \simeq 0.1 - 1$ (thus $r_0 \lesssim 3M$) the effective potential is not vanishing at the radius of the object and does not have an asymptotic trend, hence the solution of Eq. (3.3) is not a generic superposition of waves. We shall investigate the latter case in detail in Sec. 3.3.

3.2.2 Boundary conditions

The QNMs are the complex eigenvalues, $\omega = \omega_R + i\omega_I$, of the system given by Eq. (3.3) with two suitable boundary conditions. In our convention, a stable mode has $\omega_I < 0$ and corresponds to an exponentially damped sinusoidal signal with frequency $f \equiv \omega_R/(2\pi)$ and damping time $\tau_{\text{damp}} \equiv -1/\omega_I$. Conversely, an unstable mode has $\omega_I > 0$ with instability timescale $\tau_{\text{inst}} \equiv 1/\omega_I$.

As a boundary condition, we impose that the perturbation is a purely outgoing wave at infinity, i.e.,

$$\psi \sim e^{i\omega r_*}, \quad \text{as } r_* \rightarrow +\infty. \quad (3.8)$$

In the BH case, the horizon would require that the perturbation is a purely ingoing wave as $r_* \rightarrow -\infty$. In the case of a horizonless ultracompact object, the regularity at the center of the object implies the imposition of a boundary condition at the effective radius of the object. The perturbation can be decomposed a superposition of ingoing and outgoing waves at the radius of the object, i.e.,

$$\psi \sim C_{\text{in}} e^{-i\omega r_*} + C_{\text{out}} e^{i\omega r_*}, \quad \text{as } r_* \rightarrow r_*^0, \quad (3.9)$$

where we define the surface reflectivity of the object as [30]

$$\mathcal{R}(\omega) = \frac{C_{\text{out}}}{C_{\text{in}}} e^{2i\omega r_*^0}. \quad (3.10)$$

Let us notice that, for a given wave function, $|\mathcal{R}(\omega)|^2$ defines the fraction of the reflected energy flux in units of the incident one at the radius of the object. Indeed, for $\epsilon \ll 1$ the imaginary part of the QNMs vanishes sufficiently fast that $|e^{2i\omega r_*^0}|^2 \approx 1$ and $|\mathcal{R}(\omega)|^2 \approx |C_{\text{out}}|^2/|C_{\text{in}}|^2$. The BH boundary condition is recovered for $\mathcal{R} = 0$ and in the limit of $\epsilon \rightarrow 0$. Conversely, a perfectly reflecting compact object is described by $|\mathcal{R}(\omega)|^2 = 1$ where the outgoing energy flux at the effective radius of the object is equal to the incident one.

In the case of electromagnetic perturbations, a perfectly reflecting object can be modeled as a perfect conductor in which the electric and magnetic fields

satisfy $E_\theta(r_0) = E_\varphi(r_0) = 0$ and $B_r(r_0) = 0$. The former conditions translate into

$$\psi(r_0) = 0 \quad \text{Dirichlet on axial,} \quad (3.11)$$

$$d\psi(r_0)/dr_* = 0 \quad \text{Neumann on polar,} \quad (3.12)$$

where the Dirichlet boundary condition describes waves that are reflected with inverted phase ($\mathcal{R}(\omega) = -1$), whereas the Neumann boundary condition describes waves that are reflected in phase ($\mathcal{R}(\omega) = 1$). The details of the derivation are given in Appendix 3.4.

An analogous description of a perfectly reflecting compact object under gravitational perturbations is not available. We assume that the results of electromagnetic perturbations can be applied to gravitational perturbations, in which case Dirichlet and Neumann boundary conditions are imposed on axial and polar gravitational perturbations, respectively.

3.2.3 Numerical procedure

Equation (3.3) with boundary conditions at infinity in Eq. (3.8) and at the radius of the compact object in Eq. (3.11) or (3.12) can be solved numerically with a *direct integration shooting method* [231]. The method starts with an analytical high-order series expansion of the solution at large distances. We use the ansatz

$$\psi(r) = e^{i\omega r_*} \sum_{i=0}^{\infty} \frac{R_{\text{inf}}^{(i)}}{r^i}, \quad (3.13)$$

where the coefficients $R_{\text{inf}}^{(i)}$ with $i = 1, \dots, \infty$ are computed by solving Eq. (3.3) in the large distance limit order by order, and the coefficients $R_{\text{inf}}^{(i)}$ are functions of $R_{\text{inf}}^{(0)}$. For simplicity, we set $R_{\text{inf}}^{(0)} = 1$. A high truncation order of the series expansion ($i \gtrsim 10$) is needed for the numerical stability of the solution.

Eq. (3.3) is integrated with the boundary condition in Eq. (3.13) from infinity inwards up to $r = r_0$. The integration is repeated for different values of the complex frequency starting from an initial guess until the boundary condition at the radius of the object (either Eq. (3.11) or Eq. (3.12)) is satisfied. The resulting QNM should not depend on the numerical parameters of the method, i.e., the numerical value that stands for the infinity and the truncation order of the series expansion at infinity. The direct integration shooting method is robust when the imaginary part of the mode is sufficiently small with respect to the real part of the mode. Typically, this method allows us to compute the fundamental mode and possibly the first few overtones.

An alternative method is based on the *continued fraction technique*, where the eigenfunction is written as a series whose coefficients satisfy a finite-term recurrence relation [56]. The QNMs are the roots of n implicit equations $f_n(\omega) = 0$, where n is the inversion index of the continued fraction. For a given n , the method gives some spurious roots apart from the physical QNMs. The

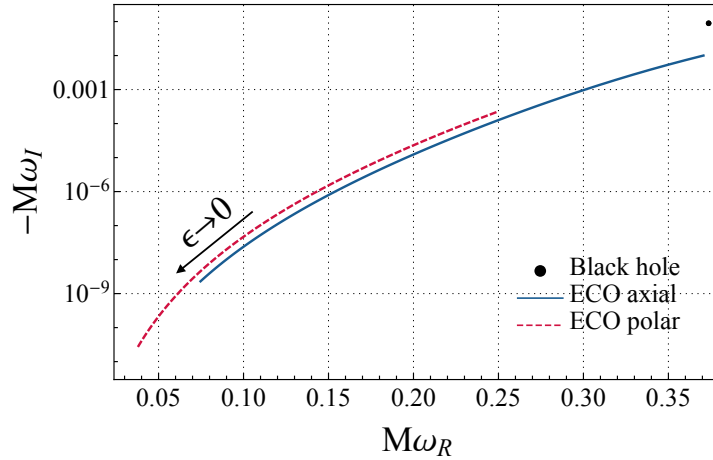


Figure 3.2. QNM spectrum of a perfectly reflecting ECO with radius $r_0 = 2M(1 + \epsilon)$ and $\epsilon \in (10^{-10}, 10^{-2})$, compared to the fundamental $\ell = 2$ gravitational QNM of a Schwarzschild BH. Axial and polar modes are not isospectral at variance with the BH case. As $\epsilon \rightarrow 0$, the ECO QNMs are low-frequencies and long-lived [19, 137].

spurious roots can be ruled out since they are not present by changing the numerical parameters of the method, i.e., the inversion index of the continued fraction. This method was derived by Leaver to compute the QNMs of Kerr BHs [56]. Appendix 3.5 contains a generalization of the method to compact objects. The continued-fraction method is also robust for overtones with a large imaginary part of the frequency for which the direct integration fails. When they both are applicable, the two methods are in excellent agreement within the numerical accuracy that is chosen to find the QNMs.

3.2.4 Black hole vs horizonless compact object spectrum

When normalized by the mass, the QNMs of the system depend on two continuous, dimensionless parameters: the closeness parameter from the horizon of a Schwarzschild BH, ϵ , and the surface reflectivity of the object, $\mathcal{R}(\omega)$. Furthermore, the QNMs depend on some integer numbers, namely the spin s , the angular number ℓ and the overtone number n of the perturbation. In the following, we shall focus on the gravitational ($s = -2$) $\ell = 2$ fundamental mode ($n = 0$) that corresponds to the mode with the smallest imaginary part, i.e., with the largest damping time.

Fig. 3.2 shows the QNM spectrum of a perfectly reflecting ECO compared to the fundamental $\ell = 2$ QNM of a Schwarzschild BH, i.e.,

$$M\omega_{\text{BH}} = M(\omega_{R,\text{BH}} + i\omega_{I,\text{BH}}) = 0.37367 - i0.088962. \quad (3.14)$$

The QNM spectrum of the ECO is derived by imposing the boundary conditions in Eqs. (3.11) and (3.12) on axial and polar perturbations, respectively. The radius of the compact object is located as in Eq. (2.1), where $\epsilon \in (10^{-10}, 10^{-2})$ from the left to the right of the plot. As shown in Fig. 3.2, an important feature of ECOs is the breaking of *isospectrality* between axial and polar modes unlike BHs in GR. Indeed, Schwarzschild BHs have a unique QNM spectrum despite the Regge-Wheeler potential for axial perturbations in Eq. (3.5) is different from the Zerilli potential for polar perturbations in Eq. (3.6). The isospectrality can be demonstrated by showing that the Regge-Wheeler and Zerilli wave functions are related by a Darboux transformation [232, 55, 233, 234]

$$\psi_{\text{RW}} = A \frac{d\psi_{\text{Z}}}{dr_*} + B(r)\psi_{\text{Z}}, \quad (3.15)$$

where

$$A = -M \left[i\omega M + \frac{1}{3}q(q+1) \right]^{-1}, \quad (3.16)$$

$$B(r) = \frac{q(q+1)(qr+3M)r^2 + 9M^2(r-2M)}{r^2(qr+3M)[q(q+1) + 3i\omega M]}. \quad (3.17)$$

At the BH horizon, both the Regge-Wheeler and the Zerilli wave functions are purely ingoing. Conversely, at the effective radius of the horizonless compact object, the boundary conditions are mapped differently from Eq. (3.15) since the Regge-Wheeler and the Zerilli wave functions are a superposition of waves as in Eq. (3.9).

Fig. 3.2 also shows that in the BH limit ($\epsilon \rightarrow 0$) the deviations from the BH QNM are arbitrarily large and the QNMs are low frequencies, i.e., $M\omega_R \ll M\omega_{R,\text{BH}}$, and long-lived, i.e., $\tau_{\text{damp}} \gg 1$ [19]. For example, for $\epsilon = 10^{-10}$ the fundamental $\ell = 2$ QNMs of a perfectly reflecting ECO are

$$M\omega_{\text{axial}} = 0.074698 - i2.2992 \times 10^{-9}, \quad (3.18)$$

$$M\omega_{\text{polar}} = 0.037914 - i2.7385 \times 10^{-11}. \quad (3.19)$$

Low-frequency QNMs are a peculiar feature of horizonless compact objects whose compactness is similar to the BH one. These modes can be understood in terms of quasi-trapped modes between the effective radius of the object and the photon sphere barrier, as shown in Fig. 3.1. The real part of the QNMs scales as the width of the cavity of the effective potential, i.e., $\omega_R \sim 1/r_*^0$; whereas the imaginary part of the QNMs is given by the modes that tunnel through the potential barrier and reach infinity, i.e., $\omega_I \sim |\mathcal{A}|^2/r_*^0$ where $|\mathcal{A}|^2$ is the tunneling probability. For $\epsilon \ll 1$, the QNMs can be derived analytically in the low-frequency regime as [31, 13]

$$\omega_R \simeq -\frac{\pi}{2|r_*^0|} \left[p + \frac{s(s+1)}{2} \right] \sim |\log \epsilon|^{-1}, \quad (3.20)$$

$$\omega_I \simeq -\frac{\beta_{s\ell}}{|r_*^0|} (2M\omega_R)^{2\ell+2} \sim -|\log \epsilon|^{-(2\ell+3)}, \quad (3.21)$$

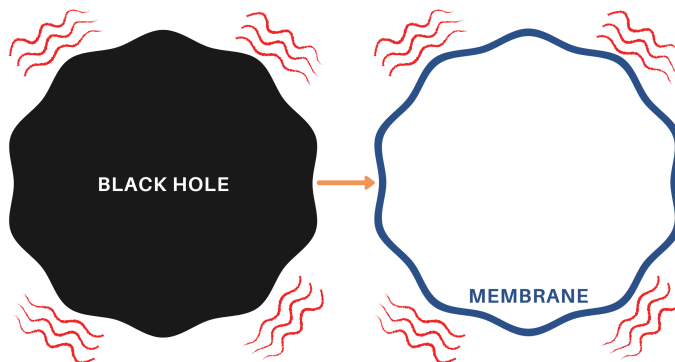


Figure 3.3. Schematic representation of the BH membrane paradigm [235, 236]. A static observer outside the horizon can replace the interior of a perturbed BH (left panel) with a perturbed fictitious membrane located at the horizon (right panel). The fictitious membrane is a viscous fluid whose properties (density, pressure, viscosity) are such that the BH phenomenology, particularly the QNM spectrum, is reproduced. [237]

where $\sqrt{\beta_{sl}} = \frac{(\ell-s)!(\ell+s)!}{(2\ell)!(2\ell+1)!}$ and p is a positive odd (even) integer for polar (axial) modes. A detailed derivation of Eqs. (3.20) and (3.21) is given in Appendix 4.8 for their generalization to the spinning case.

3.3 Membrane paradigm for compact objects

In Sec. 3.2, we derived the QNM spectrum of static ultracompact objects whose effective radius is located at $r_0 = 2M(1 + \epsilon)$ with $\epsilon \ll 1$. To derive the QNM spectrum of horizonless objects with different compactness and interior solutions, we make use of the BH membrane paradigm and generalize it to the case of horizonless objects. The membrane paradigm allows us to describe any compact object with a Schwarzschild exterior where no specific model is assumed for the object interior. GR is assumed to work sufficiently well at the radius of the compact object. This assumption is also justified in theories of gravity with higher-curvature/high-energy corrections to GR. In this case, the corrections to the metric are suppressed by powers of $l_P/r_0 \ll 1$, where r_0 is the object radius, and l_P is the Planck length or the scale of new physics. The membrane paradigm allows us to derive the QNMs of gravastars, wormholes, nonlocal stars, anisotropic stars, etc., after fixing the (possibly frequency-dependent) viscosity of the fictitious membrane according to the model.

3.3.1 Setup

According to the BH membrane paradigm, a static observer outside the horizon can replace the interior of a perturbed BH by a perturbed *fictitious* membrane

located at the horizon [235, 238, 236] (see Fig. 3.3). The features of the interior spacetime are mapped into the properties of the membrane that are fixed by the Israel-Darmois junction conditions [239, 240]

$$[[K_{ab} - Kh_{ab}]] = -8\pi T_{ab}, \quad [[h_{ab}]] = 0, \quad (3.22)$$

where $[[\dots]] = (\dots)^+ - (\dots)^-$ denotes the jump of a quantity across the membrane, \mathcal{M}^+ and \mathcal{M}^- are the exterior and the interior spacetimes to the membrane, h_{ab} is the induced metric on the membrane, K_{ab} is the extrinsic curvature, $K = K_{ab}h^{ab}$, and T_{ab} is the stress-energy tensor of the membrane.

The fictitious membrane is such that the extrinsic curvature of the interior spacetime vanishes, i.e., $K_{ab}^- = 0$ [236]. As a consequence, the junction conditions impose that the fictitious membrane is a viscous fluid with stress-energy tensor

$$T_{ab} = \rho u_a u_b + (p - \zeta \Theta) \gamma_{ab} - 2\eta \sigma_{ab}, \quad (3.23)$$

where η and ζ are the shear and bulk viscosities of the fluid, ρ , p and u_a are the density, pressure and 3-velocity of the fluid, $\Theta = u^a_{;a}$ is the expansion, $\sigma_{ab} = \frac{1}{2}(u_{a;c}\gamma_b^c + u_{b;c}\gamma_a^c - \Theta\gamma_{ab})$ is the shear tensor, $\gamma_{ab} = h_{ab} + u_a u_b$ is the projector tensor, and the semicolon is the covariant derivative compatible with the induced metric, respectively.

The BH membrane paradigm allows us to describe the interior of a perturbed BH in terms of the shear and the bulk viscosities of a fictitious viscous fluid located at the horizon, where

$$\eta_{\text{BH}} = \frac{1}{16\pi}, \quad \zeta_{\text{BH}} = -\frac{1}{16\pi}. \quad (3.24)$$

The generalization of the BH membrane paradigm to horizonless compact objects allows us to describe several models of ECOs with different interior solutions with an exterior Schwarzschild spacetime in terms of the properties of a fictitious membrane located at the ECO radius [80, 237]. The details on the calculations are given in Appendix 3.6. The shear and the bulk viscosities of the fluid are generically complex and frequency-dependent and are related to the reflective properties of the ECO. For each model of ECO, the shear and the bulk viscosities are uniquely determined. In the following, we shall focus on the case in which η and ζ are real and constant since the energy dissipation is absent when $\Re(\eta) = \Re(\zeta) = 0$.

3.3.2 Boundary conditions

Gravitational perturbations in the exterior Schwarzschild spacetime are governed by the Schrödinger-like equation in Eq. (3.3), where the effective potential is in Eqs. (3.5) and (3.6) for axial and polar perturbations, respectively.

By imposing boundary conditions at infinity and the radius of the compact object, Eq. (3.3) defines the complex QNMs of the system. We impose that

the perturbation is a purely outgoing wave at infinity, whereas the condition on the inner boundary would depend on the properties of the object. We rely on the membrane paradigm to derive the boundary condition at the radius of the compact object without assuming any specific model of ECO. As detailed in Appendix 3.6, the boundary conditions at the ECO radius are [237]

$$\frac{d\psi(r_0)/dr_*}{\psi(r_0)} = -\frac{i\omega}{16\pi\eta} - \frac{r_0^2 V_{\text{axial}}(r_0)}{2(r_0 - 3M)}, \quad \text{axial}, \quad (3.25)$$

$$\frac{d\psi(r_0)/dr_*}{\psi(r_0)} = -16\pi i\eta\omega + G(r_0, \omega, \eta, \zeta), \quad \text{polar}, \quad (3.26)$$

where $G(r_0, \omega, \eta, \zeta)$ is a cumbersome function given in Appendix 3.6. Let us notice that in the BH limit ($r_0 \rightarrow 2M$) the boundary conditions in Eqs. (3.25) and (3.26) reduce to the BH boundary condition of a purely ingoing wave at the horizon as $\eta \rightarrow \eta_{\text{BH}}$. This result agrees with the standard BH membrane.

The boundary conditions in Eqs. (3.25) and (3.26) allow us to describe several models of ECOs in terms of the shear and bulk viscosities of the fictitious membrane located at the radius of the object. For example, ultracompact thin-shell wormholes with Dirichlet (Neumann) boundary conditions [19] are described by $\eta = 0$ ($\eta \rightarrow \infty$). Whereas, ultracompact thin-shell gravastars [213] are described by a complex and frequency-dependent shear viscosity that is expressed in terms of hypergeometric functions

$$\begin{aligned} \eta = & \frac{1}{16\pi} - \frac{i\epsilon}{64\pi M\omega} \left[8 - 2\ell^2 + 2iM\omega + (1 + \ell + 2iM\omega)(2 + \ell + 2iM\omega) \right. \\ & \times \left. \frac{{}_2F_1\left(\frac{1}{2}(3 + \ell + 2iM\omega), \frac{1}{2}(4 + \ell + 2iM\omega); \frac{5}{2} + \ell; 1\right)}{{}_2F_1\left(\frac{1}{2}(1 + \ell + 2iM\omega), \frac{1}{2}(2 + \ell + 2iM\omega); \frac{3}{2} + \ell; 1\right)} \right] + \mathcal{O}(\epsilon^2). \end{aligned} \quad (3.27)$$

In particular, the axial sector depends only on the shear viscosity of the membrane, whereas the polar sector depends also on the bulk viscosity of the fictitious fluid. In the BH limit, the dependence on the bulk viscosity disappears ($G(2M) = 0$) therefore the parameter for the bulk viscosity is not fixed by the linear perturbation analysis (see Appendix 3.6 for details).

3.3.3 Effective reflectivity of compact objects

According to the membrane paradigm, the effective reflectivity of compact objects is mapped into the shear and bulk viscosities of the fictitious fluid located at the radius of the object. To illustrate their relation, we compute the effective reflectivity of the spacetime through the scattering of a wave coming from infinity and being partially reflected after being subjected to the boundary conditions in Eqs. (3.25) and (3.26) at $r = r_0$, i.e.,

$$\psi \sim e^{-i\omega r_*} + \text{Re}^{i\omega r_*}, \quad r_* \rightarrow \infty. \quad (3.28)$$

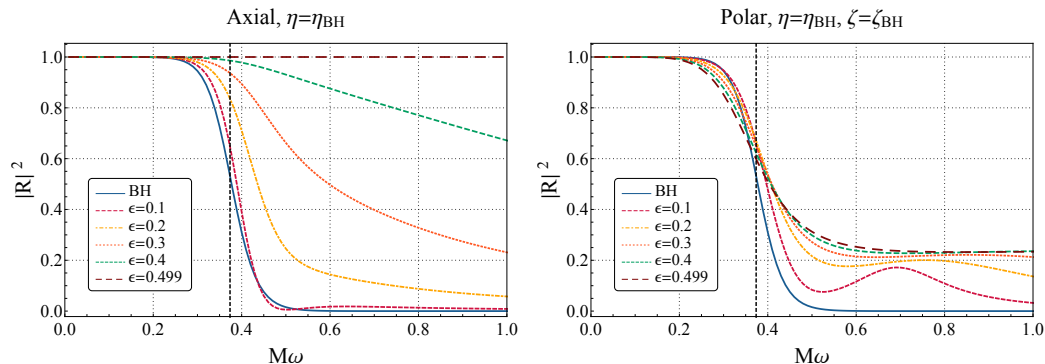


Figure 3.4. Effective reflectivity of compact objects for axial (left panel) and polar (right panel) gravitational perturbations as a function of the frequency. The radius of the compact object is located at $r_0 = 2M(1 + \epsilon)$, and the shear and bulk viscosities of the membrane are $\eta = \eta_{\text{BH}}$ and $\zeta = \zeta_{\text{BH}}$, respectively. In both panels, the vertical dashed line corresponds to the fundamental QNM frequency of a Schwarzschild BH, i.e., $M\omega_{R,\text{BH}} \sim 0.37367$. [237]

Let us notice that the effective reflectivity at infinity defined in Eq. (3.28) is different from the surface reflectivity defined in Eq. (3.10) at the radius of ultracompact objects.

In the large-frequency limit ($M\omega \gg 1$), the potential in Eq. (3.3) can be neglected and the effective reflectivity reads

$$|R|^2 = \left(\frac{1 - \eta/\eta_{\text{BH}}}{1 + \eta/\eta_{\text{BH}}} \right)^2. \quad (3.29)$$

Eq. (3.29) shows that a compact object is a perfect absorber of high-frequency waves ($|R|^2 = 0$) when $\eta = \eta_{\text{BH}}$, whereas it is a perfect reflector of high-frequency waves ($|R|^2 = 1$) when either $\eta = 0$ or $\eta \rightarrow \infty$.

In the case of horizonless ultracompact objects with $\epsilon \ll 1$, the effective reflectivity at infinity in Eq. (3.29) coincides with the surface reflectivity of the object when the latter does not have an explicit dependence on the frequency, i.e., $|R|^2 = |\mathcal{R}|^2$. For $\eta = 0$, the ultracompact object is perfectly reflecting ($|R|^2 = 1$) and the boundary conditions in Eqs. (3.25) and (3.26) reduce to Dirichlet and Neumann boundary conditions on axial and polar modes in Eqs. (3.11) and (3.12), respectively. Also for $\eta \rightarrow \infty$, the ultracompact object is perfectly reflecting.

Although η is formally a free parameter, we expect the most interesting range to be $\eta \in [0, \eta_{\text{BH}}]$. Indeed, from Eq. (3.29) negative values of η would correspond to $|R|^2 > 1$ that would lead to superradiant instabilities [29]. Similarly, for $\eta > \eta_{\text{BH}}$ the effective reflectivity is a growing function of the shear viscosity, which is unphysical. For this reason, partially absorbing ultracompact objects are analyzed by considering $\eta \in (0, \eta_{\text{BH}})$.

We compute the effective reflectivity in Eq. (3.28) for generic frequencies numerically. Fig. 3.4 shows the effective reflectivity of compact objects with

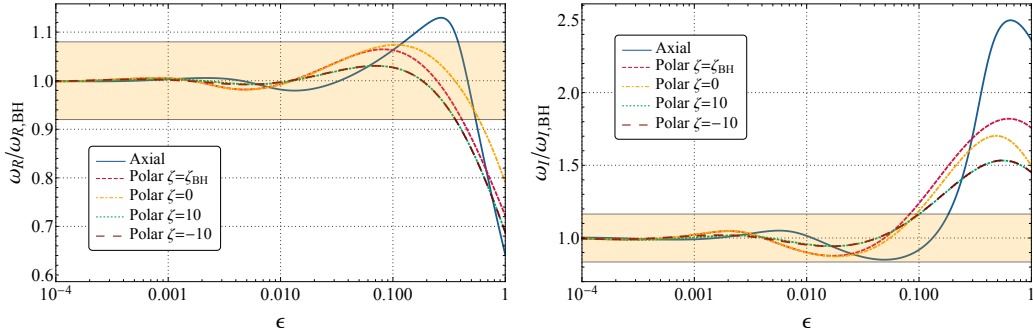


Figure 3.5. Real (left panel) and imaginary (right panel) part of the QNMs of an ECO described by a fictitious fluid with shear viscosity $\eta = \eta_{\text{BH}}$ and compared to the fundamental $\ell = 2$ gravitational QNM of a Schwarzschild BH, as a function of the closeness parameter ϵ where the ECO radius is located at $r_0 = 2M(1 + \epsilon)$. The highlighted region corresponds to the maximum deviation (with 90% credibility) for the least-damped QNM in the event GW150914 to the Kerr BH case [79]. Horizonless compact objects with $\epsilon \lesssim 0.1$ are compatible with current measurement accuracies.

different radii compared to the BH reflectivity as a function of the frequency. The left (right) panel shows the effective reflectivity for axial (polar) gravitational perturbations with shear and bulk viscosities $\eta = \eta_{\text{BH}}$ and $\zeta = \zeta_{\text{BH}}$, respectively.

Interestingly, as the ECO radius approaches the photon sphere ($\epsilon \rightarrow 1/2$) the effective reflectivity tends to unity in the axial sector for any frequency. This distinctive feature can be understood by noticing that the axial boundary condition in Eq. (3.25) reduces to $\psi(r_0) = 0$ as $r_0 \rightarrow 3M$ for any complex η . As a consequence, any ECO with $r_0 = 3M$ is a *perfect reflector* of axial GWs regardless of the interior structure¹. The same universality does not occur in the polar sector.

Let us also notice that the effective reflectivity at intermediate frequencies ($M\omega = \mathcal{O}(0.1 - 1)$) can be larger than the BH reflectivity. For example, at the fundamental QNM frequency of a Schwarzschild BH $M\omega_{R,\text{BH}} \sim 0.37367$, shown in Fig. 3.4 as a dashed vertical line, the effective reflectivity is about unity for $\epsilon = 0.4$ in the axial sector. This effect has relevant consequences in the QNM spectrum of compact objects with respect to the BH QNM spectrum, as we shall discuss in Sec. 3.3.4.

3.3.4 Quasi-normal mode spectrum

Equation (3.3) with boundary conditions at infinity in Eq. (3.8) and at the radius of the compact object in Eqs. (3.25) and (3.26) for the axial and polar

¹The only exception is when $\eta \rightarrow -\frac{3i\omega}{16\pi q}(r_0 - 3M)$ as $r_0 \rightarrow 3M$, in which case the divergence in Eq. (3.25) cancels out. This peculiar case corresponds to thin-shell gravastars [157].

sector, respectively, can be solved numerically to derive the QNM spectrum of a static horizonless compact object. When normalized by the mass, the QNMs of the object depend on three integers, i.e., the spin s , the angular number ℓ , and the overtone number n of the perturbation. The QNM spectrum also depends on some continuous parameters that are related to the properties of the system, i.e., its compactness through the parameter ϵ as in Eq. (2.2). In the axial sector, the QNMs depend on the shear viscosity of the membrane η , whereas in the polar sector there is an additional dependence on the bulk viscosity of the membrane ζ .

We compute the QNM spectrum with two numerical methods: a direct integration shooting method, as described in Sec. 3.2.3, and a method based on continued fractions, as described in Appendix 3.5. The continued fraction method is more robust than the direct integration for overtones with a large imaginary part of the frequency. When they both are applicable, we checked that the two methods are in excellent agreement.

Let us first analyze the QNM spectrum of a horizonless compact object with $\eta = \eta_{\text{BH}}$. Fig. 3.5 shows the ratio of the real (left panel) and imaginary (right panel) part of the ECO QNMs to the fundamental $\ell = 2$ QNM of a Schwarzschild BH, as a function of ϵ . As $\epsilon \rightarrow 0$, the horizonless compact object has the same QNM spectrum of a Schwarzschild BH. This is because, as $\epsilon \rightarrow 0$, the compact object has the same reflective properties of a BH for $\eta = \eta_{\text{BH}}$. For larger values of ϵ , the compactness of the object decreases and the QNMs start deviating from the BH QNM. Let us notice that the isospectrality of axial and polar modes in BHs is broken for finite values of ϵ . In the case of horizonless objects, the fundamental $\ell = 2$ modes form a characteristic *doublet*. Polar modes show a mild dependence on the bulk viscosity of the membrane. In the large- ζ limit, the QNM spectrum is independent of the bulk viscosity, as shown by the $\zeta = \pm 10$ curves in Fig. 3.5.

The highlighted regions in Fig. 3.5 correspond to the maximum allowed deviation (with 90% credibility) for the least-damped QNM in the event GW150914, and correspond to $\sim 16\%$ and $\sim 33\%$ for the real and imaginary part of the QNM, respectively [79]. Remarkably, Fig. 3.5 shows that horizonless compact objects with $\epsilon \lesssim 0.1$ are compatible with current measurement accuracies. Future ringdown detections would allow us to set more stringent constraints on the radius of compact objects.

Let us now change the reflective properties of the compact object via the parameter η . Fig. 3.6 shows the complex QNM plane of a horizonless compact object under axial perturbations for several values of ϵ . Each curve is parametrized by the shear viscosity of the membrane where $\eta \in [10^{-4}, 100]$. As a reference, the fundamental QNM of a Schwarzschild BH is marked by a black dot corresponding to $\eta = \eta_{\text{BH}}$ and $\epsilon = 0$. As the location of the radius of the object approaches the photon sphere ($\epsilon \rightarrow 1/2$), the axial QNMs become independent of η . Indeed, the QNMs tend to a universal mode (marked by an

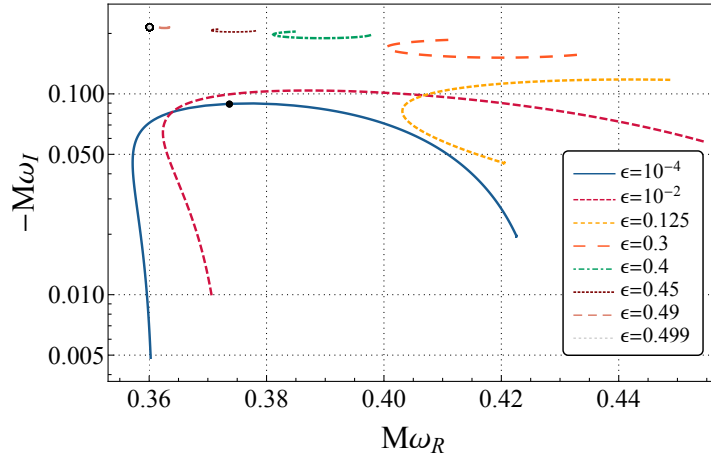


Figure 3.6. The complex QNM plane of a horizonless compact object for axial perturbations. Each curve is the QNM spectrum of a compact object with a given radius $r_0 = 2M(1+\epsilon)$ parametrized by the shear viscosity of the membrane, $\eta \in [10^{-4}, 100]$. As the radius of the object approaches the photon sphere ($\epsilon \rightarrow 1/2$), the curves converge to a universal QNM (marked with an empty black circle) regardless of the value of η . As a reference, the fundamental QNM of a Schwarzschild BH is marked by a black dot. [237]

empty black circle in Fig. 3.6) which, for $\ell = 2$, reads

$$M\omega_{\text{axial}} \sim 0.3601 - i0.2149, \quad \epsilon \rightarrow 1/2, \quad (3.30)$$

As previously discussed, in this limit the object is a perfect reflector of axial GWs, regardless of the value of η . This remarkable universality does not apply to the case of polar perturbations.

Let us analyze the transition from fundamental modes to overtones as a function of the shear viscosity of the membrane for $\epsilon \ll 1$. Indeed, in the $\epsilon \rightarrow 0$ limit, the parameter η interpolates between the BH case ($\eta = \eta_{\text{BH}}$) and the perfectly reflecting case ($\eta = 0$). Fig. 3.7 shows the tracking of the fundamental mode (blue curve) and the first overtone (red curve) of a Schwarzschild BH by changing the shear viscosity of the membrane. We notice that the change in the imaginary part of the QNMs is drastic even for small variations of the shear viscosity with respect to the BH case. Fig. 3.7 displays a crossing point after which the BH overtone has a smaller imaginary part than the BH fundamental mode and becomes more relevant in the ringdown stage. This trend is general and BH higher overtones become long-lived in the $\eta \rightarrow 0$ limit. This transition could explain the presence of low-frequency QNMs in the case of perfectly reflecting objects, as discussed in Sec. 3.2.4.

We notice that the tracking of higher overtones as a function of the shear viscosity is numerically challenging. Indeed, the BH QNM spectrum is unstable against small deformations of the eigenvalue problem [241]. In our numerical

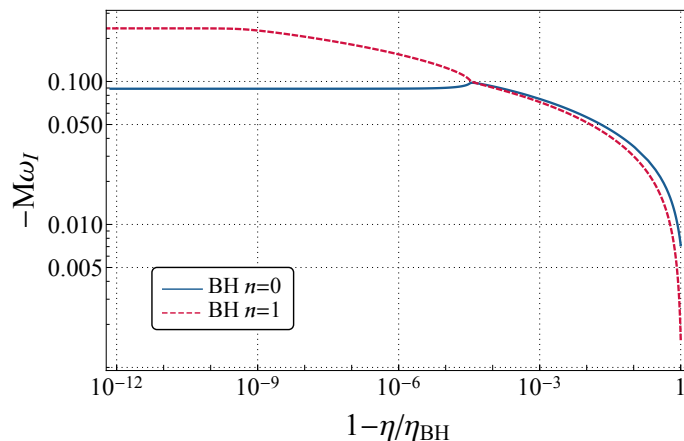


Figure 3.7. Imaginary part of the axial QNMs of a compact object with radius $r_0 = 2M(1+\epsilon)$ and $\epsilon = 10^{-10}$ as a function of the shear viscosity of the membrane. The fundamental mode (blue curve) and the first overtone (red curve) of a Schwarzschild BH are tracked from $\eta = \eta_{\text{BH}}$ (leftmost part of the plot) to the limit of a perfectly reflecting object, $\eta = 0$ (rightmost part). The figure shows a crossing point after which the imaginary part of the BH overtone becomes smaller than the one of the BH fundamental mode. [22]

analysis, we have seen hints of this instability (which is more severe for high-order overtones) due to finite- ϵ effects and the slightly different boundary conditions when approaching the BH limit.

3.3.5 Current constraints and prospects of detectability

Current measurement accuracies impose strong constraints on the compactness and reflectivity of horizonless compact objects. Fig. 3.8 shows the relative percentage difference between the BH QNM and the QNMs of a compact object with radius $r_0 = 2M(1 + \epsilon)$ as a function of the closeness parameter ϵ and the shear viscosity $\eta \in [0, \eta_{\text{BH}}]$. The left (right) panels show the relative percentage difference of the real (imaginary) part of the QNMs under axial and polar perturbations in the top and bottom panels, respectively. The contour lines correspond to the accuracy within which the least-damped QNM of the remnant of GW150914 has been measured [79]. Indeed, GW150914 gives the single-event most-stringent constraints with a maximum allowed deviation from the least-damped QNM of a Kerr BH of $\sim 16\%$ and $\sim 33\%$ for the real and imaginary part of the QNM, respectively. The dashed areas are the regions of the (ϵ, η) parameter space that would be excluded by the individual measurement of the real and imaginary part of the fundamental QNM. The dark shaded areas are the regions that would not be excluded by a simultaneous measurement of the real and imaginary part of the QNM in the axial (top panels) and polar (bottom panels) sectors.

Interestingly, already with the current LIGO/Virgo accuracy we can poten-

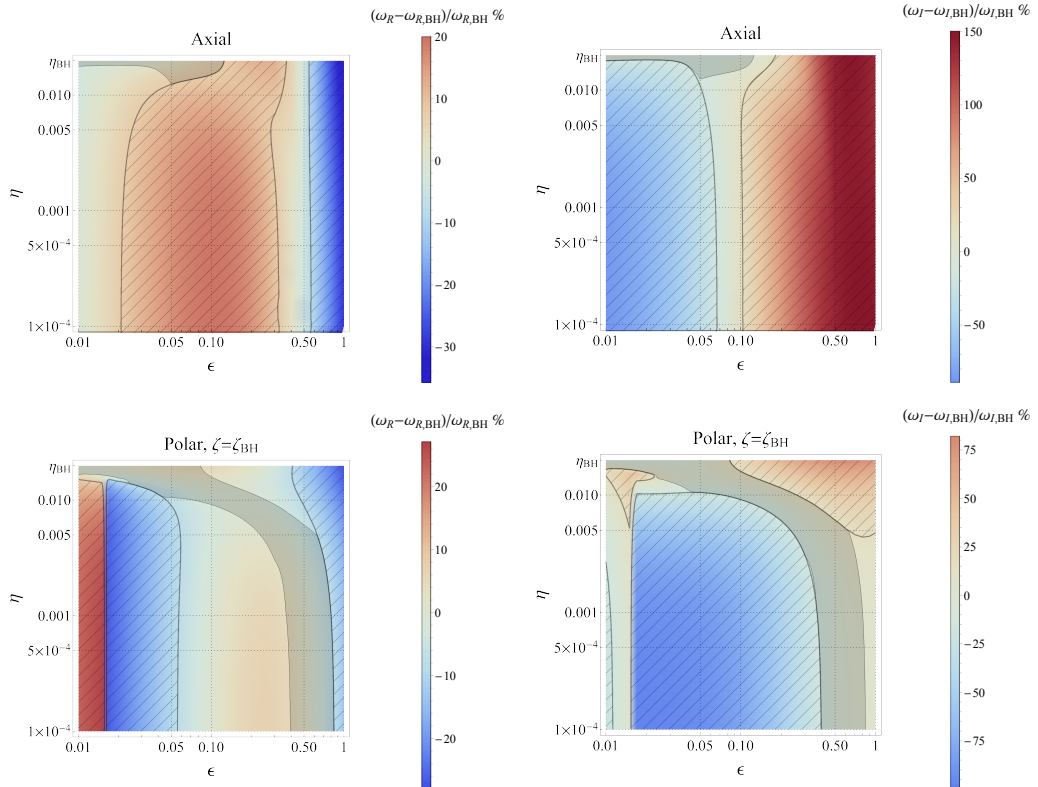


Figure 3.8. Relative percentage difference of the real (left panels) and imaginary (right panels) part of the QNMs of a horizonless compact object to the fundamental QNM of a Schwarzschild BH under axial (top panels) and polar (bottom panels) perturbations. The QNMs of the compact object are parametrized by the compactness of the object through the parameter $\epsilon \in [0.01, 1]$ and the shear viscosity $\eta \in [0, \eta_{\text{BH}}]$. The dashed areas are the regions that would be excluded by individual measurements of the real (left) and imaginary (right) part of the QNMs with the same accuracy as in GW150914 [79]. The dark shaded region is the area that would not be excluded by a simultaneous measurement of the frequency and the damping time with current measurement accuracies. [237]

tially place strong constraints on the parameter space of horizonless compact objects. By combining the information from the real and imaginary part of the QNMs, Fig. 3.8 shows that only a small region of the parameter space with $\epsilon \lesssim 0.1$ and $\eta \approx \eta_{\text{BH}}$ (dark shaded area) is compatible with current constraints in the axial sector. For polar perturbations, a wider region in the parameter space with $\epsilon \gtrsim 0.1$ and $0 < \eta < \eta_{\text{BH}}$ is compatible with current constraints. We assess that current measurement accuracies impose a strong lower bound on the compactness of the merger remnant, which cannot be smaller than 90% the BH compactness.

Next-generation detectors, i.e., the Einstein Telescope [94] and LISA [35], will have an overall improvement of the SNR by an order of magnitude. The

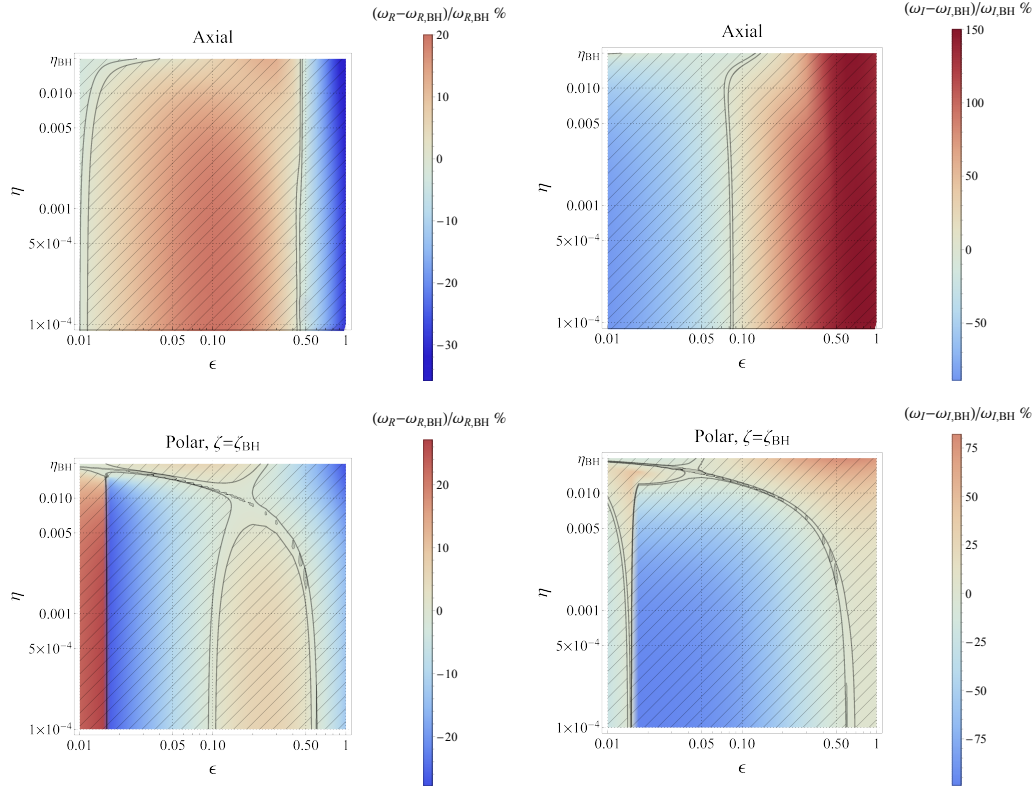


Figure 3.9. Same as Fig. 3.8. The dashed areas are the regions that would be excluded by individual measurements of the real and imaginary part of the QNMs by next-generation detectors, assuming an order of magnitude improvement in the ringdown measurements relative to current detectors. The dark shaded region that would be compatible with a simultaneous measurement of the frequency and the damping time is absent. Next-generation detectors will allow us to constraint the whole region of the (ϵ, η) parameter space shown in the diagrams.

sensitivity of the detectors will allow us to resolve the fundamental QNM at percent level. As shown in Fig. 3.9, almost the whole region of the (ϵ, η) parameter space would be constrained.

Another signature of new physics is given by the presence of the mode *doublet* in the axial and polar sectors, as discussed in Sec. 3.3.4. A necessary condition to resolve the doublet is based on the Rayleigh resolvability criterion [242]

$$\max[\sigma_{f_1}, \sigma_{f_2}] < |f_1 - f_2|, \quad (3.31)$$

$$\max[\sigma_{Q_1}, \sigma_{Q_2}] < |Q_1 - Q_2|, \quad (3.32)$$

where $f_i = \omega_R^{(i)}/2\pi$ and $Q_i = \pi f_i \tau_i$ are the frequency and the quality factor of the i -th mode, τ_i is the damping factor of the i -th mode, and σ_X is the uncertainty associated to a quantity X . The uncertainties on the parameters are computed with a Fisher analysis assuming that the amplitude ratio between

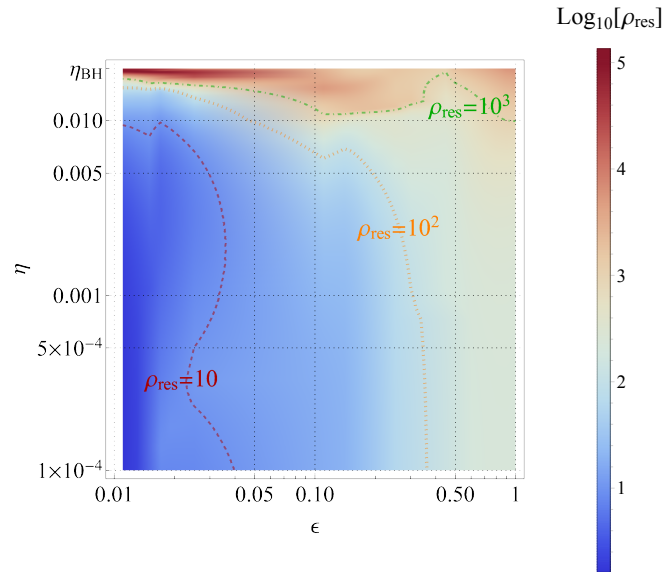


Figure 3.10. Minimum SNR required for the resolvability of the axial-polar QNM doublet according to the Rayleigh criterion. [237]

the axial and polar modes is $1/10$ (see Appendix 3.7 for details). Fig. 3.10 shows the minimum SNR required to resolve the doublet, ρ_{res} , according to the Rayleigh resolvability criterion. In the $\eta \approx \eta_{\text{BH}}$ region, $\rho_{\text{res}} > 10^3$ and it can be smaller for $\eta < \eta_{\text{BH}}$. A comparison between Fig. 3.8 and Fig. 3.10 shows that the resolution of the doublet requires a larger SNR than the detection of the deviations from the BH QNM.

3.4 Appendix: Boundary condition for perfectly reflecting objects

Let us derive the boundary conditions that describe a static and perfectly reflecting ultracompact object under electromagnetic perturbations [29]. The background geometry is the Schwarzschild metric, and the radius of the compact object is located as in Eq. (2.1) where $\epsilon \ll 1$. The background geometry is perturbed by a test electromagnetic field that is governed by the Maxwell equations

$$F^{\mu\nu}_{;\nu} = 0 \quad (3.33)$$

where $F_{\mu\nu} = A_{\nu,\mu} - A_{\mu,\nu}$ is the Maxwell tensor, A_μ is the electromagnetic four-potential, the comma stands for an ordinary derivative and the semi-colon stands for a covariant derivative. The spherical symmetry of the background

allows us to expand the electromagnetic four-potential as

$$A_\mu(t, r, \theta, \varphi) = \sum_{\ell, m} \left[\begin{pmatrix} 0 \\ 0 \\ a^{\ell m}(t, r) \underline{S}_{\ell m}(\theta, \varphi) \end{pmatrix} + \begin{pmatrix} f^{\ell m}(t, r) Y_{\ell m}(\theta, \varphi) \\ h^{\ell m}(t, r) Y_{\ell m}(\theta, \varphi) \\ k^{\ell m}(t, r) \underline{Y}_{\ell m}(\theta, \varphi) \end{pmatrix} \right], \quad (3.34)$$

where the vector spherical harmonics are given by

$$\underline{S}_{\ell m}^\top(\theta, \varphi) = \left(\frac{1}{\sin \theta} \partial_\varphi Y_{\ell m}(\theta, \varphi), -\sin \theta \partial_\theta Y_{\ell m}(\theta, \varphi) \right), \quad (3.35)$$

$$\underline{Y}_{\ell m}^\top(\theta, \varphi) = (\partial_\theta Y_{\ell m}(\theta, \varphi), \partial_\varphi Y_{\ell m}(\theta, \varphi)), \quad (3.36)$$

where $Y_{\ell m}(\theta, \varphi)$ are the scalar spherical harmonics. The first term in the right-hand side of Eq. (3.34) has parity $(-1)^{\ell+1}$ and corresponds to axial modes, whereas the second term in the right-hand side of Eq. (3.34) has parity $(-1)^\ell$ and corresponds to polar modes. By defining

$$\Upsilon^{\ell m}(t, r) = \frac{r^2}{\ell(\ell+1)} \left[\partial_t h^{\ell m}(t, r) - \partial_r f^{\ell m}(t, r) \right], \quad (3.37)$$

and by assuming the time dependence $a^{\ell m}, \Upsilon^{\ell m} \propto e^{-i\omega t}$, Eq. (3.33) translates into a Schrödinger-like equation as in Eq. (3.3), where

$$\psi(r) \equiv \begin{cases} a^{\ell m}(r) & \text{for axial modes} \\ \Upsilon^{\ell m}(r) & \text{for polar modes} \end{cases}, \quad (3.38)$$

and the effective potential is in Eq. (3.5) with $s = -1$.

We model the perfectly reflecting compact object as a perfect conductor at $r = r_0$, where the electric field has vanishing tangential components and the magnetic field has a vanishing parallel component

$$E_\theta(r_0) \propto F_{\theta t}(r_0) = 0, \quad (3.39)$$

$$E_\varphi(r_0) \propto F_{\varphi t}(r_0) = 0, \quad (3.40)$$

$$B_r(r_0) \propto F_{\varphi\theta}(r_0) = 0. \quad (3.41)$$

Eqs. (3.39)–(3.41) yield to

$$a^{\ell m}(t, r_0) = 0, \quad (3.42)$$

$$f^{\ell m}(t, r_0) - \partial_t k^{\ell m}(t, r_0) = 0, \quad (3.43)$$

and the Maxwell equations (3.33) imply

$$f^{\ell m}(t, r_0) - \partial_t k^{\ell m}(t, r_0) = -f(r_0) \partial_r \Upsilon(t, r_0). \quad (3.44)$$

Eqs. (3.42) and (3.43) correspond to Dirichlet ($\psi(r_0) = 0$) and Neumann ($\partial_r \psi(r_0) = 0$) boundary conditions on axial and polar perturbations, respectively, as detailed in Eqs. (3.11) and (3.12).

3.5 Appendix: Continued fractions method

The continued fraction method allows us to compute the QNMs of compact objects as roots of implicit equations [56]. The eigenfunction can be written as a series whose coefficients satisfy a finite-term recurrence relation. To optimize the recurrence relation, it is important to choose a suitable ansatz for the eigenfunction. We analyze the case of a horizonless compact object under gravitational perturbations that is governed by Eq. (3.3) with effective potentials in Eqs. (3.5) and (3.6) and $s = -2$. Let us first focus on axial perturbations, where the solution of Eq. (3.3) can be written as [213]

$$\psi(r) = (r - 2M)^{2iM\omega} e^{i\omega r_*} \phi(z), \quad (3.45)$$

where $\psi(r)$ is the Regge-Wheeler wave function, $z \equiv 1 - R_2/r$, and $R_2 \gtrsim r_0$ is located outside the radius of the compact object. The function $\phi(z)$ satisfies the differential equation

$$\left(c_0 + c_1 z + c_2 z^2 + c_3 z^3\right) \frac{d^2 \phi}{dz^2} + \left(d_0 + d_1 z + d_2 z^2\right) \frac{d\phi}{dz} + (e_0 + e_1 z) \phi = 0, \quad (3.46)$$

where

$$\begin{aligned} c_0 &= 1 - \frac{2M}{R_2}, \quad c_1 = \frac{6M}{R_2} - 2, \quad c_2 = 1 - \frac{6M}{R_2}, \quad c_3 = \frac{2M}{R_2}, \\ d_0 &= 2i\omega R_2 + \frac{6M}{R_2} - 2, \quad d_1 = 2 \left(1 - \frac{6M}{R_2}\right), \quad d_2 = \frac{6M}{R_2}, \\ e_0 &= \frac{6M}{R_2} - \ell(\ell + 1), \quad e_1 = -\frac{6M}{R_2}. \end{aligned} \quad (3.47)$$

Let us perform a series expansion of $\phi(z)$ as

$$\phi(z) = \sum_{n=0}^{\infty} a_n z^n. \quad (3.48)$$

By substituting Eq. (3.48) in Eq. (3.46), we derive a four-term recurrence relation for the expansion coefficients a_n :

$$\begin{aligned} \alpha_1 a_2 + \beta_1 a_1 + \gamma_1 a_0 &= 0, \quad n = 1, \\ \alpha_n a_{n+1} + \beta_n a_n + \gamma_n a_{n-1} + \delta_n a_{n-2} &= 0, \quad n \geq 2, \end{aligned} \quad (3.49)$$

where

$$\begin{aligned} \alpha_n &= n(n+1)c_0, \quad n \geq 1, \\ \beta_n &= (n-1)nc_1 + nd_0, \quad n \geq 1, \\ \gamma_n &= (n-2)(n-1)c_2 + (n-1)d_1 + e_0, \quad n \geq 1, \\ \delta_n &= (n-3)(n-2)c_3 + (n-2)d_2 + e_1, \quad n \geq 2. \end{aligned} \quad (3.50)$$

The four-term recurrence relation (3.49) can be reduced to a three-term recurrence relation via Gaussian elimination by defining [56]

$$\hat{\alpha}_0 = -1, \quad \hat{\beta}_0 = \frac{a_1}{a_0}. \quad (3.51)$$

The term a_1/a_0 is determined by imposing the continuity of the solution (3.45) and its derivative at $r = R_2$, namely

$$\frac{a_1}{a_0} = \frac{R_2}{\psi(R_2)} \left[\frac{d\psi(R_2)}{dr} - \frac{i\omega}{f(R_2)} \psi(R_2) \right], \quad (3.52)$$

where the values of $\psi(R_2)$ and $d\psi(R_2)/dr$ are computed numerically by integrating Eq. (3.3) from $r = r_0$ up to $r = R_2$ with a suitable boundary condition at r_0 . The remaining coefficients can be determined by recursion from Eq. (3.49). In the case of polar perturbations, we integrate Eq. (3.3) numerically with the effective potential in Eq. (3.6) from $r = r_0$ up to $r = R_2$. We obtain the values of the Zerilli function $\psi_Z(R_2)$ and its derivative $d\psi_Z(R_2)/dr$ from which we derive the value of the Regge-Wheeler function in Eq. (3.52) using the relation in Eq. (3.15).

Finally, by defining

$$\hat{\alpha}_n = \alpha_n, \quad \hat{\beta}_n = \beta_n, \quad \hat{\gamma}_n = \gamma_n, \quad n = 1, \quad (3.53)$$

$$\hat{\alpha}_n = \alpha_n, \quad \hat{\beta}_n = \beta_n - \frac{\hat{\alpha}_{n-1}\delta_n}{\hat{\gamma}_{n-1}}, \quad \hat{\gamma}_n = \gamma_n - \frac{\hat{\beta}_{n-1}\delta_n}{\hat{\gamma}_{n-1}}, \quad \hat{\delta}_n = 0, \quad n \geq 2, \quad (3.54)$$

the four-term recurrence relation (3.49) reduces to the following three-term relation

$$\hat{\alpha}_n a_{n+1} + \hat{\beta}_n a_n + \hat{\gamma}_n a_{n-1} = 0, \quad (3.55)$$

that can be recast in

$$0 = f_0(\omega) = \hat{\beta}_0 - \frac{\hat{\alpha}_0 \hat{\gamma}_1}{\hat{\beta}_1 -} \frac{\hat{\alpha}_1 \hat{\gamma}_2}{\hat{\beta}_2 -} \frac{\hat{\alpha}_2 \hat{\gamma}_3}{\hat{\beta}_3 -} \dots \quad (3.56)$$

Using the inversion properties of the continued fractions, Eq. (3.56) can be inverted n times to yield

$$0 = f_n(\omega) = \hat{\beta}_n - \frac{\hat{\alpha}_{n-1} \hat{\gamma}_n}{\hat{\beta}_{n-1} -} \frac{\hat{\alpha}_{n-2} \hat{\gamma}_{n-1}}{\hat{\beta}_{n-2} -} \dots \frac{\hat{\alpha}_0 \hat{\gamma}_1}{\hat{\beta}_0 -} - \frac{\hat{\alpha}_n \hat{\gamma}_{n+1}}{\hat{\beta}_{n+1} -} \frac{\hat{\alpha}_{n+1} \hat{\gamma}_{n+2}}{\hat{\beta}_{n+2} -} \frac{\hat{\alpha}_{n+2} \hat{\gamma}_{n+3}}{\hat{\beta}_{n+3} -} \dots \quad (3.57)$$

where $n = 1, 2, \dots$. The roots of Eqs. (3.56) and (3.57) are the QNMs of the system. Since the functions $f_n(\omega)$ have different convergence properties, each of them is best suited to find the QNMs in a given region of the parameter space. Searching for roots with $n = 0$ is usually sufficient, but when the QNMs have a large imaginary part there could be stable numerical solutions for $n = 1$ and $n = 2$.

Overall, the solution is convergent if we choose R_2 such that $R_2 > 2M$ and $R_2/2 < r_0 < R_2$ [243]. By defining $r_0 = 2M(1 + \epsilon)$ and $R_2 = 2M(1 + R_{2,0})$, we derive that the integration should be performed from $r = r_0$ up to $r = R_2$ with $\epsilon < R_{2,0} < 1 + 2\epsilon$ to ensure numerical stability.

3.6 Appendix: Membrane paradigm

In this Appendix, we provide details on the derivation of the boundary conditions in Eqs. (3.25) and (3.26) describing horizonless compact objects with a Schwarzschild exterior and a radius located at $r_0 = 2M(1 + \epsilon)$. The membrane paradigm allows us to map the interior of several models of ECOs in terms of the properties of a fictitious membrane located at the radius of the object. Being \mathcal{M} the whole spacetime manifold, we define \mathcal{M}^+ and \mathcal{M}^- as the exterior and the interior regions to the 3-dimensional membrane (or shell) that are described by the metrics $g_{\mu\nu}^+(x^+)$ and $g_{\mu\nu}^-(x^-)$, respectively, with coordinates

$$x^{+\mu} = (t^+, r^+, \theta^+, \varphi^+), \quad x^{-\mu} = (t^-, r^-, \theta^-, \varphi^-). \quad (3.58)$$

We assume that the exterior spacetime is described by the Schwarzschild metric in Boyer-Lindquist coordinates as in Eq. (3.1) and that GR works sufficiently well near the radius of the compact object, whereas the interior spacetime can be described by any theory of gravity.

The coordinates of the membrane are $x_m^\mu = (t, r_0, \theta, \varphi)$ so that the intrinsic 3-dimensional coordinates on the shell are

$$y^a = (t, \theta, \varphi). \quad (3.59)$$

The induced metric on the membrane is defined as

$$h_{ab} = e_a^\mu e_b^\nu g_{\mu\nu}, \quad (3.60)$$

where the basis of three independent generators for the shell can be chosen as

$$e_a^\mu = \frac{\partial x^\mu}{\partial y^a}. \quad (3.61)$$

The extrinsic curvature on the membrane is defined as

$$K_{ab} = e_a^\mu e_b^\nu \nabla_\mu n_\nu, \quad (3.62)$$

where n^μ is the normal vector to the membrane and $\nabla_\mu \equiv \partial/\partial x^\mu$. Since the membrane is a time-like surface, we impose that the normal vector to the membrane is space-like, i.e., $n_\mu n^\mu = 1$. The trace of the extrinsic curvature is derived as $K = h^{ab} K_{ab}$.

To embed the membrane in the manifold \mathcal{M} we impose the Israel-Darmois junction conditions [239, 240]:

$$h_{ab}^+ = h_{ab}^- \equiv h_{ab}, \quad (3.63)$$

and

$$(K^+ h_{ab} - K_{ab}^+) - (K^- h_{ab} - K_{ab}^-) = 8\pi T_{ab}, \quad (3.64)$$

where h_{ab}^+ (h_{ab}^-) and K_{ab}^+ (K_{ab}^-) are the induced metric and extrinsic curvature defined in the exterior (interior) spacetime to the shell, respectively, and T_{ab} is the stress-energy tensor of the matter distribution located on the membrane.

According to the original formulation of the membrane paradigm, the matter is fictitious and is such that the extrinsic curvature in the interior spacetime vanishes [236]

$$K_{ab}^- = 0, \quad (3.65)$$

so that the junction condition in Eq. (3.64) reduces to

$$Kh_{ab} - K_{ab} = 8\pi T_{ab}, \quad (3.66)$$

where, for simplicity, we define $K_{ab} \equiv K_{ab}^+$ and the coordinates of the exterior spacetime as $x^\mu = (t, r, \theta, \varphi)$. Let us notice that it is always possible to find a metric for the interior spacetime $g_{\mu\nu}^-(x^-)$ that satisfies the junction conditions in Eqs. (3.63) and (3.64) together with the assumption in Eq. (3.65).

By imposing the condition in Eq. (3.65), the membrane paradigm allows us to map the information on the interior spacetime into the stress-energy tensor of the fictitious membrane. The junction conditions in Eqs. (3.63) and (3.64) are compatible with a membrane described by the stress-energy tensor of a viscous fluid

$$T_{ab} = \rho u_a u_b + (p - \zeta \Theta) \gamma_{ab} - 2\eta \sigma_{ab}, \quad (3.67)$$

where ρ and p are the density and pressure, η and ζ are the shear and bulk viscosities, u_a is the 3-velocity of the fluid defined in terms of its 4-velocity U_μ as $u_a = e_a^\mu U_\mu$, $\Theta = u_{;a}^a$ is the expansion, $\sigma_{ab} = \frac{1}{2}(u_{a;c} \gamma_b^c + u_{b;c} \gamma_a^c - \Theta \gamma_{ab})$ is the shear tensor, $\gamma_{ab} = h_{ab} + u_a u_b$ is the projector tensor, and $u_{b;a}$ is the 3-dimensional covariant derivative compatible with the induced metric h_{ab} [244, 209].

Unperturbed background

Let us first analyze the background spacetime as in Eq. (3.1). In this case, the induced metric on the membrane reads

$$h_{tt} = -f(r_0), \quad h_{\theta\theta} = \frac{h_{\varphi\varphi}}{\sin^2\theta} = r_0^2. \quad (3.68)$$

The normal vector to the membrane is determined by imposing the four conditions $e_a^\mu n_\mu = 0$ and $n^\mu n_\mu = 1$; its components read

$$n_t = 0, \quad n_r = \frac{1}{\sqrt{f(r)}}, \quad n_\theta = 0, \quad n_\varphi = 0. \quad (3.69)$$

The extrinsic curvature is diagonal,

$$K_{tt} = -\frac{1}{2}\sqrt{f(r_0)}f'(r_0), \quad K_{\theta\theta} = \frac{K_{\varphi\varphi}}{\sin^2\theta} = r_0\sqrt{f(r_0)},$$

where the prime denotes partial derivative with respect to the argument. The stress-energy tensor of the matter distribution reduces to the one of a perfect fluid since the expansion and the shear tensor are null. Indeed, the only nonvanishing component of the fluid 4-velocity $U^\mu = (U^t, U^r, U^\theta, U^\varphi)$ is $U^t = 1/\sqrt{f(r_0)}$. This yields to the the fluid 3-velocity

$$u^a = \left(\frac{1}{\sqrt{f(r_0)}}, 0, 0 \right). \quad (3.70)$$

At the background level, the nonvanishing components of the junction condition in Eq. (3.66) are

$$\begin{aligned} tt : \quad & -\frac{2}{r_0} f^{3/2}(r_0) = 8\pi f(r_0) \rho_0, \\ \theta\theta : \quad & \frac{r_0 [2f(r_0) + r_0 f'(r_0)]}{2\sqrt{f(r_0)}} = 8\pi r_0^2 p_0, \\ \varphi\varphi : \quad & \frac{r_0 \sin^2\theta [2f(r_0) + r_0 f'(r_0)]}{2\sqrt{f(r_0)}} = 8\pi r_0^2 \sin^2\theta p_0. \end{aligned} \quad (3.71)$$

The (tt) component gives the unperturbed density of the membrane [80]

$$\rho_0(r_0) = -\frac{\sqrt{f(r_0)}}{4\pi r_0}; \quad (3.72)$$

whereas the angular components give the unperturbed pressure of the membrane

$$p_0(r_0) = \frac{2f(r_0) + r_0 f'(r_0)}{16\pi r_0 \sqrt{f(r_0)}}. \quad (3.73)$$

Eqs. (3.72) and (3.73) fix a barotropic equation of state $p = p(\rho)$. In the BH limit ($r_0 \rightarrow 2M$), the density vanishes and the pressure diverges as the redshift factor $\epsilon^{-1/2}$. The speed of sound is

$$c_s \equiv \sqrt{\frac{\partial p_0}{\partial \rho_0}} = \sqrt{\frac{1 + 2\epsilon + 4\epsilon^2}{8\epsilon(1/2 - \epsilon)}}, \quad (3.74)$$

that diverges both in the BH limit ($\epsilon \rightarrow 0$) and the photon-sphere limit ($\epsilon \rightarrow 1/2$), and is complex for $\epsilon > 1/2$. Let us notice that the properties of the fluid do not need to be physical since the membrane is fictitious.

Gravitational perturbations

Let us work in the Regge-Wheeler gauge and analyze separately the axial and polar sectors of the gravitational perturbation [229]. The perturbed metric can be cast in the following form

$$g_{\mu\nu} = g_{\mu\nu}^0(r) + \delta g_{\mu\nu}(r, \theta, t), \quad (3.75)$$

where, without loss of generality, the perturbation $\delta g_{\mu\nu}$ does not depend on the azimuthal angle φ owing to the spherical symmetry of the background $g_{\mu\nu}^0$.

Because of the metric perturbations, the dissipative components of the stress-energy tensor are switched on, and both the density and the pressure of the membrane are perturbed as follows

$$\rho = \rho_0 + \delta\rho(t, \theta), \quad (3.76)$$

$$p = p_0 + \delta p(t, \theta). \quad (3.77)$$

The location of the membrane is also affected by the perturbation, and the deviation is parametrized as

$$r_m(t, \theta) = r_0 + \delta r(t, \theta). \quad (3.78)$$

The 4-dimensional coordinates of the membrane are

$$x_m^\mu = (t, r_0 + \delta r(t, \theta), \theta, \varphi), \quad (3.79)$$

and the perturbed tangential vectors e_a^μ introduced in Eq. (3.61) are

$$\begin{aligned} e_t^\mu &= (1, \partial_t \delta r(t, \theta), 0, 0), \\ e_\theta^\mu &= (0, \partial_\theta \delta r(t, \theta), 1, 0), \\ e_\varphi^\mu &= (0, 0, 0, 1). \end{aligned} \quad (3.80)$$

Let us notice that $\delta\rho(t, \theta)$, $\delta p(t, \theta)$ and $\delta r(t, \theta)$ are scalar quantities under rotations, therefore they are only affected by the polar perturbations and can be decomposed as

$$\begin{aligned} \delta\rho(t, \theta) &= \varepsilon \rho_1 P_\ell(\cos \theta) e^{-i\omega t}, \\ \delta p(t, \theta) &= \varepsilon p_1 P_\ell(\cos \theta) e^{-i\omega t}, \\ \delta r(t, \theta) &= \varepsilon \delta r_0 P_\ell(\cos \theta) e^{-i\omega t}. \end{aligned} \quad (3.81)$$

where ρ_1 , p_1 , δr_0 depend only on the unperturbed radius r_0 , $P_\ell(\cos \theta)$ are the Legendre polynomials, and the parameter ε is the perturbation order, so that all the contributions of order $\mathcal{O}(\varepsilon^2)$ are negligible. In the following, we shall analyze the axial and polar sectors separately.

Axial sector

The nonvanishing components of the axial metric perturbations in the Regge-Wheeler gauge are [229]

$$\begin{aligned} \delta g_{t\varphi} &= \varepsilon e^{-i\omega t} h_0(r) \sin \theta \partial_\theta P_\ell(\cos \theta), \\ \delta g_{r\varphi} &= \varepsilon e^{-i\omega t} h_1(r) \sin \theta \partial_\theta P_\ell(\cos \theta). \end{aligned} \quad (3.82)$$

It follows that the only nonvanishing component of the induced metric perturbation is

$$\delta h_{t\varphi} = \varepsilon e^{-i\omega t} h_0(r_0) \sin \theta \partial_\theta P_\ell(\cos \theta). \quad (3.83)$$

In the axial case, the normal vector to the membrane is given by Eq. (3.69) up to the first order in the perturbation. As a consequence, the nonvanishing components of the extrinsic curvature perturbation are

$$\begin{aligned}\delta K_{t\varphi} &= \frac{1}{2}e^{-i\omega t}\varepsilon\sqrt{f}(i\omega h_1 + h'_0)\sin\theta\partial_\theta P_\ell(\cos\theta), \\ \delta K_{\theta\varphi} &= -\frac{1}{2}e^{-i\omega t}\varepsilon\sqrt{f}h_1\left(-\cos\theta\partial_\theta + \sin\theta\partial_\theta^2\right)P_\ell(\cos\theta).\end{aligned}$$

Concerning the fluid velocity, the components U^t , U^r and U^θ are not affected by axial perturbations, whereas $\delta u^\varphi \neq 0$ and its expression can be found by solving the $t\varphi$ component of the junction condition, i.e.,

$$\delta u^\varphi = \frac{\varepsilon e^{-i\omega t}\partial_\theta P_\ell(\cos\theta)[h_0 f' - f(i\omega h_1 + h'_0)]}{r_0 \sin\theta \sqrt{f}(2f - Rf')}. \quad (3.84)$$

The perturbed components of the stress-energy tensor are

$$\begin{aligned}\delta T_{t\varphi} &= -\varepsilon e^{-i\omega t}\rho_0 h_0 \sin\theta\partial_\theta P_\ell(\cos\theta) \\ &\quad - r_0^2 \sqrt{f} \sin^2\theta (p_0 + \rho_0)\delta u^\varphi(t, \theta), \\ \delta T_{\theta\varphi} &= -\eta r_0^2 \sin^2\theta\partial_\theta\delta u^\varphi(t, \theta).\end{aligned} \quad (3.85)$$

The $\theta\varphi$ component of the junction condition then reduces to

$$\frac{1}{2}\sqrt{f}h_1 = -\frac{8\pi\eta r_0[h_0 f' - f(i\omega h_1 + h'_0)]}{\sqrt{f}(2f - r_0 f')}. \quad (3.86)$$

In vacuum, the Regge-Wheeler functions are related to each other by [229]

$$h_0(r) = -\frac{f(r)}{i\omega} \frac{d}{dr} [f(r)h_1(r)]. \quad (3.87)$$

We use this relation to write h_0 and h'_0 in terms of h_1 , h'_1 and h''_1 . Furthermore, we replace h_1 and its derivatives by introducing the Regge-Wheeler function [229]

$$\psi_{\text{RW}}(r) = \frac{f(r)}{r} h_1(r), \quad (3.88)$$

that satisfies Eq. (3.3) with the effective potential given in Eq. (3.5). Finally, Eq. (3.86) yields to

$$\omega\psi(r_0) = 16i\pi\eta \left(\left. \frac{d\psi}{dr_*} \right|_{r_0} + \frac{r_0 V_{\text{axial}}(r_0)}{2f(r_0) - r_0 f'(r_0)} \psi(r_0) \right). \quad (3.89)$$

that coincides with the boundary condition in Eq. (3.25).

Polar sector

The nonvanishing components of the polar metric perturbation are

$$\begin{aligned}
\delta g_{tt} &= \varepsilon e^{-i\omega t} P_\ell(\cos\theta) f(r) \mathcal{H}(r), \\
\delta g_{rr} &= \varepsilon e^{-i\omega t} P_\ell(\cos\theta) \frac{\mathcal{H}(r)}{f(r)}, \\
\delta g_{tr} &= \varepsilon e^{-i\omega t} P_\ell(\cos\theta) \mathcal{H}_1(r), \\
\delta g_{\theta\theta} &= \frac{\delta g_{\varphi\varphi}}{\sin^2\theta} = \varepsilon e^{-i\omega t} P_\ell(\cos\theta) r^2 \mathcal{K}(r),
\end{aligned} \tag{3.90}$$

where the location of the membrane is perturbed as in Eqs. (3.78) and (3.81). By projecting on the 3-dimensional membrane, the nonvanishing components of the induced metric perturbation are

$$\begin{aligned}
\delta h_{tt} &= \varepsilon (f\mathcal{H} - f'\delta r_0) P_\ell(\cos\theta) e^{-i\omega t}, \\
\delta h_{\theta\theta} &= \frac{h_{\varphi\varphi}}{\sin^2\theta} = \varepsilon (r_0^2 \mathcal{K} + 2r_0 \delta r_0) P_\ell(\cos\theta) e^{-i\omega t}.
\end{aligned} \tag{3.91}$$

The perturbed components of the normal vector to the membrane up to the first order in the perturbation are

$$\begin{aligned}
\delta n_t &= \frac{\varepsilon i\omega e^{-i\omega t} P_\ell(\cos\theta) \delta r_0}{\sqrt{f(r)}}, \\
\delta n_r &= \frac{\varepsilon e^{-i\omega t} P_\ell(\cos\theta) \mathcal{H}(r)}{2\sqrt{f(r)}}, \\
\delta n_\theta &= -\frac{\varepsilon e^{-i\omega t} \partial_\theta P_\ell(\cos\theta) \delta r_0}{\sqrt{f(r)}}.
\end{aligned} \tag{3.92}$$

Concerning the perturbed fluid velocity, in the polar sector δU^t can be uniquely determined from the condition of unit norm $U_\mu U^\mu = -1$, i.e.,

$$\delta U^t = \delta u^t = \frac{\varepsilon (f\mathcal{H} - \delta r_0 f')}{2f^{3/2}} P_\ell(\cos\theta) e^{-i\omega t}. \tag{3.93}$$

Moreover, $\delta U^\varphi = \delta u^\varphi = 0$ and $\delta U^r = -\varepsilon U^t i\omega e^{-i\omega t} P_\ell(\cos\theta)$, while $\delta U^\theta = \delta u^\theta$ is nonvanishing and can be determined by solving the $t\theta$ component of the junction condition in Eq. (3.66), as we shown below.

The extrinsic curvature has the following nonvanishing components up to

first order in ε

$$\begin{aligned}
\delta K_{tt} &= \frac{\varepsilon e^{-i\omega t} P_\ell(\cos\theta) \left[\delta r_0 (4\omega^2 - f'^2) + f (-2\delta r_0 f'' + 3\mathcal{H}f' + 4i\omega\mathcal{H}_1) + 2f^2\mathcal{H}' \right]}{4\sqrt{f}}, \\
\delta K_{\theta\theta} &= \frac{\varepsilon e^{-i\omega t} [f (2\delta r_0 - r_0\mathcal{H} + r_0^2\mathcal{K}' + 2r_0\mathcal{K}) + \delta r_0 (r_0f' - 2\partial_\theta^2)] P_\ell(\cos\theta)}{2\sqrt{f}}, \\
\delta K_{\varphi\varphi} &= \frac{\varepsilon \sin^2\theta e^{-i\omega t} [f (2\delta r_0 - r_0\mathcal{H} + r_0^2\mathcal{K}' + 2r_0\mathcal{K}) + \delta r_0 (r_0f' - 2\cot\theta\partial_\theta)] P_\ell(\cos\theta)}{2\sqrt{f}}, \\
\delta K_{t\theta} &= -\frac{\varepsilon e^{-i\omega t} \partial_\theta P_\ell(\cos\theta) (f\mathcal{H}_1 - 2i\delta r_0\omega)}{2\sqrt{f}}. \tag{3.94}
\end{aligned}$$

The nonvanishing components of the perturbation to the stress-energy tensor are

$$\begin{aligned}
\delta T_{tt} &= \varepsilon e^{-i\omega t} P_\ell(\cos\theta) [\rho_0 f' \delta r_0 + f (\rho_1 - \rho_0 \mathcal{H})], \\
\delta T_{\theta\theta} &= \frac{r_0}{\sqrt{f}} \left\{ -\sqrt{f} r_0 [(\zeta + \eta) \partial_\theta \delta u^\theta + (\zeta - \eta) \cot\theta \delta u^\theta] \right. \\
&\quad \left. + \varepsilon e^{-i\omega t} P_\ell(\cos\theta) \left[\sqrt{f} (p_0 r_0 \mathcal{K} + 2p_0 \delta r_0 + p_1 r_0) + i\omega \zeta (r_0 \mathcal{K} + 2\delta r_0) \right] \right\}, \\
\delta T_{\varphi\varphi} &= \frac{r_0 \sin^2\theta}{\sqrt{f}} \left\{ -\sqrt{f} r_0 [(\zeta - \eta) \partial_\theta \delta u^\theta + (\zeta + \eta) \cot\theta \delta u^\theta] \right. \\
&\quad \left. + \varepsilon e^{-i\omega t} P_\ell(\cos\theta) \left[\sqrt{f} (p_0 r_0 \mathcal{K} + 2p_0 \delta r_0 + p_1 r_0) + i\omega \zeta (r_0 \mathcal{K} + 2\delta r_0) \right] \right\}, \\
\delta T_{t\theta} &= -r_0^2 \sqrt{f} (\rho_0 + p_0) \delta u^\theta. \tag{3.95}
\end{aligned}$$

From the tt , $\theta\theta$, and $\varphi\varphi$ components of the junction conditions we obtain analytical (albeit cumbersome) expressions for ρ_1 and p_1 , and the deviation of the membrane location

$$\delta r_0 = \frac{16\pi\eta r_0 f \mathcal{H}_1}{2f - r_0 f' - 32\pi\eta i\omega r_0}, \tag{3.96}$$

whereas from the $t\theta$ component we derive

$$\delta u^\theta = \frac{\varepsilon e^{-i\omega t} \partial_\theta P_\ell(\cos\theta) r_0 \sqrt{f} \mathcal{H}_1}{2f - r_0 f' - 32\pi\eta i\omega r_0}. \tag{3.97}$$

In vacuum, the metric perturbations, $\mathcal{H}(r)$, $\mathcal{H}_1(r)$ and $\mathcal{K}(r)$, are related by the following algebraic equation [230, 245]:

$$\begin{aligned}
\mathcal{H}(r) &= \frac{1}{qr + 3M} \left\{ \left[qr - \frac{\omega^2 r^4}{r - 2M} + M \frac{r - 3M}{r - 2M} \right] \mathcal{K}(r) \right. \\
&\quad \left. + \left[i\omega r^2 + \frac{(q+1)M}{i\omega r} \right] \mathcal{H}_1(r) \right\}, \tag{3.98}
\end{aligned}$$

where $q = (\ell - 1)(\ell + 2)/2$. The relation in Eq. (3.98) allows us to eliminate, say, $\mathcal{H}(r)$. Moreover, we can rewrite $\mathcal{H}_1(r)$ and $\mathcal{K}(r)$ in terms of the Zerilli wave function $\psi_Z(r)$ that satisfies Eq. (3.3) with the effective potential given in Eq. (3.6). Indeed, [230, 245]

$$\mathcal{H}_1(r) = \omega h(r)\psi_Z(r) + \omega k(r)\frac{d\psi_Z(r)}{dr_*}, \quad (3.99)$$

$$\mathcal{K}(r) = g(r)\psi_Z(r) + \frac{d\psi_Z(r)}{dr_*}, \quad (3.100)$$

where

$$\begin{aligned} h(r) &= i\frac{3qMr - qr^2 + 3M^2}{(r - 2M)(qr + 3M)}, \\ k(r) &= -i\frac{r^2}{r - 2M}, \\ g(r) &= \frac{q(q + 1)r^2 + 3qMr + 6M^2}{r^2(qr + 3M)}. \end{aligned} \quad (3.101)$$

The last condition that closes the system of equations and determines uniquely the boundary conditions for the polar metric perturbation is found from the barotropic equation of state $p = p(\rho)$ at the first order in the perturbation that gives

$$\delta p = c_s^2 \delta \rho, \quad (3.102)$$

where the sound speed c_s is given in Eq. (3.74).

By substituting the above algebraic equations, we obtain the following boundary condition

$$\frac{d\psi_Z(r_0)/dr_*}{\psi_Z(r_0)} = -16\pi\eta i\omega + G(r_0, \omega, \eta, \zeta), \quad (3.103)$$

where $G = A/B$ and

$$\begin{aligned} A &= (y - 2) \left\{ 9 \left[-3 - 3w^2y^3 + w^2y^4 - 48i\pi w y^2 \zeta + y(2 + 96i\pi w \zeta) \right] \right. \\ &\quad + q^3 y^2 \left(-3i + iy + 16\pi w y^2 \eta \right)^2 + 3q \left[-9 + 3y^2(1 + 64i\pi w \zeta) \right. \\ &\quad \left. - 32i\pi w y^3(3\zeta + 2\eta) + w y^4(-3w + 16i\pi \eta) + w^2 y^5(1 + 256\pi^2 \eta^2) \right] \\ &\quad + q^2 y \left[-18 + 6y^2(1 + 16i\pi w(\zeta - 2\eta)) + 256\pi^2 w^2 y^5 \eta^2 \right. \\ &\quad \left. \left. + 32\pi w y^4 \eta(i + 24\pi w \eta) - iy^3(-i + 48\pi w(\zeta + \eta)) \right] \right\}, \end{aligned} \quad (3.104)$$

$$\begin{aligned} B &= y^2(3 + qy) \left\{ 3 \left[-3 - 3w^2y^3 + w^2y^4 - 48i\pi w y^2 \zeta + y(2 + 96i\pi w \zeta) \right] \right. \\ &\quad + q \left[-9 + 9y + w^2 y^5 + y^2(-3 + 192i\pi w \zeta) + y^3(1 - 32i\pi w(3\zeta - \eta)) \right. \\ &\quad \left. - w y^4(3w + 16i\pi \eta) \right] + q^2 y \left[3 - 3y - 16i\pi w y^3(\zeta + \eta) \right. \\ &\quad \left. \left. + y^2(1 + 32i\pi w(\zeta + \eta)) \right] \right\}, \end{aligned} \quad (3.105)$$

and we define the dimensionless quantities $y = r_0/M$, $w = M\omega$. Let us notice that in the BH limit $G(2M) = 0$, and the BH boundary condition is recovered for $\eta = \eta_{\text{BH}}$. Our computations show that, in the BH limit, the boundary condition is independent of the bulk viscosity, as discussed in the main text.

3.7 Appendix: Fisher information matrix

The Fisher information matrix of a template $\tilde{h}(f)$ in the frequency domain for a detector with noise spectral density $S_n(f)$ is defined as

$$\Gamma_{ij} = \langle \partial_i \tilde{h} | \partial_j \tilde{h} \rangle, \quad (3.106)$$

where $i, j = 1, \dots, N$, N is the number of the parameters in the template, and the inner product between two waveforms (h_1 and h_2) is defined as

$$\langle h_1 | h_2 \rangle \equiv 4\Re \int_0^\infty \frac{\tilde{h}_1 \tilde{h}_2^*}{S_n(f)} df, \quad (3.107)$$

where the tilde stands for the Fourier transform of the waveform. The SNR ρ of a signal is defined as

$$\rho^2 = \langle \tilde{h} | \tilde{h} \rangle. \quad (3.108)$$

The covariance matrix of the errors on the parameters of the template is defined as the inverse of the Fisher information matrix, i.e.,

$$\Sigma_{ij} = \Gamma_{ij}^{-1}. \quad (3.109)$$

Finally, the statistical error associated with the measurement of i -th parameter is derived as

$$\sigma_i = \sqrt{\Sigma_{ii}}. \quad (3.110)$$

Chapter 4

Ergoregion instability

Una nuova popolazione cresceva sulla terra, nemica a noi. Ci davano addosso da tutte le parti, non ce ne andava bene una. Adesso qualcuno dice che il gusto di tramontare, la passione d'essere distrutti facessero parte dello spirito di noi.

Italo Calvino, *Le Cosmicomiche*

4.1 A spinning model

Let us analyze a spinning horizonless compact object whose exterior spacetime is described by the Kerr metric. The absence of the Birkhoff theorem in axisymmetry implies that the vacuum region outside a spinning object can be described by geometries other than Kerr. However, in the case of a horizonless compact object with large compactness, any deviation from the multipolar structure of a Kerr BH dies off sufficiently fast within GR or in modified theories of gravity whose effects are confined near the radius of the compact object [139, 167, 246]. This assumption is justified for gravity theories in which putative extra degrees of freedom are heavy. In this case, the corrections to the metric and field equations are suppressed by powers of $l_P/r_0 \ll 1$, where r_0 is the radius of the object, and l_P is the Planck length or the scale of new physics. In Boyer-Lindquist coordinates, the exterior spacetime reads

$$ds^2 = - \left(1 - \frac{2Mr}{\Sigma}\right) dt^2 + \frac{\Sigma}{\Delta} dr^2 - \frac{4Mr}{\Sigma} a \sin^2 \theta d\varphi dt \\ + \Sigma d\theta^2 + \left[(r^2 + a^2) \sin^2 \theta + \frac{2Mr}{\Sigma} a^2 \sin^4 \theta \right] d\varphi^2, \quad (4.1)$$

where $\Sigma = r^2 + a^2 \cos^2 \theta$, $\Delta = r^2 - 2Mr + a^2$, with M and $J \equiv aM$ the total mass and angular momentum of the object, respectively.

Motivated by models of microscopical corrections at the horizon scale, the radius of the compact object is located as in Eq. (2.1) where $\epsilon \ll 1$. The

properties of the object's interior are parametrized in terms of a complex and frequency-dependent surface reflectivity $\mathcal{R}(\omega)$.

4.2 The ergoregion

The Kerr metric in Eq. (4.1) admits two horizons at

$$r_{\pm} = M \pm \sqrt{M^2 - a^2}, \quad (4.2)$$

where the BH spin is bounded by $-M \leq a \leq M$ ¹. The horizons are null hypersurfaces that separate regions of the spacetime where $r = \text{const}$ are timelike hypersurfaces from regions where $r = \text{const}$ are spacelike hypersurfaces. In the Kerr spacetime, the horizons do not coincide with the infinite redshift surfaces located at

$$r_{S_{\pm}} = M \pm \sqrt{M^2 - a^2 \cos^2 \theta}, \quad (4.3)$$

which are the hypersurfaces where the Killing vector field $\xi^{\mu} = (1, 0, 0, 0)$ becomes spacelike. The horizons and the infinite redshift surfaces are such that $r_{S_{-}} \leq r_{-} < r_{+} \leq r_{S_{+}}$: for $\theta = 0, \pi$, the horizons coincide with the infinite redshift surfaces, i.e., $r_{S_{\pm}} = r_{\pm}$; whereas on the equatorial plane, $r_{S_{+}} = 2M > r_{+}$ and $r_{S_{-}} = 0$. Consequently, there exists a region outside the outer horizon where the Killing vector field becomes spacelike, i.e.,

$$r_{+} < r < r_{S_{+}}, \quad (4.4)$$

that is called *ergoregion*. Its outer boundary, i.e., $r = r_{S_{+}}$, is called *ergosphere*.

A characteristic feature of the Kerr spacetime is that a static observer cannot exist inside the ergoregion but is forced to corotate with the compact object. A static observer is defined as a timelike curve whose tangent vector field is proportional to the Killing vector $\xi^{\mu} = (1, 0, 0, 0)$ and whose (r, θ, φ) coordinates are constant along its worldline. Such an observer is not allowed in the ergoregion since ξ^{μ} is spacelike there. We can define a zero angular momentum observer (ZAMO) whose angular velocity has the same sign of the angular momentum of the compact object [148].

When a particle starts its motion at infinity, the constant of motion coincides with the energy of the particle as measured by a static observer at infinity. The requirement that the energy is positive implies that the constant of motion is positive. However, when a particle starts its motion in the ergoregion, its energy cannot be measured by a static observer since the latter is not allowed in the ergoregion. The particle energy can be measured, for example, by the ZAMO and does not coincide with the constant of motion. The requirement that the energy as measured by the ZAMO is positive implies that the constant of motion can be negative for counterrotating particles inside the ergoregion. This result has important consequences on the possibility of extracting energy from Kerr BHs, as described in the next section.

¹Compact objects violating the Kerr bound, i.e., with $a \geq M$, are referred to as super-spinars as detailed in Sec. 2.3.6.

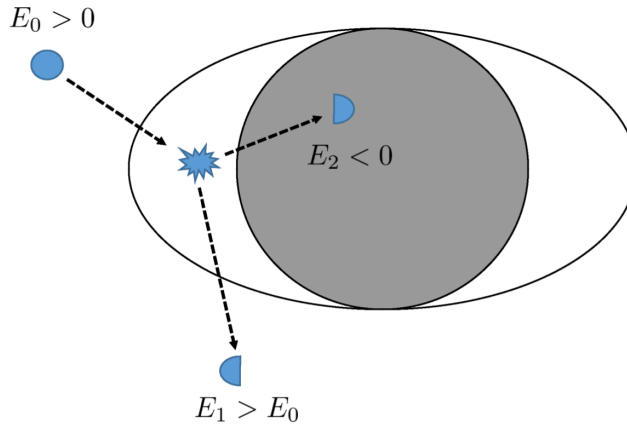


Figure 4.1. Energy extraction from a Kerr BH via the Penrose process [247]. A particle with energy E_0 decays in two particles inside the ergoregion. One particle has a negative energy ($E_2 < 0$) and falls into the BH, whereas the second particle has an energy larger than the initial value ($E_1 > E_0$) and escapes at infinity. [29]

4.3 The Penrose process

In Kerr spacetimes, it is possible to extract energy and angular momentum from BHs since the energy of a particle within the ergoregion as measured by an observer at infinity can be negative. This scenario was first discovered by Penrose [247] and is shown schematically in Fig. 4.1. Let us consider a particle with energy at infinity E_0 decaying in two particles inside the ergoregion. One of the two particles can have negative energy as measured at infinity, i.e., $E_2 < 0$, and the other particle must have energy larger than the initial value, i.e., $E_1 > E_0$. The horizon forces the negative-energy particle to fall into the BH, whereas the positive-energy particle can escape at infinity and extract energy from the BH. Indeed, the final mass of the BH is smaller than its initial value, i.e., $M_{\text{fin}} = M + E_2 < M$. The same scenario holds for the BH angular momentum. Consequently, the ergoregion allows particles to acquire energy and angular momentum at the expense of the BH.

If the compact object has an ergoregion but does not have a horizon, the physical process is different. In the case of a perfectly reflecting horizonless compact object, the negative-energy states cannot be absorbed by the object and remain in orbital motion inside the ergoregion. It is therefore energetically favorable to cascade towards more negative-energy states leading to a runaway instability. This process is called *ergoregion instability* [25]. The only way to prevent such an infinite cascade is by absorbing the negative-energy states efficiently. Indeed, Kerr BHs are stable against the ergoregion instability since they can absorb the radiation at the horizon. In the following section, we shall assess the impact of the ergoregion instability on the astrophysical viability of

horizonless compact objects.

4.4 Ergoregion instability in horizonless compact objects

The ergoregion instability was proved by Friedmann in ultracompact stars under scalar and electromagnetic perturbations [25] and analyzed in uniform-density stars [248, 26, 27, 29, 249], gravastars [250], boson stars [133], and superspinars [132]. In Kerr-like horizonless objects, the ergoregion instability is explained by the existence of long-lived modes in the potential cavity between the effective radius of the object and the photon sphere. As shown in Fig. 3.2, the imaginary part of the QNMs of a static horizonless object tends to zero in the limit of large compactness, i.e., $\epsilon \rightarrow 0$. In the rotating case, these modes can turn unstable² due to the Zeeman splitting of the frequencies as a function of the azimuthal number of the perturbation. Indeed, in the small-spin limit, the QNMs can be expanded as [251]

$$\omega_{R,I} = \omega_{R,I}^{(0)} + m\chi\omega_{R,I}^{(1)} + \mathcal{O}(\chi^2), \quad (4.5)$$

where $\chi \equiv a/M$ is the dimensionless spin, $\omega_{R,I}^{(0)}$ are the real and imaginary parts of the QNMs in the static case, and $\omega_{R,I}^{(1)}$ are the first order corrections to the QNMs in the spin. In the large compactness limit, $\omega_I^{(0)} \rightarrow 0$ and the first order term in Eq. (4.5) can turn the sign of the imaginary part of the frequency to be positive depending on the azimuthal number. The ergoregion instability affects horizonless compact objects regardless of the azimuthal number of the perturbation due to the symmetries of the Teukolsky wave function

$$m \rightarrow -m, \quad \omega \rightarrow -\omega^*, \quad {}_sA_{\ell m} \rightarrow {}_sA_{\ell -m}^*, \quad (4.6)$$

as detailed in Sec. 4.4.1. Let us derive the QNM spectrum of a spinning horizonless object and analyze the region of the parameter space in which the object is affected by the ergoregion instability.

4.4.1 Linear perturbations in the Kerr background

Let us perturb the background geometry in Eq. (4.1) with a spin- s perturbation, where $s = 0, \pm 1, \pm 2$ for scalar, electromagnetic and gravitational perturbations, respectively. The perturbation can be decomposed as in Eq. (3.2) where

²We remind the reader that, in our convention, a stable mode has a negative imaginary part of the frequency and corresponds to an exponentially damped sinusoidal signal, whereas an unstable mode has a positive imaginary part of the frequency and corresponds to an exponential growth.

the radial and the angular functions are governed by the Teukolsky master equations [252, 253, 54]

$$\Delta^{-s} \frac{d}{dr} \left(\Delta^{s+1} \frac{d_s R_{\ell m}}{dr} \right) + \left[\frac{K^2 - 2is(r-M)K}{\Delta} + 4is\omega r - \lambda \right] {}_s R_{\ell m} = 0, \quad (4.7)$$

$$\left[(1-x^2) {}_s S_{\ell m, x} \right]_{,x} + \left[(a\omega x)^2 - 2a\omega s x + s \right. \\ \left. + {}_s A_{\ell m} - \frac{(m+sx)^2}{1-x^2} \right] {}_s S_{\ell m} = 0, \quad (4.8)$$

where ${}_s S_{\ell m}(\theta) e^{im\varphi}$ are the spin-weighted spheroidal harmonics, $x \equiv \cos \theta$, $K = (r^2 + a^2)\omega - am$, and the separation constants λ and ${}_s A_{\ell m}$ are related by $\lambda \equiv {}_s A_{\ell m} + a^2\omega^2 - 2am\omega$. When $a = 0$, the angular eigenvalues are $\lambda = (\ell - s)(\ell + s + 1)$, whereas when $a \neq 0$ the angular eigenvalues can be computed either numerically or with approximated analytical expansions (see Sec. 4.4.3 for more details).

It is convenient to introduce the Detweiler function [254]

$${}_s X_{\ell m} = \Delta^{s/2} (r^2 + a^2)^{1/2} \left[\alpha {}_s R_{\ell m} + \beta \Delta^{s+1} \frac{d_s R_{\ell m}}{dr} \right], \quad (4.9)$$

where α and β are radial functions that are given in Appendix 4.6. By defining the tortoise coordinate such that $dr_*/dr = (r^2 + a^2)/\Delta$, Eq. (4.7) becomes a Schrödinger-like equation

$$\frac{d_s^2 X_{\ell m}}{dr_*^2} - V(r, \omega) {}_s X_{\ell m} = 0, \quad (4.10)$$

where the effective potential is

$$V(r, \omega) = \frac{U\Delta}{(r^2 + a^2)^2} + G^2 + \frac{dG}{dr_*}, \quad (4.11)$$

where

$$G = \frac{s(r-M)}{r^2 + a^2} + \frac{r\Delta}{(r^2 + a^2)^2}, \quad (4.12)$$

$$U = V_S + \frac{2\alpha' + (\beta'\Delta^{s+1})'}{\beta\Delta^s}, \quad (4.13)$$

$$V_S = -\frac{1}{\Delta} \left[K^2 - is\Delta'K + \Delta(2isK' - \lambda) \right], \quad (4.14)$$

and the prime denotes a derivative with respect to r . In the following, we shall define $R_s \equiv {}_s R_{\ell m}$, $X_s \equiv {}_s X_{\ell m}$ and omit the ℓ, m subscripts for brevity.

The radial functions α and β are such that the effective potential in Eq. (4.11) is purely real (see Appendix 4.6 for a derivation). Let us notice that the Detweiler effective potential has the following asymptotics

$$V(r, \omega) \sim \begin{cases} -\omega^2 & \text{as } r_* \rightarrow +\infty \\ -k^2 & \text{as } r_* \rightarrow -\infty \end{cases}, \quad (4.15)$$

where $k = \omega - m\Omega_H$ and $\Omega_H = a/(2Mr_+)$ is the angular velocity of a Kerr BH at the horizon. Consequently, the two independent solutions of Eq. (4.10) have the asymptotic behavior

$$X_s^+ \sim \begin{cases} e^{+i\omega r_*} & \text{as } r_* \rightarrow +\infty \\ B_{\text{out}}(\omega)e^{+ikr_*} + B_{\text{in}}(\omega)e^{-ikr_*} & \text{as } r_* \rightarrow -\infty \end{cases}, \quad (4.16)$$

$$X_s^- \sim \begin{cases} A_{\text{out}}(\omega)e^{+i\omega r_*} + A_{\text{in}}(\omega)e^{-i\omega r_*} & \text{as } r_* \rightarrow +\infty \\ e^{-ikr_*} & \text{as } r_* \rightarrow -\infty \end{cases}, \quad (4.17)$$

where the Wronskian of the solutions is

$$W_{\text{BH}} = \frac{dX_s^+}{dr_*} X_s^- - X_s^+ \frac{dX_s^-}{dr_*} = 2ikB_{\text{out}}. \quad (4.18)$$

Since the effective potential in Eq. (4.11) is real, X_s^\pm and their complex conjugates $X_s^{\pm*}$ are independent solutions to the same equation which satisfy complex conjugated boundary conditions. Via the Wronskian relationships, the asymptotic coefficients satisfy the relations [255, 256]

$$\begin{aligned} |B_{\text{out}}|^2 - |B_{\text{in}}|^2 &= \omega/k, \\ |A_{\text{in}}|^2 - |A_{\text{out}}|^2 &= k/\omega, \\ \omega A_{\text{in}} &= kB_{\text{out}}, \quad \omega A_{\text{out}}^* = -kB_{\text{in}}. \end{aligned} \quad (4.19)$$

4.4.2 Boundary conditions

The QNMs of a Kerr-like horizonless object are derived by adding to Eq. (4.10) two suitable boundary conditions. At infinity, we impose that the perturbation is a purely outgoing wave

$$X_s \sim e^{i\omega r_*}, \quad \text{as } r_* \rightarrow +\infty. \quad (4.20)$$

The regularity at the center of the object implies the imposition of a boundary condition at the effective radius of the object. For $\epsilon \ll 1$, the effective potential in the Detweiler equation is constant at the radius of the object, $V \approx -k^2$, so that the perturbation can be decomposed as a superposition of ingoing and outgoing waves, i.e.,

$$X_s \sim \mathbb{C}_{\text{in}} e^{-ikr_*} + \mathbb{C}_{\text{out}} e^{ikr_*}, \quad \text{as } r_* \rightarrow r_*^0. \quad (4.21)$$

where we define the surface reflectivity of the object as

$$\mathcal{R}(\omega) = \frac{\mathbb{C}_{\text{out}}}{\mathbb{C}_{\text{in}}} e^{2ikr_*^0}. \quad (4.22)$$

A perfectly reflecting object, where the outgoing energy flux at the effective radius is equal to the incident one, has $|\mathcal{R}(\omega)|^2 = 1$. Two notable examples of perfectly reflecting boundary conditions are

$$X_s(r_0) = 0 \quad \text{Dirichlet on axial} \quad (4.23)$$

$$dX_s(r_0)/dr_* = 0 \quad \text{Neumann on polar} \quad (4.24)$$

where the Dirichlet boundary condition describes waves that are totally reflected with inverted phase ($\mathcal{R}(\omega) = -1$), whereas the Neumann boundary condition describes waves that are totally reflected in phase ($\mathcal{R}(\omega) = 1$). In general, a partially absorbing object is described by the boundary condition

$$\left. \frac{dX_s/dr_*}{X_s} \right|_{r_0} = -ik \frac{1 - \mathcal{R}(\omega)}{1 + \mathcal{R}(\omega)}, \quad (4.25)$$

that reduces to the BH boundary condition of a purely ingoing wave when $\mathcal{R} = 0$. In the following, we shall derive the QNMs of a perfectly reflecting ultracompact object.

In the case of electromagnetic perturbations, a perfectly reflecting object can be modeled as a perfect conductor. In Appendix 4.7, we show that this condition translates into Dirichlet and Neumann boundary conditions on axial and polar modes, respectively. An analogous description of a perfectly reflecting compact object under gravitational perturbations is not available. We assume that the results of electromagnetic perturbations can also be applied to gravitational perturbations.

4.4.3 Numerical procedure

Equation (4.10) with boundary conditions at infinity in Eq. (4.20) and the radius of the object in Eqs. (4.23) and (4.24) can be solved numerically with a direct integration shooting method. We start with an analytical high-order series expansion of the solution at infinity and we integrate Eq. (4.10) from infinity to the radius of the object. We repeat the integration for different values of the complex frequency until the boundary condition in Eq. (4.23) or (4.24) is satisfied.

The angular eigenvalues are computed numerically using continued fractions [257]. For $a\omega \ll 1$, the eigenvalues can also be expanded analytically as

$${}_s A_{\ell m} = \sum_{p=0}^{\infty} f_{s\ell m}^{(p)}(a\omega)^p, \quad (4.26)$$

where $f_{slm}^{(p)}$ are known expansion coefficients [257]

$$f_{slm}^{(0)} = (\ell - s)(\ell + s + 1), \quad (4.27)$$

$$f_{slm}^{(1)} = -\frac{2ms^2}{\ell(\ell + 1)}, \quad (4.28)$$

$$f_{slm}^{(2)} = h(\ell + 1) - h(\ell) - 1, \quad (4.29)$$

and

$$h(\ell) = \frac{\left[\ell^2 - (\max(|m|, |s|))^2\right] \left[\ell^2 - \left(\frac{ms}{\max(|m|, |s|)}\right)^2\right] (\ell^2 - s^2)}{2 \left(\ell - \frac{1}{2}\right) \ell^3 \left(\ell + \frac{1}{2}\right)}. \quad (4.30)$$

We verified that the analytical approximation up to the second order is in agreement with the numerical computation: the approximation differs from the exact eigenvalue of $\lesssim 2\%$ in the electromagnetic QNMs and $\lesssim 4\%$ in the gravitational QNMs for a compact object with high spin.

4.4.4 Instability in the quasi-normal mode spectrum

The QNM spectrum of the system depends on two continuous dimensionless parameters, i.e., the spin of the object χ and its compactness through the parameter ϵ . We focus on perfectly reflecting compact objects that are described by the boundary conditions in Eq. (4.23) and (4.24).

Furthermore, the QNMs depend on four integers, i.e., the spin s , the angular number ℓ , the azimuthal number m , and the overtone number n of the perturbation. We focus on fundamental modes ($n = 0$) with $\ell = m = 1$ for scalar and electromagnetic perturbations, and $\ell = m = 2$ for gravitational perturbations that, in the unstable case, correspond to the modes with the largest imaginary part and thus the shortest instability timescale. The symmetries of the Teukolsky wave function guarantee that we can focus on the modes with $m \geq 0$ without loss of generality.

Fig. 4.2 shows the scalar QNMs of a perfectly reflecting compact object as a function of the spin, where the radius of the object is located at $r_0 = r_+(1 + \epsilon)$ and $\epsilon = 10^{-10}$. The real part of the QNM has a zero crossing at a critical value of the spin that depends on Dirichlet or Neumann boundary condition. Most importantly, the imaginary part of the QNM changes sign for the same critical value of the spin, turning the object from stable to unstable.

Above the threshold of the ergoregion instability, the imaginary part of the QNMs is positive and the modes are unstable. An interesting feature is that the threshold of the instability is the same both for scalar and electromagnetic perturbations with Dirichlet (Neumann) boundary conditions on electromagnetic axial (polar) modes. This feature is because, in the zero-frequency limit, the scalar and electromagnetic wave functions are related by a Darboux

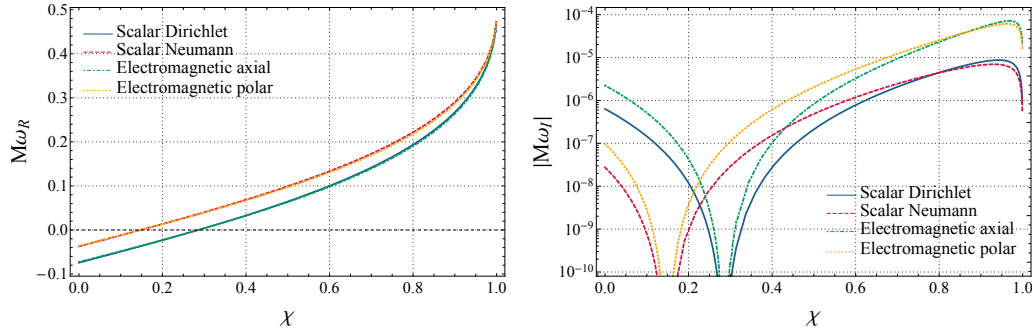


Figure 4.2. Real (left panel) and imaginary (right panel) part of the scalar and electromagnetic QNMs ($\ell = m = 1$, $n = 0$) of an ECO as a function of the spin. The radius of the object is located at $r_0 = r_+(1 + \epsilon)$, where $\epsilon = 10^{-10}$. The cusps in the imaginary part of the frequency correspond to the threshold of the ergoregion instability above which the QNMs are unstable. The scalar QNMs with Dirichlet (Neumann) boundary conditions are isospectral to the electromagnetic axial (polar) QNMs. [30, 31]

transformation [31], i.e.,

$$R_{-1} = R_0 + \frac{i\Delta}{am} R'_0, \quad (4.31)$$

or equivalently

$$R_0 = -\frac{iam}{\ell(\ell+1)} \left(R'_{-1} + \frac{iam}{\Delta} R_{-1} \right), \quad (4.32)$$

where the prime denotes a derivative with respect to r . In the gravitational case, the threshold of the ergoregion instability is slightly shifted, as shown in Fig. 4.3 for axial and polar perturbations, respectively. For $\epsilon \ll 1$, the QNMs can be derived analytically in the low-frequency regime [31, 13]

$$\omega_R \simeq -\frac{\pi}{2|r_*^0|} \left[p + \frac{s(s+1)}{2} \right] + m\Omega_H, \quad (4.33)$$

$$\omega_I \simeq -\frac{\beta_{sl}}{|r_*^0|} \left(\frac{2Mr_+}{r_+ - r_-} \right) [\omega_R(r_+ - r_-)]^{2\ell+1} (\omega_R - m\Omega_H), \quad (4.34)$$

where $\sqrt{\beta_{sl}} = \frac{(\ell-s)!(\ell+s)!}{(2\ell)!(2\ell+1)!}$, p is a positive odd (even) integer for Neumann (Dirichlet) boundary conditions on scalar perturbations and polar (axial) modes in electromagnetic and gravitational perturbations. A detailed derivation of Eqs. (3.20) and (3.21) is given in Appendix 4.8. As shown in Fig. 4.3, the analytical QNMs agree with the numerical QNMs in the regime of validity of the approximation, i.e., $M\omega \ll 1$.

Furthermore, the critical value of the spin can be computed analytically from Eqs. (4.33) and (4.34) that are accurate when $\omega_R \simeq \omega_I \simeq 0$. The ergoregion

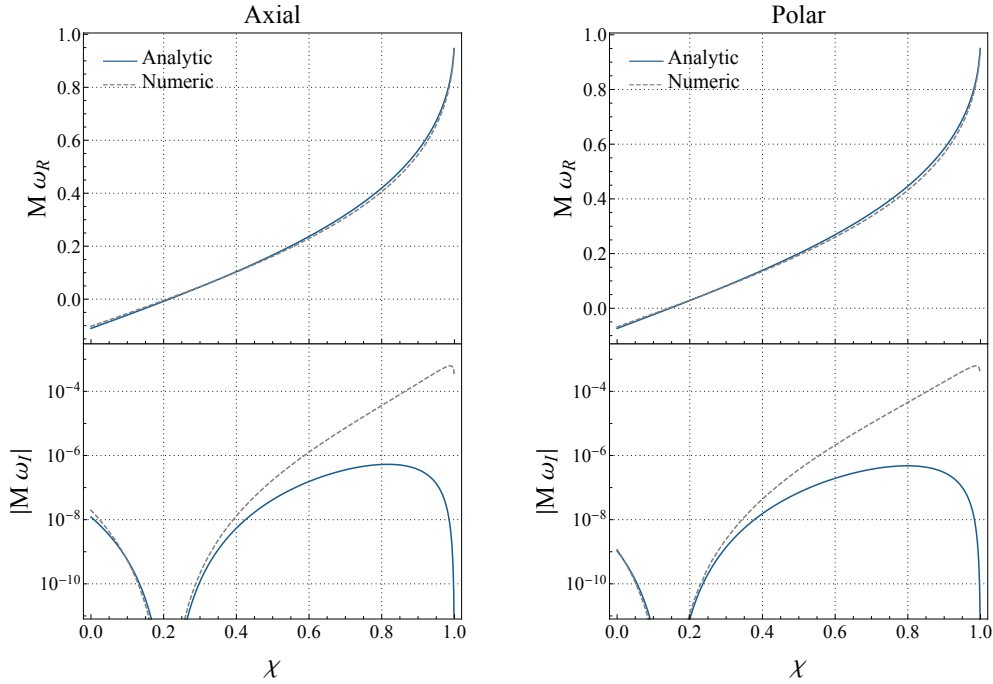


Figure 4.3. Real (left panel) and imaginary (right panel) part of the gravitational QNMs ($\ell = m = 2$, $n = 0$) of an ECO as a function of the spin. The radius of the object is located at $r_0 = r_+(1 + \epsilon)$, where $\epsilon = 10^{-10}$. The cusps in the imaginary part of the frequency correspond to the threshold of the ergoregion instability above which the QNMs are unstable. The QNMs computed numerically (dashed curves) agree with the QNMs computed analytically (continuous curves) using Eqs. (4.33) and (4.34) that are valid when $M\omega \ll 1$ [31].

instability occurs for $\chi > \chi_{\text{crit}}$ where [31, 13]

$$\chi_{\text{crit}} \simeq \frac{\pi}{m|\log \epsilon|} \left[p + \frac{s(s+1)}{2} \right]. \quad (4.35)$$

Fig. 4.4 shows the threshold of the ergoregion instability for gravitational $\ell = m = 2$ perturbations as a function of the compactness of the object. For example, an ECO with Planckian corrections at the horizon scale ($\epsilon \sim 10^{-40}$) is unstable if spinning above $\chi_{\text{crit}} \simeq 0.03, 0.05$ for axial and polar perturbations, respectively. We conclude that even slowly spinning Kerr-like horizonless objects are unstable due to the ergoregion instability.

The timescale of the instability is defined as $\tau_{\text{inst}} \equiv 1/\omega_I$. From Fig. 4.3, for an ECO with $\epsilon = 10^{-10}$ and spin $\chi = 0.7$, the instability timescale of the $\ell = m = 2$ mode is

$$\tau_{\text{inst}} \in (5, 7) \left(\frac{M}{10M_{\odot}} \right) \text{ s}, \quad (4.36)$$

where the lower (upper) bound is for polar (axial) gravitational perturbations. Let us notice that the low-frequency approximation of ω_I in Eq. (4.34) is not

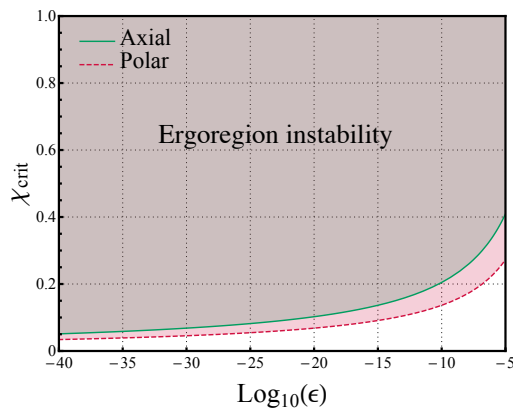


Figure 4.4. Critical value of the spin above which a Kerr-like horizonless object is affected by the ergoregion instability as a function of the compactness of the object. The threshold is computed as in Eq. (4.35) for axial and polar gravitational $\ell = m = 2$ perturbations. [31, 13]

accurate for the unstable modes with large spin, as shown in Fig. 4.3 from the disagreement between the numerical and the analytical curves. For this reason, we use the numerical values of the imaginary part of the QNMs for the calculation of the instability timescales.

The ergoregion instability acts on a timescale which is short compared to the accretion timescale of astrophysical BHs, i.e., $\tau_{\text{Salpeter}} \sim 4 \times 10^7$ yr. However, the instability timescale is longer than the decay time of the BH ringdown, i.e., $\tau_{\text{ringdown}} \sim 0.5$ ms for a $10M_{\odot}$ compact object. If the remnant of a compact binary coalescence was an ECO, the ergoregion instability would spin down the remnant over a timescale τ_{inst} until the condition for the stability, $\chi = \chi_{\text{crit}}$, is satisfied [29] via the emission of GWs. The incoherent superposition of the GW signals from the unresolved sources in the population would produce a stochastic GW background due to spin loss [258, 259]. The absence of such background in the first observing run of Advanced LIGO already puts strong constraints on perfectly reflecting ECOs that can be a small percentage of the astrophysical population [260].

4.5 How to quench the ergoregion instability

The case of a horizonless compact object with a perfectly reflecting surface is an idealization. In reality, we expect a compact object to absorb part of the ingoing radiation through viscosity, dissipation, fluid mode excitation, nonlinear effects, etc. Given that Kerr BHs can absorb radiation efficiently and are stable against the ergoregion instability, it is relevant to ask whether some absorption at the surface of Kerr-like compact objects can quench the ergoregion instability.

Let us define the reflection and transmission coefficients of a wave coming

from the left of the photon-sphere barrier with unitary amplitude as

$$\mathcal{R}_{\text{BH}} = \frac{B_{\text{in}}}{B_{\text{out}}}, \quad \mathcal{T}_{\text{BH}} = \frac{1}{B_{\text{out}}}. \quad (4.37)$$

After each bounce in the cavity between the ECO radius and the photon sphere the perturbation acquires a factor $\mathcal{R}\mathcal{R}_{\text{BH}}$, where \mathcal{R} is the ECO surface reflectivity and \mathcal{R}_{BH} is defined in Eq. (4.37). Due to the conservation of the Wronskian, $|\mathcal{R}_{\text{BH}}| = |A_{\text{out}}/A_{\text{in}}|$ where A_{in} and A_{out} are the coefficients of the incident and reflected wave, respectively, at the photon sphere for a left-moving wave originating at infinity. It follows that the amplification factor in the cavity is the same as the amplification factor of BHs which is defined as

$$Z_{s\ell m} = \left| \frac{A_{\text{out}}}{A_{\text{in}}} \right|^2 - 1. \quad (4.38)$$

The condition for the energy in the cavity to grow indefinitely is $|\mathcal{R}\mathcal{R}_{\text{BH}}|^2 > 1$ which implies that the object is unstable for the ergoregion instability if

$$|\mathcal{R}|^2 > \frac{1}{1 + Z_{s\ell m}}. \quad (4.39)$$

By definition, the surface reflectivity is $|\mathcal{R}|^2 \leq 1$, therefore Eq. (4.39) implies that the ergoregion instability occurs when the real part of the QNM is in the superradiant regime, i.e., $Z_{s\ell m} > 0$. In order to quench the ergoregion instability at any frequencies, the surface absorption, $1 - |\mathcal{R}|^2$, needs to be larger than the maximum amplification factor of superradiance, namely

$$1 - |\mathcal{R}|^2 \gtrsim Z_{\text{max}}. \quad (4.40)$$

Figure 4.5 shows the amplification factor of a BH as a function of the frequency under scalar, electromagnetic and gravitational perturbations and for several values of the BH spin. In order to have a stable Kerr-like horizonless object under any type of perturbation, the surface absorption needs to be at least 0.3% (6%) for an ECO with $\chi = 0.7$ ($\chi = 0.9$). Let us notice that the maximum amplification factor of an extremal BH is $\approx 138\%$ for $\ell = m = 2$ gravitational perturbations [29, 54], therefore an absorption rate of $\approx 60\%$ would allow for stable Kerr-like horizonless objects with any spin.

A natural question is whether this level of absorption is achievable by standard matter in compact objects. The reflective properties of compact objects depend on the specific model, but should generically be more extreme than those of an ordinary NS. For NSs, the most efficient absorption mechanism is due to viscosity. A rough estimate of the kinematic viscosity yields [261]

$$\nu \approx 10^{-17} \left(\frac{\rho}{10^{14} \text{ g/cm}^3} \right)^{5/4} \left(\frac{T}{10^8 \text{ K}} \right)^{-2} \text{ s}. \quad (4.41)$$

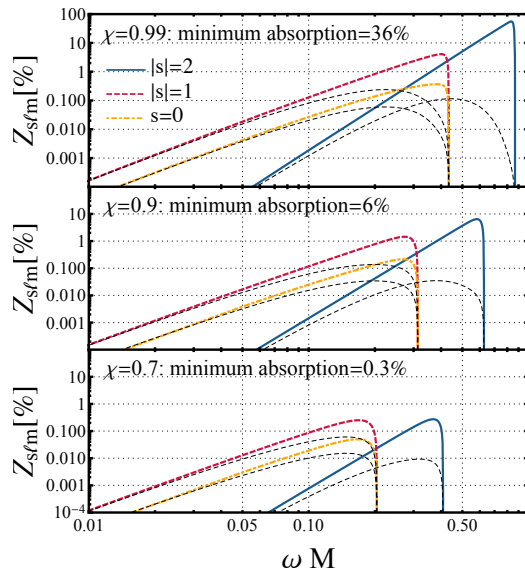


Figure 4.5. Superradiant amplification factor of a BH as a function of the frequency for $(\ell = m = 1)$ scalar, electromagnetic and $(\ell = m = 2)$ gravitational perturbations. The analytical approximation valid at low-frequency (black dashed lines) is compared to the exact numerical result. The minimum absorption rate to have a stable Kerr-like horizonless object for any type of perturbation is 0.3% (6%) for a remnant with spin $\chi = 0.7$ ($\chi = 0.9$). [31]

where ρ and T are the typical density and temperature of a NS, respectively. As a response to some external perturbation, a viscous fluid can dissipate radiation. The fraction of gravitational energy converted into mechanical energy in a viscous and compressible fluid was estimated in Refs. [262, 263], finding that dissipation occurs through sound waves that propagate in the interior of the fluid and through shear waves that heat the surface. In the limit $\nu\omega \ll 1$, which is valid in the entire parameter space of interest, and after an angle average, the fraction of absorbed energy in the flat spacetime approximation reads [262]

$$\begin{aligned}
 1 - |\mathcal{R}|^2 &\sim \frac{64\rho}{3\omega^2}(\omega\nu)^{3/2} \\
 &\approx 0.004 \left(\frac{M}{r_0}\right)^{27/4} \left[\frac{10^3 K}{T}\right]^3 \sqrt{\frac{0.01}{\omega M}} \left(\frac{20M_\odot}{M}\right)^4, \quad (4.42)
 \end{aligned}$$

where we have normalized the physical quantities by their typical values expected for an ECO in the BH limit, namely a density similar to that of a fastly spinning Kerr BH, $r_0 \sim M$, and a low temperature. As a reference, the local temperature of an isolated gravastar is of the order of the Hawking

temperature $T_{\text{H}} \approx 10^{-7}$ K for $M \sim 20 M_{\odot}$ [100]. This temperature is negligible in astrophysical scenarios and the object would be in thermal equilibrium with the hotter environment. The temperature of the interstellar medium typically ranges between 10 K and 10^4 K, so the normalization $T \approx 10^3$ K adopted above is a conservative upper bound. The estimate in Eq. (4.42) is only indicative and shows that absorption at percent level can be naturally achieved by ECOs.

Some models of quantum BHs have a frequency-dependent reflectivity $\mathcal{R}(\omega) = e^{-|k|/(2T_{\text{H}})}$ that allows for stable solutions against the ergoregion instability for any spin [264]. This model of horizonless compact object is analyzed in Sec. 6.7.

4.6 Appendix: The Detweiler transformation

In this appendix, we derive the transformation that brings the Teukolsky equation (4.7) in the Schrödinger-like form in Eq. (4.10) with real effective potential. In doing so, we revisit and extend the original calculations by Detweiler [254]. In particular, we refer the reader to the original work in Ref. [254] for the explicit transformations in the electromagnetic case. In the gravitational case, instead, we correct several mistakes in Eqs. (B3)–(B14) in Ref. [254] and provide explicit expressions of \mathbf{a} and \mathbf{b} extending the calculations in Ref. [265] to gravitational perturbations.

The Starobinsky identity for gravitational perturbations is [54]

$$\frac{1}{4}R_2 = \mathcal{D}\mathcal{D}\mathcal{D}\mathcal{D}R_{-2}, \quad (4.43)$$

where $\mathcal{D} = \partial_r - iK/\Delta$. According to Eq. (4.43), we can write

$$R_2 = \mathbf{a}R_{-2} + \frac{\mathbf{b}}{\Delta} \frac{dR_{-2}}{dr}, \quad (4.44)$$

where

$$\mathbf{a} = (a_1 + ia_2), \quad (4.45)$$

$$\mathbf{b} = ib_2, \quad (4.46)$$

and

$$a_1 = 4 \left[\frac{8K^4}{\Delta^4} + \frac{8K^2}{\Delta^3} \left(\frac{M^2 - a^2}{\Delta} - \lambda \right) - \frac{4\omega K}{\Delta^3} (3r^2 + 2Mr - 5a^2) + \frac{12r^2\omega^2 + \lambda(\lambda + 2)}{\Delta^2} \right], \quad (4.47)$$

$$a_2 = 4 \left[-\frac{24\omega r K^2}{\Delta^3} + \frac{1}{\Delta^2} \left(\frac{4\lambda(r - M)K}{\Delta} + 4\omega r \lambda + 12\omega M \right) \right], \quad (4.48)$$

$$b_2 = 4 \left[\frac{8K^3}{\Delta^2} + \frac{4K}{\Delta} \left(\frac{2(M^2 - a^2)}{\Delta} - \lambda \right) - \frac{8\omega}{\Delta} (Mr - a^2) \right]. \quad (4.49)$$

The radial functions α and β that define the Detweiler function in Eq. (4.9) are

$$\alpha = \frac{\kappa a \Delta^2 + |\kappa|^2}{\sqrt{2} |\kappa| [a_1 \Delta^2 + \Re(\kappa)]^{1/2}}, \quad (4.50)$$

$$\beta = \frac{i \kappa b_2 \Delta^2}{\sqrt{2} |\kappa| [a_1 \Delta^2 + \Re(\kappa)]^{1/2}}, \quad (4.51)$$

where

$$\begin{aligned} \kappa = & 4 \left[\lambda^2 (\lambda + 2)^2 + 144 a^2 \omega^2 (m - a\omega)^2 - a^2 \omega^2 (40\lambda^2 - 48\lambda) \right. \\ & \left. + a\omega m (40\lambda^2 + 48\lambda) \right]^{1/2} + 48i\omega M, \end{aligned} \quad (4.52)$$

$$\begin{aligned} \Re(\kappa) = & 4 \left[\lambda^2 (\lambda + 2)^2 + 144 a^2 \omega^2 (m - a\omega)^2 - a^2 \omega^2 (40\lambda^2 - 48\lambda) \right. \\ & \left. + a\omega m (40\lambda^2 + 48\lambda) \right]^{1/2}, \end{aligned} \quad (4.53)$$

$$\begin{aligned} |\kappa| = & \left\{ 16 \left[\lambda^2 (\lambda + 2)^2 + 144 a^2 \omega^2 (m - a\omega)^2 - a^2 \omega^2 (40\lambda^2 - 48\lambda) \right. \right. \\ & \left. \left. + a\omega m (40\lambda^2 + 48\lambda) \right] + (48\omega M)^2 \right\}^{1/2}. \end{aligned} \quad (4.54)$$

With this choice of the parameters, α and β satisfy the following relation

$$\alpha^2 - \alpha' \beta \Delta^{s+1} + \alpha \beta' \Delta^{s+1} - \beta^2 \Delta^{2s+1} V_s = \kappa, \quad (4.55)$$

which guarantees that the Detweiler function defined in Eq. (4.9) satisfies the Schrödinger-like equation in Eq. (4.10). Eq. (4.11) gives the following expression of the effective potential

$$V(r, \omega) = \frac{-K^2 + \Delta \lambda}{(r^2 + a^2)^2} + \frac{\Delta (b_2 p' \Delta)'}{(r^2 + a^2)^2 b_2 p} + G^2 + \frac{dG}{dr_*}, \quad (4.56)$$

where

$$p = |\kappa| \left\{ 2 \left[a_1 \Delta^2 + \Re(\kappa) \right] \right\}^{-1/2}. \quad (4.57)$$

The effective potential in Eq. (4.56) is purely real and has the following asymptotics: at infinity $V(r \rightarrow +\infty, \omega) \rightarrow -\omega^2$, and at the horizon $V(r \rightarrow r_+, \omega) \rightarrow -k^2$.

Finally, the conserved energy flux is the same if computed by the two independent solutions of the Teukolsky equation [Eq. (4.7)] or the two independent solutions of the Detweiler equation [Eq. (4.10)] [265]. This is an important consistency check since the energy flux is a measurable quantity and cannot depend on the transformation of the perturbation variable.

4.7 Appendix: Boundary condition for spinning perfectly reflecting objects

In this Appendix, we derive the boundary conditions that describe a perfectly reflecting Kerr-like object under electromagnetic perturbations [29]. The

horizonless object can be modeled as a perfect conductor, whose electric and magnetic fields satisfy $E_\theta(r_0) = E_\varphi(r_0) = 0$ and $B_r(r_0) = 0$. In the Newman-Penrose formalism, the previous conditions can be written in terms of the three complex scalars of the electromagnetic field ϕ_0, ϕ_1, ϕ_2 in the frame of a ZAMO [266]

$$E_\theta = \left[\frac{\Delta^{1/2}(r^2 + a^2)}{\sqrt{2}\hat{\rho}^* A^{1/2}(r^2 + a^2 \cos^2 \theta)} \left(\frac{\phi_0}{2} - \frac{\phi_2}{\hat{\rho}^2 \Delta} \right) + \text{c.c.} \right] - \frac{2a\Delta^{1/2}}{A^{1/2}} \sin \theta \Im(\phi_1), \quad (4.58)$$

$$E_\varphi = \left[-\frac{i\Delta^{1/2}\hat{\rho}}{\sqrt{2}} \left(\frac{\phi_0}{2} + \frac{\phi_2}{\hat{\rho}^2 \Delta} \right) + \text{c.c.} \right], \quad (4.59)$$

$$B_r = \left[\frac{a \sin \theta}{\sqrt{2}\hat{\rho} A^{1/2}} \left(\phi_2 - \Delta \hat{\rho}^2 \frac{\phi_0}{2} \right) + \text{c.c.} \right] + 2 \frac{r^2 + a^2}{A^{1/2}} \Im(\phi_1), \quad (4.60)$$

where $\hat{\rho} = -(r - ia \cos \theta)^{-1}$, $A = (r^2 + a^2)^2 - a^2 \Delta \sin^2 \theta$, and c.c. stands for the complex conjugate of the previous term. The conditions of a perfect conductor translate into

$$|\Phi_0|^2 = \frac{|\Phi_2|^2}{\Delta^2}, \quad \Im(\phi_1) = 0, \quad (4.61)$$

where $\Phi_0 \equiv \phi_0$ and $\Phi_2 \equiv 2\hat{\rho}^{-2}\phi_2$. We use the decomposition

$$\Phi_0 = \int d\omega e^{-i\omega t} \sum_{\ell m} e^{im\varphi} {}_s S_{\ell m}(\theta) {}_s R_{\ell m}(r), \quad (4.62)$$

$$\Phi_2 = \int d\omega e^{-i\omega t} \sum_{\ell m} e^{im\varphi} {}_{-s} S_{\ell m}(\theta) {}_{-s} R_{\ell m}(r), \quad (4.63)$$

and omit the ℓ, m subscripts for brevity. The radial and the angular functions are related by the Starobinsky identities [54, 267]

$$\mathcal{D}\mathcal{D}R_{-1} = BR_1, \quad \mathcal{L}_0\mathcal{L}_1S_1 = BS_{-1}, \quad (4.64)$$

where $B = \sqrt{\lambda^2 + 4m\omega a - 4a^2\omega^2}$, $\mathcal{D} = \partial_r - iK/\Delta$, and $\mathcal{L}_n = \partial_\theta + m \csc \theta - a\omega \sin \theta + n \cot \theta$. By substituting Eqs. (4.62), (4.63) and (4.64) in the condition for a perfect conductor in Eq. (4.61), we obtain the boundary condition for a perfectly reflecting compact object on the Teuksolsky wave function

$$\partial_r R_{-1} = \left[\frac{iK}{\Delta} - \frac{i}{2K} (\lambda \pm B + 2i\omega r) \right] R_{-1}, \quad (4.65)$$

where the plus and minus signs refer to polar and axial perturbations, respectively. In the following, we show that the boundary conditions in Eq. (4.65) are equivalent to Dirichlet and Neumann boundary conditions on the Detweiler wave function for axial and polar perturbations, respectively, as in Eqs. (4.23) and (4.24).

Near the radius of an ultracompact object ($\epsilon \ll 1$), the Teuksolsky wave function has the following asymptotics [54]

$$R_{-1} \sim \mathcal{A}\Delta e^{-ikr_*} + \mathcal{B}e^{+ikr_*}, \quad r_* \rightarrow -\infty, \quad (4.66)$$

where $\mathcal{A} = \mathcal{A}_0 + \eta\mathcal{A}_1 + \dots$ and $\mathcal{B} = \mathcal{B}_0 + \eta\mathcal{B}_1 + \dots$, with $\eta \equiv r - r_+$. Since $\Delta \sim (r_+ - r_-)\eta$ near the surface, we consider in Eq. (4.66) $\mathcal{A} = \mathcal{A}_0$ and $\mathcal{B} = \mathcal{B}_0 + \eta\mathcal{B}_1$ where [255]

$$\mathcal{B}_0 = -\frac{2^{1/2}(r_+^2 + a^2)^{1/2}k}{B}, \quad (4.67)$$

$$\mathcal{A}_0 = -\frac{iB}{4K_+\mathbb{R}^*} \mathcal{B}_0 B_{\text{in}}/B_{\text{out}}, \quad (4.68)$$

and $K_+ = K(r_+)$, $\mathbb{R} = iK_+ + (r_+ - r_-)/2$, and B_{in} and B_{out} are the asymptotic amplitudes defined in Eq. (4.16). By inserting Eq. (4.66) in the Teukolsky equation (4.7), we find

$$\mathcal{B}_1 = \left(\frac{iam}{M(r_+ - r_-)} + \frac{2\omega r_+ - i\lambda}{4Mr_+k} \right) \mathcal{B}_0. \quad (4.69)$$

Equation (4.66) with Eqs. (4.67), (4.68) and (4.69) defines the asymptotic expansion of the Teukolsky wave function R_{-1} near the horizon at the first order in η . By inserting Eq. (4.66) in the boundary condition (4.65), we get the following expression

$$B_{\text{out}}e^{ikr_*^0} \mp B_{\text{in}}e^{-ikr_*^0} = 0, \quad (4.70)$$

for the two signs of Eq. (4.65) that correspond to polar (−) and axial (+) modes, respectively. Eq. (4.70) takes the same form of Eqs. (4.23) and (4.24), therefore the perfect-conductor boundary conditions imply Dirichlet and Neumann boundary conditions on the Detweiler wave function for axial and polar modes, respectively. Let us emphasize that the boundary conditions are derived when the radius of the compact object is at microscopical distance from the would-be horizon, i.e., $\epsilon \ll 1$.

4.8 Appendix: Analytical quasi-normal modes

In this appendix, we derive the QNMs of a Kerr-like horizonless object analytically in the small-frequency regime. We focus on an ultracompact object whose radius is located as in Eq. (2.1) with $\epsilon \ll 1$, and whose surface is perfectly reflecting. We use a matched asymptotic expansion according to which the radial domain of the exterior spacetime is split into two regions: the near-region, i.e., $r - r_+ \ll 1/\omega$, and the far-region, i.e., $r - r_+ \gg M$. We solve the radial Teukolsky equation (4.7) in each region and we match the inner and outer solutions in the overlapping region where $M \ll r - r_+ \ll 1/\omega$. Finally, we impose the perfectly reflecting boundary conditions as in Eqs. (4.23) and (4.24) and we derive the characteristic frequencies of the object.

In the region near the radius of the compact object, the radial wave equation (4.7) reduces to [267]

$$[z(z+1)]^{1-s} \partial_z \left\{ [z(z+1)]^{s+1} \partial_z R_s \right\} + [Q^2 + iQs(1+2z) - \lambda z(z+1)] R_s = 0, \quad (4.71)$$

where $z = (r - r_+)/ (r_+ - r_-)$, $Q = (r_+^2 + a^2)(m\Omega_H - \omega) / (r_+ - r_-)$, and $\lambda = (\ell - s)(\ell + s + 1)$. Eq. (4.71) is valid when $M\omega \ll 1$ and it is derived by neglecting the terms proportional to ω in Eq. (4.7) except for the ones which enter into Q . The general solution of Eq. (4.71) is a linear combination of hypergeometric functions, i.e.,

$$R_s = (1+z)^{iQ} \left[C_1 z^{-iQ} {}_2F_1 \left(-\ell + s, \ell + 1 + s; 1 - \bar{Q} + s; -z \right) + C_2 z^{iQ-s} {}_2F_1 \left(-\ell + \bar{Q}, \ell + 1 + \bar{Q}; 1 + \bar{Q} - s; -z \right) \right], \quad (4.72)$$

where $\bar{Q} \equiv 2iQ$. The large- r behavior of the solution is

$$R_s \sim \left(\frac{r}{r_+ - r_-} \right)^{\ell-s} \Gamma(2\ell + 1) \left[\frac{C_1 \Gamma(1 - \bar{Q} + s)}{\Gamma(\ell + 1 - \bar{Q}) \Gamma(\ell + 1 + s)} + \frac{C_2 \Gamma(1 + \bar{Q} - s)}{\Gamma(\ell + 1 + \bar{Q}) \Gamma(\ell + 1 - s)} \right] + \left(\frac{r}{r_+ - r_-} \right)^{-\ell-1-s} \frac{(-1)^{\ell+1+s}}{2\Gamma(2\ell + 2)} \left[\frac{C_1 \Gamma(\ell + 1 - s) \Gamma(1 - \bar{Q} + s)}{\Gamma(-\ell - \bar{Q})} + \frac{C_2 \Gamma(\ell + 1 + s) \Gamma(1 + \bar{Q} - s)}{\Gamma(-\ell + \bar{Q})} \right], \quad (4.73)$$

where the ratio of the coefficients C_1/C_2 is fixed by the boundary condition at the radius of the compact object.

At infinity, the radial wave equation (4.7) reduces to [268]

$$r \partial_r^2 f_s + 2(\ell + 1 - i\omega r) \partial_r f_s - 2i(\ell + 1 - s) \omega f_s = 0, \quad (4.74)$$

where $f_s \equiv e^{i\omega r} r^{-\ell+s} R_s$. The general solution of Eq. (4.74) is a linear combination of a confluent hypergeometric function and a Laguerre polynomial, i.e.,

$$R_s = e^{-i\omega r} r^{\ell-s} \left[C_3 U(\ell + 1 - s, 2\ell + 2, 2i\omega r) + C_4 L_{-\ell-1+s}^{2\ell+1}(2i\omega r) \right], \quad (4.75)$$

where $C_4 = (-1)^{\ell-s} C_3 \Gamma(-\ell + s)$ by imposing purely outgoing waves at infinity. The small- r behavior of the solution is

$$R_s \sim C_3 \left[r^{\ell-s} \frac{(-1)^{\ell-s} \Gamma(\ell + 1 + s)}{2\Gamma(2\ell + 2)} + r^{-\ell-1-s} (2i\omega)^{-2\ell-1} \frac{\Gamma(2\ell + 1)}{\Gamma(\ell + 1 - s)} \right]. \quad (4.76)$$

The matching of Eqs. (4.73) and (4.76) in the intermediate region where $M \ll r - r_+ \ll 1/\omega$ yields

$$\frac{C_1}{C_2} = - \frac{\Gamma(\ell + 1 + s)}{\Gamma(\ell + 1 - s)} \left[\frac{R_+ + i(-1)^\ell (\omega(r_+ - r_-))^{2\ell+1} L S_+}{R_- + i(-1)^\ell (\omega(r_+ - r_-))^{2\ell+1} L S_-} \right], \quad (4.77)$$

where

$$R_\pm \equiv \frac{\Gamma(1 \pm \bar{Q} \mp s)}{\Gamma(\ell + 1 \pm \bar{Q})}, \quad S_\pm \equiv \frac{\Gamma(1 \pm \bar{Q} \mp s)}{\Gamma(-\ell \pm \bar{Q})}, \quad L \equiv \frac{1}{2} \left[\frac{2^\ell \Gamma(\ell + 1 + s) \Gamma(\ell + 1 - s)}{\Gamma(2\ell + 1) \Gamma(2\ell + 2)} \right]^2. \quad (4.78)$$

Electromagnetic perturbations

For $s = -1$, the ratio C_1/C_2 is derived by imposing the boundary conditions (4.23) and (4.24) in the near-horizon expansion of the solution in the near-region. At the radius of the object, we obtain

$$\frac{C_1}{C_2} = \mp B^{-1} \bar{Q} z_0^{\bar{Q}}. \quad (4.79)$$

where $z_0 \equiv z(r_0)$, and the minus and plus signs refer to polar and axial perturbations, respectively. By equating Eq. (4.77) with Eq. (4.79), we obtain an algebraic equation for the real part of the QNM frequencies. An approximate solution can be found in the small-spin and small-frequency regime for which $\bar{Q} \ll 1$. In this regime, Eq. (4.77) reduces to $C_1/C_2 = \bar{Q}/[\ell(\ell+1)]$, whereas $B \approx \ell(\ell+1)$ in Eq. (4.79). It follows

$$z_0^{-2iQ} = \mp 1. \quad (4.80)$$

By using the tortoise coordinate where $\log(z_0) \sim r_*^0(r_+ - r_-)/(r_+^2 + a^2)$, Eq. (4.80) yields

$$e^{-2iQr_*^0(r_+ - r_-)/(r_+^2 + a^2)} = \mp 1, \quad (4.81)$$

which is analogous to Eq. (A18) in Ref. [268] in the case of scalar perturbations. The solution of Eq. (4.81) is

$$\omega_R = -\frac{\pi p}{2|r_*^0|} + m\Omega_H, \quad (4.82)$$

where p is a positive odd (even) integer for polar (axial) modes. Equation (4.82) is also valid for scalar perturbations where p is a positive odd (even) integer for the modes with Neumann (Dirichlet) boundary condition.

Gravitational perturbations

For $s = -2$, the ratio C_1/C_2 is derived by imposing the boundary conditions (4.23) and (4.24) in the near-horizon expansion of the solution in the near-region. When $\bar{Q} \ll 1$, we obtain at the radius of the object

$$\frac{C_1}{C_2} = \mp \frac{2}{(\ell+2)(\ell+1)\ell(\ell-1)} \bar{Q} z_0^{\bar{Q}}, \quad (4.83)$$

where the minus and plus signs refer to polar and axial perturbations, respectively. For $\bar{Q} \ll 1$, Eq. (4.77) reduces to $C_1/C_2 = -2\bar{Q}/[(\ell+2)(\ell+1)\ell(\ell-1)]$. By equating the latter equation with Eq. (4.83), it follows

$$z_0^{-2iQ} = \pm 1, \quad (4.84)$$

whose solution is

$$\omega_R = -\frac{\pi(p+1)}{2|r_*^0|} + m\Omega_H, \quad (4.85)$$

where p is a positive odd (even) integer for polar (axial) modes. By comparing Eq. (4.82) with Eq. (4.85), we notice that the gravitational QNM frequencies have a π phase shift with respect to the scalar and electromagnetic ones.

The analytic expression of the real part of the QNMs for a generic spin- s perturbation is given in Eq. (4.33).

Imaginary part of the quasi-normal mode frequencies

To compute the imaginary part of the QNMs analytically, we impose the boundary conditions in Eq. (4.23) and (4.24) on the near-horizon asymptotics of the Detweiler wave function in Eq. (4.16). The computation yields

$$\omega = -\frac{1}{2|r_*^0|} \left(p\pi + \Phi - i \ln \left| \frac{B_{\text{in}}}{B_{\text{out}}} \right| \right) + m\Omega_H, \quad (4.86)$$

where Φ is a phase that depends on the spin- s of the perturbation and it is derived with the matching asymptotic expansion described above.

According to the Wronskian relations in Eq. (4.19), $|B_{\text{in}}/B_{\text{out}}| = |A_{\text{out}}/A_{\text{in}}|$ therefore the amplification factor of perturbations in the cavity between the radius of the object and the photon sphere is related to the amplification factor of BHs. For a perturbation of spin s , the amplification factor of BHs is defined as

$$Z_{s\ell m} = \left| \frac{A_{\text{out}}}{A_{\text{in}}} \right|^2 - 1, \quad (4.87)$$

that has the following form in the low-frequency regime as computed by Starobinsky [267]

$$Z_{s\ell m} \equiv -D_{s\ell m} = 4Q\beta_{sl} \prod_{k=1}^{\ell} \left(1 + \frac{4Q^2}{k^2} \right) [\omega(r_+ - r_-)]^{2\ell+1}. \quad (4.88)$$

In our calculations, we impose $Z_{s\ell m} \equiv -\Re(D_{s\ell m})$ since $\omega_I \ll \omega_R$. By inserting Eq. (4.88) in Eq. (4.87) and using the Wronskian relations, we derive

$$\left| \frac{B_{\text{in}}}{B_{\text{out}}} \right|^2 - 1 = -\Re(D_{s\ell m}). \quad (4.89)$$

Eqs. (4.86) and (4.89) yield to the analytical expression of the imaginary part of the QNM frequencies in the low-frequency regime

$$\omega_I \simeq -\frac{\Re(D_{s\ell m})}{4|r_*^0|}, \quad (4.90)$$

that coincides with Eq. (4.34). Let us notice that $Z_{s\ell m} > 0$ (i.e., $\omega_I > 0$) in the superradiant regime, where $\omega_R(\omega_R - m\Omega) < 0$. Consequently, the unstable modes of a perfectly-reflecting Kerr-like object can be understood in terms of waves amplified in the ergoregion and being reflected at the boundary.

Chapter 5

Gravitational-wave echoes

Una notte osservavo come al solito il cielo col mio telescopio. Notai che da una galassia lontana cento milioni d'anni-luce sporgeva un cartello. C'era scritto: TI HO VISTO. [...] Proprio duecento milioni d'anni prima, né un giorno di più né un giorno di meno, m'era successo qualcosa che avevo sempre cercato di nascondere.

Italo Calvino, *Le Cosmicomiche*

5.1 Schematic picture

GW echoes are an additional signal that would be emitted in the postmerger phase of a compact binary coalescence when the remnant is a horizonless ultracompact object. Possible sources of GW echoes are near-horizon quantum structures [19, 220, 32], ultracompact NSs [223, 224], and BHs in modified theories of gravity in which the graviton reflects effectively on a hard wall [180, 181]. The key feature of the sources of GW echoes is the existence of a cavity in the effective potential of the perturbed object between the photon sphere and the effective radius of the object, as shown in Fig. 5.1. If the object is sufficiently compact, the cavity can support quasi-trapped modes that leak out of the potential barrier through tunneling effects and are responsible for the emission of GW echoes.

To describe the dynamical emission of GW echoes, we analyze the scattering of a Gaussian pulse starting from infinity and going towards the compact object. As shown in Fig. 5.1, when the pulse crosses the photon-sphere barrier and perturbs it, a prompt ringdown signal is emitted at infinity [256, 23, 13]. The prompt ringdown emitted by an ultracompact horizonless object is almost indistinguishable from the BH ringdown since the photon sphere is approximately at the same location and has a similar shape [19]. Afterward, the perturbation travels inside the photon-sphere barrier and is reflected by

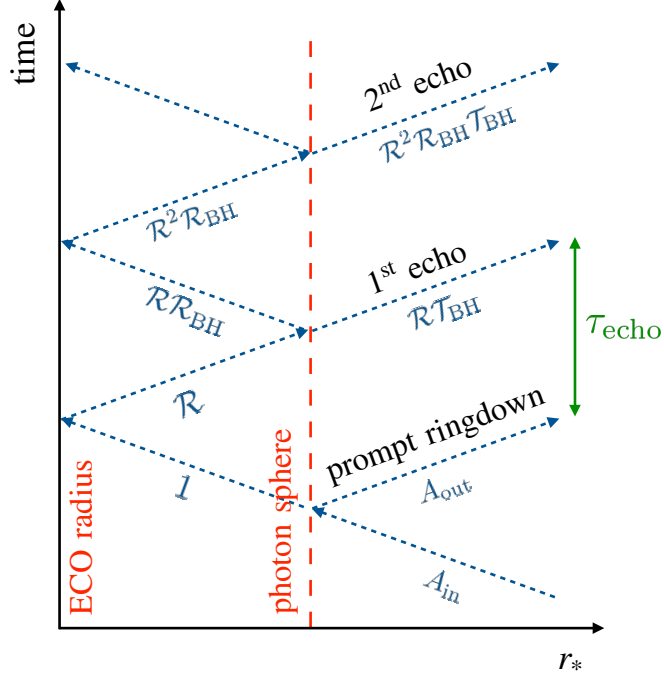


Figure 5.1. Schematic diagram of the propagation of a perturbation in the background geometry of a horizonless compact object [256, 23, 13]. When the perturbation excites the photon sphere, a prompt ringdown signal is emitted at infinity. Subsequent bounces of the perturbation in the cavity between the radius of the object and the photon sphere are responsible for the emission of GW echoes. [137]

the surface of the compact object. A fraction of the radiation is absorbed by the compact object depending on its reflective properties [31, 264].

After each interaction with the photon sphere, a GW echo is emitted at infinity with a progressively smaller amplitude. The amplitude of the GW echoes depends on the surface reflectivity of the object \mathcal{R} and the reflection (\mathcal{R}_{BH}) and transmission (\mathcal{T}_{BH}) coefficients of the wave coming from the left of the photon sphere. After each bounce in the cavity between the ECO radius and the photon sphere, the perturbation acquires a factor $\mathcal{R}\mathcal{R}_{\text{BH}}$.

The photon-sphere barrier acts as a frequency-dependent high-pass filter. The characteristic frequencies governing the prompt ringdown are approximately the BH QNM frequencies despite the latter are not part of the QNM spectrum of horizonless compact objects. Each subsequent GW echo has a lower frequency content, and at late times the GW signal is dominated by the low-frequency QNMs of horizonless compact objects.

The delay time between subsequent GW echoes is proportional to the width of the cavity, therefore, the compactness of the object. The delay time can be computed as the round-trip time of the radiation from the photon sphere to

the boundary. In the non-spinning case [19, 220]

$$\tau_{\text{echo}} = 2M [1 - 2\epsilon - 2 \log(2\epsilon)] , \quad (5.1)$$

where the logarithmic dependence on ϵ would allow detecting even Planckian corrections ($\epsilon \sim l_{\text{Planck}}/M$) at the horizon scale few ms after the merger of a compact binary coalescence with a remnant of $M \sim 10M_{\odot}$.

5.2 Analytical template

In this Section, we shall derive an analytical template for the ringdown and the GW echoes emitted by a spinning horizonless compact object. The waveform is parametrized by the standard ringdown parameters plus two quantities related to the properties of the exotic remnant. The template can be easily implemented to perform matched-filter-based searches for GW echoes and constrain models of horizonless compact objects.

5.2.1 Transfer function

We analyze a spinning horizonless compact object whose exterior spacetime is described by the Kerr metric, as detailed in Sec. 4.1. The radius of the object is located as in Eq. (2.1), where we focus on ultracompact models with $\epsilon \ll 1$. We require the location of the surface to be at a proper length $\delta \ll M$ from the would-be horizon, where

$$\delta = \int_{r_+}^{r_0} dr \sqrt{g_{rr}}|_{\theta=0} , \quad (5.2)$$

and the relation between the proper length δ and ϵ is given by

$$\epsilon \simeq \sqrt{1 - \chi^2} \frac{\delta^2}{4r_+^2} . \quad (5.3)$$

Let us perturb the background geometry with a spin- s perturbation. The radial component of the perturbation is governed by the inhomogeneous equation

$$\frac{d^2 X_s}{dr_*^2} - V(r, \omega) X_s = \tilde{S} , \quad (5.4)$$

where X_s is the Detweiler function defined in Eq. (4.9), $V(r, \omega)$ is the effective potential in Eq. (4.11), and \tilde{S} is a source term. At asymptotic infinity, we require the solution of Eq. (5.4) to be a purely outgoing wave, $X_s(\omega, r_* \rightarrow \infty) = \tilde{Z}^+(\omega) e^{i\omega r_*}$.

In the frequency domain, the GW signal emitted by a horizonless compact object can be written in terms of the GW signal that would be emitted by a BH and reprocessed by a transfer function [84], i.e.,

$$\tilde{Z}^+(\omega) = \tilde{Z}_{\text{BH}}^+(\omega) + \mathcal{K}(\omega) \tilde{Z}_{\text{BH}}^-(\omega) , \quad (5.5)$$

where $\tilde{Z}_{\text{BH}}^{\pm}$ are the responses of a Kerr BH (at infinity and near the horizon, for the plus and minus signs, respectively) to the source \tilde{S} , i.e.,

$$\tilde{Z}_{\text{BH}}^{\pm} = \frac{1}{W_{\text{BH}}} \int_{-\infty}^{+\infty} dr_* \tilde{S} X_s^{\mp}, \quad (5.6)$$

where X_s^{\pm} are the two independent solutions of the homogeneous equation associated to Eq. (5.4) with asymptotics in Eqs. (4.16) and (4.17), and W_{BH} is the Wronskian defined in Eq. (4.18). The details of the horizonless compact object are all contained in the transfer function that is defined as [84]

$$\mathcal{K}(\omega) = \frac{\mathcal{T}_{\text{BH}} \mathcal{R}(\omega) e^{-2ikr_*^0}}{1 - \mathcal{R}_{\text{BH}} \mathcal{R}(\omega) e^{-2ikr_*^0}}, \quad (5.7)$$

where \mathcal{R}_{BH} and \mathcal{T}_{BH} are the reflection and transmission coefficients of a wave coming from the left of the photon-sphere barrier defined in Eq. (4.37), and $\mathcal{R}(\omega)$ is the surface reflectivity of the object defined in Eq. (4.22).

According to Eq. (5.5), the GW signal emitted at infinity by a horizonless compact object is the same as the one emitted by a BH at infinity with an extra GW emission that depends on the reflectivity and compactness of the object. To get an insight of the additional GW emission, let us expand the transfer function in Eq. (5.7) as a geometric series [84, 269]

$$\mathcal{K}(\omega) = \mathcal{T}_{\text{BH}} \mathcal{R}(\omega) e^{-2ikr_*^0} \sum_{j=1}^{\infty} [\mathcal{R}_{\text{BH}} \mathcal{R}(\omega)]^{j-1} e^{-2i(j-1)kr_*^0}. \quad (5.8)$$

Given Eq. (5.8), the GW signal takes the form of a series of pulses where the index j stands for the signal emitted by the j -th echo. The phase factor $2ikr_*^0$ corresponds to the time delay between two pulses due to the round-trip time of the perturbation between the photon sphere and the radius of the object. Subsequent echoes can have a phase inversion to each other when the factor $\mathcal{R}_{\text{BH}} \mathcal{R}(\omega)$ has a negative sign.

Eq. (5.5) allows us to construct an analytical template for the GW signal emitted by a horizonless compact object. In the following sections, we provide an analytical approximation of each term in Eq. (5.5), namely the BH reflection coefficient and the BH responses at infinity and the horizon. In this way, the analytical template depends only on the BH ringdown parameters and the parameters of the ECO, i.e., its compactness and reflectivity.

5.2.2 Black hole reflection coefficient in the low-frequency approximation

The low-frequency regime is the most interesting regime for GW echoes since the latter are obtained by the reprocessing of the ringdown signal, whose frequency content is initially dominated by the BH fundamental QNM and subsequently decreases in time. Hence, the low-frequency approximation

becomes increasingly more accurate at late times. The analytical approximation of the BH reflection coefficient in the small-frequency regime is computed in Appendix 4.8 through a matched asymptotic expansion. In particular, the BH reflection coefficient is defined in Eq. (4.37) as the ratio of the ingoing and outgoing coefficients in the near-horizon asymptotics of the Detweiler function in Eq. (4.16). The latter coefficients are related to the coefficients in the near-horizon expansion of the Teukolsky function derived in the small-frequency regime in Eq. (4.77). For $\ell = 2$, the BH reflection coefficient reads

$$\begin{aligned} \mathcal{R}_{\text{BH}}^{\text{LF}} = & -8Mke^{\frac{\zeta(\gamma-1)}{\gamma+1}} \frac{2Mk - i(\gamma-1)}{(\gamma-1)^2} \left[\frac{-M(\gamma-1)\xi}{L} \right]^{\zeta(\gamma-1)} \times \\ & \left[\frac{16k^2M^2}{(\gamma-1)^2} + 1 \right] \frac{\Gamma(-2+\zeta)\Gamma(-1-\zeta)}{\Gamma(-2-\zeta)\Gamma(3-\zeta)} \times \\ & \frac{1800i\Gamma(-2-\zeta) + (\omega M(\gamma-1)\xi)^5 \Gamma(3-\zeta)}{1800i\Gamma(-2+\zeta) + (\omega M(\gamma-1)\xi)^5 \Gamma(3+\zeta)}, \end{aligned} \quad (5.9)$$

where $\gamma = r_-/r_+$, $\xi = 1 + \sqrt{1 - \chi^2}$, $\zeta = i(2\omega M - m\sqrt{\gamma})(\gamma+1)\xi/(\gamma-1)$, and L is an arbitrary constant with the dimension of a length. The low-frequency expression of \mathcal{R}_{BH} for generic values of the angular number ℓ is provided in a publicly available MATHEMATICA[®] notebook [270].

In the high-frequency regime, $\mathcal{R}_{\text{BH}} \sim e^{-2\pi\omega/\kappa_H}$, where $\kappa_H = \frac{1}{2}(r_+ - r_-)/(r_+^2 + a^2)$ is the surface gravity of a Kerr BH [271]. We use a Fermi-Dirac interpolating function to connect the two regimes in frequency domain:

$$\mathcal{R}_{\text{BH}} = \mathcal{R}_{\text{BH}}^{\text{LF}} \frac{\exp\left(\frac{-2\pi\omega_R}{\kappa_H}\right) + 1}{\exp\left(\frac{2\pi(|\omega| - \omega_R)}{\kappa_H}\right) + 1}, \quad (5.10)$$

where ω_R is the real part of the fundamental QNM of a Kerr BH with spin χ . For $|\omega| \ll \omega_R$ the reflection coefficient reduces to $\mathcal{R}_{\text{BH}}^{\text{LF}}$, whereas it is exponentially suppressed when $|\omega| \gg \omega_R$.

5.2.3 Modeling the black hole response at infinity

We model the BH response at infinity using the fundamental $\ell = m = 2$ QNM. We consider a generic linear combination of two independent polarizations, namely [242, 272]

$$Z_{\text{BH}}^+(t) \sim \Theta(t - t_0) [\mathcal{A}_+ \cos(\omega_R t + \phi_+) + i\mathcal{A}_\times \sin(\omega_R t + \phi_\times)] e^{-t/\tau}, \quad (5.11)$$

where $\Re(Z_{\text{BH}}^+)$ and $\Im(Z_{\text{BH}}^+)$ are the two ringdown polarizations $h_+(t)$ and $h_\times(t)$, respectively. In the above relation, $\Theta(t)$ is the Heaviside function, t_0 is the starting time of the ringdown, $\mathcal{A}_{+, \times} \in \mathbb{R}$ and $\phi_{+, \times} \in \mathbb{R}$ are the amplitudes and the phases of the two polarizations, respectively, and $\tau = -1/\omega_I$ is the damping time. Let us notice that Eq. (5.11) is the most generic expression for

the ringdown with the fundamental $\ell = m = 2$ mode and assumes that $\mathcal{A}_{+,\times}$ and $\phi_{+,\times}$ are four independent parameters. The most relevant case of a binary BH ringdown is that of circularly polarized waves [272], that can be obtained from Eq. (5.11) by setting $\mathcal{A}_+ = \mathcal{A}_\times$ and $\phi_+ = \phi_\times$.

Given the BH response in the time domain, the waveform in the frequency-domain is obtained through a Fourier transform

$$\tilde{Z}_{\text{BH}}^\pm(\omega) = \int_{-\infty}^{+\infty} \frac{dt}{\sqrt{2\pi}} Z_{\text{BH}}^\pm(t) e^{i\omega t}, \quad (5.12)$$

where the response at infinity is

$$\tilde{Z}_{\text{BH}}^+(\omega) \sim \frac{e^{i\omega t_0}}{2\sqrt{2\pi}} \left(\frac{\alpha_{1+}\mathcal{A}_+ - \alpha_{1\times}\mathcal{A}_\times}{\omega - \omega_{\text{QNM}}} + \frac{\alpha_{2+}\mathcal{A}_+ - \alpha_{2\times}\mathcal{A}_\times}{\omega + \omega_{\text{QNM}}^*} \right), \quad (5.13)$$

where $\omega_{\text{QNM}} = \omega_R + i\omega_I$, $\alpha_{1+,\times} = ie^{-i(\phi_{+,\times} + t_0\omega_{\text{QNM}})}$, and $\alpha_{2+,\times} = -\alpha_{1+,\times}^*$.

5.2.4 Modeling the black hole response at the horizon

The BH response at the horizon, defined in Eq. (5.6), has the same poles in the complex frequency plane as the BH response at infinity. Therefore, the near-horizon response at intermediate times can be written as in Eq. (5.13) with different amplitudes and phases. Let us assume that the source has support in the interior of the object, i.e., on the left of the effective potential barrier, where $V(r, \omega) \approx -k^2$. This is a reasonable assumption since the source in the exterior can hardly perturb the spacetime within the cavity [32, 264]. In this case, it is easy to show that

$$\tilde{Z}_{\text{BH}}^- = \frac{\mathcal{R}_{\text{BH}}}{\mathcal{T}_{\text{BH}}} \tilde{Z}_{\text{BH}}^+ + \frac{1}{\mathcal{T}_{\text{BH}}W_{\text{BH}}} \int_{-\infty}^{+\infty} dr_* \tilde{S} e^{ikr_*}. \quad (5.14)$$

Using Eq. (5.6) and the fact that \tilde{S} has support only where $V(r, \omega) \approx -k^2$, the above equation can be written as

$$\tilde{Z}_{\text{BH}}^- = \frac{\mathcal{R}_{\text{BH}} \tilde{Z}_{\text{BH}}^+ + \tilde{\mathcal{Z}}_{\text{BH}}^+}{\mathcal{T}_{\text{BH}}}, \quad (5.15)$$

where $\tilde{\mathcal{Z}}_{\text{BH}}^+$ is the BH response at infinity to an effective source $\tilde{\mathcal{S}}(\omega, x) = \tilde{S}(\omega, x) e^{2ikx}$ within the cavity. As such, the ringdown part of $\tilde{\mathcal{Z}}_{\text{BH}}^+$ can also be generically written as in Eq. (5.13) with different amplitudes and phases. Two interesting features of Eq. (5.15) are noteworthy. First, the final response of the horizonless compact object (in Eq. (5.5)) does not depend on the BH transmission coefficient, since the term \mathcal{T}_{BH} in the denominator of Eq. (5.15) cancels out with that in the transfer function in Eq. (5.7). Second, the first term on the right-hand side of Eq. (5.15) can be computed analytically using the low-frequency approximation of the BH reflection coefficient in Eq. (5.10) and the BH response at infinity in Eq. (5.11). For this reason, in the following, we focus only on the first term of the right-hand side of Eq. (5.15). A discussion on the expressions of $\tilde{\mathcal{Z}}_{\text{BH}}^+$ for several sources is given in Appendix 5.6.

ϵ	compactness of the ECO
$\mathcal{R}(\omega)$	reflection coefficient at the surface of the ECO
M	total mass
χ	spin
$\mathcal{A}_{+, \times}$	amplitudes of the polarizations of the BH ringdown
$\phi_{+, \times}$	phases of the polarizations of the BH ringdown
t_0	starting time of the BH ringdown

Table 5.1. Parameters of the ringdown+echo template in Ref. [22]. The parameters ϵ and $\mathcal{R}(\omega)$ characterize the horizonless compact object, whereas the remaining 7 parameters characterize the BH ringdown.

5.2.5 Parameters and validity of the template

In the frequency domain, the ringdown+echo template is given by [22]

$$\tilde{Z}^+(\omega) = \tilde{Z}_{\text{BH}}^+(\omega) \left(1 + \frac{\mathcal{R}_{\text{BH}} \mathcal{R}(\omega) e^{-2ikr_*^0}}{1 - \mathcal{R}_{\text{BH}} \mathcal{R}(\omega) e^{-2ikr_*^0}} \right), \quad (5.16)$$

where the BH response at infinity is in Eq. (5.13) and the low-frequency approximation of the BH reflection coefficient is in Eq. (5.10). For $\mathcal{R} = 0$, we recover the template of a BH ringdown emitted at infinity. The additional term in Eq. (5.16) is associated with the GW echoes that are emitted in the case of horizonless compact objects. Overall, the final template depends on the 7 parameters of a standard BH ringdown (i.e., mass and spin of the remnant, amplitudes and phases of the plus and cross polarizations of the signal, and starting time of the ringdown) plus two parameters that are related to the properties of the horizonless compact object (i.e., its compactness and reflectivity), see Table 5.1. For circularly polarized waves ($\mathcal{A}_+ = \mathcal{A}_\times$ and $\phi_+ = \phi_\times$) or linearly polarized waves ($\mathcal{A}_\times = 0$), the number of the BH ringdown parameters reduces to 5.

Fig. 5.2 shows the agreement at low frequency of the analytical template with the result of a numerical integration of the Teukolsky equations. The left panels show the validity of the analytical approximation of the BH reflection coefficient in the low-frequency regime, both for a non-spinning and a spinning remnant. The right panels of Fig. 5.2 show the quantity that is responsible for the emission of GW echoes as a function of the frequency, i.e., $\mathcal{K} \tilde{Z}_{\text{BH}}^-$ normalized by the BH response \tilde{Z}_{BH}^+ . The peaks in the GW response are due to the excitation of the low-frequency QNMs that characterize horizonless compact objects (see a related discussion in Sec. 3.2.4). The agreement between the analytical template and the numerical integration is very good at low frequencies (both in the absolute value and imaginary part), whereas deviations are present in the transition region where $M\omega \sim 0.1$. Crucially, the low-frequency resonances – which dominate the response at infinity – are properly reproduced.

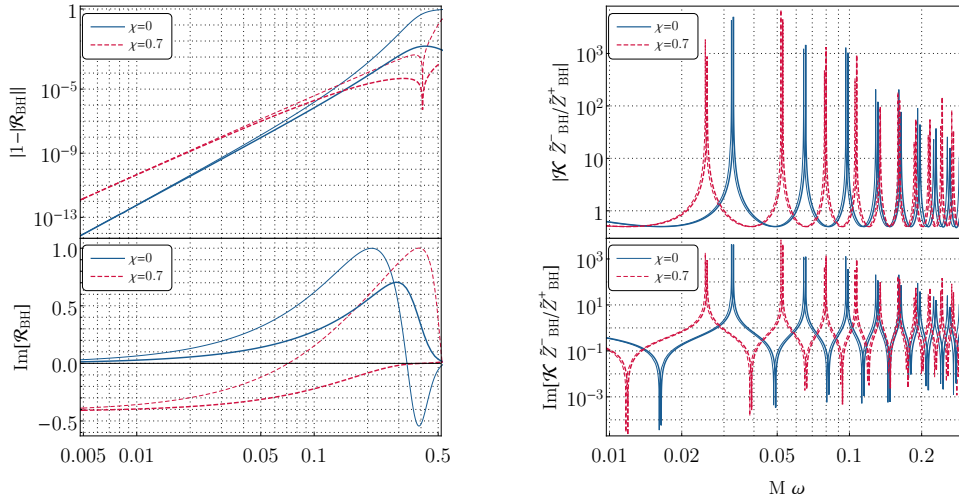


Figure 5.2. Comparison between the analytical template (thick curves) and the result of a numerical integration of the Teukolsky equation (thin curves) for $\chi = 0$ and $\chi = 0.7$. Left panels: the complex BH reflection coefficient. Right panels: the absolute value (top) and the imaginary part (bottom) of the response of GW echoes $\mathcal{K} \tilde{Z}_{\text{BH}}^- / \tilde{Z}_{\text{BH}}^+$ as a function of the frequency. In all the panels, $\ell = m = 2$ and, in the right panels, $\delta = 10^{-10}M$ and $\mathcal{R} = 1$. [22]

To quantify the validity of the template, we compute the overlap

$$O = \frac{|\langle \tilde{h}_A | \tilde{h}_N \rangle|}{\sqrt{|\langle \tilde{h}_N | \tilde{h}_N \rangle| |\langle \tilde{h}_A | \tilde{h}_A \rangle|}} \quad (5.17)$$

between the analytical signal \tilde{h}_A and the numerical one \tilde{h}_N in frequency domain, where the inner product is defined in Eq. (3.107) in Appendix 3.7. When $|\mathcal{R}| \sim 1$, the presence of very high and narrow resonances makes a quantitative comparison challenging since a slight displacement of the resonances (due for instance to finite- ω truncation errors) deteriorates the overlap. For example, for the representative case shown in Fig. 5.2 ($\delta = 10^{-10}M$, $\chi = 0.7$, and $\mathcal{R} = 1$), the overlap is excellent ($O \gtrsim 0.999$) when the integration is performed before the first resonance, however it reduces quickly to zero after that. To overcome this issue, we compute the overlap in the case in which the resonances are less pronounced, i.e., $|\mathcal{R}|^2 < 1$. Let us consider a remnant with $M = 30 M_\odot$, $\chi = 0.7$, $\delta = 10^{-10}M$, and the aLIGO noise spectral density [273]. For $\mathcal{R} = 0.9$ and in the frequency range $f \in (20, 100)$ Hz (whose upper end corresponds to the threshold $\omega M \sim 0.1$ beyond which the low-frequency approximation is not accurate), the overlap is $O = 0.48$. This small value is mostly due to a small displacement of the resonances. Indeed, by shifting the mass of the analytical waveform by only 1.6%, the overlap increases significantly, $O = 0.995$. For $\mathcal{R} = 0.8$ and in the same conditions, the overlap is $O \approx 0.8$ without the mass shift and $O \gtrsim 0.999$ with the same mass shift as above. Let us notice that

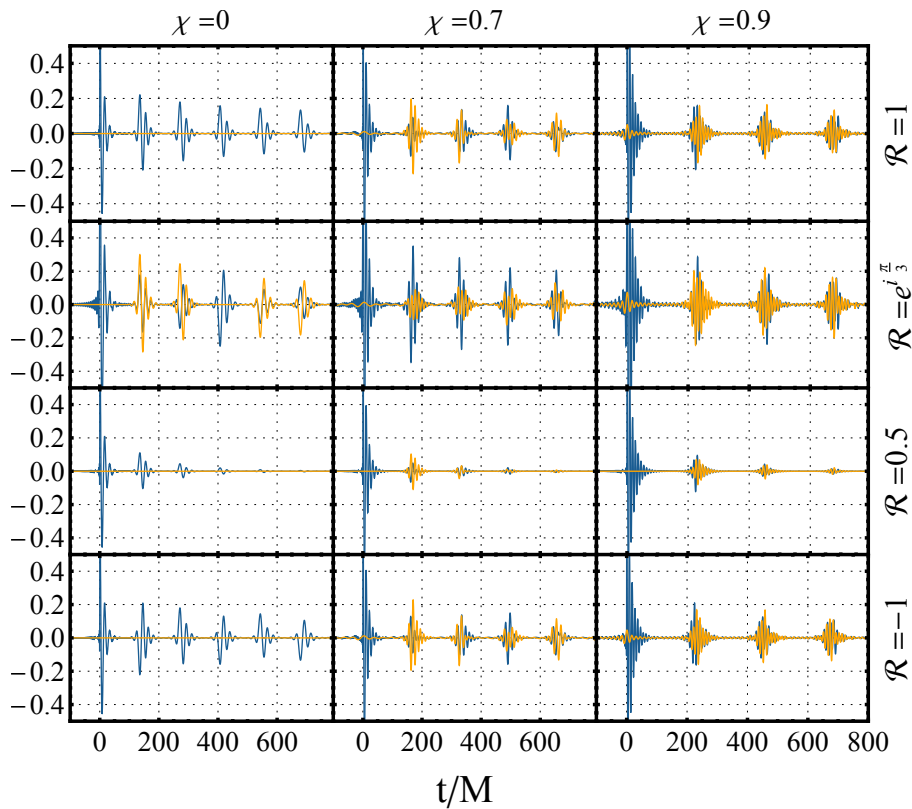


Figure 5.3. Examples of the gravitational ringdown+echo template in the time domain for a horizonless compact object with $\delta/M = 10^{-7}$ and different values of the surface reflectivity $\mathcal{R}(\omega) = \text{const}$ and the spin χ . The real (blue curve) and the imaginary (orange curve) part of the waveform are the plus and cross polarization of the signal, respectively. For simplicity, the ringdown signal is purely plus-polarized. Each waveform is normalized to the peak of $|\Re[h(t)]|$ in the ringdown. Additional waveforms are provided online [270, 22].

the agreement between the analytical template and the numerics improves as $\delta \rightarrow 0$. In this limit, the ECO QNMs appear at lower frequency and the resonant frequencies are better reproduced by the analytical framework.

5.3 Properties of gravitational-wave echoes

The GW signal emitted by a horizonless compact object in the time domain is computed through an inverse Fourier transform of the analytical template in Eq. (5.16), i.e.,

$$h(t) = \frac{1}{\sqrt{2\pi}} \int_{-\infty}^{+\infty} d\omega \tilde{Z}^+(\omega) e^{-i\omega t}, \quad (5.18)$$

where $\Re[h(t)]$ and $\Im[h(t)]$ are the plus and cross polarizations of the GW signal, respectively. Fig. 5.3 shows the ringdown+echo waveform as a function of time for a remnant with $\delta = 10^{-7}M$ and several values of the surface reflectivity and spin. For simplicity, we focus on a purely plus-polarized ringdown signal, i.e., $A_{\times} = 0$, and each waveform is normalized to the peak of $|\Re[h(t)]|$ in the ringdown (the peak is not shown in the range of the y axis to visualize the GW echoes better).

The time delay between subsequent echoes is constant and depends on the compactness and spin of the object. The time delay is computed as the round-trip time of the perturbation from the photon sphere to the radius of the object. In the spinning case [23, 274]

$$\tau_{\text{echo}} \sim 2M \left[1 + (1 - \chi^2)^{-1/2} \right] |\log \epsilon|. \quad (5.19)$$

The logarithmic dependence on the compactness of the object allows the GW echoes to appear on a short timescale after the ringdown even for Planckian corrections at the horizon scale ($\epsilon \sim l_{\text{Planck}}/M$).

The amplitude of the absolute value of the signal decreases monotonically and it is proportional to the product $\mathcal{R}\mathcal{R}_{\text{BH}}$, i.e., it depends on the combined action of the reflection at the ECO surface and the photon-sphere barrier. Let us notice that the spin of the object and the phase of the surface reflectivity introduce novel effects compared to previous studies [84, 85] such as a nontrivial amplitude modulation of subsequent echoes in each polarization of the GW signal. This is evident, for example, in the panels of Fig. 5.3 corresponding to $\chi = 0.7$, $\mathcal{R} = 1$ and $\chi = 0$, $\mathcal{R} = e^{i\pi/3}$.

5.3.1 Mixing of polarizations

An interesting feature of the GW echoes is that the signal can contain both the plus and cross polarizations even if the initial ringdown is purely plus polarized (i.e., $\mathcal{A}_{\times} = 0$). This feature occurs in the cases of a spinning remnant or a complex surface reflectivity, as shown in Fig. 5.3. This property can be explained as follows. In the non-spinning case, and provided

$$\mathcal{R}_{\chi=0}(\omega) = \mathcal{R}_{\chi=0}^*(-\omega^*), \quad (5.20)$$

the transfer function satisfies the symmetry property

$$\mathcal{K}_{\chi=0}(\omega) = \mathcal{K}_{\chi=0}^*(-\omega^*). \quad (5.21)$$

The time domain echo waveforms are real (imaginary) if the ringdown waveform is real (imaginary). Therefore, in the non-spinning case, the echo signal contains the same polarization of the BH ringdown and the two polarizations do not mix. Remarkably, this property is broken in the following cases:

1. when \mathcal{R} is complex and does not satisfy Eq. (5.20), as shown in the second row of Fig. 5.3;

2. in the spinning case, even when \mathcal{R} is real or satisfies Eq. (5.20), as shown in the second and third columns of Fig. 5.3.

In either cases, a mixing of the polarizations occurs. In particular, in the spinning case and when \mathcal{R} is real, the transfer function satisfies an extended version of Eq. (5.21)

$$\mathcal{K}(\omega, m) = \mathcal{K}^*(-\omega^*, -m), \quad (5.22)$$

that does not prevent the mixing of the polarizations due to the $m \rightarrow -m$ transformation.

As shown in Fig. 5.3, if the BH ringdown is a purely plus-polarized wave, it can acquire a cross-polarization component upon reflection by the photon-sphere barrier (when $\chi \neq 0$) or by the surface (when \mathcal{R} is complex and does not satisfy Eq. (5.20)). The mixing of the polarizations can explain the involved echo pattern shown in some panels of Fig. 5.3. For example, for $\chi = 0$ and $\mathcal{R} = e^{i\pi/3}$ each echo is multiplied by a factor $e^{i\pi/3}$ relative to the previous one. As a consequence, every three echoes the imaginary part of the signal (i.e., the cross polarization) is null.

5.3.2 Phase inversion

The phase of each subsequent echo depends on the term $\mathcal{R}\mathcal{R}_{\text{BH}}$, i.e., on the combined action of the reflection at the surface of the object and the photon-sphere barrier. The phase inversion occurs whenever $\mathcal{R}\mathcal{R}_{\text{BH}} \approx -1$ for low frequencies. In Fig. 5.3, the first, the second, and fourth row all correspond to perfect reflectivity, $|\mathcal{R}| = 1$, however their echo structure is different. This is because a phase term in the surface reflectivity introduces a nontrivial echo pattern.

It is worth mentioning that there exist several definitions of the radial wave function describing the perturbations of a Kerr metric; these are all related to each other by a linear transformation similar to Eq. (4.9). The BH reflection coefficients that are defined for each function differ by a phase, while the quantity $|\mathcal{R}_{\text{BH}}|^2$ (that is related to the energy damping/amplification) is invariant [233].

The transfer function in Eq. (5.7) contains both the absolute value and the phase of \mathcal{R}_{BH} . Therefore, one might wonder whether the ambiguity in the phase could affect the ECO response. For a given model, it should be noted that the surface reflectivity \mathcal{R} is affected by the same phase ambiguity, in accordance with the perturbation variable chosen to describe the problem. Since the transfer function depends on the combination $\mathcal{R}\mathcal{R}_{\text{BH}}$, the phase ambiguity in \mathcal{R} cancels out with that in \mathcal{R}_{BH} . This ensures that the transfer function is invariant under the choice of the radial perturbation function, as expected for any measurable quantity.

For example, at small frequencies the BH reflection coefficient derived from the asymptotics of the Regge-Wheeler function at $x \rightarrow -\infty$ has a phase

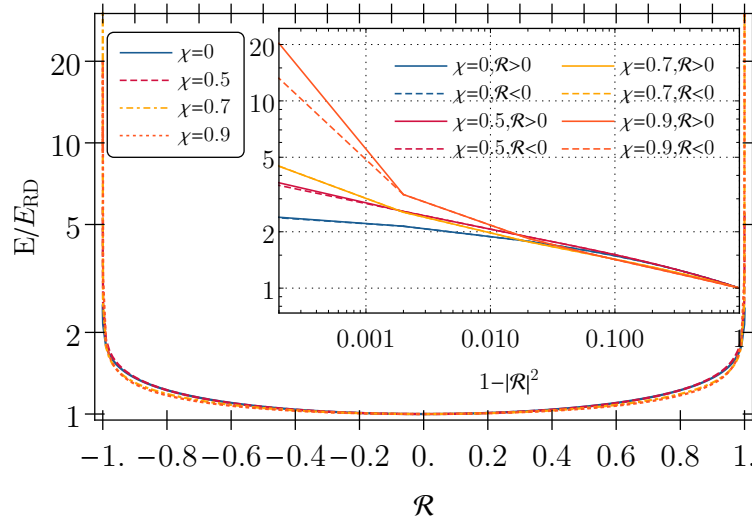


Figure 5.4. Total energy emitted in the ringdown+echo signal normalized by the one of the BH ringdown as a function of the surface reflectivity \mathcal{R} and for several values of the spin χ . The total energy is much larger than the BH ringdown energy in the limit $\mathcal{R} \rightarrow 1$. We set $\delta = 10^{-5}M$ and consider only one ringdown polarization with $\phi_+ = 0$; the result is independent of δ in the $\delta \ll M$ limit. [22]

difference of π compared to the BH reflection coefficient derived from the Detweiler function with $\chi = 0$. Consistently, the surface reflectivity associated to the former differs by a phase π to the latter, i.e., if $\mathcal{R} = 1$ for the Regge-Wheeler function then $\mathcal{R} = -1$ for the Detweiler function in the same model. All the choices of the radial wave functions are equivalent and – in the same ECO model – the surface reflectivity \mathcal{R} should be different for each of them. This fact is particularly important in light of the mixing of the polarizations. As shown in the second row of Fig. 5.3, a phase in \mathcal{R} introduces a mixing of the polarizations for any spin that results in a more involved pattern for the GW echoes.

The phase of the surface reflectivity \mathcal{R} depends on the specific model of horizonless compact object. In the analyses of Sec. 5.5, we parametrize the surface reflectivity in a model-agnostic way as

$$\mathcal{R} = |\mathcal{R}|e^{i\phi}. \quad (5.23)$$

In principle, both the absolute value and the phase are generically frequency-dependent; for simplicity, we choose them to be constants. Hence, we parametrize the template by $|\mathcal{R}|$ and ϕ , different choices of which correspond to different models of horizonless compact objects.

5.3.3 Energy emission and superradiant instability

The energy emitted in the ringdown+echo signal is shown in Fig. 5.4, where the energy

$$E \propto \int_{-\infty}^{\infty} d\omega \omega^2 |\hat{Z}^+|^2 \quad (5.24)$$

is normalized by the one corresponding to the ringdown alone, i.e., $E_{\text{RD}} \equiv E(\mathcal{R} = 0)$, and it is a function of the surface reflectivity \mathcal{R} . We use the prescription of Ref. [275] to compute the ringdown energy, i.e., \hat{Z}_{BH}^+ is the full response in the frequency domain obtained by a Fourier transform of

$$Z_{\text{BH}}^+(t) \sim \mathcal{A}_+ \cos(\omega_R t + \phi_+) e^{-|t|/\tau}, \quad (5.25)$$

where the absolute value of t is at variance with Eq. (5.11). This prescription circumvents the problem associated with the Heaviside function in Eq. (5.11) that produces a spurious high-frequency behavior in the energy flux, leading to an infinite energy in the ringdown signal. With the above prescription, the energy defined in Eq. (5.24) is finite and reduces to the energy of the BH ringdown in Ref. [275] when $\mathcal{R} = 0$.

The energy emitted by a horizonless compact object can be much larger than the BH ringdown, as shown in Fig. 5.4 when $\mathcal{R} \approx 1$. This feature is due to the reflection and the amplification of waves in the cavity between the photon-sphere barrier and the radius of the compact object. The energy contained in the echo part of the signal grows fast as $|\mathcal{R}| \rightarrow 1$ reaching a maximum value that depends on the spin and can be larger than the energy of the BH ringdown. This feature is due to the excitation of the resonances corresponding to the low-frequency QNMs of the compact object. However, it is worth noticing that the low-frequency resonances are excited only at late times, therefore the first few echoes contain a small fraction of the total energy of the signal. Conversely, when \mathcal{R} is significantly smaller than unity, subsequent echoes are suppressed and their total energy is modest compared to the one of the BH ringdown.

Let us notice that when $|\mathcal{R}| \approx 1$ the total energy is expected to diverge due to the ergoregion instability, as discussed in Sec. 4. This feature is not captured by the inverse Fourier transform of $\hat{Z}^+(\omega)$ since the time-domain signal is not integrable when $t \gtrsim \tau_{\text{inst}}$. Since the instability timescale is much longer than the echo delay time, the time interval of validity of the waveform includes a large number of echoes. In particular, the ergoregion instability does not affect the first $N \sim |\log \delta/M|$ echoes [13]. At late times, the signal grows when $|\mathcal{R}\mathcal{R}_{\text{BH}}| > 1$, i.e. when the combined action of the reflection by the surface and the BH barrier yields an amplification factor larger than unity. When $|\mathcal{R}| \approx 1$, this requires $|\mathcal{R}_{\text{BH}}| > 1$ which occurs when the condition for superradiance, $\omega < m\Omega_H$, is satisfied.

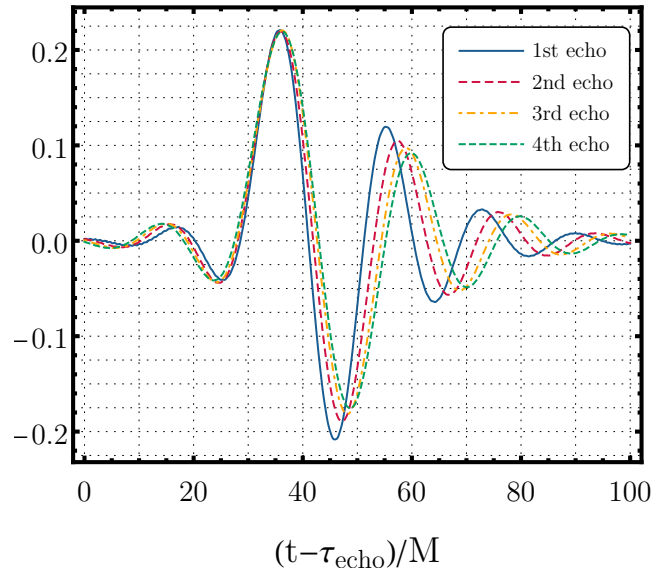


Figure 5.5. The first four echoes in the time-domain waveform for a horizonless compact object with $\chi = 0$, $\mathcal{R} = 1$, $\delta/M = 10^{-7}$. The waveform has been shifted in time and rescaled in amplitude so that the global maxima of each echo are aligned. Note that each subsequent echo has a lower frequency content than the previous one. [22]

5.3.4 Frequency content

The photon-sphere barrier acts as a high-pass filter; therefore, each GW echo has a lower frequency content than the previous one. This expectation is confirmed by Fig. 5.5, where we display the first four echoes that are shifted in time and rescaled in amplitude so that their global maxima are aligned, for a horizonless compact object with $\delta = 10^{-7}M$, $\mathcal{R} = 1$, and $\chi = 0$.

The frequency content of the signal starts roughly at the BH QNM frequency even if the latter is not part of the QNM spectrum of a horizonless compact object. The frequency content of each subsequent echo decreases until the signal is dominated by the low-frequency ECO QNMs at late times. In the example shown in Fig. 5.5, the frequencies of the first four echoes are approximately $M\omega \approx 0.34, 0.32, 0.3, 0.29$, whereas the real part of the fundamental QNM of a Schwarzschild BH is $M\omega_R \approx 0.37367$. Therefore, the frequency content between the first and the fourth echo decreases by $\approx 17\%$.

Let us notice that the case shown in Fig. 5.5 is the one that provides the simplest echo pattern since $\chi = 0$ and \mathcal{R} is real. The spinning case $\chi \neq 0$ or a complex choice of the surface reflectivity would provide a more involved echo pattern and polarization mixing.

Our results show that two different situations can occur:

- A) the reflectivity \mathcal{R} of the object is small enough so that the amplitude of subsequent echoes is suppressed. In this case, most of the SNR is

contained in the first few echoes with a frequency slightly smaller than the fundamental BH QNM.

- B) the reflectivity \mathcal{R} is close to unity so that subsequent echoes are relevant and contribute to the total SNR significantly. In this case, the frequency content becomes much smaller than the fundamental BH QNM at late times.

Clearly, the low-frequency approximation used to derive the analytical template is expected to be accurate in case B) and less accurate in case A).

5.4 Modifications to the prompt ringdown

The prompt ringdown is associated with the scattering of a wave packet off the photon-sphere barrier. If ϵ is sufficiently small, the following causality argument shows that the boundary conditions at the radius of the object cannot affect the prompt ringdown. The decay timescale of the prompt ringdown is associated with the instability timescale of the photon orbits at the light ring, or equivalently to the decay time of the BH fundamental QNM. Thus, the boundary condition at the radius of the compact object does not affect the prompt ringdown if the round-trip time of the radiation from the photon sphere to the boundary is much longer than the decay time of the BH fundamental QNM. In the Schwarzschild case, the round-trip time of the radiation in the cavity is in Eq. (5.1), whereas the decay time of the fundamental QNM is $\tau_{\text{damp}} = -1/\omega_I \approx 10M$. Consequently, when $\epsilon \ll \mathcal{O}(0.01)$ the prompt ringdown is not modified and late-time GW echoes are emitted. On the other hand, if $\epsilon \gtrsim \mathcal{O}(0.01)$ the object's interior should affect the prompt ringdown.

These expectations are confirmed by the ringdown waveforms shown in Fig. 5.6, that are obtained by solving the linearized problem for axial perturbations in the Schwarzschild background. The boundary condition at the radius of the compact object is obtained as the inverse Fourier transform of the boundary condition in Eq. (3.25). The perturbation has an initial Gaussian profile where $\psi(r_*, 0) = 0$ and $\partial_t \psi(r_*, 0) = \exp[-(r_* - 7)^2]$. The integration is performed using a fourth-order Runge-Kutta finite-difference scheme. The top panel of Fig. 5.6 shows the case in which $\epsilon \ll \mathcal{O}(0.01)$. Confirming previous results, the prompt ringdown is universal and the details of the object's interior appear as GW echoes after the initial ringdown. The time delay is given in Eq. (5.1), and their phase and frequency content are modulated by the boundary conditions and the tunneling through the potential barrier. The amplitude of the GW echoes depends on the shear viscosity η of the fictitious fluid located at the radius of the compact object, as described in Sec. 3.3.3. In particular, $\eta \approx 0$ corresponds to $|\mathcal{R}|^2 \approx 1$ for which the amplitudes of the subsequent echoes are only mildly damped, whereas the absorption is maximized as $\eta \approx \eta_{\text{BH}}$. In the latter case, the linear response is identical to that of a BH, since the boundary conditions are the same in the limit $\eta \rightarrow \eta_{\text{BH}}$ and $\epsilon \rightarrow 0$.

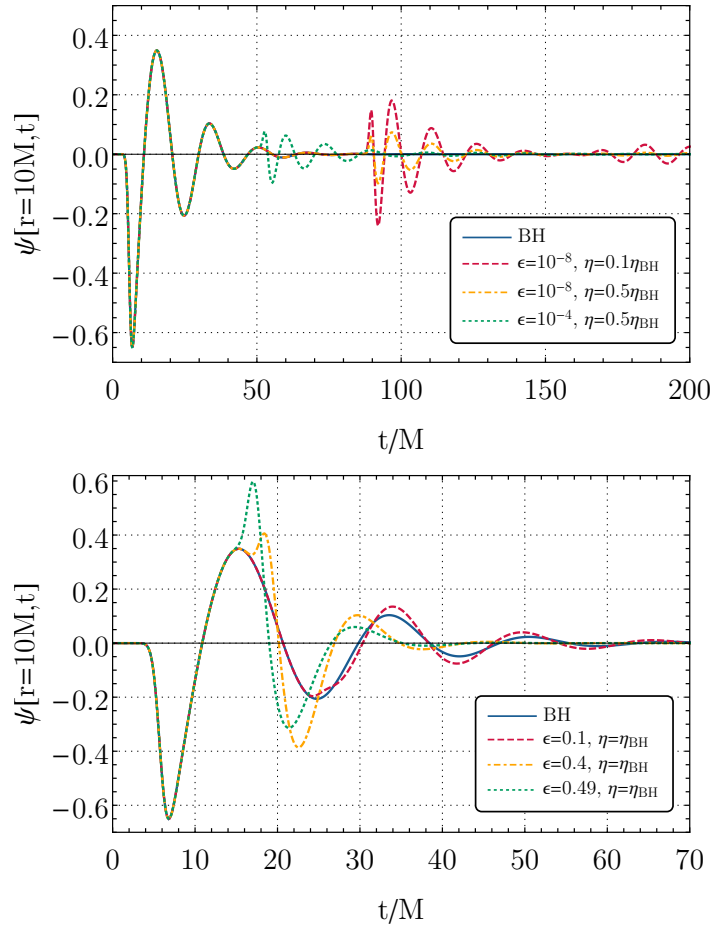


Figure 5.6. Ringdown of a horizonless compact object with radius $r_0 = 2M(1 + \epsilon)$ and effective shear viscosity η . We consider axial perturbations and an initial Gaussian profile. Top panel: when $\epsilon \ll 0.01$, GW echoes appear for several values of η related to the reflectivity of the object. Bottom panel: a selection of ringdown waveforms for $\epsilon \gtrsim 0.01$. In this case, the prompt ringdown is modified and GW echoes are absent. [237]

The bottom panel of Fig. 5.6 focuses on the case $\epsilon \gtrsim \mathcal{O}(0.01)$, where the prompt ringdown is modified and no subsequent echoes appear. The changes to the prompt ringdown can be understood by considering that the part of the wave packet that initially tunnels through the barrier has enough time to be reflected at the radius of the object and tunnel to infinity. This process results in a superposition of the two pulses (the one directly reflected by the potential barrier and the one reflected by the object), which can interfere in an involved pattern. When the two pulses sum in phase, the interference can produce high peaks in the prompt ringdown. At late time, the prompt ringdown is dominated by the fundamental QNM of the object, that is not the mode of the universal prompt ringdown in the BH case. Indeed, by fitting the time-domain waveform at late times with a damped sinusoid, we can verify that the prompt

ringdown is governed by the fundamental QNM of the horizonless object shown in Fig. 3.5.

Finally, one might wonder why there are no echoes for $\epsilon \gtrsim \mathcal{O}(0.01)$. The reason is that only waves with frequency $V(r_0) < \omega^2 < V_{\max}$ can be trapped between the radius of the object and the potential barrier. Therefore, when the compactness decreases, the resulting cavity is small. Furthermore, the transmission coefficient of the potential barrier is large when $\omega^2 \lesssim V_{\max}$ which implies that these frequencies cannot be trapped efficiently. In practice, for $\epsilon \gtrsim \mathcal{O}(0.01)$ one only sees the interference between the prompt ringdown and the first echo, while subsequent reflections are strongly suppressed or absent, as in the bottom panel of Fig. 5.6.

5.5 Prospects of detection with current and future detectors

In this section, we use the template derived in Sec. 5.2 for a preliminary error estimation of the ECO properties with current and future GW detectors.

The ringdown+echo signal in the frequency domain displays resonances that originate from the long-lived QNMs of horizonless compact objects, as shown in the right panel of Fig. 5.2. The relative amplitude of each resonance depends on the source and the dominant modes are not necessarily the fundamental harmonics [84, 217]. Moreover, the amplitude of the echo signal depends strongly on the surface reflectivity of the object, especially when $|\mathcal{R}| \approx 1$. This suggests that the detectability of (or the constraints on) the echoes depends strongly on the surface reflectivity and would be more feasible when $|\mathcal{R}| \approx 1$. In the following, we quantify this expectation using a Fisher matrix analysis that is accurate at large SNR [276]. The analysis is performed as in Ref. [85], additionally including the spin of the object and allowing for a complex reflection coefficient.

We compute the Fisher matrix with the template $\tilde{h}(f) = \tilde{Z}^+(f)$, using the sensitivity curves of aLIGO with the design-sensitivity ZERO_DET_high_P [273] and two configurations for the third-generation instruments: Cosmic Explorer in the narrow band variant [277, 278], and Einstein Telescope in its ET-D configuration [94]. We also consider the noise spectral density of LISA proposed in Ref. [35]. Details on the Fisher information matrix are given in Appendix 3.7. We focus on the most relevant case of $\ell = m = 2$ gravitational perturbations we consider a remnant with $M = 30 M_\odot$ ($M = 10^6 M_\odot$) for ground (space) based detectors.

As discussed in Sec. 5.2.5, the most generic BH ringdown template contains 7 parameters (mass, spin, two amplitudes, two phases, and starting time). For simplicity, we focus on a linearly polarized ringdown, and we do not include the parameters \mathcal{A}_\times and ϕ_\times . This implies that the Fisher analysis has 5 standard ringdown parameters. Furthermore, the template depends on two

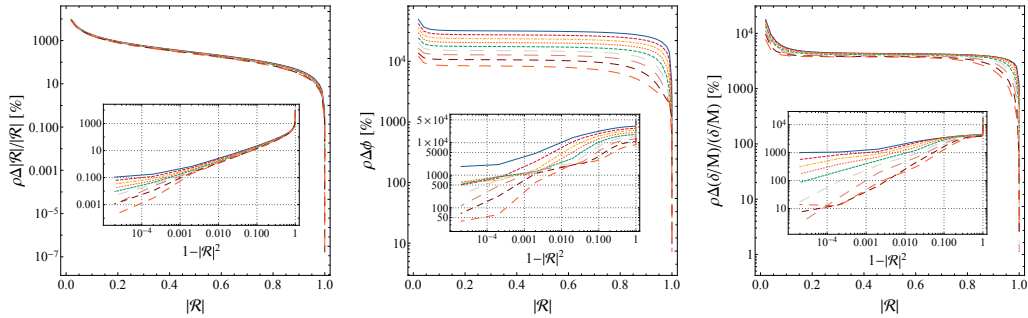


Figure 5.7. Left panel: relative percentage error on the reflection coefficient, $\Delta|\mathcal{R}|/|\mathcal{R}|$ multiplied by the SNR, as a function of $|\mathcal{R}|$ for different values of the spin. The inset shows the same quantity as a function of $1 - |\mathcal{R}|^2$ in a logarithmic scale. From top to bottom: $\chi = (0.9, 0.8, 0.7, 0.6, 0.5, 0.4, 0.3, 0.2, 0.1)$. Middle panel: same as in the left panel but for the absolute percentage error on the phase ϕ of the reflection coefficient, i.e., $\rho\Delta\phi$. Right panel: same as in the left panel but for the compactness parameter δ/M , i.e., $\Delta(\delta/M)/(\delta/M)$. We assume $\delta = 10^{-7}M$, where the errors are independent of δ when $\delta \ll M$. We set $\phi = 0$ (i.e., we consider a real and positive \mathcal{R}), but other choices give similar results. [22]

ECO quantities, i.e., the surface reflectivity and the compactness of the ECO. We parametrize the surface reflectivity as in Eq. (5.23), where $|\mathcal{R}|$ and ϕ are assumed to be frequency independent for simplicity. This yields three ECO dimensionless parameters: δ/M , $|\mathcal{R}|$, and ϕ .

We analyze two cases: (i) a conservative case, in which the errors on the $5 + 3$ parameters are extracted in a Fisher matrix framework, and (ii) a more optimistic case, in which the standard ringdown parameters can be measured independently in the prompt ringdown and we are left with the measurement errors on the 3 ECO parameters.

5.5.1 Conservative case: 5 ringdown+3 ECO parameters

The main results for the statistical errors on the ECO parameters are shown in Fig. 5.7. In the large SNR limit, the errors scale as $1/\rho$, where ρ is defined in Eq. (3.108) in Appendix 3.7. Hence, Fig. 5.7 shows the quantities $\rho\Delta|\mathcal{R}|/|\mathcal{R}|$ (left panel), $\rho\Delta\phi$ (middle panel), and $\rho\Delta(\delta/M)/(\delta/M)$ (right panel) as a function of the surface reflectivity for several values of the spin.

For a given SNR, the relative errors are almost independent of the sensitivity curve of the detector, at least for the signals that are located near the minimum of each sensitivity curve. Moreover, the statistical errors are almost independent of the compactness of the object when $\delta/M \ll 1$. Fig. 5.7 shows that the statistical errors depend strongly on the surface reflectivity of the object. The reason for this can be traced back to the presence of resonances as $\mathcal{R} \approx 1$.

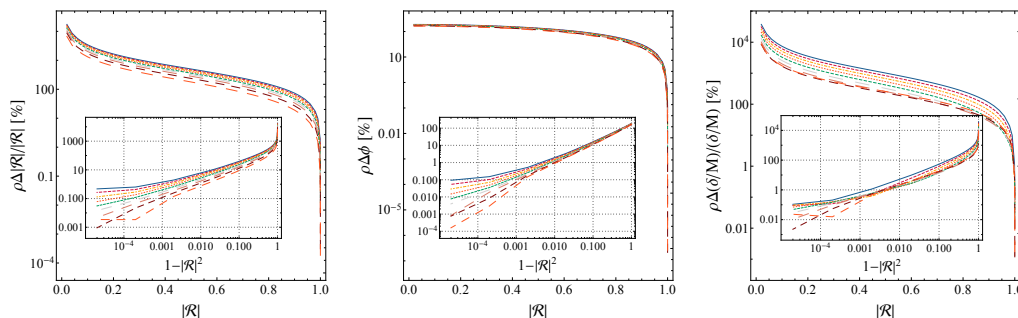


Figure 5.8. Same as in Fig. 5.7 but including only the three ECO parameters ($|\mathcal{R}|$, ϕ , and δ/M) in the Fisher analysis. [22]

This feature confirms that it should be relatively straightforward to rule out or detect models with $|\mathcal{R}| \approx 1$, whereas it is increasingly more difficult to constrain models with smaller values of $|\mathcal{R}|$.

We also notice that the value of the spin of the remnant affects the errors on $|\mathcal{R}|$ mildly, whereas it has a stronger impact on the phase of \mathcal{R} (probably due to the aforementioned mixing of the polarizations) and a moderate impact on the errors on δ/M . Overall, the specific value of ϕ does not affect the errors significantly, although it is important to include it as an independent parameter to not underestimate the errors.

5.5.2 Optimistic case: 3 ECO parameters

Let us now assume that the standard ringdown parameters (mass, spin, amplitude, phase, and starting time) can be measured independently in the prompt ringdown signal, that is identical for BHs and ECOs with $\delta/M \ll 1$. In this case, the remaining three ECO parameters ($|\mathcal{R}|$, ϕ , and δ/M) can be measured a posteriori, assuming that the standard ringdown parameters are known.

A representative example for this optimistic scenario is shown in Fig. 5.8. As expected, the errors are significantly smaller, especially the ones on the phase of the reflectivity. The errors on the surface reflectivity are only mildly affected, and the projected constraints on $|\mathcal{R}|$ at different confidence levels are similar to the ones shown in Fig. 5.9.

5.5.3 Constraints on the reflectivity

Let us calculate the SNR that is necessary to discriminate a partially-absorbing horizonless compact object from a BH on the basis of a measurement of the surface reflectivity at some confidence level. Clearly, if $\Delta|\mathcal{R}|/|\mathcal{R}| > 100\%$, any measurement would be compatible with the BH case ($\mathcal{R} = 0$). On the other hand, relative errors $\Delta|\mathcal{R}|/|\mathcal{R}| < (4.5, 0.27, 0.007, 0.00006)\%$ suggest that it is possible to detect or rule out a given model at $(2, 3, 4, 5)\sigma$ confidence level, respectively. The result of this analysis is shown in Fig. 5.9 that represents the

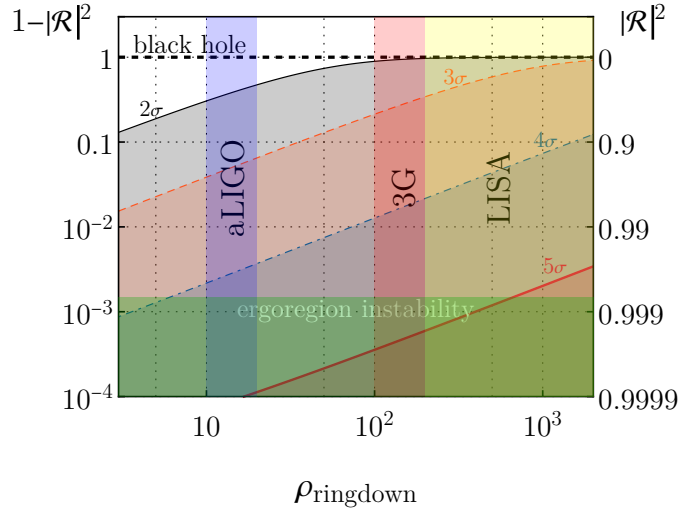


Figure 5.9. Projected exclusion plot for the ECO reflectivity $|\mathcal{R}|$ as a function of the SNR in the ringdown phase. The shaded areas are the regions that can be excluded at a given confidence level (2σ , 3σ , 4σ , 5σ). Vertical bands are the typical SNRs achievable by aLIGO/Virgo, third-generation ground-based detectors, and LISA in the ringdown phase; the horizontal band is the region excluded by the ergoregion instability [30, 31]. We assume $\chi = 0.7$ for the spin of the remnant, and the result depends mildly on the spin. [22]

exclusion plot for the parameter $|\mathcal{R}|$ as a function of the SNR in the ringdown phase, ρ_{ringdown} . The shaded areas are the regions that can be excluded at some given confidence level. Large SNRs would allow us to probe values of the surface reflectivity close to the BH limit, $\mathcal{R} \approx 0$.

The extent of the constraints depends strongly on the confidence level. For example, $\rho_{\text{ringdown}} \approx 100$ would allow us to distinguish horizonless compact objects with $|\mathcal{R}|^2 \gtrsim 0.1$ from BHs at 2σ confidence level, but a 3σ detection would be possible if $|\mathcal{R}|^2 \gtrsim 0.8$.

Our analysis suggests that horizonless models with $|\mathcal{R}|^2 \approx 1$ can be detected or ruled out with aLIGO/Virgo (for events with $\rho_{\text{ringdown}} \gtrsim 8$) at 5σ confidence level. These events could also allow us to probe values of the reflectivity as small as $|\mathcal{R}|^2 \approx 0.8$ at 2σ confidence level. Horizonless compact objects with $|\mathcal{R}|^2 = 1$ are already ruled out by the ergoregion instability [30, 31], the absence of a GW stochastic background in the LIGO O1 run due to spin loss [260], and the negative searches for GW echoes [10].

Excluding or detecting echoes for models with smaller values of the reflectivity (for which the ergoregion instability is absent) requires SNRs in the postmerger phase of $\mathcal{O}(100)$. This will be achievable only with third-generation detectors (Einstein Telescope and Cosmic Explorer) and with the space-based mission LISA. Our preliminary analysis confirms that very stringent constraints on (or detection of) ultracompact horizonless objects can be obtained with

current (and especially future) interferometers.

5.6 Appendix: Black hole response for particular sources

In this appendix, we provide the expressions for the BH response at the horizon for some specific toy models of the source. In the following, we assume that the source is localized within the cavity.

The simplest case is that of a Gaussian source localized in space in which the frequency dependence can be factored out

$$\tilde{S}(r_*, \omega) = C(\omega) \exp\left(-\frac{(r_* - r_*^s)^2}{\sigma^2}\right), \quad (5.26)$$

where r_*^s is the location of the source in the tortoise coordinate, and $|r_*^s| \ll M$. It is easy to show that

$$\tilde{Z}_{\text{BH}}^+ = e^{2ikr_*^s} \tilde{Z}_{\text{BH}}^+. \quad (5.27)$$

The latter equation, together with Eq. (5.15), yields

$$\tilde{Z}_{\text{BH}}^- = \left(\frac{e^{2ikr_*^s} + \mathcal{R}_{\text{BH}}}{\mathcal{T}_{\text{BH}}}\right) \tilde{Z}_{\text{BH}}^+. \quad (5.28)$$

Remarkably, the above relation is independent of the width σ of the Gaussian source and the function $C(\omega)$ characterizing the source.

Inspired by Eq. (5.27), we can also parametrize the BH response \tilde{Z}_{BH}^+ in a model-agnostic way with a generically complex proportionality factor

$$\tilde{Z}_{\text{BH}}^+ = \eta e^{i\nu} \tilde{Z}_{\text{BH}}^+, \quad (5.29)$$

where η and ν are (real) parameters of the template. Since the BH response at intermediate times is dominated by the QNM frequencies, a model in which $\tilde{Z}_{\text{BH}}^+ = \mathcal{F}(\omega) \tilde{Z}_{\text{BH}}^+$ can be reduced effectively to $\tilde{Z}_{\text{BH}}^+ = \mathcal{F}(\omega_R) \tilde{Z}_{\text{BH}}^+$. In such case, the term $\mathcal{F}(\omega_R) = \eta e^{i\nu}$ can be interpreted as a generic parametrization of a complex number.

Finally, another possible model for the source is a plane-wave source that travels towards $r_* \rightarrow \pm\infty$, where

$$\tilde{S}(r_*, \omega) = \int dt e^{i\omega t} S(r_*, t) = \int dt e^{i\omega t} S(0, t \mp r_*) = \tilde{S}(0, \omega) e^{\pm i\omega r_*}. \quad (5.30)$$

Using Eq. (5.6), we obtain

$$\tilde{Z}_{\text{BH}}^+(\omega) = \tilde{Z}_{\text{BH}}^-(\omega) \frac{\int_{-\infty}^{+\infty} dr_* X_s^- e^{\pm i\omega r_*}}{\int_{-\infty}^{+\infty} dr_* X_s^+ e^{\pm i\omega r_*}}, \quad (5.31)$$

or, more explicitly,

$$\begin{aligned}
\tilde{Z}_{\text{BH}}^+(\omega) &= \tilde{Z}_{\text{BH}}^-(\omega) \left[\int_{r_* \sim 0} dr_* X_s^- e^{i\omega r_*} + \int^\infty (A_{\text{out}} e^{2i\omega r_*} + A_{\text{in}}) dr_* \right. \\
&\quad + \left. \int_{-\infty} dr_* e^{im\Omega r_*} \right] / \left[\int_{r_* \sim 0} dr_* X_s^+ e^{i\omega r_*} + \int^\infty e^{2i\omega r_*} dr_* \right. \\
&\quad + \left. \int_{-\infty} (B_{\text{out}} e^{2i\omega r_* - im\Omega r_*} + B_{\text{in}} e^{im\Omega r_*}) dr_* \right], \tag{5.32}
\end{aligned}$$

where $r_* \sim 0$ is the region where the potential is non-zero and we considered the case of a plane wave traveling to $r_* \rightarrow +\infty$ for ease of notation. Since $\tilde{Z}_{\text{BH}}^+(\omega)$ has poles at $\omega_{\text{QNM}} = \omega_R + i\omega_I$, we also expect $\tilde{Z}_{\text{BH}}^-(\omega)$ to have the same poles. Given that $\omega_I < 0$, the terms $\int^{+\infty} dr_*$ dominate the numerator and the denominator of Eq. (5.32) for $\omega \approx \omega_{\text{QNM}}$ and yield

$$\tilde{Z}_{\text{BH}}^+ \approx - \left(\frac{\mathcal{R}_{\text{BH}}}{\mathcal{T}_{\text{BH}}} \right)^* \tilde{Z}_{\text{BH}}^-. \tag{5.33}$$

The case of a plane wave traveling towards $r_* \rightarrow -\infty$ gives the same relation.

Chapter 6

Extreme mass-ratio inspirals around a horizonless source

Com'era il nostro gioco? È presto detto. Lo spazio essendo curvo, attorno alla sua curva facevamo correre gli atomi, come delle biglie, e chi mandava più avanti il suo atomo vinceva. Nel dare il colpo all'atomo bisognava calcolare bene gli effetti, le traiettorie, saper sfruttare i campi magnetici e i campi di gravitazione, se no la pallina finiva fuori pista ed era eliminata dalla gara.

Italo Calvino, *Le Cosmicomiche*

EMRIs are binary systems in which a stellar-mass compact object orbits around a supermassive compact object at the center of a galaxy. EMRIs are one of the main target sources of the space-based interferometer LISA, and are unique probes of the nature of supermassive compact objects. The defining feature of a classical BH is to be a perfect absorber since its event horizon is a one-way hypersurface. Thus, any evidence of partial reflectivity would indicate a departure from the classical BH picture. In this chapter, we shall show that LISA would be able to probe the reflectivity of compact objects with unprecedented accuracy.

6.1 A model for the central compact object

We analyze a central horizonless compact object whose exterior spacetime is described by the Kerr metric, as detailed in Sec. 4.1. The radius of the compact object is located as in Eq. (2.1) where $\epsilon \ll 1$. For example, if the radius of the object is at $r_0 = r_+ + l_{\text{Planck}}$, then $\epsilon \sim 10^{-44}$ for a supermassive compact object with mass $M = 10^6 M_\odot$ and spin $\chi = 0.9$.

The properties of the interior structure are modeled in terms of a complex and frequency-dependent reflectivity coefficient $\mathcal{R}(\omega)$ at the surface of the object. Spinning horizonless compact objects with a perfectly reflecting surface ($|\mathcal{R}|^2 = 1$) are affected by an ergoregion instability when spinning sufficiently fast. In the following, we focus on stable spinning models with partial absorption ($|\mathcal{R}|^2 < 1$), as detailed in Sec. 4.5. We also analyze a model of quantum BH with Boltzmann reflectivity ($|\mathcal{R}(\omega)|^2 = e^{-|k|/T_{\text{H}}}$, where k is the corotating frequency and T_{H} is the Hawking temperature), that is stable against the ergoregion instability for any spin [264].

6.2 Linear perturbations from a point particle

We analyze a pointlike source orbiting around a central compact object which is either a Kerr BH or a Kerr-like horizonless object. The pointlike source moves along circular equatorial orbits from large distances to the ISCO. In line with the discussion in Sec. 4.1, we assume that the gravitational perturbations in the exterior spacetime are described as in the Kerr case. According to the Newman-Penrose formalism, the Weyl scalar Ψ_4 can be expanded as

$$\Psi_4 = \hat{\rho}^4 \sum_{\ell m} \int d\omega R_{\ell m \omega}(r) {}_{-2}S_{\ell m \omega}(\theta) e^{i(m\varphi - \omega t)}, \quad (6.1)$$

where $\hat{\rho} = (r - ia \cos \theta)^{-1}$, and the sum runs over $\ell \geq 2$ and $-\ell \leq m \leq \ell$. The radial wave function $R_{\ell m \omega}(r)$ obeys to the Teukolsky master equation [279, 52, 54]

$$\Delta^2 \frac{d}{dr} \left(\frac{1}{\Delta} \frac{dR_{\ell m \omega}}{dr} \right) + \left[\frac{K^2 + 4i(r - M)K}{\Delta} - 8i\omega r - \lambda \right] R_{\ell m \omega} = \mathcal{T}_{\ell m \omega}, \quad (6.2)$$

and the spin-weighted spheroidal harmonics ${}_{-2}S_{\ell m \omega}(\theta) e^{im\varphi}$ satisfy Eq. (4.8) with $s = -2$. The polar part of the spin-weighted spheroidal harmonics is normalized such that

$$\int_{-1}^1 |{}_{-2}S_{\ell m \omega}(\cos \theta)|^2 d \cos \theta = 1. \quad (6.3)$$

The source term $\mathcal{T}_{\ell m \omega}$ is constructed by projecting the stress-energy tensor $T^{\alpha\beta}$ of a pointlike source with respect to the Newman-Penrose tetrad, where [280]

$$T^{\alpha\beta} = \mu \frac{u^\alpha u^\beta}{\Sigma \sin \theta u^t} \delta(r - r(t)) \delta(\theta - \theta(t)) \delta(\varphi - \varphi(t)), \quad (6.4)$$

with μ being the mass of the small orbiting body, $u^\alpha = dz^\alpha/d\tau$, $z^\alpha = (t, r(t), \theta(t), \varphi(t))$ is the geodesic trajectory, and τ is the particle proper time. The mass ratio of the system is defined as $q \equiv \mu/M$.

In the case of circular equatorial orbits, $\theta(t) = \pi/2$. In corotating orbits, the orbital radius is related to the orbital angular frequency by

$$\Omega = \sqrt{M}/(a\sqrt{M} + r^{3/2}). \quad (6.5)$$

6.2.1 Central black hole

Let us first review the standard BH case. Owing to the presence of the horizon, the two independent homogeneous solutions of Eq. (6.2) have the following asymptotic behavior

$$R_{\ell m \omega}^{\text{in}} \sim \begin{cases} B_{\ell m \omega}^{\text{trans}} \Delta^2 e^{-ikr_*} & \text{as } r_* \rightarrow -\infty \\ r^3 B_{\ell m \omega}^{\text{ref}} e^{i\omega r_*} + r^{-1} B_{\ell m \omega}^{\text{inc}} e^{-i\omega r_*} & \text{as } r_* \rightarrow +\infty \end{cases}, \quad (6.6)$$

$$R_{\ell m \omega}^{\text{up}} \sim \begin{cases} C_{\ell m \omega}^{\text{up}} e^{ikr_*} + \Delta^2 C_{\ell m \omega}^{\text{ref}} e^{-ikr_*} & \text{as } r_* \rightarrow -\infty \\ r^3 C_{\ell m \omega}^{\text{trans}} e^{i\omega r_*} & \text{as } r_* \rightarrow +\infty \end{cases}, \quad (6.7)$$

where $k = \omega - m\Omega_H$, and $\Omega_H = a/(2Mr_+)$ is the angular velocity at the horizon of the Kerr BH. The inhomogeneous solution of the Teukolsky equation (6.2) is constructed as [280]

$$R_{\ell m \omega} = \frac{1}{W_{\ell m \omega}} \left\{ R_{\ell m \omega}^{\text{up}}(r) \int_{r_+}^r dr' \frac{\mathcal{T}_{\ell m \omega}(r') R_{\ell m \omega}^{\text{in}}(r')}{\Delta^2(r')} + R_{\ell m \omega}^{\text{in}}(r) \int_r^{\infty} dr' \frac{\mathcal{T}_{\ell m \omega}(r') R_{\ell m \omega}^{\text{up}}(r')}{\Delta^2(r')} \right\}, \quad (6.8)$$

where $W_{\ell m \omega}$ is the Wronskian given by

$$\begin{aligned} W_{\ell m \omega} &= \Delta^{-1} \left(R_{\ell m \omega}^{\text{in}} \frac{dR_{\ell m \omega}^{\text{up}}}{dr} - R_{\ell m \omega}^{\text{up}} \frac{dR_{\ell m \omega}^{\text{in}}}{dr} \right) \\ &= 2i\omega C_{\ell m \omega}^{\text{trans}} B_{\ell m \omega}^{\text{inc}}. \end{aligned} \quad (6.9)$$

The inhomogeneous solution in Eq. (6.8) has the following asymptotic behavior

$$R_{\ell m \omega} \sim \begin{cases} Z_{\ell m \omega}^H \Delta^2 e^{-ikr_*} & \text{as } r_* \rightarrow -\infty \\ Z_{\ell m \omega}^{\infty} r^3 e^{i\omega r_*} & \text{as } r_* \rightarrow +\infty \end{cases}, \quad (6.10)$$

where

$$Z_{\ell m \omega}^H = C_{\ell m \omega}^H \int_{r_+}^{\infty} dr' \frac{\mathcal{T}_{\ell m \omega}(r') R_{\ell m \omega}^{\text{up}}(r')}{\Delta^2(r')}, \quad (6.11)$$

$$Z_{\ell m \omega}^{\infty} = C_{\ell m \omega}^{\infty} \int_{r_+}^{\infty} dr' \frac{\mathcal{T}_{\ell m \omega}(r') R_{\ell m \omega}^{\text{in}}(r')}{\Delta^2(r')}, \quad (6.12)$$

and

$$C_{\ell m \omega}^H = \frac{B_{\ell m \omega}^{\text{trans}}}{2i\omega C_{\ell m \omega}^{\text{trans}} B_{\ell m \omega}^{\text{inc}}}, \quad C_{\ell m \omega}^{\infty} = \frac{1}{2i\omega B_{\ell m \omega}^{\text{inc}}}. \quad (6.13)$$

The amplitudes $Z_{\ell m \omega}^H$ and $Z_{\ell m \omega}^{\infty}$ determine the gravitational energy fluxes emitted at infinity and through the horizon [54, 194]:

$$\dot{E}^{\infty} = \sum_{\ell m} \frac{|Z_{\ell m \omega}^{\infty}|^2}{4\pi(m\Omega)^2}, \quad (6.14)$$

$$\dot{E}^H = \sum_{\ell m} \frac{\alpha_{\ell m} |Z_{\ell m \omega}^H|^2}{4\pi(m\Omega)^2}, \quad (6.15)$$

where

$$\alpha_{\ell m} = \frac{256(2Mr_+)^5 k(k^2 + 4\varpi^2)(k^2 + 16\varpi^2)(m\Omega)^3}{|c_{\ell m}|^2}, \quad (6.16)$$

where $\varpi = \sqrt{M^2 - a^2}/(4Mr_+)$ and

$$\begin{aligned} |c_{\ell m}|^2 &= [(\lambda + 2)^2 + 4ma(m\Omega) - 4a^2(m\Omega)^2] \\ &\times [\lambda^2 + 36ma(m\Omega) - 36a^2(m\Omega)^2] \\ &+ (2\lambda + 3)[96a^2(m\Omega)^2 - 48ma(m\Omega)] \\ &+ 144(m\Omega)^2(M^2 - a^2). \end{aligned} \quad (6.17)$$

For circular equatorial orbits, the angular momentum fluxes are related to the energy fluxes, at infinity and the horizon, by $J^{\infty, H} = \dot{E}^{\infty, H}/\Omega$.

In the case of a central BH, the total energy flux emitted by a point particle in a circular equatorial orbit with orbital angular frequency Ω is

$$\dot{E}(\Omega) = \dot{E}^{\infty}(\Omega) + \dot{E}^H(\Omega), \quad (6.18)$$

where $\dot{E}^{\infty}(\Omega)$ and $\dot{E}^H(\Omega)$ are defined in Eqs. (6.14) and (6.15), respectively.

6.2.2 Central horizonless compact object

Let us analyze the case of a horizonless compact object whose corrections to the Kerr case are incorporated in the boundary condition at the radius of the object. A gravitational perturbation can be written as a superposition of ingoing and outgoing waves at the radius of the object as in Eq. (4.21), where the surface reflectivity of the object is defined in Eq. (4.22). For a generically complex and frequency-dependent reflectivity, a horizonless compact object is described by the boundary condition in Eq. (4.25) that reduces to the BH boundary condition when $\mathcal{R} = 0$.

In the horizonless case, the solutions of the homogeneous Teukolsky equation are such that the ‘up’ modes have the same asymptotics as in Eq. (6.7), whereas the ‘in’ modes have the following asymptotics

$$R_{\ell m \omega}^{\text{in}} \sim \begin{cases} B_{\ell m \omega}^{\text{trans}} \Delta^2 e^{-ikr_*} + C_{\ell m \omega}^{\text{up}} e^{ikr_*} & \text{as } r_* \rightarrow r_*^0 \\ r^3 B_{\ell m \omega}^{\text{ref}} e^{i\omega r_*} + r^{-1} B_{\ell m \omega}^{\text{inc}} e^{-i\omega r_*} & \text{as } r_* \rightarrow +\infty \end{cases}, \quad (6.19)$$

where

$$B_{\ell m \omega}^{\text{trans}} = B_{\ell m \omega}^{\text{trans}} + c_1 C_{\ell m \omega}^{\text{ref}}, \quad (6.20)$$

$$C_{\ell m \omega}^{\text{up}} = c_1 C_{\ell m \omega}^{\text{up}}, \quad (6.21)$$

$$B_{\ell m \omega}^{\text{ref}} = B_{\ell m \omega}^{\text{ref}} + c_1 C_{\ell m \omega}^{\text{trans}}, \quad (6.22)$$

$$B_{\ell m \omega}^{\text{inc}} = B_{\ell m \omega}^{\text{inc}}, \quad (6.23)$$

and the coefficient c_1 is determined by imposing the boundary condition in Eq. (4.25) where

$$R_{\ell m \omega} = R_{\ell m \omega}^{\text{in}} + c_1 R_{\ell m \omega}^{\text{up}}. \quad (6.24)$$

The inhomogeneous solution of the Teukolsky function is derived as in Eq. (6.8), with $R_{\ell m \omega}^{\text{in}}$ as in Eq. (6.19) and $R_{\ell m \omega}^{\text{up}}$ as in Eq. (6.7), and it has the following asymptotic behavior

$$R_{\ell m \omega} \sim \begin{cases} Z_{\ell m \omega}^{H^+} \Delta^2 e^{-ikr_*} + Z_{\ell m \omega}^{H^-} e^{ikr_*} & \text{as } r_* \rightarrow r_*^0 \\ Z_{\ell m \omega}^{\infty} r^3 e^{i\omega r_*} & \text{as } r_* \rightarrow +\infty \end{cases}, \quad (6.25)$$

where

$$Z_{\ell m \omega}^{H^+} = Z_{\ell m \omega}^H, \quad Z_{\ell m \omega}^{H^-} = \frac{C_{\ell m \omega}^{\text{up}}}{B_{\ell m \omega}^{\text{trans}}} Z_{\ell m \omega}^H. \quad (6.26)$$

To determine the energy emitted by the particle in the horizonless case, we note that – by assumption – the gravitational perturbations in the neighbourhood of the particle are exactly those of a Kerr background, albeit with unusual boundary conditions. We can, therefore, determine the emitted energy by appealing to the energy balance law in the Kerr background. The energy flux to infinity is formally given by the same formula as in the BH case, Eq. (6.14). The energy flux to the ECO side is determined by extending $R_{\ell m \omega}$ analytically to the horizon of the Kerr background and measuring the flux there. Thus, the internal energy flux on the ECO side \dot{E}^{int} is given by

$$\dot{E}^{\text{int}} = \dot{E}^{H^+} - \dot{E}^{H^-}, \quad (6.27)$$

where \dot{E}^{H^+} and \dot{E}^{H^-} are the energy fluxes across the future and past horizon, respectively. The energy flux across the future horizon is given in Eq. (6.15) as in the BH case, whereas the energy flux coming in across the past horizon is [54]

$$\dot{E}^{H^-} = \sum_{\ell m} \frac{\omega}{4\pi k (2Mr_+)^3 (k^2 + 4\varpi^2)} |Z_{\ell m \omega}^{H^-}|^2. \quad (6.28)$$

In the case of $\mathcal{R} = 0$, Eq. (6.27) reduces to $\dot{E}^{\text{int}} = \dot{E}^{H^+}$. When $|\mathcal{R}(\omega)|^2 = 1$, the outgoing flux is equal to the ingoing flux at the radius of the object and $\dot{E}^{\text{int}} = 0$, as expected from perfectly reflecting boundary conditions.

In the ECO case, the total energy flux emitted by a point particle in a circular equatorial orbit is

$$\dot{E}(\Omega) = \dot{E}^{\infty}(\Omega) + \dot{E}^{\text{int}}(\Omega), \quad (6.29)$$

where $\dot{E}^{\infty}(\Omega)$ and $\dot{E}^{\text{int}}(\Omega)$ are defined in Eqs. (6.14) and (6.27), respectively.

6.3 Numerical procedure

We study the dynamics of a point particle in circular equatorial orbits around a Kerr-like horizonless object by adapting the frequency-domain Teukolsky code

originally developed in Refs. [281, 282, 283, 284]. In particular, the solutions to the homogeneous Teukolsky equation are calculated via the numerical Mano-Suzuki-Takasugi method [285, 286, 280, 287]. We have modified the boundary conditions at the radius of the compact object in terms of $\mathcal{R}(\omega)$ and ϵ as discussed in Sec. 6.2.2, and computed the energy and angular-momentum fluxes at infinity and through the object's surface.

Our algorithm is as follows:

1. Choose the intrinsic parameters of the binary, namely the central mass M , the mass ratio $q \ll 1$, the primary spin χ , the reflectivity $\mathcal{R}(\omega)$, and the compactness of the central object via ϵ .
2. For a given $\ell = m$ mode, produce the data for a bound orbit with orbital radius r and compute the energy fluxes in the cases of a central BH and a central horizonless compact object, respectively.
3. Loop on the orbital radii with an equally spaced (radial) grid starting from the ISCO radius to $r = 10M$.
4. Find the local maxima and minima in the energy fluxes at infinity for a central horizonless compact object. If present, these extrema bracket resonances in the flux that should be resolved by increasing the grid resolution. Let us notice that the initial equally-spaced grid in the orbital radii needs to be dense enough to find local maxima and minima in the energy fluxes. For this reason, we set the initial discretization in the orbital radii to be $0.003M$.
5. Refine the grid on the orbital radii around the local maxima and minima through the bisection method until a target accuracy is reached. The refinement of the grid stops either when the difference between two subsequent orbital radii is $< 10^{-5}M$ or when the difference in the energy fluxes of two subsequent points is $< 10^{-5}q^2$.
6. For a given ℓ and each $m = \ell - 1, \dots, 1$ loop on the orbital radii with an equally spaced grid from the ISCO radius. The loop on the orbital radii stops when the total energy flux in the case of a central BH (defined in Eq. (6.18)) in a given ℓ, m mode is 10^{-6} times smaller than the total energy flux in the dominant mode with $\ell = m$.
7. For a given ℓ and each $m = \ell - 1, \dots, 1$ repeat steps 4 and 5.
8. For the harmonic index $\ell = 2, \dots, \ell_{\max} = 12$ repeat the steps 2 to 7.
9. For each ℓ, m mode, interpolate the total energy flux as a function of the orbital angular frequency.
10. Sum over the modes and perform an integration to compute the orbital phase both in the BH and in the horizonless cases. The initial condition

on the orbital angular frequency is $\Omega_0 = \Omega(r = 10M)$ and the integration stops at the inspiral-plunge transition frequency $\Omega(t_{\max}) = \Omega(r = r_{\text{ISCO}} + 4q^{2/3})$ [288].

We compute the gravitational waveform where for the modes with negative m we make use of the following symmetries

$$Z_{\ell-m\omega}^{\infty} = (-1)^{\ell} (Z_{\ell m\omega}^{\infty})^*, \quad (6.30)$$

$${}_{-2}S_{\ell-m\omega}(\theta) = (-1)^{\ell} {}_{-2}S_{\ell m\omega}(\pi - \theta). \quad (6.31)$$

For each ℓ, m mode the asymptotic amplitudes at infinity and the spin-weighted spheroidal harmonics are interpolated functions of the time-dependent orbital angular frequency. The waveform is constructed by summing over the modes with $\ell \leq 4$ and $-\ell \leq m \leq \ell$. In the case of small reflectivity ($|\mathcal{R}|^2 \leq 10^{-6}$) the waveform is constructed by summing over the ℓ, m modes until $\ell = 5$ since one needs higher accuracy to keep the truncation errors smaller than the ECO corrections. We checked that the mismatch between the BH and ECO waveforms does not change quantitatively by including modes with higher ℓ in the waveforms.

We tested our code by reproducing the standard results for the Kerr BH case [195, 289, 290, 291]. Furthermore, we reproduced the results of Ref. [39], where the horizonless case is obtained from the BH case by artificially imposing that only a fraction $(1 - |\mathcal{R}|^2)$ of the radiation is absorbed at the surface.

The fractional truncation error of the code in the dephasing is estimated as $\Delta^{\text{tr}} = 1 - \Delta\phi_{\ell_{\max}+1}(t_f)/\Delta\phi_{\ell_{\max}}(t_f)$, where the energy fluxes are truncated at $\ell_{\max} = 12$ and t_f is the time in which the orbital radius reaches $r = r_{\text{ISCO}} + 4q^{2/3}$. For a reference compact object with $\chi = 0.9$, $|\mathcal{R}|^2 = 0.9$, $\epsilon = 10^{-10}$, and $q = 3 \times 10^{-5}$, we find $\Delta^{\text{tr}} = 2 \times 10^{-5}$.

6.4 Energy fluxes and excitation of resonances

Horizonless compact objects contain low-frequency modes in their spectrum that are associated with long-lived states confined within the photon sphere, as described in Sec. 3.2.4. At variance with the BH case, these low-frequency modes can be excited during the inspiral when the orbital frequency matches the QNM frequencies, leading to resonances in the fluxes [292, 211, 293]. The role of the resonances in the EMRI dynamics was studied in Ref. [37] for a perfectly reflecting and non-spinning horizonless object in the low-frequency approximation. The analysis of Ref. [37] assessed that the impact of such excitations is negligible since the resonances are very narrow and are crossed quickly during the inspiral. In the following, we shall extend the analysis of Ref. [37] to the case of a partially absorbing compact object with generic spin. As we shall show, differently from the analysis in Ref. [37], in more generic cases the presence of resonances provides an important contribution to the EMRI dynamics.

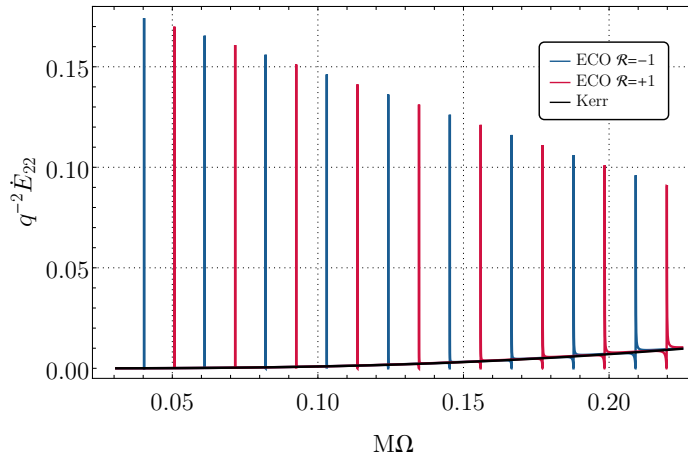


Figure 6.1. Total energy flux of the $\ell = m = 2$ mode as a function of the orbital angular frequency for a point particle in quasicircular equatorial orbits from $r = 10M$ (low frequency) to $r = r_{\text{ISCO}}$ (high frequency). The energy flux emitted in the case of a central BH with spin $\chi = 0.9$ is compared to the case of a central horizonless compact object with a perfectly reflecting surface ($|\mathcal{R}|^2 = 1$), spin $\chi = 0.9$, and $\epsilon = 10^{-10}$. In the latter case, the energy flux is resonantly excited when the orbital frequency matches the low-frequency QNMs of the ECO [38].

Another relevant feature of horizonless compact objects is the presence of partial reflectivity at the surface. In Ref. [39] a phenomenological approach was adopted to parametrize the energy flux emitted by a point particle around a horizonless and partially absorbing compact object. In particular, the energy flux at infinity is modeled as the one in the BH case, whereas the energy flux on the ECO side is modeled by removing a ($|\mathcal{R}|^2$) fraction of TH from the BH energy flux through the horizon, i.e., [39]

$$\dot{E}(\Omega) = E_{\text{BH}}^{\infty}(\Omega) + (1 - |\mathcal{R}|^2) E_{\text{BH}}^H(\Omega). \quad (6.32)$$

The TH is associated with the energy and angular-momentum absorption by the compact object and results in an increase of the mass and angular momentum of the latter, unless superradiance occurs [29]. Let us notice that Eq. (6.32) does not include the excitation of the low-frequency resonances in the energy fluxes both at infinity and on the ECO side. Moreover, Eq. (6.32) does not fix a specific location of the radius of the compact object. According to the analysis in Ref. [39], EMRIs could provide constraints on the reflectivity of compact objects at the level of $|\mathcal{R}|^2 \lesssim 10^{-4}$. We shall show that, by taking a consistent model of horizonless compact object, the bounds derived by Ref. [39] can be further improved by several orders of magnitude.

Let us analyze the energy flux emitted by a point particle in quasicircular equatorial orbits around a spinning horizonless compact object, as detailed

in Sec. 6.2.2. The energy flux is computed as in Eq. (6.29) that takes into account both the excitation of the low-frequency resonances and the reflective properties of the compact object. As a representative example, Fig. 6.1 shows the $\ell = m = 2$ component of the energy flux as a function of the orbital frequency for a horizonless compact object with $\epsilon = 10^{-10}$, $\chi = 0.9$, and two choices of perfectly reflecting boundary conditions (Dirichlet and Neumann for the lower and upper case, respectively, $\mathcal{R} = \pm 1$). As expected, the flux is resonantly excited when the orbital frequency matches the low-frequency QNMs of the central object, i.e.,

$$\Omega = \frac{\omega_R}{m}, \quad (6.33)$$

where ω_R is the real part of the QNM and m is the azimuthal number of the perturbation. This is a striking difference with respect to the BH case in which the QNMs have higher frequencies and cannot be resonantly excited by quasicircular inspirals. In the small- ϵ limit, the Dirichlet and Neumann modes are described by Eqs. (4.33) and (4.34) with $s = -2$. As shown in Fig. 6.1, for a compact object with a given spin and compactness, the modes are equispaced by

$$\Delta\omega_R = \frac{\pi}{|r_*^0|} \sim |\log \epsilon|^{-1}, \quad (6.34)$$

whereas consecutive Dirichlet and Neumann mode frequencies are separated by half this width. The difference between consecutive resonances scales as $|\log \epsilon|^{-1}$. It follows that the resonances are denser in the $\epsilon \rightarrow 0$ limit.

Interestingly, the resonances appear at the same frequencies in all the individual fluxes: \dot{E}^∞ , \dot{E}^{H^+} , and \dot{E}^{H^-} . This is because the QNMs are associated with the poles of the Wronskian appearing in the solutions of the Teukolsky equation (as in Eq. (6.8)). However, when $|\mathcal{R}|^2 = 1$, the fluxes \dot{E}^{H^+} and \dot{E}^{H^-} are exactly equal to each other since $\dot{E}^{\text{int}} = 0$. Consequently, for perfectly reflecting compact objects the resonances appear only in the energy flux at infinity.

Equation (4.34) shows that $\omega_I \ll \omega_R$, which implies that the resonances are typically very narrow and hard to resolve [292, 37, 293]. To assess the relation between the width of the resonances and the imaginary part of the QNMs, we make use of the harmonic oscillator model [294]. According to the latter, a compact object which resonates at a QNM frequency can be modeled as a forced harmonic oscillator that satisfies [294]

$$\ddot{\xi} - 2\omega_I \dot{\xi} + (\omega_R^2 + \omega_I^2) \xi = b\omega^2 e^{-i\omega t}, \quad (6.35)$$

where ξ is the amplitude of the GW emitted at infinity normalized by a reference amplitude, e.g., the amplitude of the GW emitted at infinity when the central object is a BH, and the orbiting point particle acts as a driving force. The solution is $\xi(t) = \xi(\omega)e^{-i\omega t}$, where

$$\xi(\omega) = \frac{-b\omega^2}{\omega^2 - \omega_R^2 - \omega_I^2 - 2i\omega_I\omega}. \quad (6.36)$$

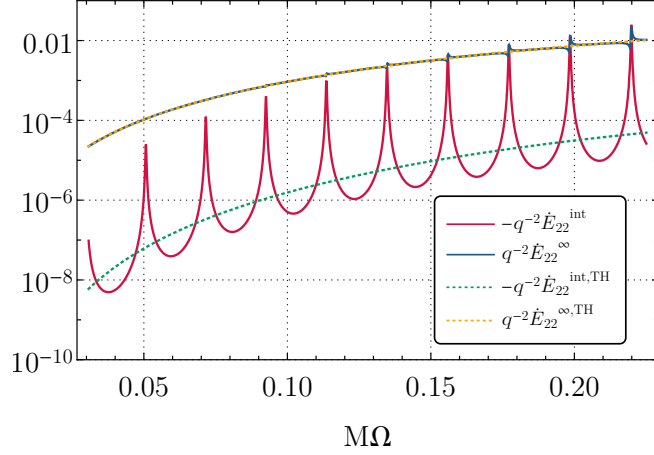


Figure 6.2. Energy fluxes that are emitted on the ECO side and at infinity by a point particle around a central ECO with $\chi = 0.9$, $\epsilon = 10^{-10}$, and $\mathcal{R} = \sqrt{0.9}$ for the $\ell = m = 2$ mode. The fluxes are compared with those of Ref. [39] in which the effect of the ECO was accounted for by removing a fraction of the tidal heating (TH) from the standard Kerr flux. [38]

Near the resonance, the amplitude of the GW is the sum of two contributions, one due to the orbital motion and one due to the resonance to the QNM. The normalized energy flux across a single resonance is well fitted by the model [294]

$$\frac{\dot{E}^{\text{ECO}}}{\dot{E}^{\text{BH}}} = |1 - \xi(\omega)|^2 = \frac{[(1 - b)\omega^2 - \omega_R^2 - \omega_I^2]^2 + (2\omega_I\omega)^2}{(\omega^2 - \omega_R^2 - \omega_I^2)^2 + (2\omega_I\omega)^2}, \quad (6.37)$$

where \dot{E} is the total energy flux as computed in Eq. (6.18) and Eq. (6.29) for the BH and ECO cases, respectively, $b = 1 - (\Omega_{\text{max}}/\Omega_{\text{min}})^2$, and Ω_{max} and Ω_{min} are the orbital angular frequencies of the maximum and the minimum of each resonance. The width of each resonance in the orbital frequency scales as $\delta\Omega \sim \omega_I$ [37], where $\omega_I \sim \omega_R^{2\ell+2}$ from Eq. (4.34). It follows that the width of the resonances increases with the orbital angular frequency, as it is shown in Fig. 6.1.

In the non-spinning and perfectly reflecting case, we recover the results of Ref. [37], namely that low-frequency resonances do not contribute significantly to the GW phase due to their narrow width. However, for highly spinning compact objects, the ISCO frequency occurs at higher frequencies to the non-spinning case. Consequently, the resonances with larger width can be excited and contribute to a significant dephasing to the BH case (as shown in Sec. 6.5).

The system shown in Fig. 6.1 is purely indicative since a horizonless compact object with a perfectly reflecting surface is unstable due to the ergoregion instability and would spin down on short timescales (see Secs. 4.4.4 and 4.5 for a related discussion). Stable models of horizonless compact objects require either small values of the spin or partial absorption [30, 31]. In both cases,

the resonances are less evident, as shown in Fig. 6.2 for a partially absorbing compact object with $|\mathcal{R}|^2 = 0.9$, a value that guarantees stability for a central object with spin $\chi = 0.9$.

Fig. 6.2 shows that, also for reflectivities smaller than unity, the resonances are excited both in the energy flux at infinity (\dot{E}^∞) and on the ECO side (\dot{E}^{int}). The resonances are less peaked than in the perfectly reflecting case but, as shown below, can still have a sufficiently large width to be efficiently excited. Overall, the energy flux on the ECO side is several orders of magnitude smaller than the energy flux at infinity. However near the ISCO frequency, \dot{E}^{int} is comparable to \dot{E}^∞ and contributes significantly to the GW phase.

Finally, Fig. 6.2 also shows the energy fluxes at infinity and on the ECO side computed in Ref. [39] by removing a fraction of TH from the BH energy flux as in Eq. (6.32). In this case, the energy flux at infinity is similar to the exact result except for the presence of the resonances that are absent in the model of Ref. [39]. On the other hand, the energy flux of the ECO side can change significantly. Due to the presence of the resonances, \dot{E}^{int} computed in Ref. [39] is a sort of averaged value of the exact result. The latter is modulated by the presence of resonances that can be as high as the flux at infinity.

In Fig. 6.3 we show the difference between the total energy flux of the $\ell = m = 2$ mode in the horizonless case with respect to the BH case, both in our consistent model and in the phenomenological approach of Ref. [39]. In particular, the top panel shows the absolute value of the difference between the ECO and BH fluxes on a logarithmic scale, to appreciate the relatively small numbers involved. The bottom panel, instead, shows the difference between the energy fluxes on a linear scale, to appreciate the change of sign during the oscillations, for several values of the reflectivity.

For $|\mathcal{R}|^2 \approx 1$ the differences between the consistent model and the model of Ref. [39] are due to two factors: the excitation of the resonances and the (subleading) effect that the flux computation in the consistent model accounts for the fraction of the GWs that are reflected by the object and make their way to infinity rather than being reabsorbed by the particle, as implicitly assumed in Ref. [39]. For small values of the reflectivity, the difference between the consistent model and the phenomenological one is even more important. In this case, the resonances are suppressed in amplitude but still appear in the total energy flux with a larger width, as shown in the top panel of Fig. 6.3. The bottom panel grid in Fig. 6.3 shows the oscillatory trend of the total energy flux in the horizonless case compared to the energy flux in Ref. [39] for small reflectivities. The amplitude of the oscillations increases with the orbital angular frequency and decreases with the reflectivity. The oscillations are related to the resonances and, as we shall see in Sec. 6.5, they can contribute significantly to the GW phase also for small values of the reflectivity.

Interestingly, when the superradiance condition is met, $\Omega < \Omega_H$, the flux on the ECO side can be negative due to the energy and angular-momentum extraction from the central object [29]. Since \dot{E}^{int} and \dot{E}^∞ have the opposite

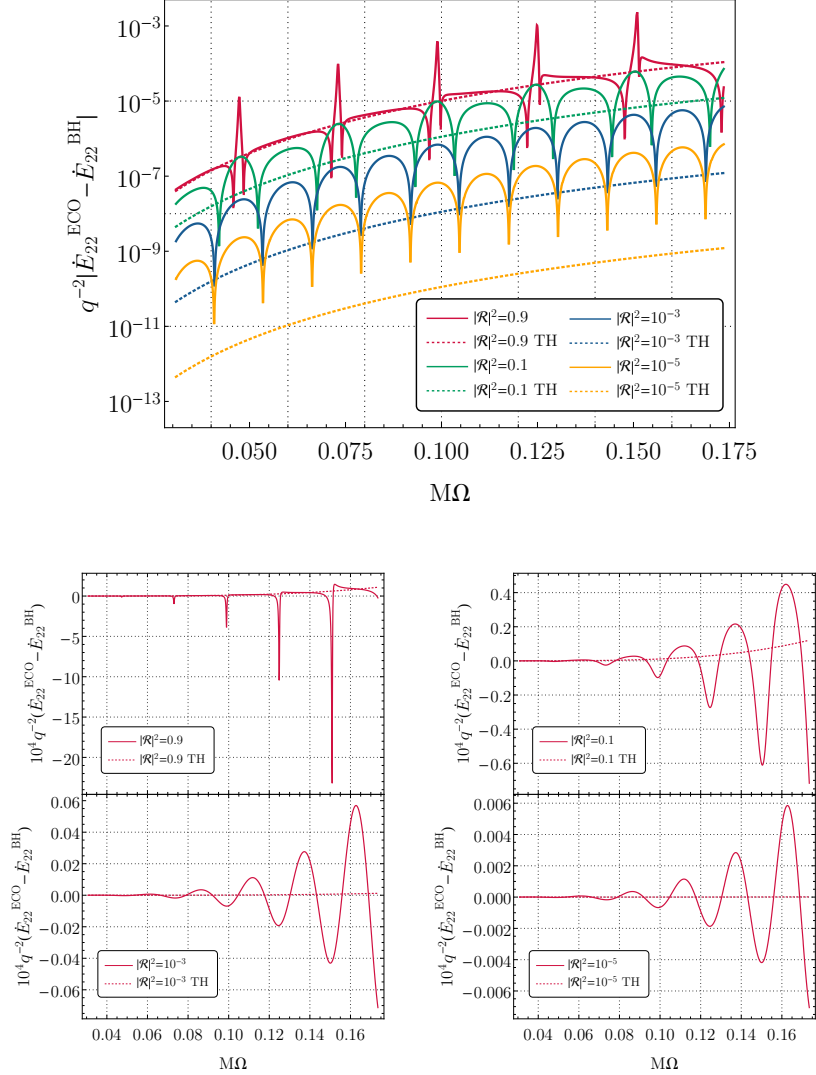


Figure 6.3. Difference between the total energy flux of the $\ell = m = 2$ mode in the ECO case with respect to the BH case. Top panel: absolute value of the difference for a central object with $\chi = 0.8$, $\epsilon = 10^{-10}$, and several values of the reflectivity. The dotted lines are the estimated differences in the total energy flux due to the absence of TH relative to the BH case, as in Ref. [39]. Bottom panels: same as in the top panel but without the absolute value and in a linear scale, to appreciate the change of sign of the oscillations associated with the resonances. [38]

sign, it is interesting to check whether they can compensate each other at some given frequency, giving rise to a total zero flux and hence to “floating” orbits [295, 296]. As clear from Fig. 6.2, in the case of a single mode (e.g., $\ell = m = 2$) such orbits would exist near the high-frequency resonances, where \dot{E}^{int} (which is typically subdominant) can be as large as \dot{E}^{∞} in absolute value. When including the contribution of multipoles, we find that the total flux at

infinity is larger than the flux on the ECO side because modes with different (ℓ, m) are resonantly excited at different frequencies. The net result is that the total flux, $\dot{E}^\infty + \dot{E}^{\text{int}}$, is overall positive and the orbit shrinks during the adiabatic evolution.

6.5 Adiabatic evolution and dephasing

In EMRIs, the radiation-reaction timescale is much longer than the orbital period. For this reason, at the first order in the mass ratio the orbital parameters can be evolved using an adiabatic expansion [297]. For a particle in a circular, equatorial and corotating orbit, the evolution of the orbital angular frequency Ω and the orbital phase ϕ are governed by

$$\dot{\Omega} = - \left(\frac{dE_b}{d\Omega} \right)^{-1} \dot{E}(\Omega), \quad (6.38)$$

$$\dot{\phi} = \Omega, \quad (6.39)$$

where E_b is the binding energy of the system

$$E_b = \mu \frac{1 - 2v^2 + \chi v^3}{\sqrt{1 - 3v^2 + 2\chi v^3}}, \quad (6.40)$$

where $v \equiv \sqrt{M/r}$, r is the orbital radius that is related to the orbital angular frequency through Eq. (6.5), and $\dot{E}(\Omega)$ is the total energy flux defined in Eqs. (6.18) and (6.29) in the BH and the ECO case, respectively.

Equations (6.38) and (6.39) can be solved by adding two initial conditions, namely

$$\Omega(t=0) = \Omega_0, \quad (6.41)$$

$$\phi(t=0) = 0, \quad (6.42)$$

without loss of generality. The GW phase of the dominant mode is related to the orbital phase by $\phi_{\text{GW}} = 2\phi$. We compute the GW dephasing accumulated up to a certain time between the cases of a central BH and a central horizonless compact object as [39]

$$\Delta\phi(t) = \phi_{\text{GW}}^{\text{BH}}(t) - \phi_{\text{GW}}^{\text{ECO}}(t). \quad (6.43)$$

6.5.1 Non-spinning central object

Let us analyze the case of a central compact object which is non-spinning. Fig. 6.4 shows the dephasing in the case of a perfectly reflecting ECO relative to the Schwarzschild BH, for different values of the compactness parameter ϵ . As shown in Fig. 6.4, the dephasing does not depend on ϵ and is not affected by

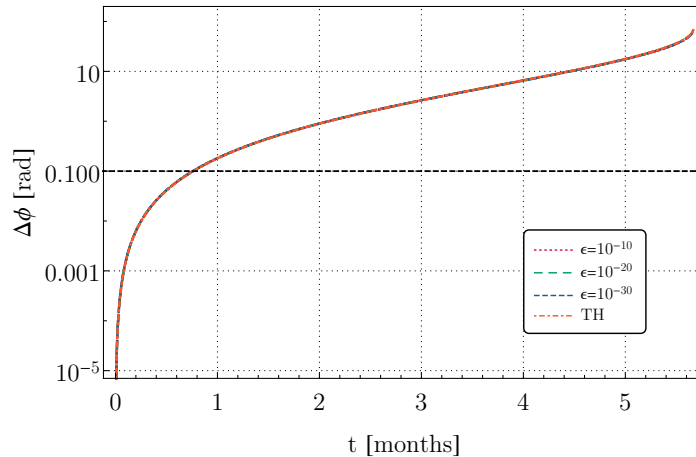


Figure 6.4. Dephasing as a function of time in the case of a non-spinning and perfectly reflecting ECO relative to the Schwarzschild BH case for different values of the compactness parameter ϵ and $q = 3 \times 10^{-5}$. The resonances in the energy flux do not contribute to the dephasing which is well approximated by the phenomenological model in Ref. [39] marked as TH. [38]

the resonances, that are too narrow to be efficiently excited in the non-spinning case. For this reason, the dephasing is well approximated by the model adopted in Ref. [39] that removes a fraction of TH from the BH energy flux. Overall, the results in Fig. 6.4 are compatible with the analytical estimates in Ref. [37] which assessed that the impact of resonances is negligible in the case of a non-spinning and perfectly reflecting compact object.

6.5.2 Spinning central object

Let us analyze the dephasing between a spinning horizonless compact object and the standard Kerr case. This is shown in Fig. 6.5 for a fiducial binary with primary mass $M = 10^6 M_\odot$, secondary mass $\mu = 30 M_\odot$, and a central object with spin $\chi = 0.8$ and $\epsilon = 10^{-10}$. We analyze different values of the reflectivity and for each of them, we compare our exact result with the one of the model in Ref. [39].

The dephasing increases monotonically in time and also as a function of the reflectivity. When $|\mathcal{R}|^2 \approx 1$, the difference to the model in Ref. [39] is small until the inspiral moves across a resonance. In particular, for $|\mathcal{R}|^2 = 0.9$, the dephasing in the horizonless case deviates from the dephasing due to the absence of TH at $t = 9.47$ months (marked in Fig. 6.5 by a dashed vertical line) due to the presence of a $\ell = m = 2$ resonance with $M\Omega = 0.0473$ and $M\omega_I = -4.22 \times 10^{-5}$. Subsequent resonances are excited at later times and are responsible for the deviations of the dephasing from the model adopted in Ref. [39].

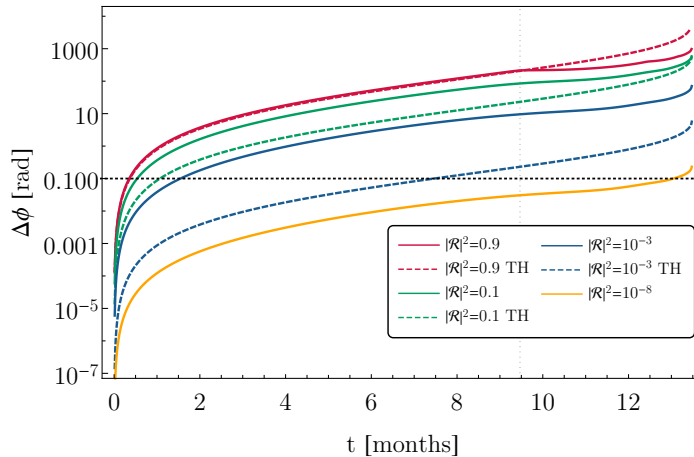


Figure 6.5. GW dephasing between the BH and the ECO case as a function of time for a binary with mass ratio $q = 3 \times 10^{-5}$ and a central object with spin $\chi = 0.8$, $\epsilon = 10^{-10}$ and several values of the reflectivity. The dashed lines show the dephasing due to the absence of TH relative to the BH case as in Ref. [39]. The vertical dashed line corresponds to the time in which a resonant orbital frequency is excited. The horizontal line is a reference value $\Delta\phi = 0.1$ rad for the resolvability of the dephasing by LISA. [38]

Interestingly, the phenomenological model of Ref. [39] and the exact result differ significantly for small reflectivities even if the resonances are less evident. This is due to several factors: the energy fluxes at infinity and on the ECO side display some differences in the two models since a fraction of the energy is reflected by the object and leaves the system; moreover, both fluxes (at infinity and on the ECO side) can be resonantly excited only in our model and these resonances contribute significantly to the GW phase even for intermediate values of \mathcal{R} . The dephasing in the consistent model is always larger than the dephasing with TH only. For small values of \mathcal{R} , the two models differ from each other but both produce a small dephasing to the Kerr case.

For a signal with $\text{SNR} \sim 30$, a dephasing $\Delta\phi = 0.1$ rad is considered to be resolvable by LISA [298, 299]. Fig. 6.5 shows that the phase difference is above this threshold only after half a month of observation for a horizonless compact object with $|\mathcal{R}|^2 = 0.9$. After twelve months of inspiral, values of the reflectivity as small as $|\mathcal{R}|^2 = 10^{-8}$ would be detectable by LISA. In Sec. 6.6, we shall assess the measurability of the reflectivity with a more robust method based on the computation of the overlap between the waveforms.

6.5.3 The role of the compactness

In this section, we analyze the role of the compactness in the energy fluxes emitted by an EMRI with a central horizonless compact object. The top

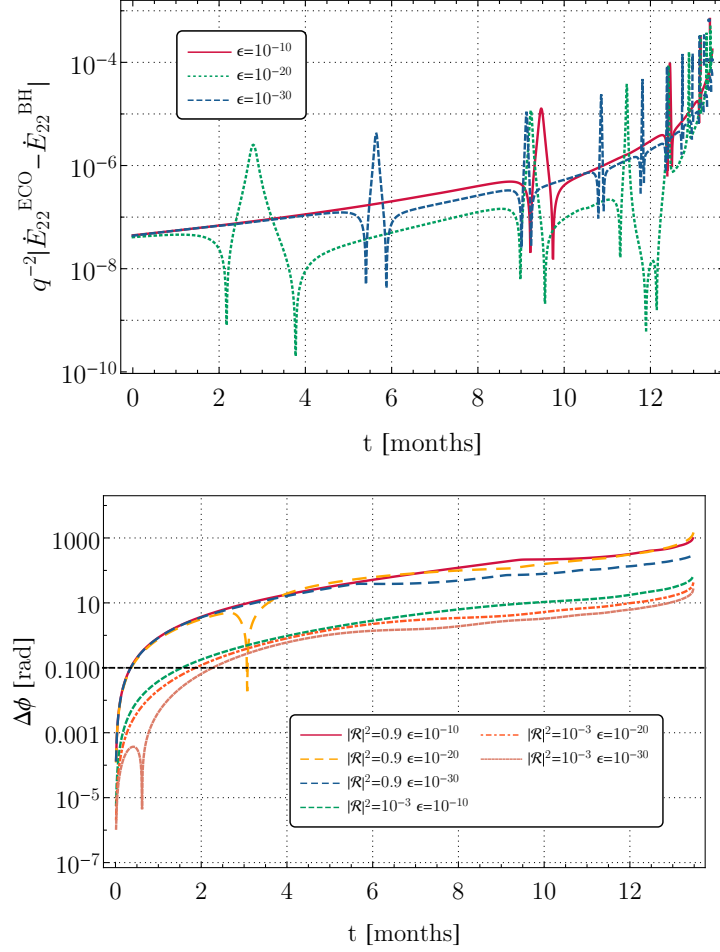


Figure 6.6. Top panel: Resonances in the $\ell = m = 2$ energy flux for an ECO with $\chi = 0.8$, $|\mathcal{R}|^2 = 0.9$ and several values of ϵ , as a function of time. Bottom panel: GW dephasing between the BH and the ECO case as a function of time for $q = 3 \times 10^{-5}$, $\chi = 0.8$ and several values of ϵ . [38]

panel of Fig. 6.6 shows the difference between the ECO and BH energy fluxes for several values of ϵ as a function of time. We note that for $\epsilon \rightarrow 0$, more resonances appear and they also appear at lower frequencies. The first low-frequency resonances could give a large contribution to the GW phase since the orbital evolution is slower at low frequency and the particle can spend more time across the resonance. On the other hand, the width of each resonance is proportional to the imaginary part of the QNMs where $\omega_I \sim \omega_R^{2\ell+2}$, therefore low-frequency resonances are also more narrow. The two effects are competitive and the actual contribution of a resonance on the GW phase depends on the specific parameters of the configuration.

The bottom panel of Fig. 6.6 shows the dephasing between the ECO and the BH case for several values of the reflectivity and compactness. The dependence on ϵ is mild, except for the excitation of the resonances whose impact depends

on the specific values of χ , ϵ and \mathcal{R} .

6.6 Waveform and overlap

The waveform emitted by an EMRI is computed from the Weyl scalar in Eq. (6.1) at infinity and reads [195, 300]

$$h_+ - ih_\times = -\frac{2}{\sqrt{2\pi}} \frac{\mu}{D} \sum_{\ell m} \frac{Z_{\ell m \omega}^\infty(t)}{[m\Omega(t)]^2} e^{im(\Omega(t)r_*^D - \phi(t))} {}_{-2}S_{\ell m \omega}(\theta, t) e^{im\varphi}, \quad (6.44)$$

where D is the luminosity distance of the source from the detector, $r_*^D \equiv r_*(D)$, and (θ, φ) identify the direction of the detector in a reference frame centered at the source in Boyer-Lindquist coordinates. Since the initial phase is degenerate with the azimuthal direction, we rescale the initial phase as $\varphi \equiv \phi(t=0)$.

Although the dephasing $\Delta\phi$ between two waveforms (h_1 and h_2) is a useful and quick measure to estimate the measurability of any deviation from a reference signal, a more reliable and robust measure is given by the overlap:

$$\mathcal{O}(h_1|h_2) = \frac{\langle h_1|h_2 \rangle}{\sqrt{\langle h_1|h_1 \rangle \langle h_2|h_2 \rangle}}, \quad (6.45)$$

where the inner product is defined in Eq. (3.107) of Appendix 3.7. For the power spectral density, we adopt the LISA curve of Ref. [301] adding the contribution of the confusion noise from the unresolved Galactic binaries for a one-year mission lifetime. Since the waveforms are defined up to an arbitrary time and phase shift, it is also necessary to maximize the overlap in Eq. (6.45) over these quantities. This can be done by computing [302]

$$\mathcal{O}(h_1|h_2) = \frac{4}{\sqrt{\langle h_1|h_1 \rangle \langle h_2|h_2 \rangle}} \max_{t_0} \left| \mathcal{F}^{-1} \left[\frac{\tilde{h}_1 \tilde{h}_2^*}{S_n(f)} \right] (t_0) \right|, \quad (6.46)$$

where $\mathcal{F}^{-1}[g(f)](t) = \int_{-\infty}^{+\infty} g(f) e^{-2\pi i f t} df$ is the inverse Fourier transform. The overlap is defined such that $\mathcal{O} = 1$ indicates a perfect agreement between two waveforms. It is also customary to define the mismatch as $\mathcal{M} \equiv 1 - \mathcal{O}$.

In Fig. 6.7 we show the mismatch between the waveforms in the ECO case and in the Kerr case with the same mass and spin for various values of the reflectivity and two choices of ϵ . Let us notice that the compactness does not affect the mismatch significantly when $\epsilon \ll 1$. Consistently with dephasing presented in Sec. 6.5, the mismatch is larger in the consistent model than in the phenomenological approach of Ref. [39], especially at small reflectivity.

As a useful rule of thumb, two waveforms are indistinguishable for parameter estimation purposes if [303, 298]

$$\mathcal{M} \lesssim 1/(2\rho^2), \quad (6.47)$$

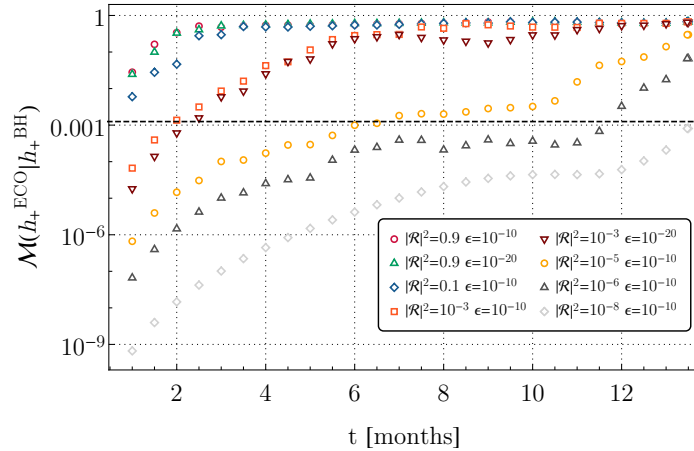


Figure 6.7. Mismatch between the plus polarization of the waveforms with a central ECO and a central BH as a function of time, for a binary with mass ratio $q = 3 \times 10^{-5}$ and a central object with spin $\chi = 0.8$ and several values of the reflectivity and the compactness. The horizontal line is a reference value $\mathcal{M} \approx 10^{-3}$ for the resolvability by LISA. [38]

where ρ is the SNR of the true signal. For an EMRI with $\rho \approx 20$ ($\rho \approx 100$) one has $\mathcal{M} \lesssim 10^{-3}$ ($\mathcal{M} \lesssim 5 \times 10^{-5}$). In Fig. 6.7, the more conservative threshold $\mathcal{M} = 10^{-3}$ is denoted with a dashed horizontal line. Exceeding this threshold is a necessary but not sufficient condition for a deviation to be detectable. This level of mismatch is quickly exceeded after less than one year of data even for small values of the reflectivity. For example, for the fiducial case considered in Fig. 6.7 ($\chi = 0.8$, $M = 10^6 M_\odot$ and $\mu = 30 M_\odot$), and assuming $\rho = 20$, the threshold is exceeded after roughly one year unless

$$|\mathcal{R}|^2 \lesssim 10^{-8}. \quad (6.48)$$

This result is in agreement with the estimation based on the dephasing in Sec. 6.5. It shows that EMRIs could place stringent constraints on the reflectivity of supermassive compact objects at the remarkable level of $\mathcal{O}(10^{-6})\%$. Let us notice that the bound in Eq. (6.48) is solely based on the mismatch calculation and does not take into account, e.g., correlations with the waveform parameters. Rigorous parameter estimation is necessary to derive an accurate projected upper bound in the case of no detection.

6.7 A case study: Boltzmann reflectivity

The surface reflectivity of a horizonless compact object can be a complex function of the parameters of the model and the frequency. In this section, we consider a case study for the ECO reflectivity. In particular, we analyze a

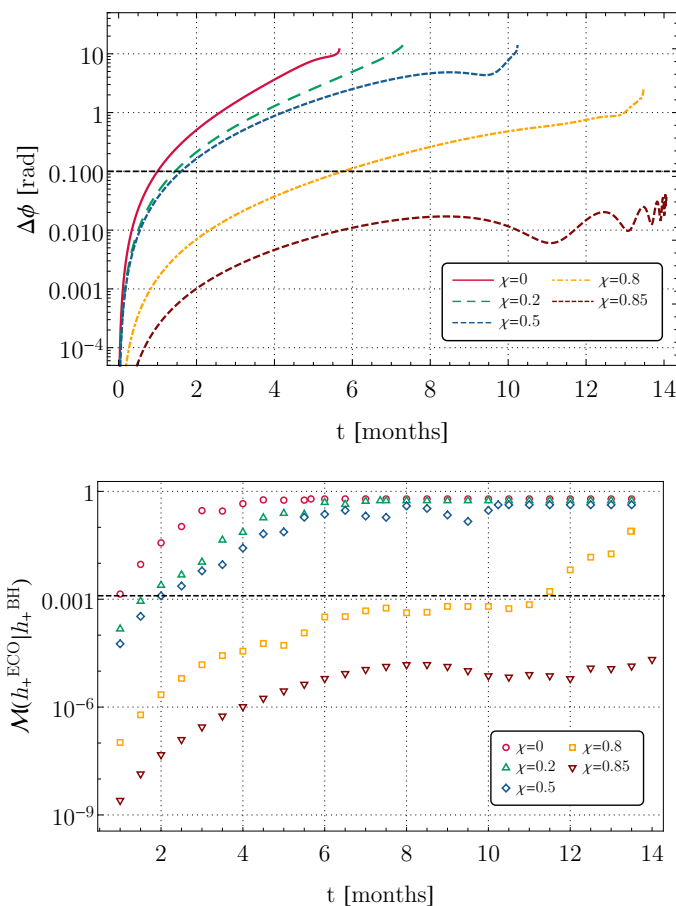


Figure 6.8. Top panel: GW dephasing between the Kerr case and a quantum BH horizon with Boltzmann reflectivity [in Eq. (6.49)], where $q = 3 \times 10^{-5}$, $\epsilon = 10^{-10}$ as a function of time. Bottom panel: Mismatch between the plus polarization of the waveform with a quantum BH horizon with Boltzmann reflectivity and a standard BH as a function of time for several values of the spin. [38]

model recently proposed to describe quantum BH horizons that gives rise to the “Boltzmann” reflectivity [264, 32]

$$\mathcal{R}(\omega) = e^{-\frac{|k|}{2T_{\text{H}}}}, \quad (6.49)$$

where $T_{\text{H}} = \frac{r_+ - r_-}{4\pi(r_+^2 + a^2)}$ is the Hawking temperature of a Kerr BH. In this model, the reflectivity depends explicitly on the frequency and the spin of the compact object. The reflectivity in Eq. (6.49) provides sufficient absorption to quench the ergoregion instability and have a stable horizonless compact object with any spin [264]. Let us notice that Eq. (6.49) can also contain a phase term, that depends on the specific model and the perturbation function on which the corresponding boundary condition is imposed [264, 32, 304]. Recently, Refs. [305, 304] proposed a model of the reflectivity that is related to the tidal response of the ECO to external curvature perturbations. In this model,

the reflectivity contains extra terms that multiply the Boltzmann factor. For simplicity, we neglect such phase terms, which would not affect our analysis significantly.

Figure 6.8 shows the dephasing (top panel) and the overlap (bottom panel) obtained in the Boltzmann reflectivity model as compared to the classical BH case. An interesting feature of this model is that there is no free parameter that continuously connects the model to the classical Kerr case, so there is a concrete chance to rule it out with observations or to provide evidence for it. Interestingly, owing to its spin dependence, the Boltzmann reflectivity is much smaller at the relevant orbital frequencies when the central object is highly spinning. Consequently, the dephasing and the mismatch to the standard Kerr BH case are very small when $\chi \gtrsim 0.8$ as shown in Fig. 6.8. The oscillatory trend in the dephasing in the top panel is due to the contribution of high-frequency resonances appearing at late times.

Conclusions and future prospects

According to the BH paradigm, any compact object heavier than a few solar masses is described by the Kerr metric. In this thesis, we considered the possibility that the compact objects in the Universe are horizonless and singularity-free. This hypothesis is supported by several models of ECOs that have been conceived in extensions of GR [12, 13]. ECOs are a tool that allows us to quantify the existence of horizons in astrophysical sources.

In this thesis, we derived the characteristic frequencies of horizonless compact objects in the ringdown [30, 237]. We developed a model-independent framework relying on the membrane paradigm to quantify the deviations from the BH spectrum [237]. We assessed that current measurement accuracies impose a strong lower bound on the compactness of the merger remnant of 90% of the BH compactness.

Spinning horizonless compact objects might be affected by an ergoregion instability when rotating sufficiently fast [25]. In this thesis, we assessed the astrophysical viability of spinning horizonless compact objects under linear perturbations. From the analysis of the QNM frequencies, we determined the conditions for which horizonless compact objects are unstable [30, 31]. Finally, we found a mechanism that allows for stable solutions, i.e., energy absorption within the object [30]. We showed that a surface absorption of 60% ensures the stability of horizonless compact objects for any spin [31].

In this thesis, we also explored the fingerprints of horizonless compact sources in the appearance of a modulated train of GW echoes at late times in the ringdown [19]. We provided an analytical template for the GW echoes that relates the key parameters of ECOs with the gravitational waveform [22]. This template would allow us to constrain the parameters of exotic sources or perform model selection in the case of detection of GW echoes.

We also assessed how the future space-based interferometer LISA will allow us to perform tests of the BH paradigm, especially with new sources like EMRIs [242]. We derived the gravitational waveform emitted by a stellar-mass object in orbital motion around a supermassive horizonless compact object. During the inspiral, we assessed the impact of extra resonances that would be excited when the orbital frequency matches the characteristic frequencies of

the central ECO [37, 38]. Finally, we estimated that EMRIs could potentially place the most stringent constraint on the reflectivity of supermassive compact objects at the remarkable level of $\mathcal{O}(10^{-6})\%$ [38].

A possible future research direction would be the development of data analysis techniques to infer the properties of compact sources from GW observations. Current constraints on the deviations from GR can be converted into constraints on the parameters of astrophysical sources. The mapping between the two descriptions needs to be developed and would be relevant to understand the nature of compact sources.

Moreover, full inspiral-merger-ringdown waveforms in various modified theories of gravity and alternative sources need to be developed. The accurate modeling of the gravitational waveform in alternative scenarios is crucial to look for new physics with current and future GW detections. The comparison of the echo templates obtained within perturbation theory with the postmerger signal of an ECO coalescence is an open problem. Numerical simulations of these systems are currently unavailable.

Furthermore, the extension of the membrane paradigm to spinning horizonless compact objects is left for future work. The membrane paradigm would allow us to describe several models of spinning ECOs with different interior solutions. The ECO phenomenology would be parametrized in terms of the properties of a fictitious rotating membrane located at the effective radius of the object.

Concerning EMRIs detectable by LISA, a natural extension concerns the generalization to eccentric and inclined orbits. The bounds on the reflectivity of compact objects estimated in our work are based on the overlap calculation, and therefore neglect possible correlations among the waveform parameters. An interesting research line would be to perform accurate data analyses with exact waveforms either using the Fisher-information matrix or Bayesian inference.

Bibliography

- [1] **LIGO Scientific, Virgo** Collaboration, B. P. Abbott *et al.*, “GWTC-1: A Gravitational-Wave Transient Catalog of Compact Binary Mergers Observed by LIGO and Virgo during the First and Second Observing Runs,” *Phys. Rev. X* **9** no. 3, (2019) 031040, arXiv:1811.12907 [astro-ph.HE].
- [2] **LIGO Scientific, Virgo** Collaboration, R. Abbott *et al.*, “GWTC-2: Compact Binary Coalescences Observed by LIGO and Virgo During the First Half of the Third Observing Run,” *Phys. Rev. X* **11** (2021) 021053, arXiv:2010.14527 [gr-qc].
- [3] **LIGO Scientific, VIRGO** Collaboration, R. Abbott *et al.*, “GWTC-2.1: Deep Extended Catalog of Compact Binary Coalescences Observed by LIGO and Virgo During the First Half of the Third Observing Run,” arXiv:2108.01045 [gr-qc].
- [4] **LIGO Scientific, VIRGO, KAGRA** Collaboration, R. Abbott *et al.*, “GWTC-3: Compact Binary Coalescences Observed by LIGO and Virgo During the Second Part of the Third Observing Run,” arXiv:2111.03606 [gr-qc].
- [5] **LIGO Scientific, Virgo** Collaboration, B. P. Abbott *et al.*, “Tests of general relativity with GW150914,” *Phys. Rev. Lett.* **116** no. 22, (2016) 221101, arXiv:1602.03841 [gr-qc]. [Erratum: *Phys.Rev.Lett.* 121, 129902 (2018)].
- [6] **LIGO Scientific, Virgo** Collaboration, B. P. Abbott *et al.*, “GW170817: Observation of Gravitational Waves from a Binary Neutron Star Inspiral,” *Phys. Rev. Lett.* **119** no. 16, (2017) 161101, arXiv:1710.05832 [gr-qc].
- [7] **LIGO Scientific, Virgo, Fermi GBM, INTEGRAL, IceCube, AstroSat Cadmium Zinc Telluride Imager Team, IPN, Insight-Hxmt, ANTARES, Swift, AGILE Team, 1M2H Team, Dark Energy Camera GW-EM, DES, DLT40, GRAWITA, Fermi-LAT, ATCA, ASKAP, Las Cumbres Observatory**

- Group, OzGrav, DWF (Deeper Wider Faster Program), AST3, CAASTRO, VINROUGE, MASTER, J-GEM, GROWTH, JAGWAR, CaltechNRAO, TTU-NRAO, NuSTAR, Pan-STARRS, MAXI Team, TZAC Consortium, KU, Nordic Optical Telescope, ePESSTO, GROND, Texas Tech University, SALT Group, TOROS, BOOTES, MWA, CALET, IKI-GW Follow-up, H.E.S.S., LOFAR, LWA, HAWC, Pierre Auger, ALMA, Euro VLBI Team, Pi of Sky, Chandra Team at McGill University, DFN, ATLAS Telescopes, High Time Resolution Universe Survey, RIMAS, RATIR, SKA South Africa/MeerKAT Collaboration, B. P. Abbott *et al.*, “Multi-messenger Observations of a Binary Neutron Star Merger,” *Astrophys. J. Lett.* **848** no. 2, (2017) L12, arXiv:1710.05833 [astro-ph.HE].
- [8] **LIGO Scientific, Virgo** Collaboration, R. Abbott *et al.*, “GW190521: A Binary Black Hole Merger with a Total Mass of $150M_{\odot}$,” *Phys. Rev. Lett.* **125** no. 10, (2020) 101102, arXiv:2009.01075 [gr-qc].
- [9] **LIGO Scientific, Virgo** Collaboration, B. Abbott *et al.*, “Tests of General Relativity with the Binary Black Hole Signals from the LIGO-Virgo Catalog GWTC-1,” *Phys. Rev. D* **100** no. 10, (2019) 104036, arXiv:1903.04467 [gr-qc].
- [10] **LIGO Scientific, Virgo** Collaboration, R. Abbott *et al.*, “Tests of general relativity with binary black holes from the second LIGO-Virgo gravitational-wave transient catalog,” *Phys. Rev. D* **103** no. 12, (2021) 122002, arXiv:2010.14529 [gr-qc].
- [11] **LIGO Scientific, VIRGO, KAGRA** Collaboration, R. Abbott *et al.*, “Tests of General Relativity with GWTC-3,” arXiv:2112.06861 [gr-qc].
- [12] G. F. Giudice, M. McCullough, and A. Urbano, “Hunting for Dark Particles with Gravitational Waves,” *JCAP* **1610** no. 10, (2016) 001, arXiv:1605.01209 [hep-ph].
- [13] V. Cardoso and P. Pani, “Testing the nature of dark compact objects: a status report,” *Living Rev. Rel.* **22** no. 1, (2019) 4, arXiv:1904.05363 [gr-qc].
- [14] S. D. Mathur, “The Information paradox: A Pedagogical introduction,” *Class. Quant. Grav.* **26** (2009) 224001, arXiv:0909.1038 [hep-th].
- [15] M. A. Abramowicz, W. Kluzniak, and J.-P. Lasota, “No observational proof of the black hole event-horizon,” *Astron. Astrophys.* **396** (2002) L31–L34, arXiv:astro-ph/0207270 [astro-ph].

- [16] **Event Horizon Telescope** Collaboration, K. Akiyama *et al.*, “First M87 Event Horizon Telescope Results. V. Physical Origin of the Asymmetric Ring,” *Astrophys. J. Lett.* **875** no. 1, (2019) L5, arXiv:1906.11242 [astro-ph.GA].
- [17] J. C. Bustillo, N. Sanchis-Gual, A. Torres-Forné, J. A. Font, A. Vajpeyi, R. Smith, C. Herdeiro, E. Radu, and S. H. W. Leong, “GW190521 as a Merger of Proca Stars: A Potential New Vector Boson of 8.7×10^{-13} eV,” *Phys. Rev. Lett.* **126** no. 8, (2021) 081101, arXiv:2009.05376 [gr-qc].
- [18] **LIGO Scientific, Virgo** Collaboration, R. Abbott *et al.*, “GW190814: Gravitational Waves from the Coalescence of a 23 Solar Mass Black Hole with a 2.6 Solar Mass Compact Object,” *Astrophys. J. Lett.* **896** no. 2, (2020) L44, arXiv:2006.12611 [astro-ph.HE].
- [19] V. Cardoso, E. Franzin, and P. Pani, “Is the gravitational-wave ringdown a probe of the event horizon?,” *Phys. Rev. Lett.* **116** no. 17, (2016) 171101, arXiv:1602.07309 [gr-qc]. [Erratum: *Phys.Rev.Lett.* **117**, 089902 (2016)].
- [20] B. Carter, “Axisymmetric Black Hole Has Only Two Degrees of Freedom,” *Phys. Rev. Lett.* **26** (1971) 331–333.
- [21] D. Robinson, “Uniqueness of the Kerr black hole,” *Phys. Rev. Lett.* **34** (1975) 905–906.
- [22] E. Maggio, A. Testa, S. Bhagwat, and P. Pani, “Analytical model for gravitational-wave echoes from spinning remnants,” *Phys. Rev.* **D100** no. 6, (2019) 064056, arXiv:1907.03091 [gr-qc].
- [23] J. Abedi, H. Dykaar, and N. Afshordi, “Echoes from the Abyss: Tentative evidence for Planck-scale structure at black hole horizons,” *Phys. Rev.* **D96** no. 8, (2017) 082004, arXiv:1612.00266 [gr-qc].
- [24] J. Westerweck, A. Nielsen, O. Fischer-Birnholtz, M. Cabero, C. Capano, T. Dent, B. Krishnan, G. Meadors, and A. H. Nitz, “Low significance of evidence for black hole echoes in gravitational wave data,” *Phys. Rev.* **D97** no. 12, (2018) 124037, arXiv:1712.09966 [gr-qc].
- [25] J. L. Friedman, “Generic instability of rotating relativistic stars,” *Commun. Math. Phys.* **62** no. 3, (1978) 247–278.
- [26] S. Yoshida and Y. Eriguchi, “Ergoregion instability revisited — a new and general method for numerical analysis of stability,” *Monthly Notices of the Royal Astronomical Society* **282** no. 2, (09, 1996) 580–586.
- [27] K. D. Kokkotas, J. Ruoff, and N. Andersson, “The w-mode instability of ultracompact relativistic stars,” *Phys.Rev.* **D70** (2004) 043003, arXiv:astro-ph/0212429 [astro-ph].

- [28] V. Cardoso, L. C. B. Crispino, C. F. B. Macedo, H. Okawa, and P. Pani, “Light rings as observational evidence for event horizons: long-lived modes, ergoregions and nonlinear instabilities of ultracompact objects,” *Phys.Rev.* **D90** (2014) 044069, arXiv:1406.5510 [gr-qc].
- [29] R. Brito, V. Cardoso, and P. Pani, *Superradiance: Energy Extraction, Black-Hole Bombs and Implications for Astrophysics and Particle Physics*, vol. 906. Springer, 2015. arXiv:1501.06570 [gr-qc].
- [30] E. Maggio, P. Pani, and V. Ferrari, “Exotic Compact Objects and How to Quench their Ergoregion Instability,” *Phys. Rev.* **D96** no. 10, (2017) 104047, arXiv:1703.03696 [gr-qc].
- [31] E. Maggio, V. Cardoso, S. R. Dolan, and P. Pani, “Ergoregion instability of exotic compact objects: electromagnetic and gravitational perturbations and the role of absorption,” *Phys. Rev.* **D99** no. 6, (2019) 064007, arXiv:1807.08840 [gr-qc].
- [32] Q. Wang, N. Oshita, and N. Afshordi, “Echoes from Quantum Black Holes,” *Phys. Rev. D* **101** no. 2, (2020) 024031, arXiv:1905.00446 [gr-qc].
- [33] M. Punturo *et al.*, “The Einstein Telescope: A third-generation gravitational wave observatory,” *Class. Quant. Grav.* **27** (2010) 194002.
- [34] D. Reitze *et al.*, “Cosmic Explorer: The U.S. Contribution to Gravitational-Wave Astronomy beyond LIGO,” *Bull. Am. Astron. Soc.* **51** no. 7, (2019) 035, arXiv:1907.04833 [astro-ph.IM].
- [35] LISA Collaboration, P. Amaro-Seoane *et al.*, “Laser Interferometer Space Antenna,” arXiv:1702.00786 [astro-ph.IM].
- [36] J. R. Gair, S. Babak, A. Sesana, P. Amaro-Seoane, E. Barausse, C. P. Berry, E. Berti, and C. Sopuerta, “Prospects for observing extreme-mass-ratio inspirals with LISA,” *J. Phys. Conf. Ser.* **840** no. 1, (2017) 012021, arXiv:1704.00009 [astro-ph.GA].
- [37] V. Cardoso, A. del Rio, and M. Kimura, “Distinguishing black holes from horizonless objects through the excitation of resonances during inspiral,” *Phys. Rev. D* **100** (2019) 084046, arXiv:1907.01561 [gr-qc]. [Erratum: *Phys.Rev.D* 101, 069902 (2020)].
- [38] E. Maggio, M. van de Meent, and P. Pani, “Extreme mass-ratio inspirals around a spinning horizonless compact object,” arXiv:2106.07195 [gr-qc].
- [39] S. Datta, R. Brito, S. Bose, P. Pani, and S. A. Hughes, “Tidal heating as a discriminator for horizons in extreme mass ratio inspirals,” *Phys. Rev.* **D101** no. 4, (2020) 044004, arXiv:1910.07841 [gr-qc].

- [40] **LIGO Scientific, Virgo** Collaboration, B. P. Abbott *et al.*, “Observation of Gravitational Waves from a Binary Black Hole Merger,” *Phys. Rev. Lett.* **116** no. 6, (2016) 061102, [arXiv:1602.03837 \[gr-qc\]](#).
- [41] B. P. Abbott *et al.*, “Sensitivity of the Advanced LIGO detectors at the beginning of gravitational wave astronomy,” *Phys. Rev. D* **93** no. 11, (2016) 112004, [arXiv:1604.00439 \[astro-ph.IM\]](#). [Addendum: *Phys.Rev.D* 97, 059901 (2018)].
- [42] **VIRGO** Collaboration, F. Acernese *et al.*, “Advanced Virgo: a second-generation interferometric gravitational wave detector,” *Class. Quant. Grav.* **32** no. 2, (2015) 024001, [arXiv:1408.3978 \[gr-qc\]](#).
- [43] **LIGO Scientific, Virgo** Collaboration, R. Abbott *et al.*, “GW190412: Observation of a Binary-Black-Hole Coalescence with Asymmetric Masses,” *Phys. Rev. D* **102** no. 4, (2020) 043015, [arXiv:2004.08342 \[astro-ph.HE\]](#).
- [44] Z. Barkat, G. Rakavy, and N. Sack, “Dynamics of Supernova Explosion Resulting from Pair Formation,” *Phys. Rev. Lett.* **18** (1967) 379–381.
- [45] F. Ozel, D. Psaltis, R. Narayan, and J. E. McClintock, “The Black Hole Mass Distribution in the Galaxy,” *Astrophys. J.* **725** (2010) 1918–1927, [arXiv:1006.2834 \[astro-ph.GA\]](#).
- [46] **LIGO Scientific, KAGRA, VIRGO** Collaboration, R. Abbott *et al.*, “Observation of Gravitational Waves from Two Neutron Star–Black Hole Coalescences,” *Astrophys. J. Lett.* **915** no. 1, (2021) L5, [arXiv:2106.15163 \[astro-ph.HE\]](#).
- [47] L. Blanchet, “Gravitational Radiation from Post-Newtonian Sources and Inspiralling Compact Binaries,” *Living Rev. Rel.* **17** (2014) 2, [arXiv:1310.1528 \[gr-qc\]](#).
- [48] L. Blanchet, T. Damour, B. R. Iyer, C. M. Will, and A. G. Wiseman, “Gravitational radiation damping of compact binary systems to second postNewtonian order,” *Phys. Rev. Lett.* **74** (1995) 3515–3518, [arXiv:gr-qc/9501027](#).
- [49] L. E. Kidder, “Coalescing binary systems of compact objects to postNewtonian 5/2 order. 5. Spin effects,” *Phys. Rev. D* **52** (1995) 821–847, [arXiv:gr-qc/9506022](#).
- [50] T. Damour, P. Jaranowski, and G. Schaefer, “Dimensional regularization of the gravitational interaction of point masses,” *Phys. Lett. B* **513** (2001) 147–155, [arXiv:gr-qc/0105038](#).

- [51] K. G. Arun, A. Buonanno, G. Faye, and E. Ochsner, “Higher-order spin effects in the amplitude and phase of gravitational waveforms emitted by inspiraling compact binaries: Ready-to-use gravitational waveforms,” *Phys. Rev. D* **79** (2009) 104023, [arXiv:0810.5336 \[gr-qc\]](#). [Erratum: *Phys.Rev.D* 84, 049901 (2011)].
- [52] S. A. Teukolsky, “Perturbations of a rotating black hole. 1. Fundamental equations for gravitational electromagnetic and neutrino field perturbations,” *Astrophysical Journal* **185** (1973) 635–647.
- [53] W. H. Press and S. A. Teukolsky, “Perturbations of a Rotating Black Hole. II. Dynamical Stability of the Kerr Metric,” *Astrophysical Journal* **185** (1973) 649–674.
- [54] S. Teukolsky and W. Press, “Perturbations of a rotating black hole. III - Interaction of the hole with gravitational and electromagnetic radiation,” *Astrophysical Journal* **193** (1974) 443–461.
- [55] S. Chandrasekhar and S. L. Detweiler, “The quasi-normal modes of the Schwarzschild black hole,” *Proc.Roy.Soc.Lond.* **A344** (1975) 441–452.
- [56] E. Leaver, “An Analytic representation for the quasi normal modes of Kerr black holes,” *Proc.Roy.Soc.Lond.* **A402** (1985) 285–298.
- [57] K. D. Kokkotas and B. G. Schmidt, “Quasinormal modes of stars and black holes,” *Living Rev.Rel.* **2** (1999) 2, [arXiv:gr-qc/9909058 \[gr-qc\]](#).
- [58] E. Berti, V. Cardoso, and A. O. Starinets, “Quasinormal modes of black holes and black branes,” *Class.Quant.Grav.* **26** (2009) 163001, [arXiv:0905.2975 \[gr-qc\]](#).
- [59] A. Ghosh *et al.*, “Testing general relativity using golden black-hole binaries,” *Phys. Rev.* **D94** no. 2, (2016) 021101, [arXiv:1602.02453 \[gr-qc\]](#).
- [60] T. Li, W. Del Pozzo, S. Vitale, C. Van Den Broeck, M. Agathos, J. Veitch, K. Grover, T. Sidery, R. Sturani, and A. Vecchio, “Towards a generic test of the strong field dynamics of general relativity using compact binary coalescence,” *Phys. Rev. D* **85** (2012) 082003, [arXiv:1110.0530 \[gr-qc\]](#).
- [61] M. Agathos, W. Del Pozzo, T. G. F. Li, C. Van Den Broeck, J. Veitch, and S. Vitale, “TIGER: A data analysis pipeline for testing the strong-field dynamics of general relativity with gravitational wave signals from coalescing compact binaries,” *Phys. Rev. D* **89** no. 8, (2014) 082001, [arXiv:1311.0420 \[gr-qc\]](#).

- [62] N. Wex, “Testing Relativistic Gravity with Radio Pulsars,” arXiv:1402.5594 [gr-qc].
- [63] N. Yunes and F. Pretorius, “Fundamental Theoretical Bias in Gravitational Wave Astrophysics and the Parameterized Post-Einsteinian Framework,” *Phys.Rev.* **D80** (2009) 122003, arXiv:0909.3328 [gr-qc].
- [64] N. Yunes, K. Yagi, and F. Pretorius, “Theoretical Physics Implications of the Binary Black-Hole Mergers GW150914 and GW151226,” *Phys. Rev.* **D94** no. 8, (2016) 084002, arXiv:1603.08955 [gr-qc].
- [65] E. Poisson, “Gravitational waves from inspiraling compact binaries: The Quadrupole moment term,” *Phys. Rev. D* **57** (1998) 5287–5290, arXiv:gr-qc/9709032.
- [66] R. O. Hansen, “Multipole moments of stationary space-times,” *J. Math. Phys.* **15** (1974) 46–52.
- [67] G. Pappas and T. A. Apostolatos, “Revising the multipole moments of numerical spacetimes, and its consequences,” *Phys. Rev. Lett.* **108** (2012) 231104, arXiv:1201.6067 [gr-qc].
- [68] I. Harry and T. Hinderer, “Observing and measuring the neutron-star equation-of-state in spinning binary neutron star systems,” *Class. Quant. Grav.* **35** no. 14, (2018) 145010, arXiv:1801.09972 [gr-qc].
- [69] F. D. Ryan, “Spinning boson stars with large selfinteraction,” *Phys.Rev.* **D55** (1997) 6081–6091.
- [70] C. A. R. Herdeiro and E. Radu, “Kerr black holes with scalar hair,” *Phys.Rev.Lett.* **112** (2014) 221101, arXiv:1403.2757 [gr-qc].
- [71] N. V. Krishnendu, K. G. Arun, and C. K. Mishra, “Testing the binary black hole nature of a compact binary coalescence,” *Phys. Rev. Lett.* **119** no. 9, (2017) 091101, arXiv:1701.06318 [gr-qc].
- [72] O. Dreyer, B. J. Kelly, B. Krishnan, L. S. Finn, D. Garrison, and R. Lopez-Aleman, “Black hole spectroscopy: Testing general relativity through gravitational wave observations,” *Class. Quant. Grav.* **21** (2004) 787–804, arXiv:gr-qc/0309007.
- [73] S. Gossan, J. Veitch, and B. Sathyaprakash, “Bayesian model selection for testing the no-hair theorem with black hole ringdowns,” *Phys. Rev. D* **85** (2012) 124056, arXiv:1111.5819 [gr-qc].
- [74] R. Brito, A. Buonanno, and V. Raymond, “Black-hole Spectroscopy by Making Full Use of Gravitational-Wave Modeling,” *Phys. Rev. D* **98** no. 8, (2018) 084038, arXiv:1805.00293 [gr-qc].

- [75] G. Carullo, W. Del Pozzo, and J. Veitch, “Observational Black Hole Spectroscopy: A time-domain multimode analysis of GW150914,” *Phys. Rev. D* **99** no. 12, (2019) 123029, [arXiv:1902.07527 \[gr-qc\]](#).
[Erratum: *Phys.Rev.D* 100, 089903 (2019)].
- [76] M. Isi, M. Giesler, W. M. Farr, M. A. Scheel, and S. A. Teukolsky, “Testing the no-hair theorem with GW150914,” *Phys. Rev. Lett.* **123** no. 11, (2019) 111102, [arXiv:1905.00869 \[gr-qc\]](#).
- [77] S. Bhagwat, X. J. Forteza, P. Pani, and V. Ferrari, “Ringdown overtones, black hole spectroscopy, and no-hair theorem tests,” *Phys. Rev. D* **101** no. 4, (2020) 044033, [arXiv:1910.08708 \[gr-qc\]](#).
- [78] C. D. Capano, M. Cabero, J. Westerweck, J. Abedi, S. Kasta, A. H. Nitz, A. B. Nielsen, and B. Krishnan, “Observation of a multimode quasi-normal spectrum from a perturbed black hole,” [arXiv:2105.05238 \[gr-qc\]](#).
- [79] A. Ghosh, R. Brito, and A. Buonanno, “Constraints on quasinormal-mode frequencies with LIGO-Virgo binary-black-hole observations,” *Phys. Rev. D* **103** no. 12, (2021) 124041, [arXiv:2104.01906 \[gr-qc\]](#).
- [80] J. Abedi, N. Afshordi, N. Oshita, and Q. Wang, “Quantum Black Holes in the Sky,” *Universe* **6** no. 3, (2020) 43, [arXiv:2001.09553 \[gr-qc\]](#).
- [81] H. Nakano, N. Sago, H. Tagoshi, and T. Tanaka, “Black hole ringdown echoes and howls,” *PTEP* **2017** no. 7, (2017) 071E01, [arXiv:1704.07175 \[gr-qc\]](#).
- [82] Q. Wang and N. Afshordi, “Black hole echology: The observer’s manual,” *Phys. Rev. D* **97** no. 12, (2018) 124044, [arXiv:1803.02845 \[gr-qc\]](#).
- [83] A. Maselli, S. H. Völkel, and K. D. Kokkotas, “Parameter estimation of gravitational wave echoes from exotic compact objects,” *Phys. Rev. D* **96** no. 6, (2017) 064045, [arXiv:1708.02217 \[gr-qc\]](#).
- [84] Z. Mark, A. Zimmerman, S. M. Du, and Y. Chen, “A recipe for echoes from exotic compact objects,” *Phys. Rev.* **D96** no. 8, (2017) 084002, [arXiv:1706.06155 \[gr-qc\]](#).
- [85] A. Testa and P. Pani, “Analytical template for gravitational-wave echoes: signal characterization and prospects of detection with current and future interferometers,” *Phys. Rev.* **D98** no. 4, (2018) 044018, [arXiv:1806.04253 \[gr-qc\]](#).
- [86] K. W. Tsang, M. Rollier, A. Ghosh, A. Samajdar, M. Agathos, K. Chatziioannou, V. Cardoso, G. Khanna, and C. Van Den Broeck, “A

- morphology-independent data analysis method for detecting and characterizing gravitational wave echoes,” *Phys. Rev.* **D98** no. 2, (2018) 024023, [arXiv:1804.04877 \[gr-qc\]](#).
- [87] K. W. Tsang, A. Ghosh, A. Samajdar, K. Chatziioannou, S. Mastrogiovanni, M. Agathos, and C. Van Den Broeck, “A morphology-independent search for gravitational wave echoes in data from the first and second observing runs of Advanced LIGO and Advanced Virgo,” *Phys. Rev. D* **101** no. 6, (2020) 064012, [arXiv:1906.11168 \[gr-qc\]](#).
- [88] R. S. Conklin, B. Holdom, and J. Ren, “Gravitational wave echoes through new windows,” *Phys. Rev.* **D98** no. 4, (2018) 044021, [arXiv:1712.06517 \[gr-qc\]](#).
- [89] R. S. Conklin and B. Holdom, “Gravitational wave echo spectra,” *Phys. Rev.* **D100** no. 12, (2019) 124030, [arXiv:1905.09370 \[gr-qc\]](#).
- [90] J. Abedi and N. Afshordi, “Echoes from the Abyss: A highly spinning black hole remnant for the binary neutron star merger GW170817,” *JCAP* **11** (2019) 010, [arXiv:1803.10454 \[gr-qc\]](#).
- [91] A. B. Nielsen, C. D. Capano, O. Birnholtz, and J. Westerweck, “Parameter estimation and statistical significance of echoes following black hole signals in the first Advanced LIGO observing run,” *Phys. Rev.* **D99** no. 10, (2019) 104012, [arXiv:1811.04904 \[gr-qc\]](#).
- [92] N. Uchikata, H. Nakano, T. Narikawa, N. Sago, H. Tagoshi, and T. Tanaka, “Searching for black hole echoes from the LIGO-Virgo Catalog GWTC-1,” *Phys. Rev.* **D100** no. 6, (2019) 062006, [arXiv:1906.00838 \[gr-qc\]](#).
- [93] R. K. L. Lo, T. G. F. Li, and A. J. Weinstein, “Template-based Gravitational-Wave Echoes Search Using Bayesian Model Selection,” *Phys. Rev.* **D99** no. 8, (2019) 084052, [arXiv:1811.07431 \[gr-qc\]](#).
- [94] S. Hild *et al.*, “Sensitivity Studies for Third-Generation Gravitational Wave Observatories,” *Class. Quant. Grav.* **28** (2011) 094013, [arXiv:1012.0908 \[gr-qc\]](#).
- [95] A. Klein *et al.*, “Science with the space-based interferometer eLISA: Supermassive black hole binaries,” *Phys. Rev.* **D93** no. 2, (2016) 024003, [arXiv:1511.05581 \[gr-qc\]](#).
- [96] L. Barack and C. Cutler, “Using LISA EMRI sources to test off-Kerr deviations in the geometry of massive black holes,” *Phys. Rev. D* **75** (2007) 042003, [arXiv:gr-qc/0612029](#).

- [97] K. Glampedakis and S. Babak, “Mapping spacetimes with LISA: Inspiral of a test-body in a ‘quasi-Kerr’ field,” *Class. Quant. Grav.* **23** (2006) 4167–4188, [arXiv:gr-qc/0510057](#).
- [98] A. M. Ghez *et al.*, “Measuring Distance and Properties of the Milky Way’s Central Supermassive Black Hole with Stellar Orbits,” *Astrophys. J.* **689** (2008) 1044–1062, [arXiv:0808.2870 \[astro-ph\]](#).
- [99] **Event Horizon Telescope** Collaboration, K. Akiyama *et al.*, “First M87 Event Horizon Telescope Results. I. The Shadow of the Supermassive Black Hole,” *Astrophys. J. Lett.* **875** (2019) L1, [arXiv:1906.11238 \[astro-ph.GA\]](#).
- [100] P. O. Mazur and E. Mottola, “Gravitational condensate stars: An alternative to black holes,” [arXiv:gr-qc/0109035 \[gr-qc\]](#).
- [101] S. D. Mathur, “The Fuzzball proposal for black holes: An Elementary review,” *Fortsch. Phys.* **53** (2005) 793–827, [arXiv:hep-th/0502050 \[hep-th\]](#).
- [102] S. W. Hawking, “Black hole explosions,” *Nature* **248** (1974) 30–31.
- [103] S. W. Hawking, “Black Holes and Thermodynamics,” *Phys. Rev. D* **13** (1976) 191–197.
- [104] J. D. Bekenstein, “Black holes and entropy,” *Phys. Rev. D* **7** (1973) 2333–2346.
- [105] S. B. Giddings, “Black holes and massive remnants,” *Phys. Rev. D* **46** (1992) 1347–1352, [arXiv:hep-th/9203059 \[hep-th\]](#).
- [106] S. B. Giddings, “Nonlocality versus complementarity: A Conservative approach to the information problem,” *Class. Quant. Grav.* **28** (2011) 025002, [arXiv:0911.3395 \[hep-th\]](#).
- [107] S. B. Giddings, “Black holes, quantum information, and unitary evolution,” *Phys. Rev. D* **85** (2012) 124063, [arXiv:1201.1037 \[hep-th\]](#).
- [108] O. Lunin and S. D. Mathur, “Statistical interpretation of Bekenstein entropy for systems with a stretched horizon,” *Phys. Rev. Lett.* **88** (2002) 211303, [arXiv:hep-th/0202072 \[hep-th\]](#).
- [109] P. O. Mazur and E. Mottola, “Gravitational vacuum condensate stars,” *Proc. Nat. Acad. Sci.* **101** (2004) 9545–9550, [arXiv:gr-qc/0407075 \[gr-qc\]](#).
- [110] S. D. Mathur, “Fuzzballs and the information paradox: A Summary and conjectures,” [arXiv:0810.4525 \[hep-th\]](#).

- [111] N. Engelhardt and A. C. Wall, “Quantum Extremal Surfaces: Holographic Entanglement Entropy beyond the Classical Regime,” *JHEP* **01** (2015) 073, [arXiv:1408.3203 \[hep-th\]](#).
- [112] A. Almheiri, N. Engelhardt, D. Marolf, and H. Maxfield, “The entropy of bulk quantum fields and the entanglement wedge of an evaporating black hole,” *JHEP* **12** (2019) 063, [arXiv:1905.08762 \[hep-th\]](#).
- [113] D. Marolf and H. Maxfield, “Observations of Hawking radiation: the Page curve and baby universes,” *JHEP* **04** (2021) 272, [arXiv:2010.06602 \[hep-th\]](#).
- [114] P. Nicolini, A. Smailagic, and E. Spallucci, “Noncommutative geometry inspired Schwarzschild black hole,” *Phys. Lett. B* **632** (2006) 547–551, [arXiv:gr-qc/0510112](#).
- [115] I. Bena and N. P. Warner, “Black holes, black rings and their microstates,” *Lect. Notes Phys.* **755** (2008) 1–92, [arXiv:hep-th/0701216 \[hep-th\]](#).
- [116] S. B. Giddings, “Possible observational windows for quantum effects from black holes,” *Phys. Rev.* **D90** no. 12, (2014) 124033, [arXiv:1406.7001 \[hep-th\]](#).
- [117] A. S. Koshelev and A. Mazumdar, “Do massive compact objects without event horizon exist in infinite derivative gravity?,” *Phys. Rev.* **D96** no. 8, (2017) 084069, [arXiv:1707.00273 \[gr-qc\]](#).
- [118] S. L. Liebling and C. Palenzuela, “Dynamical Boson Stars,” *Living Rev. Rel.* **15** (2012) 6, [arXiv:1202.5809 \[gr-qc\]](#).
- [119] R. Brito, V. Cardoso, C. A. R. Herdeiro, and E. Radu, “Proca stars: Gravitating Bose Einstein condensates of massive spin 1 particles,” *Phys. Lett.* **B752** (2016) 291–295, [arXiv:1508.05395 \[gr-qc\]](#).
- [120] D. A. Feinblum and W. A. McKinley, “Stable States of a Scalar Particle in Its Own Gravitational Field,” *Phys. Rev.* **168** no. 5, (1968) 1445.
- [121] D. J. Kaup, “Klein-Gordon Geon,” *Phys. Rev.* **172** (1968) 1331–1342.
- [122] R. Ruffini and S. Bonazzola, “Systems of selfgravitating particles in general relativity and the concept of an equation of state,” *Phys. Rev.* **187** (1969) 1767–1783.
- [123] E. Seidel and W. Suen, “Oscillating soliton stars,” *Phys. Rev. Lett.* **66** (1991) 1659–1662.
- [124] A. Einstein and N. Rosen, “The Particle Problem in the General Theory of Relativity,” *Phys. Rev.* **48** (1935) 73–77.

- [125] M. S. Morris and K. S. Thorne, “Wormholes in space-time and their use for interstellar travel: A tool for teaching general relativity,” *Am. J. Phys.* **56** (1988) 395–412.
- [126] T. Damour and S. N. Solodukhin, “Wormholes as black hole foils,” *Phys. Rev.* **D76** (2007) 024016, [arXiv:0704.2667 \[gr-qc\]](#).
- [127] R. L. Bowers and E. P. T. Liang, “Anisotropic Spheres in General Relativity,” *Astrophys. J.* **188** (1974) 657–665.
- [128] E. G. Gimon and P. Horava, “Astrophysical violations of the Kerr bound as a possible signature of string theory,” *Phys.Lett.* **B672** (2009) 299–302, [arXiv:0706.2873 \[hep-th\]](#).
- [129] R. Brustein and A. J. M. Medved, “Black holes as collapsed polymers,” *Fortsch. Phys.* **65** (2017) 0114, [arXiv:1602.07706 \[hep-th\]](#).
- [130] B. Holdom and J. Ren, “Not quite a black hole,” *Phys. Rev.* **D95** no. 8, (2017) 084034, [arXiv:1612.04889 \[gr-qc\]](#).
- [131] L. Buoninfante and A. Mazumdar, “Nonlocal star as a blackhole mimicker,” *Phys. Rev. D* **100** no. 2, (2019) 024031, [arXiv:1903.01542 \[gr-qc\]](#).
- [132] P. Pani, E. Barausse, E. Berti, and V. Cardoso, “Gravitational instabilities of superspinars,” *Phys.Rev.* **D82** (2010) 044009, [arXiv:1006.1863 \[gr-qc\]](#).
- [133] V. Cardoso, P. Pani, M. Cadoni, and M. Cavaglia, “Ergoregion instability of ultracompact astrophysical objects,” *Phys.Rev.* **D77** (2008) 124044, [arXiv:0709.0532 \[gr-qc\]](#).
- [134] J. P. S. Lemos and O. B. Zaslavskii, “Black hole mimickers: Regular versus singular behavior,” *Phys. Rev. D* **78** (2008) 024040, [arXiv:0806.0845 \[gr-qc\]](#).
- [135] E. Seidel and W.-M. Suen, “Formation of solitonic stars through gravitational cooling,” *Phys. Rev. Lett.* **72** (1994) 2516–2519, [arXiv:gr-qc/9309015](#).
- [136] **LIGO Scientific, Virgo** Collaboration, R. Abbott *et al.*, “Properties and Astrophysical Implications of the 150 M_{\odot} Binary Black Hole Merger GW190521,” *Astrophys. J. Lett.* **900** no. 1, (2020) L13, [arXiv:2009.01190 \[astro-ph.HE\]](#).
- [137] E. Maggio, P. Pani, and G. Raposo, “Testing the nature of dark compact objects with gravitational waves,” [arXiv:2105.06410 \[gr-qc\]](#).

- [138] V. Cardoso and P. Pani, “Tests for the existence of black holes through gravitational wave echoes,” *Nature Astron.* **1** no. 9, (2017) 586–591, [arXiv:1709.01525 \[gr-qc\]](#).
- [139] G. Raposo, P. Pani, and R. Emparan, “Exotic compact objects with soft hair,” *Phys. Rev. D* **99** no. 10, (2019) 104050, [arXiv:1812.07615 \[gr-qc\]](#).
- [140] H. A. Buchdahl, “General Relativistic Fluid Spheres,” *Phys. Rev.* **116** (1959) 1027.
- [141] A. Urbano and H. Veermäe, “On gravitational echoes from ultracompact exotic stars,” *JCAP* **04** (2019) 011, [arXiv:1810.07137 \[gr-qc\]](#).
- [142] R. L. Bowers and E. P. T. Liang, “Anisotropic Spheres in General Relativity,” *Astrophys. J.* **188** (Mar., 1974) 657.
- [143] G. Raposo, P. Pani, M. Bezares, C. Palenzuela, and V. Cardoso, “Anisotropic stars as ultracompact objects in General Relativity,” *Phys. Rev. D* **99** no. 10, (2019) 104072, [arXiv:1811.07917 \[gr-qc\]](#).
- [144] E. Mottola and R. Vaulin, “Macroscopic Effects of the Quantum Trace Anomaly,” *Phys. Rev. D* **74** (2006) 064004, [arXiv:gr-qc/0604051 \[gr-qc\]](#).
- [145] M. Visser, *Lorentzian wormholes: From Einstein to Hawking*. AIP Press, American Institute of Physics, 1995.
- [146] P. Jetzer, “Boson stars,” *Phys. Rep.* **220** (1992) 163–227.
- [147] F. Schunck and E. Mielke, “General relativistic boson stars,” *Class. Quant. Grav.* **20** (2003) R301–R356, [arXiv:0801.0307 \[astro-ph\]](#).
- [148] R. M. Wald, *General relativity*. Chicago Univ. Press, Chicago, IL, 1984. <https://cds.cern.ch/record/106274>.
- [149] H. Okawa, V. Cardoso, and P. Pani, “Collapse of self-interacting fields in asymptotically flat spacetimes: do self-interactions render Minkowski spacetime unstable?,” *Phys. Rev. D* **89** no. 4, (2014) 041502, [arXiv:1311.1235 \[gr-qc\]](#).
- [150] C. Palenzuela, L. Lehner, and S. L. Liebling, “Orbital Dynamics of Binary Boson Star Systems,” *Phys. Rev. D* **77** (2008) 044036, [arXiv:0706.2435 \[gr-qc\]](#).
- [151] C. Palenzuela, P. Pani, M. Bezares, V. Cardoso, L. Lehner, and S. Liebling, “Gravitational Wave Signatures of Highly Compact Boson Star Binaries,” *Phys. Rev. D* **96** no. 10, (2017) 104058, [arXiv:1710.09432 \[gr-qc\]](#).

- [152] N. Sanchis-Gual, C. Herdeiro, J. A. Font, E. Radu, and F. Di Giovanni, “Head-on collisions and orbital mergers of Proca stars,” *Phys. Rev. D* **99** no. 2, (2019) 024017, [arXiv:1806.07779 \[gr-qc\]](#).
- [153] T. D. Lee and Y. Pang, “Stability of Mini - Boson Stars,” *Nucl. Phys.* **B315** (1989) 477.
- [154] M. Colpi, S. Shapiro, and I. Wasserman, “Boson Stars: Gravitational Equilibria of Selfinteracting Scalar Fields,” *Phys. Rev. Lett.* **57** (1986) 2485–2488.
- [155] R. Friedberg, T. D. Lee, and Y. Pang, “Scalar Soliton Stars and Black Holes,” *Phys. Rev.* **D35** (1987) 3658. [,73(1986)].
- [156] T. D. Lee, “Soliton Stars and the Critical Masses of Black Holes,” *Phys. Rev. D* **35** (1987) 3637.
- [157] M. Visser and D. L. Wiltshire, “Stable gravastars: An Alternative to black holes?,” *Class. Quant. Grav.* **21** (2004) 1135–1152, [arXiv:gr-qc/0310107 \[gr-qc\]](#).
- [158] P. O. Mazur and E. Mottola, “Surface tension and negative pressure interior of a non-singular "black hole",” *Class. Quant. Grav.* **32** no. 21, (2015) 215024, [arXiv:1501.03806 \[gr-qc\]](#).
- [159] P. Kanti, B. Kleihaus, and J. Kunz, “Wormholes in Dilatonic Einstein-Gauss-Bonnet Theory,” *Phys. Rev. Lett.* **107** (2011) 271101, [arXiv:1108.3003 \[gr-qc\]](#).
- [160] J. A. Gonzalez, F. S. Guzman, and O. Sarbach, “Instability of wormholes supported by a ghost scalar field. I. Linear stability analysis,” *Class. Quant. Grav.* **26** (2009) 015010, [arXiv:0806.0608 \[gr-qc\]](#).
- [161] K. A. Bronnikov, R. A. Konoplya, and A. Zhidenko, “Instabilities of wormholes and regular black holes supported by a phantom scalar field,” *Phys. Rev.* **D86** (2012) 024028, [arXiv:1205.2224 \[gr-qc\]](#).
- [162] O. Lunin and S. D. Mathur, “AdS / CFT duality and the black hole information paradox,” *Nucl. Phys.* **B623** (2002) 342–394, [arXiv:hep-th/0109154 \[hep-th\]](#).
- [163] V. Balasubramanian, J. de Boer, S. El-Showk, and I. Messamah, “Black Holes as Effective Geometries,” *Class. Quant. Grav.* **25** (2008) 214004, [arXiv:0811.0263 \[hep-th\]](#).
- [164] I. Bena and N. P. Warner, “Resolving the Structure of Black Holes: Philosophizing with a Hammer,” [arXiv:1311.4538 \[hep-th\]](#).

- [165] G. W. Gibbons and N. P. Warner, “Global structure of five-dimensional fuzzballs,” *Class. Quant. Grav.* **31** (2014) 025016, [arXiv:1305.0957 \[hep-th\]](#).
- [166] B. Bates and F. Denef, “Exact solutions for supersymmetric stationary black hole composites,” *JHEP* **11** (2011) 127, [arXiv:hep-th/0304094](#).
- [167] M. Bianchi, D. Consoli, A. Grillo, J. F. Morales, P. Pani, and G. Raposo, “Distinguishing fuzzballs from black holes through their multipolar structure,” *Phys. Rev. Lett.* **125** no. 22, (2020) 221601, [arXiv:2007.01743 \[hep-th\]](#).
- [168] M. Bianchi, D. Consoli, A. Grillo, J. F. Morales, P. Pani, and G. Raposo, “The multipolar structure of fuzzballs,” *JHEP* **01** (2021) 003, [arXiv:2008.01445 \[hep-th\]](#).
- [169] S. S. Bayin, “Anisotropic Fluid Spheres in General Relativity,” *Phys. Rev.* **D26** (1982) 1262.
- [170] K. Dev and M. Gleiser, “Anisotropic stars: Exact solutions,” *Gen. Rel. Grav.* **34** (2002) 1793–1818, [arXiv:astro-ph/0012265 \[astro-ph\]](#).
- [171] M. K. Mak and T. Harko, “Anisotropic stars in general relativity,” *Proc. Roy. Soc. Lond.* **A459** (2003) 393–408, [arXiv:gr-qc/0110103 \[gr-qc\]](#).
- [172] H. Andreasson, “Sharp bounds on $2m/r$ of general spherically symmetric static objects,” *J. Diff. Eq.* **245** (2008) 2243–2266, [arXiv:gr-qc/0702137 \[gr-qc\]](#).
- [173] K. Dev and M. Gleiser, “Anisotropic stars. 2. Stability,” *Gen. Rel. Grav.* **35** (2003) 1435–1457, [arXiv:gr-qc/0303077 \[gr-qc\]](#).
- [174] L. Herrera, A. Di Prisco, J. Martin, J. Ospino, N. O. Santos, and O. Troconis, “Spherically symmetric dissipative anisotropic fluids: A General study,” *Phys. Rev.* **D69** (2004) 084026, [arXiv:gr-qc/0403006 \[gr-qc\]](#).
- [175] D. D. Doneva and S. S. Yazadjiev, “Gravitational wave spectrum of anisotropic neutron stars in Cowling approximation,” *Phys. Rev.* **D85** (2012) 124023, [arXiv:1203.3963 \[gr-qc\]](#).
- [176] H. O. Silva, C. F. B. Macedo, E. Berti, and L. C. B. Crispino, “Slowly rotating anisotropic neutron stars in general relativity and scalar-tensor theory,” *Class. Quant. Grav.* **32** (2015) 145008, [arXiv:1411.6286 \[gr-qc\]](#).

- [177] K. Yagi and N. Yunes, “I-Love-Q anisotropically: Universal relations for compact stars with scalar pressure anisotropy,” *Phys. Rev.* **D91** no. 12, (2015) 123008, [arXiv:1503.02726 \[gr-qc\]](#).
- [178] A. Almheiri, D. Marolf, J. Polchinski, and J. Sully, “Black Holes: Complementarity or Firewalls?,” *JHEP* **02** (2013) 062, [arXiv:1207.3123 \[hep-th\]](#).
- [179] D. E. Kaplan and S. Rajendran, “Firewalls in General Relativity,” *Phys. Rev.* **D99** no. 4, (2019) 044033, [arXiv:1812.00536 \[hep-th\]](#).
- [180] J. Zhang and S.-Y. Zhou, “Can the graviton have a large mass near black holes?,” *Phys. Rev. D* **97** no. 8, (2018) 081501, [arXiv:1709.07503 \[gr-qc\]](#).
- [181] N. Oshita and N. Afshordi, “Probing microstructure of black hole spacetimes with gravitational wave echoes,” *Phys. Rev. D* **99** no. 4, (2019) 044002, [arXiv:1807.10287 \[gr-qc\]](#).
- [182] V. P. Frolov, “Mass-gap for black hole formation in higher derivative and ghost free gravity,” *Phys. Rev. Lett.* **115** no. 5, (2015) 051102, [arXiv:1505.00492 \[hep-th\]](#).
- [183] L. Buoninfante, A. S. Cornell, G. Harmsen, A. S. Koshelev, G. Lambiase, J. a. Marto, and A. Mazumdar, “Towards nonsingular rotating compact object in ghost-free infinite derivative gravity,” *Phys. Rev. D* **98** no. 8, (2018) 084041, [arXiv:1807.08896 \[gr-qc\]](#).
- [184] G. A. Piovano, A. Maselli, and P. Pani, “Model independent tests of the Kerr bound with extreme mass ratio inspirals,” *Phys. Lett. B* **811** (2020) 135860, [arXiv:2003.08448 \[gr-qc\]](#).
- [185] C. A. R. Herdeiro, J. Kunz, I. Perapechka, E. Radu, and Y. Shnir, “Multipolar boson stars: macroscopic Bose-Einstein condensates akin to hydrogen orbitals,” *Phys. Lett. B* **812** (2021) 136027, [arXiv:2008.10608 \[gr-qc\]](#).
- [186] I. Bena and D. R. Mayerson, “Multipole Ratios: A New Window into Black Holes,” *Phys. Rev. Lett.* **125** no. 22, (2020) 22, [arXiv:2006.10750 \[hep-th\]](#).
- [187] I. Bena and D. R. Mayerson, “Black Holes Lessons from Multipole Ratios,” *JHEP* **03** (2021) 114, [arXiv:2007.09152 \[hep-th\]](#).
- [188] P. Pani, “I-Love-Q relations for gravastars and the approach to the black-hole limit,” *Phys. Rev.* **D92** no. 12, (2015) 124030, [arXiv:1506.06050 \[gr-qc\]](#).

- [189] G. Raposo and P. Pani, “Axisymmetric deformations of neutron stars and gravitational-wave astronomy,” *Phys. Rev. D* **102** no. 4, (2020) 044045, [arXiv:2002.02555 \[gr-qc\]](#).
- [190] S. Kastha, A. Gupta, K. Arun, B. Sathyaprakash, and C. Van Den Broeck, “Testing the multipole structure of compact binaries using gravitational wave observations,” *Phys. Rev. D* **98** no. 12, (2018) 124033, [arXiv:1809.10465 \[gr-qc\]](#).
- [191] S. Babak, J. Gair, A. Sesana, E. Barausse, C. F. Sopuerta, C. P. L. Berry, E. Berti, P. Amaro-Seoane, A. Petiteau, and A. Klein, “Science with the space-based interferometer LISA. V: Extreme mass-ratio inspirals,” *Phys. Rev. D* **95** no. 10, (2017) 103012, [arXiv:1703.09722 \[gr-qc\]](#).
- [192] S. Kastha, A. Gupta, K. Arun, B. Sathyaprakash, and C. Van Den Broeck, “Testing the multipole structure and conservative dynamics of compact binaries using gravitational wave observations: The spinning case,” *Phys. Rev. D* **100** no. 4, (2019) 044007, [arXiv:1905.07277 \[gr-qc\]](#).
- [193] J. B. Hartle, “Tidal Friction in Slowly Rotating Black Holes,” *Phys. Rev. D* **8** (1973) 1010–1024.
- [194] S. A. Hughes, “The Evolution of circular, nonequatorial orbits of Kerr black holes due to gravitational wave emission,” *Phys. Rev. D* **61** no. 8, (2000) 084004, [arXiv:gr-qc/9910091](#). [Erratum: *Phys. Rev. D* **63**, 049902 (2001), Erratum: *Phys. Rev. D* **65**, 069902 (2002), Erratum: *Phys. Rev. D* **67**, 089901 (2003), Erratum: *Phys. Rev. D* **78**, 109902 (2008), Erratum: *Phys. Rev. D* **90**, 109904 (2014)].
- [195] S. A. Hughes, “Evolution of circular, nonequatorial orbits of Kerr black holes due to gravitational wave emission. 2. Inspiral trajectories and gravitational wave forms,” *Phys. Rev. D* **64** (2001) 064004, [arXiv:gr-qc/0104041 \[gr-qc\]](#).
- [196] A. Maselli, P. Pani, V. Cardoso, T. Abdelsalhin, L. Gualtieri, and V. Ferrari, “Probing Planckian corrections at the horizon scale with LISA binaries,” *Phys. Rev. Lett.* **120** no. 8, (2018) 081101, [arXiv:1703.10612 \[gr-qc\]](#).
- [197] E. Poisson and C. Will, *Gravity: Newtonian, Post-Newtonian, Relativistic*. Cambridge University Press, 2014. <https://books.google.it/books?id=PZ5cAwwAAQBAJ>.
- [198] T. Binnington and E. Poisson, “Relativistic theory of tidal Love numbers,” *Phys. Rev. D* **80** (2009) 084018, [arXiv:0906.1366 \[gr-qc\]](#).

- [199] T. Damour and A. Nagar, “Relativistic tidal properties of neutron stars,” *Phys. Rev. D* **80** (2009) 084035, [arXiv:0906.0096 \[gr-qc\]](#).
- [200] E. Poisson, “Tidal deformation of a slowly rotating black hole,” *Phys. Rev. D* **91** no. 4, (2015) 044004, [arXiv:1411.4711 \[gr-qc\]](#).
- [201] P. Landry and E. Poisson, “Tidal deformation of a slowly rotating material body. External metric,” *Phys. Rev. D* **91** (2015) 104018, [arXiv:1503.07366 \[gr-qc\]](#).
- [202] P. Pani, L. Gualtieri, A. Maselli, and V. Ferrari, “Tidal deformations of a spinning compact object,” *Phys. Rev. D* **92** no. 2, (2015) 024010, [arXiv:1503.07365 \[gr-qc\]](#).
- [203] H. S. Chia, “Tidal deformation and dissipation of rotating black holes,” *Phys. Rev. D* **104** no. 2, (2021) 024013, [arXiv:2010.07300 \[gr-qc\]](#).
- [204] A. Le Tiec and M. Casals, “Spinning Black Holes Fall in Love,” *Phys. Rev. Lett.* **126** no. 13, (2021) 131102, [arXiv:2007.00214 \[gr-qc\]](#).
- [205] A. Le Tiec, M. Casals, and E. Franzin, “Tidal Love Numbers of Kerr Black Holes,” *Phys. Rev. D* **103** no. 8, (2021) 084021, [arXiv:2010.15795 \[gr-qc\]](#).
- [206] V. Cardoso, E. Franzin, A. Maselli, P. Pani, and G. Raposo, “Testing strong-field gravity with tidal Love numbers,” *Phys. Rev.* **D95** no. 8, (2017) 084014, [arXiv:1701.01116 \[gr-qc\]](#). [Addendum: *Phys. Rev.* **D95**, no. 8, 089901(2017)].
- [207] N. Sennett, T. Hinderer, J. Steinhoff, A. Buonanno, and S. Ossokine, “Distinguishing Boson Stars from Black Holes and Neutron Stars from Tidal Interactions in Inspiring Binary Systems,” *Phys. Rev. D* **96** no. 2, (2017) 024002, [arXiv:1704.08651 \[gr-qc\]](#).
- [208] R. F. P. Mendes and H. Yang, “Tidal deformability of boson stars and dark matter clumps,” *Class. Quant. Grav.* **34** no. 18, (2017) 185001, [arXiv:1606.03035 \[astro-ph.CO\]](#).
- [209] N. Uchikata, S. Yoshida, and P. Pani, “Tidal deformability and I-Love-Q relations for gravastars with polytropic thin shells,” *Phys. Rev. D* **94** no. 6, (2016) 064015, [arXiv:1607.03593 \[gr-qc\]](#).
- [210] E. Berti and V. Cardoso, “Supermassive black holes or boson stars? Hair counting with gravitational wave detectors,” *Int. J. Mod. Phys.* **D15** (2006) 2209–2216, [arXiv:gr-qc/0605101 \[gr-qc\]](#).
- [211] C. F. Macedo, P. Pani, V. Cardoso, and L. C. B. Crispino, “Astrophysical signatures of boson stars: quasinormal modes and inspiral resonances,” *Phys. Rev.* **D88** no. 6, (2013) 064046, [arXiv:1307.4812 \[gr-qc\]](#).

- [212] C. B. Chirenti and L. Rezzolla, “How to tell a gravastar from a black hole,” *Class. Quant. Grav.* **24** (2007) 4191–4206, [arXiv:0706.1513](#) [gr-qc].
- [213] P. Pani, E. Berti, V. Cardoso, Y. Chen, and R. Norte, “Gravitational wave signatures of the absence of an event horizon. I. Nonradial oscillations of a thin-shell gravastar,” *Phys. Rev.* **D80** (2009) 124047, [arXiv:0909.0287](#) [gr-qc].
- [214] C. Chirenti and L. Rezzolla, “Did GW150914 produce a rotating gravastar?,” *Phys. Rev.* **D94** no. 8, (2016) 084016, [arXiv:1602.08759](#) [gr-qc].
- [215] S. H. Völkel and K. D. Kokkotas, “A Semi-analytic Study of Axial Perturbations of Ultra Compact Stars,” *Class. Quant. Grav.* **34** no. 12, (2017) 125006, [arXiv:1703.08156](#) [gr-qc].
- [216] R. A. Konoplya and A. Zhidenko, “Wormholes versus black holes: quasinormal ringing at early and late times,” *JCAP* **1612** no. 12, (2016) 043, [arXiv:1606.00517](#) [gr-qc].
- [217] P. Bueno, P. A. Cano, F. Goelen, T. Hertog, and B. Vernocke, “Echoes of Kerr-like wormholes,” *Phys. Rev.* **D97** no. 2, (2018) 024040, [arXiv:1711.00391](#) [gr-qc].
- [218] V. Cardoso, O. J. Dias, J. L. Hovdebo, and R. C. Myers, “Instability of non-supersymmetric smooth geometries,” *Phys. Rev.* **D73** (2006) 064031, [arXiv:hep-th/0512277](#) [hep-th].
- [219] F. C. Eperon, H. S. Reall, and J. E. Santos, “Instability of supersymmetric microstate geometries,” *JHEP* **10** (2016) 031, [arXiv:1607.06828](#) [hep-th].
- [220] V. Cardoso, S. Hopper, C. F. B. Macedo, C. Palenzuela, and P. Pani, “Gravitational-wave signatures of exotic compact objects and of quantum corrections at the horizon scale,” *Phys. Rev. D* **94** no. 8, (2016) 084031, [arXiv:1608.08637](#) [gr-qc].
- [221] C. Barceló, R. Carballo-Rubio, and L. J. Garay, “Gravitational wave echoes from macroscopic quantum gravity effects,” *JHEP* **05** (2017) 054, [arXiv:1701.09156](#) [gr-qc].
- [222] R. Brustein, A. J. M. Medved, and K. Yagi, “When black holes collide: Probing the interior composition by the spectrum of ringdown modes and emitted gravitational waves,” *Phys. Rev.* **D96** no. 6, (2017) 064033, [arXiv:1704.05789](#) [gr-qc].

- [223] V. Ferrari and K. Kokkotas, “Scattering of particles by neutron stars: Time evolutions for axial perturbations,” *Phys. Rev. D* **62** (2000) 107504, arXiv:gr-qc/0008057.
- [224] P. Pani and V. Ferrari, “On gravitational-wave echoes from neutron-star binary coalescences,” *Class. Quant. Grav.* **35** no. 15, (2018) 15LT01, arXiv:1804.01444 [gr-qc].
- [225] K. Glampedakis and G. Pappas, “How well can ultracompact bodies imitate black hole ringdowns?,” *Phys. Rev. D* **97** no. 4, (2018) 041502, arXiv:1710.02136 [gr-qc].
- [226] M. Okounkova, L. C. Stein, M. A. Scheel, and D. A. Hemberger, “Numerical binary black hole mergers in dynamical Chern-Simons gravity: Scalar field,” *Phys. Rev. D* **96** no. 4, (2017) 044020, arXiv:1705.07924 [gr-qc].
- [227] J. L. Blázquez-Salcedo, C. F. B. Macedo, V. Cardoso, V. Ferrari, L. Gualtieri, F. S. Khoo, J. Kunz, and P. Pani, “Perturbed black holes in Einstein-dilaton-Gauss-Bonnet gravity: Stability, ringdown, and gravitational-wave emission,” *Phys. Rev. D* **94** no. 10, (2016) 104024, arXiv:1609.01286 [gr-qc].
- [228] O. J. Tattersall and P. G. Ferreira, “Quasinormal modes of black holes in Horndeski gravity,” *Phys. Rev. D* **97** no. 10, (2018) 104047, arXiv:1804.08950 [gr-qc].
- [229] T. Regge and J. A. Wheeler, “Stability of a Schwarzschild singularity,” *Phys.Rev.* **108** (1957) 1063–1069.
- [230] F. J. Zerilli, “Effective potential for even parity Regge-Wheeler gravitational perturbation equations,” *Phys.Rev.Lett.* **24** (1970) 737–738.
- [231] P. Pani, “Advanced Methods in Black-Hole Perturbation Theory,” *Int.J.Mod.Phys.* **A28** (2013) 1340018, arXiv:1305.6759 [gr-qc].
- [232] S. Chandrasekhar, “On the equations governing the perturbations of the Schwarzschild black hole,” *Proc. Roy. Soc. Lond. A* **343** no. 1634, (1975) 289–298.
- [233] S. Chandrasekhar, *The mathematical theory of black holes*. Oxford University Press, 1983.
- [234] K. Glampedakis, A. D. Johnson, and D. Kennefick, “Darboux transformation in black hole perturbation theory,” *Phys. Rev. D* **96** no. 2, (2017) 024036, arXiv:1702.06459 [gr-qc].
- [235] T. Damour, “Surface Effects in Black-Hole Physics,” in *Marcel Grossmann Meeting: General Relativity*, p. 587. Jan., 1982.

- [236] K. S. Thorne, R. Price, and D. Macdonald, *Black holes: the membrane paradigm*. Yale University Press, 1986.
- [237] E. Maggio, L. Buoninfante, A. Mazumdar, and P. Pani, “How does a dark compact object ringdown?,” *Phys. Rev. D* **102** no. 6, (2020) 064053, [arXiv:2006.14628](https://arxiv.org/abs/2006.14628) [gr-qc].
- [238] R. Price and K. Thorne, “Membrane Viewpoint on Black Holes: Properties and Evolution of the Stretched Horizon,” *Phys. Rev. D* **33** (1986) 915–941.
- [239] G. Darmois, “Les équations de la gravitation einsteinienne,” *Mémorial de Sciences Mathématiques fascicule* **25** (1927) 1–48.
- [240] W. Israel, “Singular hypersurfaces and thin shells in general relativity,” *Nuovo Cim.* **B44S10** (1966) 1. [Nuovo Cim.B44,1(1966)].
- [241] J. L. Jaramillo, R. Panosso Macedo, and L. Al Sheikh, “Pseudospectrum and Black Hole Quasinormal Mode Instability,” *Phys. Rev. X* **11** no. 3, (2021) 031003, [arXiv:2004.06434](https://arxiv.org/abs/2004.06434) [gr-qc].
- [242] E. Berti, V. Cardoso, and C. M. Will, “On gravitational-wave spectroscopy of massive black holes with the space interferometer LISA,” *Phys.Rev.* **D73** (2006) 064030, [arXiv:gr-qc/0512160](https://arxiv.org/abs/gr-qc/0512160) [gr-qc].
- [243] P. Pani, E. Berti, V. Cardoso, Y. Chen, and R. Norte, “Gravitational-wave signature of a thin-shell gravastar,” *J. Phys. Conf. Ser.* **222** (2010) 012032.
- [244] Y. Kojima, “Equations governing the nonradial oscillations of a slowly rotating relativistic star,” *Phys.Rev.* **D46** (1992) 4289–4303.
- [245] F. Zerilli, “Gravitational field of a particle falling in a schwarzschild geometry analyzed in tensor harmonics,” *Phys.Rev.* **D2** (1970) 2141–2160.
- [246] I. Bah, I. Bena, P. Heidmann, Y. Li, and D. R. Mayerson, “Gravitational footprints of black holes and their microstate geometries,” *JHEP* **10** (2021) 138, [arXiv:2104.10686](https://arxiv.org/abs/2104.10686) [hep-th].
- [247] R. Penrose, “Gravitational collapse: The role of general relativity,” *Riv. Nuovo Cim.* **1** (1969) 252–276.
- [248] N. Comins and B. F. Schutz, “On the ergoregion instability,” *Proceedings of the Royal Society of London. Series A, Mathematical and Physical Sciences* **364** no. 1717, (1978) pp. 211–226. <http://www.jstor.org/stable/79759>.

- [249] G. Moschidis, “A Proof of Friedman’s Ergosphere Instability for Scalar Waves,” *Commun. Math. Phys.* **358** no. 2, (2018) 437–520, [arXiv:1608.02035 \[math.AP\]](#).
- [250] C. B. Chirenti and L. Rezzolla, “On the ergoregion instability in rotating gravastars,” *Phys.Rev.* **D78** (2008) 084011, [arXiv:0808.4080 \[gr-qc\]](#).
- [251] P. Pani, V. Cardoso, L. Gualtieri, E. Berti, and A. Ishibashi, “Perturbations of slowly rotating black holes: massive vector fields in the Kerr metric,” *Phys.Rev.* **D86** (2012) 104017, [arXiv:1209.0773 \[gr-qc\]](#).
- [252] S. A. Teukolsky, “Rotating black holes: Separable wave equations for gravitational and electromagnetic perturbations,” *Phys. Rev. Lett.* **29** (Oct, 1972) 1114–1118.
<https://link.aps.org/doi/10.1103/PhysRevLett.29.1114>.
- [253] S. A. Teukolsky, “Perturbations of a Rotating Black Hole. I. Fundamental Equations for Gravitational, Electromagnetic, and Neutrino-Field Perturbations,” *The Astroph. J.* **185** (Oct., 1973) 635–648.
- [254] S. Detweiler, “On resonant oscillations of a rapidly rotating black hole,” *Proceedings of the Royal Society of London Series A* **352** (July, 1977) 381–395.
- [255] M. Casals and A. C. Ottewill, “Canonical quantization of the electromagnetic field on the Kerr background,” *Phys. Rev. D* **71** (2005) 124016, [arXiv:gr-qc/0501005](#).
- [256] A. Vilenkin, “Exponential Amplification of Waves in the Gravitational Field of Ultrarelativistic Rotating Body,” *Phys.Lett.* **B78** (1978) 301–303.
- [257] E. Berti, V. Cardoso, and M. Casals, “Eigenvalues and eigenfunctions of spin-weighted spheroidal harmonics in four and higher dimensions,” *Phys.Rev.* **D73** (2006) 024013, [arXiv:gr-qc/0511111 \[gr-qc\]](#).
- [258] X.-L. Fan and Y.-B. Chen, “Stochastic gravitational-wave background from spin loss of black holes,” *Phys. Rev. D* **98** no. 4, (2018) 044020, [arXiv:1712.00784 \[gr-qc\]](#).
- [259] S. M. Du and Y. Chen, “Searching for near-horizon quantum structures in the binary black-hole stochastic gravitational-wave background,” *Phys. Rev. Lett.* **121** no. 5, (2018) 051105, [arXiv:1803.10947 \[gr-qc\]](#).
- [260] E. Barausse, R. Brito, V. Cardoso, I. Dvorkin, and P. Pani, “The stochastic gravitational-wave background in the absence of horizons,”

- Class. Quant. Grav.* **35** no. 20, (2018) 20LT01, arXiv:1805.08229 [gr-qc].
- [261] C. Cutler and L. Lindblom, “The Effect of Viscosity on Neutron Star Oscillations,” *The Astrophysical Journal* **314** (Mar., 1987) 234.
- [262] F. P. Esposito, “Absorption of Gravitational Energy by a Viscous Compressible Fluid,” *The Astrophysical Journal* **165** (Apr., 1971) 165.
- [263] D. Papadopoulos and F. P. Esposito, “Absorption of gravitational energy by a viscous compressible fluid in a curved spacetime,” *The Astrophysical Journal* **292** (May, 1985) 330–338.
- [264] N. Oshita, Q. Wang, and N. Afshordi, “On Reflectivity of Quantum Black Hole Horizons,” *JCAP* **04** (2020) 016, arXiv:1905.00464 [hep-th].
- [265] S. Detweiler, “On the equations governing the electromagnetic perturbations of the kerr black hole,” *Proceedings of the Royal Society of London. Series A, Mathematical and Physical Sciences* **349** no. 1657, (1976) 217–230. <http://www.jstor.org/stable/79029>.
- [266] A. R. King, “Black-hole magnetostatics,” *Math. Proc. Camb. Phil. Soc.* **81** (1977) 149.
- [267] A. A. Starobinskij and S. M. Churilov, “Amplification of electromagnetic and gravitational waves scattered by a rotating black hole.,” *Zhurnal Eksperimentalnoi i Teoreticheskoi Fiziki* **65** (1973) 3–11.
- [268] V. Cardoso, P. Pani, M. Cadoni, and M. Cavaglia, “Instability of hyper-compact Kerr-like objects,” *Class. Quant. Grav.* **25** (2008) 195010, arXiv:0808.1615 [gr-qc].
- [269] M. R. Correia and V. Cardoso, “Characterization of echoes: A Dyson-series representation of individual pulses,” *Phys. Rev. D* **97** no. 8, (2018) 084030, arXiv:1802.07735 [gr-qc].
- [270] <http://www.darkgra.org>.
- [271] T. Harmark, J. Natario, and R. Schiappa, “Greybody Factors for d-Dimensional Black Holes,” *Adv. Theor. Math. Phys.* **14** no. 3, (2010) 727–794, arXiv:0708.0017 [hep-th].
- [272] A. Buonanno, G. B. Cook, and F. Pretorius, “Inspirals, merger and ring-down of equal-mass black-hole binaries,” *Phys. Rev. D* **75** (2007) 124018, arXiv:gr-qc/0610122.
- [273] LIGO Collaboration, D. Shoemaker, “Advanced ligo anticipated sensitivity curves,” Tech. Rep. T0900288-v3, 2010. <https://dcc.ligo.org/LIGO-T0900288/public>.

- [274] V. Cardoso and P. Pani, “The observational evidence for horizons: from echoes to precision gravitational-wave physics,” [arXiv:1707.03021](#) [gr-qc].
- [275] E. E. Flanagan and S. A. Hughes, “Measuring gravitational waves from binary black hole coalescences: 1. Signal-to-noise for inspiral, merger, and ringdown,” *Phys. Rev. D* **57** (1998) 4535–4565, [arXiv:gr-qc/9701039](#).
- [276] M. Vallisneri, “Use and abuse of the Fisher information matrix in the assessment of gravitational-wave parameter-estimation prospects,” *Phys. Rev. D* **77** (2008) 042001, [arXiv:gr-qc/0703086](#).
- [277] **LIGO Scientific** Collaboration, B. P. Abbott *et al.*, “Exploring the Sensitivity of Next Generation Gravitational Wave Detectors,” *Class. Quant. Grav.* **34** no. 4, (2017) 044001, [arXiv:1607.08697](#) [astro-ph.IM].
- [278] R. Essick, S. Vitale, and M. Evans, “Frequency-dependent responses in third generation gravitational-wave detectors,” *Phys. Rev.* **D96** no. 8, (2017) 084004, [arXiv:1708.06843](#) [gr-qc].
- [279] S. A. Teukolsky, “Rotating black holes - separable wave equations for gravitational and electromagnetic perturbations,” *Phys. Rev. Lett.* **29** (1972) 1114–1118.
- [280] R. Fujita and H. Tagoshi, “New numerical methods to evaluate homogeneous solutions of the Teukolsky equation,” *Prog. Theor. Phys.* **112** (2004) 415–450, [arXiv:gr-qc/0410018](#).
- [281] M. van de Meent, “Resonantly enhanced kicks from equatorial small mass-ratio inspirals,” *Phys. Rev. D* **90** no. 4, (2014) 044027, [arXiv:1406.2594](#) [gr-qc].
- [282] M. van de Meent and A. G. Shah, “Metric perturbations produced by eccentric equatorial orbits around a Kerr black hole,” *Phys. Rev. D* **92** no. 6, (2015) 064025, [arXiv:1506.04755](#) [gr-qc].
- [283] M. van de Meent, “Gravitational self-force on eccentric equatorial orbits around a Kerr black hole,” *Phys. Rev. D* **94** no. 4, (2016) 044034, [arXiv:1606.06297](#) [gr-qc].
- [284] M. van de Meent, “Gravitational self-force on generic bound geodesics in Kerr spacetime,” *Phys. Rev. D* **97** no. 10, (2018) 104033, [arXiv:1711.09607](#) [gr-qc].
- [285] S. Mano, H. Suzuki, and E. Takasugi, “Analytic solutions of the Teukolsky equation and their low frequency expansions,” *Prog. Theor. Phys.* **95** (1996) 1079–1096, [arXiv:gr-qc/9603020](#).

- [286] S. Mano and E. Takasugi, “Analytic solutions of the Teukolsky equation and their properties,” *Prog. Theor. Phys.* **97** (1997) 213–232, [arXiv:gr-qc/9611014](#).
- [287] R. Fujita, W. Hikida, and H. Tagoshi, “An Efficient Numerical Method for Computing Gravitational Waves Induced by a Particle Moving on Eccentric Inclined Orbits around a Kerr Black Hole,” *Prog. Theor. Phys.* **121** (2009) 843–874, [arXiv:0904.3810 \[gr-qc\]](#).
- [288] A. Ori and K. S. Thorne, “The Transition from inspiral to plunge for a compact body in a circular equatorial orbit around a massive, spinning black hole,” *Phys. Rev. D* **62** (2000) 124022, [arXiv:gr-qc/0003032](#).
- [289] S. Bernuzzi, A. Nagar, and A. Zenginoglu, “Horizon-absorption effects in coalescing black-hole binaries: An effective-one-body study of the non-spinning case,” *Phys. Rev. D* **86** (2012) 104038, [arXiv:1207.0769 \[gr-qc\]](#).
- [290] A. Taracchini, A. Buonanno, S. A. Hughes, and G. Khanna, “Modeling the horizon-absorbed gravitational flux for equatorial-circular orbits in Kerr spacetime,” *Phys. Rev. D* **88** (2013) 044001, [arXiv:1305.2184 \[gr-qc\]](#). [Erratum: *Phys.Rev.D* 88, 109903 (2013)].
- [291] E. Harms, S. Bernuzzi, A. Nagar, and A. Zenginoglu, “A new gravitational wave generation algorithm for particle perturbations of the Kerr spacetime,” *Class. Quant. Grav.* **31** no. 24, (2014) 245004, [arXiv:1406.5983 \[gr-qc\]](#).
- [292] P. Pani, E. Berti, V. Cardoso, Y. Chen, and R. Norte, “Gravitational-wave signatures of the absence of an event horizon. II. Extreme mass ratio inspirals in the spacetime of a thin-shell gravastar,” *Phys. Rev.* **D81** (2010) 084011, [arXiv:1001.3031 \[gr-qc\]](#).
- [293] K. Fransen, G. Koekoek, R. Tielemans, and B. Vercoocke, “Modeling and detecting resonant tides of exotic compact objects,” *Phys. Rev. D* **104** no. 4, (2021) 044044, [arXiv:2005.12286 \[gr-qc\]](#).
- [294] J. A. Pons, E. Berti, L. Gualtieri, G. Miniutti, and V. Ferrari, “Gravitational signals emitted by a point mass orbiting a neutron star: Effects of stellar structure,” *Phys. Rev.* **D65** (2002) 104021, [arXiv:gr-qc/0111104 \[gr-qc\]](#).
- [295] S. J. Kapadia, D. Kennefick, and K. Glampedakis, “Do floating orbits in extreme mass ratio binary black holes exist?,” *Phys. Rev.* **D87** no. 4, (2013) 044050, [arXiv:1302.1016 \[gr-qc\]](#).
- [296] V. Cardoso, S. Chakrabarti, P. Pani, E. Berti, and L. Gualtieri, “Floating and sinking: The Imprint of massive scalars around rotating

- black holes,” *Phys.Rev.Lett.* **107** (2011) 241101, arXiv:1109.6021 [gr-qc].
- [297] T. Hinderer and E. E. Flanagan, “Two timescale analysis of extreme mass ratio inspirals in Kerr. I. Orbital Motion,” *Phys. Rev.* **D78** (2008) 064028, arXiv:0805.3337 [gr-qc].
- [298] L. Lindblom, B. J. Owen, and D. A. Brown, “Model Waveform Accuracy Standards for Gravitational Wave Data Analysis,” *Phys. Rev. D* **78** (2008) 124020, arXiv:0809.3844 [gr-qc].
- [299] B. Bonga, H. Yang, and S. A. Hughes, “Tidal resonance in extreme mass-ratio inspirals,” *Phys. Rev. Lett.* **123** no. 10, (2019) 101103, arXiv:1905.00030 [gr-qc].
- [300] G. A. Piovano, A. Maselli, and P. Pani, “Extreme mass ratio inspirals with spinning secondary: a detailed study of equatorial circular motion,” *Phys. Rev. D* **102** no. 2, (2020) 024041, arXiv:2004.02654 [gr-qc].
- [301] T. Robson, N. J. Cornish, and C. Liug, “The construction and use of LISA sensitivity curves,” *Class. Quant. Grav.* **36** no. 10, (2019) 105011, arXiv:1803.01944 [astro-ph.HE].
- [302] B. Allen, W. G. Anderson, P. R. Brady, D. A. Brown, and J. D. E. Creighton, “FINDCHIRP: An Algorithm for detection of gravitational waves from inspiraling compact binaries,” *Phys. Rev. D* **85** (2012) 122006, arXiv:gr-qc/0509116.
- [303] E. E. Flanagan and S. A. Hughes, “Measuring gravitational waves from binary black hole coalescences: 2. The Waves’ information and its extraction, with and without templates,” *Phys. Rev. D* **57** (1998) 4566–4587, arXiv:gr-qc/9710129.
- [304] S. Xin, B. Chen, R. K. L. Lo, L. Sun, W.-B. Han, X. Zhong, M. Srivastava, S. Ma, Q. Wang, and Y. Chen, “Gravitational-wave echoes from spinning exotic compact objects: numerical waveforms from the Teukolsky equation,” arXiv:2105.12313 [gr-qc].
- [305] B. Chen, Q. Wang, and Y. Chen, “Tidal response and near-horizon boundary conditions for spinning exotic compact objects,” *Phys. Rev. D* **103** no. 10, (2021) 104054, arXiv:2012.10842 [gr-qc].